

Cover Page



Universiteit Leiden



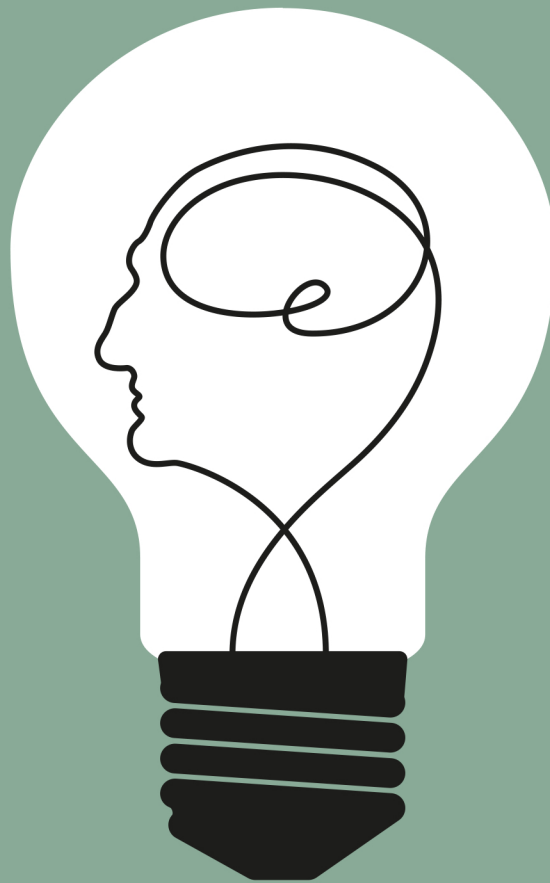
The handle <http://hdl.handle.net/1887/25831> holds various files of this Leiden University dissertation.

**Author:** Nabuurs, Rob Johannes Antonius

**Title:** Molecular neuroimaging of Alzheimer's disease

**Issue Date:** 2014-05-28

*Molecular Neuroimaging of Alzheimer's Disease*



R.J.A.Nabuurs



# *Molecular Neuroimaging of Alzheimer's Disease*

R.J.A.Nabuurs

## **Colophon**

Molecular Neuroimaging of Alzheimer's disease

© Rob J.A. Nabuurs 2014

Thesis Leiden University Medical Center

Cover illustration: Vincent Widlak

Lay-out: Wendy Schoneveld, [www.wenziD.nl](http://www.wenziD.nl)

Printed by: Gildeprint drukkerijen, Enschede

ISBN: 9789461086761

All rights reserved. No part of this book may be reproduced or transmitted, in any form or by any means, without written permission of the author.

# Molecular Neuroimaging of Alzheimer's Disease

Proefschrift

ter verkrijging van de graad van Doctor aan de Universiteit Leiden,  
op gezag van Rector Magnificus prof.mr. C.J.J.M. Stolker,  
volgens besluit van het College voor Promoties  
te verdedigen op woensdag 28 mei 2014  
klokke 15:00

door

**Rob Johannes Antonius Nabuurs**

geboren te Nijmegen in 1981

## **Promotiecommissie**

Promotor: prof.dr. M.A. van Buchem

Co-promotor: dr.ir. L. van der Weerd

Overige leden: prof.dr. B.J. Bacskai (Harvard University, Boston, USA)  
prof.dr. J.J.G. Geurts (Vrije Universiteit Medisch Centrum, Amsterdam)  
prof.dr. A.D. Windhorst (Vrije Universiteit, Amsterdam)  
prof.dr.ir. S.M. van der Maarel  
prof.dr. A.G. Webb  
dr. S.G. van Duinen

The work presented in this thesis was carried out at the department of Radiology at the Leiden University Medical Center.

Part of the research described in this thesis was supported by the Center for Translational Molecular Medicine ([www.ctmm.nl](http://www.ctmm.nl)), project LeARN (grant 02N-101).

Financial support by Internationale Stichting Alzheimer Onderzoek, to-BBB, Guerbet Nederland B.V., Philips Healthcare, ABN Amro and ChipSoft B.V. for the publication of this thesis is gratefully acknowledged.



# Content

Chapter 1	General Introduction	9
-----------	----------------------	---

## **PART ONE** | Native MRI contrast

Chapter 2	Introduction to MRI	19
Chapter 3	MRI artifacts in human brain tissue after prolonged formalin storage	31
Chapter 4	High-field MRI of single histological slices using an inductively coupled, self-resonant microcoil: application to <i>ex vivo</i> samples of patients with Alzheimer's disease	49
Chapter 5	MR microscopy of human amyloid- $\beta$ deposits: characterization of parenchymal amyloid, diffuse plaques, and vascular amyloid	63
Chapter 6	Detection of cortical changes in Alzheimer's disease at ultra-high field MRI	83

## **PART TWO** | Development of Molecular Imaging strategies

Chapter 7	MR-based molecular imaging of the brain: the next frontier	103
Chapter 8	Transmigration of beta amyloid specific heavy chain antibody fragments across the <i>in vitro</i> blood-brain barrier	119
Chapter 9	<i>In vivo</i> detection of amyloid- $\beta$ deposits using heavy chain antibody fragments in a transgenic mouse model for Alzheimer's disease	131
Chapter 10	Polyfluorinated bis-styrylbenzenes as amyloid- $\beta$ plaque binding ligands	151
Chapter 11	Bis-pyridylethenylbenzene as novel backbone for amyloid- $\beta$ binding compounds	177
Chapter 12	Summary and General Discussion	199

## APPENDICES

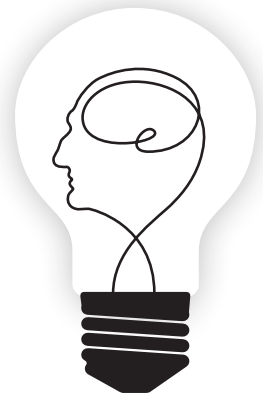
I	Building blocks of poly-fluorinated bis-styrylbenzenes	211
II	Samenvatting	221
III	Dankwoord	227
IV	Curriculum vitae	231
V	Publication list	235





# Chapter 1

General Introduction



Worldwide millions of elderly and their relatives suffer from the devastating effects of dementia, with Alzheimer's disease (AD) as its most common cause.<sup>1</sup> Age is its main risk factor, and as the worldwide average life expectancy is increasing, the incidence of dementia is expected to rise. Clinically, AD is characterized by a progressive loss of episodic memory in combination with impairment in other cognitive domains and behavioral changes. Eventually severe loss of cognition leaves the patient completely dependent, with death occurring on average nine years after manifestation of the first symptoms. As a result, AD represents an important socio-economic and public health concern.<sup>2</sup> Unfortunately, an effective therapy is currently not available, which is due to our incomplete understanding of the pathogenesis of AD. Our inability to detect the disease at its early stages prevents furthering our insight into the pathogenesis on the one hand, and on the other it prevents us to detect the disease at a stage early enough to expect a beneficial effect of treatment. Nowadays, a definitive diagnose of AD still requires an autopsy. Therefore, novel diagnostic methods are warranted that are capable of obtaining a definite diagnosis during life and preferably as early in the disease process as possible.

### Pathogenesis

Microscopic examination of AD brain tissue typically reveals the presence of both extracellular deposits of fibrillar amyloid- $\beta$  peptides and intracellular neurofibrillary tangles in the medial temporal lobe structures and cortical areas of the brain in combination with a deterioration of neurons and synapses. (Figure 1.1) These changes are assumed to play a vital role in the pathogenesis of the disease.

### Neurofibrillary tangles

Neurofibrillary tangles (NFTs) consist of abnormally phosphorylated tau proteins that predominantly accumulate in neurons. Normally, tau proteins promote the assembly of microtubule and their stability, and as such they are involved in structural and regulatory functions of the cytoskeleton.<sup>3,4</sup> However, when tau becomes hyperphosphorylated it exerts the exact opposite effect, leading to the disassembly of the same microtubules. The resulting

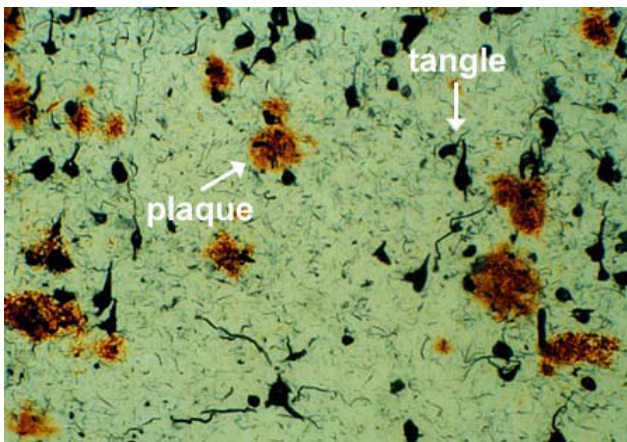


**Figure 1.1 Neuropathological characteristics of Alzheimer's disease**

AD is neuropathologically hallmarked by the cortical deposition of amyloid- $\beta$  peptides into amyloid or senile plaques that are surrounded by neurofibrillary tangles present in the axons and neuronal cell bodies.

loss of neuronal structure impairs axonal transport, thereby disturbing proper synaptic and neuronal signaling.<sup>3</sup> In addition, as hyperphosphorylated tau tends to aggregate into insoluble filaments, it becomes sequestered into NFTs deposited in neurons and neuronal processes, also known as neuropil threads. These NFTs further disrupt normal neuronal function and eventually lead to neuronal death.

Although tau-pathology is observed within several neurodegenerative disorders<sup>3</sup>, its characteristic topographical spreading observed in AD led to the description of a histological staging of the disease by Braak and Braak.<sup>5</sup> This AD staging sequentially describes the involvement of the transentorhinal and entorhinal cortex (stage I and II), the hippocampus (stage III and IV), and finally the isocortex (stage V and VI). Of all pathological hallmarks, tau pathology has shown the best clinicopathological correlation in AD patients.<sup>6</sup> However, the pathophysiological role of hyperphosphorylation and tangle formation is still incompletely understood.

### Deposition of amyloid- $\beta$

Amyloid- $\beta$  ( $A\beta$ ) peptide is generated by proteolytic cleavage of a transmembrane protein, amyloid precursor protein (APP), by  $\beta$ - and  $\gamma$ -secretase to form predominantly  $A\beta_{1-40}$  or  $A\beta_{1-42}$ . Under normal conditions, cerebral  $A\beta$  is either degraded or cleared from the brain by a balanced process of influx and efflux across the blood-brain barrier (BBB). According to the amyloid cascade hypothesis, AD is initiated by an imbalance in  $A\beta$  production and clearance.<sup>7,8</sup> This is supported by observations in familial AD, accountable for < 5% of all cases, in which mutations in the genes encoding for APP or parts of the secretase complexes cause  $A\beta$  overproduction. In the majority of cases, so called sporadic AD, a failure of  $A\beta$  clearance is thought to gradually increase cerebral levels of  $A\beta$  over time.

Its fibrillogenic nature causes high local concentrations of  $A\beta_{1-42}$  to aggregate, first into soluble oligomers. These eventually cluster into larger insoluble  $A\beta$  fibrils that allow the formation of  $\beta$ -sheet structures characteristic for amyloid. Serving as a seeding point this triggers the misfolding of other  $A\beta$  species, including the more soluble  $A\beta_{1-40}$ .

Histologically,  $A\beta$  deposits in the brain parenchyma can be classified into two distinct types: non-neuritic (diffuse) or neuritic (senile)  $A\beta$  plaques. Diffuse plaques typically only show up on  $A\beta$  immunohistochemistry, whereas no amyloid structure is detected by Congo red or Thioflavin staining.<sup>9</sup> In contrast, senile plaques consist of an amyloid core of predominantly  $A\beta_{1-42}$  surrounded by a neuritic corona bearing degenerative synaptic endings with hyperphosphorylated tau, together with activated astrocytes and microglia.<sup>9</sup>

In addition, deposits of amyloid, mainly  $A\beta_{1-40}$ , can also be found in the cerebral vessel wall where it leads to a loss of structure and rigidity. This so-called cerebral amyloid angiopathy (CAA) can occur by itself without any parenchymal involvement, and is considered a major cause of cerebral microbleeds, hemorrhages and cognitive loss. In 90% of all cases, however, AD and CAA are concomitant.<sup>10</sup>

Similar to tau, the presence of  $A\beta$  deposits can be staged based on the spread of cortical involvement: (A) only basal portions of the isocortex; (B) throughout the isocortex except the primary cortices and with the hippocampus mildly affected; (C) the entire isocortex.<sup>5</sup> A correlation between cerebral  $A\beta$  accumulation and cognitive status has been shown, albeit less significant

in comparison to tau. However, the soluble pool of (oligomeric) A $\beta$  are thought to contribute more to A $\beta$ -mediated pathology than the histological insoluble A $\beta$  deposits; and the occurrence of oligomers has been shown to correlate better with the cognitive status.<sup>11</sup>

### Hypothetical models

Based on observations in large-scale post-mortem studies in the general aging population, the AD induced neurodegeneration is estimated to start two decades before clinical onset and is thought to have reached a plateau at the time of clinical presentation.<sup>12,13</sup> (Figure 1.2) The exact underlying pathogenesis responsible for the A $\beta$  imbalance, the hyperphosphorylation of tau and their intimate association remains one of the major unresolved questions regarding AD. What triggers their formation and is their presence a cause or only a consequence of the disease? Besides the aforementioned amyloid cascade hypothesis, some claim that the dyshomeostasis of cerebral iron plays an intricate and crucial role. Increased cortical accumulation of iron is often found within the premises of the amyloid plaques. As its presence is known to lead to formation of reactive oxygen species that induce neurotoxicity, this could eventually lead to neuronal cell death and loss of cognitive function. Interestingly, not only APP and A $\beta$  but also tau is involved in the chelation and transport of cerebral iron. Others go one step further: as iron is essential for the enzymes responsible the maintenance of myelin structure and integrity, they have suggested that a mismatch in de- and remyelination might change iron homeostasis leading to increased iron deposition, which, subsequently, could lead to increased production of A $\beta$  and tau.<sup>14</sup> However, as yet no clear single explanation regarding the pathogenesis of AD has been found.

### Diagnosis

At present, the definite diagnosis of AD can only be made based on microscopical detection of A $\beta$  and NFTs in brain tissue, which in general happens at autopsy. Clinically, the diagnosis “probable AD” can be made at best based on criteria set by the Diagnostic and Statistical Manual of Mental Disorders (DSM IV) and the NINCDS-ADRDA (National Institute of Neurological and Communicative Disorders and Stroke and the Alzheimer’s Disease and Related Disorders Association).<sup>15</sup> These criteria require a detailed (hetero) anamnestic assessment of the type and course of symptoms, while other somatic causes of dementia, such as cerebral infarcts, neoplasms or hypothyroidism, have to be excluded. Clinically, AD is characterized by progressive loss of memory and gradual decline of other cognitive domains affecting social and occupational functioning. Typically, the symptoms start with isolated short-term memory loss. Over time, long-term memory becomes involved too. Characteristically for AD, long-term memory loss occurs in a retrograde manner with early memories being preserved longer than recent ones. Apart from memory loss, apathy occurs as well as cognitive loss in other domains resulting in difficulties in speech (aphasia), practical skills (apraxia), recognition (agnosia) and/or executive functions. As a result, patients become restricted in their activities of daily living (ADL) and lose their ability to safely support themselves, which eventually leaves them fully dependent on family or institutionalized care.

The criteria developed by NINCDS-ARDA provide a clinical diagnostic tool with a relatively high sensitivity and specificity (>80%) to distinguish AD patients from elderly people without dementia.

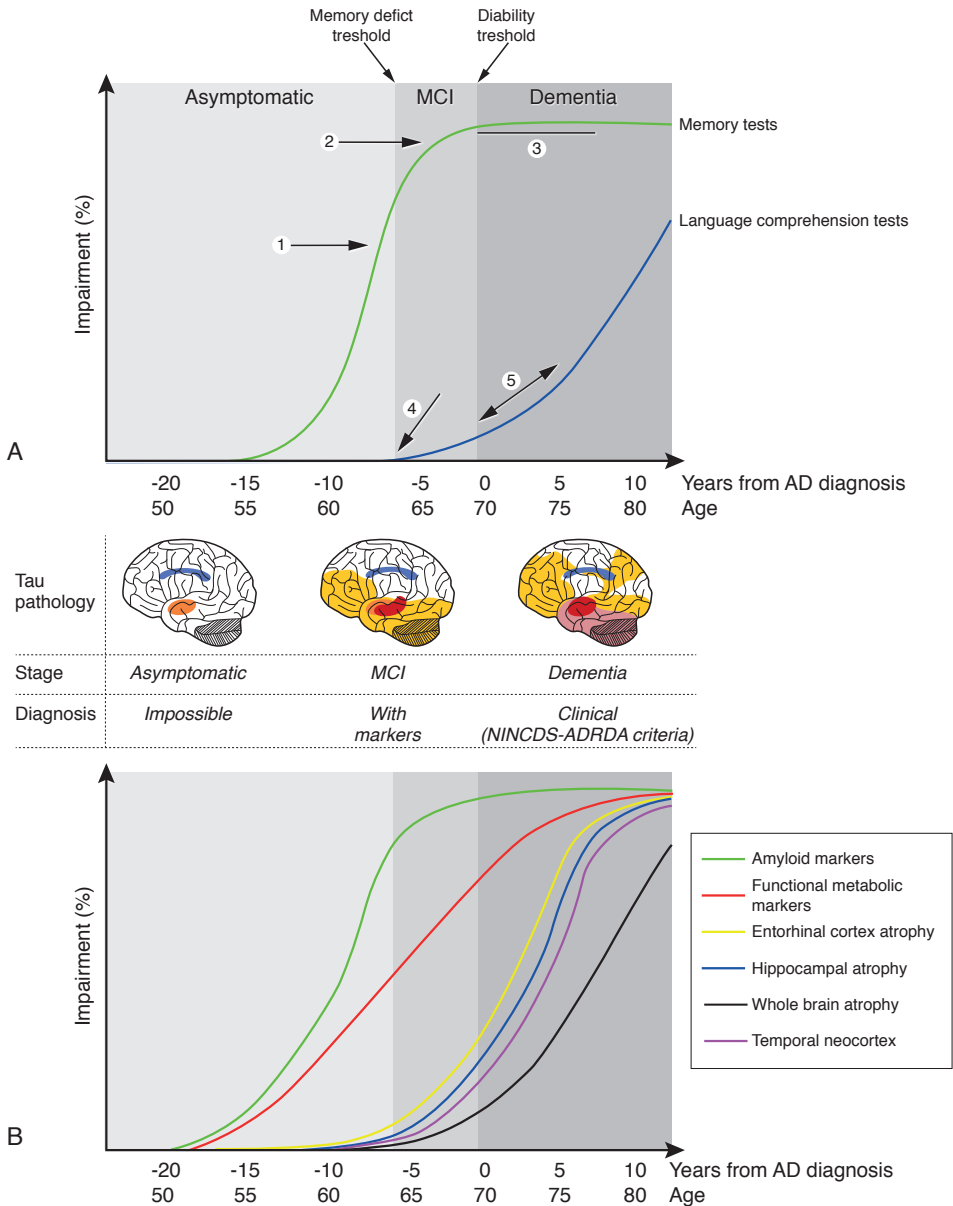


**Figure 1.2** A theoretical model of the natural progression of cognitive and biological markers of Alzheimer's disease (reprinted and adapted with permission<sup>13</sup>)

(A) Regarding cognition the memory tests are among the first to change (1). As they quickly reach their maximal level of impairment (2), they are useful for diagnosis at MCI, but are less adequate to track disease progression (3). Later in the disease, the language comprehension starts to change with mild or no impairment during MCI (4), and a steep increase during dementia (5). (B) Amyloid markers, e.g.  $[A\beta_{42}]$  in the cerebral spine fluid and amyloid PET, represent the earliest detectable changes in AD, but plateau at the MCI stage. Metabolic and functional biomarkers, like  $^{18}F$ -FDG PET and fMRI, are abnormal at the MCI stage, and continue to change far into the dementia stage. Cerebral atrophy appears later and follows a temporal pattern mirroring the deposition of tau pathology.

Using these criteria, the distinction between AD and other neurodegenerative dementias however is less accurate (23–88%).<sup>16</sup> In an earlier stage of the disease when objective memory complaints are present but daily functioning remains normal and other cognitive domains are still intact, subjects qualify for the diagnosis mild cognitive impairment (MCI). However, not all MCI subjects are believed to have AD and to develop dementia later in life. (Figure 1.2)

### The role of imaging biomarkers in AD

Although its precise etiology remains unknown, the onset of AD is assumed to start two decades before the induced neuronal damage has reached a sufficient level to lead to noticeable clinical symptoms.<sup>12,13</sup> Our incomplete understanding of the pathophysiology of AD is partly to be blamed on our inability to detect the early phases of the disease reliably *in vivo*, and our lack of understanding of the pathophysiology of AD is a major hurdle in developing effective treatment. Apart from being instrumental to the development of AD treatment, having early markers of the disease is also relevant since it would allow distinguishing among elderly individuals with memory loss between those in whom this symptom is an early manifestation of AD and progression to dementia can be expected from those in whom functional loss is not expected to spread to other cognitive domains or when other diseases than AD play a role. Furthermore, once effective treatment will be available, it would be useful to detect even earlier, preferably presymptomatic, stages of the disease, in order to have a wider time window for treatment. Finally, a test that would allow for detection of the early stages of the disease would also be a very useful tool to assess the efficacy of candidate treatment in trials.

In general such a diagnostic method or so-called biomarker refers to an objectively measurable physiologic, biochemical, or anatomic parameter that represents a (patho)physiologic process or a therapeutic response.<sup>17</sup> In search of a biomarker for AD major efforts have been made to develop methods that allow non-invasive *in vivo* detection of AD-specific changes using neuroimaging techniques.

### Structural, functional and metabolic neuroimaging techniques

Initially CT and MRI scans of the brain were just used in patients with dementia to detect possible treatable causes of the symptoms, such as subdural hematomas and meningiomas, but not for the detection of the more prevalent neurodegenerative disorders in such patients. Later, these techniques were used to detect radiological manifestations of these neurodegenerative diseases. In AD patients structural MRI studies revealed specific patterns of regional cerebral atrophy. Severity of atrophy was observed to correlate well with loss of cognitive function as well as with post-mortem Braak staging. Of all putative biomarkers, volumetric measures of hippocampal and medial temporal lobe atrophy showed the best correlation with the severity of clinical symptoms. According to the dynamic biomarker model (Figure 1.2), however, brain atrophy is a late stage event, and therefore structural MRI may not be the method of choice for early or pre-symptomatic diagnosis.

In addition to brain atrophy, the feasibility to detect the histological hallmarks of AD using MRI has also been explored. In general these efforts have focused on detecting individual amyloid plaques. Recently it was demonstrated that increased iron accumulation in amyloid plaques combined with the aggregated protein itself induce a magnetic susceptibility effect, visible as

hypointense foci on  $T_2^*$ -weighted or susceptibility-weighted (SW) MRI in the cerebral cortex of transgenic AD mouse models and in human post-mortem brain slices.<sup>18-20</sup> The high magnetic field strengths needed to obtain these results only recently became available for *in vivo* human use. These high field whole body human MRI systems ( $\geq 7$  Tesla) may offer new possibilities to specifically detect these neuropathological hallmarks of AD; perhaps even at an earlier stage than the traditional MRI biomarker of brain atrophy.

Besides these conventional MRI techniques the versatile character of MRI offers additional possibilities to study changes caused by AD, as has been extensively reviewed elsewhere.<sup>21-23</sup> In short, functional MRI (fMRI) reflects brain activation when a specific task is performed, and in subjects at risk to develop AD fMRI discovered areas of hyperactivation following specific tasks. Using task-free resting state fMRI a decrease in activity of the brain's default functional network was seen in AD subjects. Additionally, specific regions of cerebral hypoperfusion were found in relation to AD using non-invasive arterial spin labeling MR perfusion techniques. Whereas microstructural changes due to AD may not be directly visible, their effect on bulk MR signal could allow detection by quantitative MRI techniques, as shown by initial studies using magnetic transfer imaging (MTI), diffusion tensor imaging (DTI) and MR relaxometry. Finally, changes in brain metabolites have been observed in AD subjects as MR spectroscopy revealed a consistent decrease in *myo*-inositol combined with elevated levels of *N*-acetylaspartate (NAA). Although these MRI techniques just recently gained much interest, currently none has been characterized and validated well enough yet to be included as a neuroimaging biomarker for AD.

### **Molecular imaging techniques**

Direct visualization of the histological hallmarks of AD has been attempted by the application of molecular imaging strategies. These strategies aim for the *in vivo* imaging of specific molecular or cellular signatures of the disease with the aid of targeted contrast agents. Thus far two molecular imaging strategies have been developed for AD: detection of glucose hypometabolism using  $^{18}\text{F}$ - fluorodeoxyglucose (FDG) PET, and visualization of cerebral amyloid load by radioactive PET ligands. FDG-PET reflects brain metabolism, which in general is a function of neuronal or synaptic activity. Typically for AD is a decrease in FDG uptake in the lateral temporal-parietal, posterior cingulate and precuneus regions that indicates impaired neuronal activity in these areas.<sup>12</sup> Even when corrected for brain atrophy these patterns of glucose hypometabolism were seen. Despite the fact that these patterns of glucose hypometabolism occur prior to the development brain atrophy detectable on neuroimaging, following the amyloid cascade hypothesis their specificity is limited and they are considered a relatively late phenomenon. Therefore major efforts have been made to develop imaging agents that specifically bind to AD's neuropathological hallmarks. Based on known histological amyloid dyes, like Congo Red and Thioflavin, various radioactive contrast agents have been synthesized for the *in vivo* detection of cerebral amyloid by either PET or SPECT imaging. The initial *in vivo* breakthrough came with the development of Pittsburgh Compound B (PiB), a neutral  $^{11}\text{C}$  derivative of Thioflavin.<sup>24</sup> Despite many *in vivo* human studies its broad applicability is hampered by its short radioactive half-life ( $< 20$ min), requiring the availability of a cyclotron and therefore its application is mainly limited to research. Another limitation of PiB PET imaging is the inability to distinguish between  $\text{A}\beta$

deposits in parenchymal plaques and in the vessel wall (as in CAA). Thus, A $\beta$  targeting imaging techniques are needed that can be performed on widespread neuroimaging platforms and that are able to discriminate between the different types of A $\beta$  deposits.

### **Aim of this thesis**

This thesis is aimed at the development of innovative diagnostic imaging techniques to detect the histological signatures of AD using emerging ultra-high field MRI technologies and molecular imaging strategies. The work in this thesis comprises two complementary parts.

**Part One** aims at developing novel MRI techniques for the *in vivo* detection of cortical changes in AD exploiting innovative ultra-high field MRI technology (7 Tesla). Initially, we focused on developing techniques optimized for tissue iron detection at ultra-high magnetic field. Then we strived to obtain a better understanding of the source of native MRI contrast changes specific for AD neuropathology by studying post-mortem AD tissue at experimental MRI systems with optimized MR techniques and by systematically comparing MRI and histological data.

The main objective of **Part Two** is the detection of A $\beta$  deposits using targeted contrast agents. Firstly, we aimed at developing imaging probes that allow distinguishing specific types of A $\beta$  deposition, e.g. vascular versus parenchymal, based on llama antibody fragments. Secondly, we aimed at improving small amyloid binding molecules to serve as *in vivo* imaging probes for  $^{19}\text{F}$  MRI or other imaging modalities.



## References

1. Ferri, CP, Prince, M, Brayne, C, *et al.* Global prevalence of dementia: a Delphi consensus study. *Lancet.* 2005; 366:2112-2117.
2. WHO. World Health Report 2003 - Shaping the future.
3. Ballatore, C, Lee, VM, and Trojanowski, JQ. Tau-mediated neurodegeneration in Alzheimer's disease and related disorders. *Nat Rev Neurosci.* 2007; 8:663-672.
4. Alonso, AC, Li, B, Grundke-Iqbal, I, *et al.* Mechanism of tau-induced neurodegeneration in Alzheimer disease and related tauopathies. *Curr Alzheimer Res.* 2008; 5:375-384.
5. Braak, H and Braak, E. Neuropathological staging of Alzheimer-related changes. *Acta Neuropathol.* 1991; 82:239-259.
6. Riley, KP, Snowdon, DA, and Markesbery, WR. Alzheimer's neurofibrillary pathology and the spectrum of cognitive function: findings from the Nun Study. *Ann Neurol.* 2002; 51:567-577.
7. Hardy, J and Selkoe, DJ. The amyloid hypothesis of Alzheimer's disease: progress and problems on the road to therapeutics. *Science.* 2002; 297:353-356.
8. Hardy, J. The amyloid hypothesis for Alzheimer's disease: a critical reappraisal. *J Neurochem.* 2009; 110:1129-1134.
9. Duyckaerts, C, Delatour, B, and Potier, MC. Classification and basic pathology of Alzheimer disease. *Acta Neuropathol.* 2009; 118:5-36.
10. Weller, RO, Preston, SD, Subash, M, *et al.* Cerebral amyloid angiopathy in the aetiology and immunotherapy of Alzheimer disease. *Alzheimers Res Ther.* 2009; 1:6.
11. McLean, CA, Cherny, RA, Fraser, FW, *et al.* Soluble pool of Abeta amyloid as a determinant of severity of neurodegeneration in Alzheimer's disease. *Ann Neurol.* 1999; 46:860-866.
12. Jack, CR, Knopman, DS, Jagust, WJ, *et al.* Hypothetical model of dynamic biomarkers of the Alzheimer's pathological cascade. *Lancet Neurol.* 2010; 9:119-128.
13. Frisoni, GB, Fox, NC, Jack, CR, Jr., *et al.* The clinical use of structural MRI in Alzheimer disease. *Nat Rev Neurol.* 2010; 6:67-77.
14. Bartzokis, G. Alzheimer's disease as homeostatic responses to age-related myelin breakdown. *Neurobiol Aging.* 2011; 32:1341-1371.
15. McKhann, G, Drachman, D, Folstein, M, *et al.* Clinical diagnosis of Alzheimer's disease: report of the NINCDS-ADRDA Work Group under the auspices of Department of Health and Human Services Task Force on Alzheimer's Disease. *Neurology.* 1984; 34:939-944.
16. Ballard, C, Gauthier, S, Corbett, A, *et al.* Alzheimer's disease. *Lancet.* 2011; 377:1019-1031.
17. Jack, CR, Jr., Knopman, DS, Jagust, WJ, *et al.* Hypothetical model of dynamic biomarkers of the Alzheimer's pathological cascade. *Lancet Neurol.* 2010; 9:119-128.
18. Chamberlain, R, Wengenack, TM, Poduslo, JF, *et al.* Magnetic resonance imaging of amyloid plaques in transgenic mouse models of Alzheimer's disease. *Curr Med Imaging Rev.* 2011; 7:3-7.
19. Meadowcroft, MD, Connor, JR, Smith, MB, *et al.* MRI and histological analysis of beta-amyloid plaques in both human Alzheimer's disease and APP/PS1 transgenic mice. *J Magn Reson Imaging.* 2009; 29:997-1007.
20. van Rooden, S, Maat-Schieman, ML, Nabuurs, RJ, *et al.* Cerebral amyloidosis: post-mortem detection with human 7.0-T MR imaging system. *Radiology.* 2009; 253:788-796.
21. Jack, CR, Jr. Alzheimer disease: new concepts on its neurobiology and the clinical role imaging will play. *Radiology.* 2012; 263:344-361.
22. Li, TQ and Wahlund, LO. The search for neuroimaging biomarkers of Alzheimer's disease with advanced MRI techniques. *Acta Radiol.* 2011; 52:211-222.
23. Risacher, SL and Saykin, AJ. Neuroimaging and other biomarkers for Alzheimer's disease: the changing landscape of early detection. *Annu Rev Clin Psychol.* 2013; 9:621-648.
24. Klunk, WE, Engler, H, Nordberg, A, *et al.* Imaging brain amyloid in Alzheimer's disease with Pittsburgh Compound-B. *Ann Neurol.* 2004; 55:306-319.

## PART ONE | Native MRI contrast

1 Department of Radiology, Leiden University Medical Center, the Netherlands

2 Department of Medical Physics and Bioengineering, University College London, United Kingdom

3 Lysholm Department of Neuroradiology, National Hospital for Neurology and Neurosurgery, London, United Kingdom

4 Centre for Advanced Biomedical Imaging, Department of Medicine and Institute of Child Health, University College London, United Kingdom

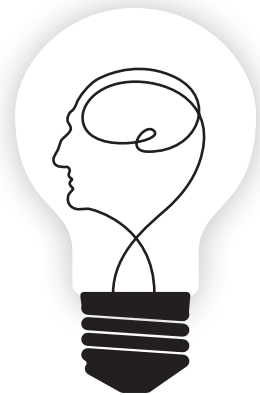
5 Department of Anatomy & Embryology, Leiden University Medical Center, the Netherlands

# Chapter 2

## Introduction to MRI

*Extracted from Essential Bioimaging Methods (2009); Ch.13, 263-293*

**Rob J.A. Nabuurs<sup>1</sup>**  
David L. Thomas<sup>2</sup>  
John S. Thornton<sup>3</sup>  
Mark F. Lythgoe<sup>4</sup>  
Louise van der Weerd<sup>1,5</sup>



## Abstract

Over recent years, magnetic resonance imaging (MRI) has become an essential tool for the investigation of human brain disease. This chapter describes some of the principal MRI methods that are currently used for neuroimaging: T<sub>1</sub>, T<sub>2</sub>, susceptibility-contrast, diffusion and magnetisation transfer imaging. The mechanisms underlying the sensitivity of these techniques to pathophysiological state are explained.

## Introduction

The present review will be restricted to the most common and for this thesis relevant applications of magnetic resonance imaging (MRI) in the brain, namely the depiction of hydrogen nuclei (protons) of mobile water molecules. The utility of MRI with respect to disease lies in the sensitivity of the technique to both micro- and macroscopic molecular motions. Nervous tissue consists of 70-80% water by weight, these water molecules being distributed through a variety of microscopic environments and physiological compartments. It is possible to generate MR images whose contrast reflects, amongst other factors, random molecular rotational motions ( $T_1$  and  $T_2$ ), random translational motion (diffusion), exchange with macromolecular protons (MTC) and blood flow (perfusion). The concentration and mobility of water molecules is modified in many pathologies and this is the basis of the high sensitivity of MRI to cerebral disease processes.

Furthermore, MRI contrast agents can also change these parameters allowing detection. In recent years this led to the emerging field of molecular and cellular imaging, where contrast agents targeted against disease-specific hallmarks or cells labelled with such agents are explored for early diagnostics and therapy follow-up. Also within the field of experimental neuroimaging this has taken a leap. A more extensive review is given in **Chapter 7**.

## Biophysical background and methods

Some important principles are discussed here to provide a background for the rest of this article. For a more detailed introduction to MRI the reader is refer to various excellent textbooks.<sup>1,2</sup> Protons possess a nuclear magnetic moment (or 'spin'). In the absence of an external magnetic field these magnetic moments are randomly distributed in every direction. In the presence of a magnetic field however, a thermal equilibrium is achieved between spins oriented parallel and antiparallel to the magnetic field. The result is a net macroscopic magnetic moment, the bulk magnetisation ( $M_0$ ), orientated in the direction of the external field (conventionally taken to be the z-axis). The individual spins precess around the z-axis at the Larmor frequency ( $\omega$ , rad s<sup>-1</sup>), which is proportional to the external magnetic field ( $B_0$ , Tesla):

$$\omega = \gamma B_0 \quad [2.1]$$

where  $\gamma$  is a constant called the gyromagnetic ratio (26.751 10<sup>7</sup> rad T<sup>-1</sup> s<sup>-1</sup> for protons).

## Relaxation

$M_0$  is proportional to the total number of protons present in the sample, and hence is also called the proton density. To be able to distinguish the magnetisation  $M_0$  from the external magnetic field,  $M_0$  is rotated by 90° into the transverse (xy) plane using a radiofrequency (RF) pulse at the Larmor frequency. Immediately following this 90° pulse, the initial magnetisation level can be detected. In time, the thermal equilibrium is restored, and the magnetisation vector returns to the z-axis. The characteristic times involved in this process are the spin relaxation

times: longitudinal relaxation time ( $T_1$ ) for the restoration of the magnetisation along the z-axis, and the transverse relaxation time ( $T_2$ ) for the decay in the  $xy$ -plane. (**Figure 2.1**)

### $T_2$ and $T_2^*$

The transverse relaxation time  $T_2$  is also called the spin-spin relaxation time, referring to the molecular interactions behind the transverse relaxation process. The protons experience intramolecular dipolar interactions between two protons within the same molecule, as well as intermolecular interactions with protons of neighbouring molecules. This interaction becomes more efficient when the contact time between protons is relatively long, *e.g.* in viscous media. When the rotational correlation time of the molecules is short, as is the case for free water molecules,  $T_2$  is relatively long ( $\sim 3$  sec). Water molecules interacting with macromolecules or solid surfaces generally have slower tumbling rates, which leads to a reduction in the relaxation time. Because water mobility often varies substantially between tissue types, and changes in situations of cellular stress,  $T_2$ -dependent contrast is very commonly used in MRI studies.

In addition to these spin-spin interactions, the transverse magnetisation is also perturbed by small local magnetic field differences. This results in different (local) Larmor precession frequencies of the spins under observation and thus in a loss of phase coherence causing a faster decay of the magnetisation in the  $xy$ -plane. The corresponding apparent relaxation time is called  $T_2^*$  to distinguish it from the intrinsic transverse relaxation time  $T_2$ .

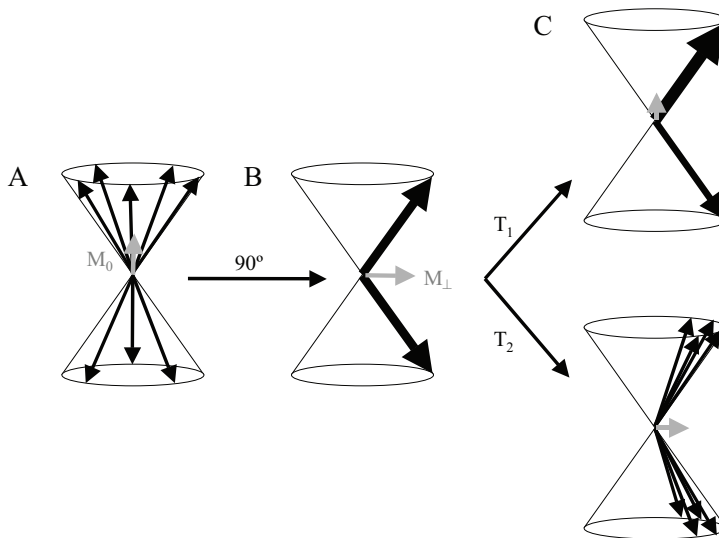


**Figure 2.1 Schematic representation of the nuclear magnetic resonance principle**

(A) The sample magnetisation  $M_0$  arises from the uneven distribution of the spins (black arrows) between two different states, either parallel or anti-parallel to the main magnetic field  $B_0$ . The spins precess around the main magnetic field direction with the Larmor frequency  $\omega$ . (B) After the application of a  $90^\circ$  pulse, the original distribution is shifted into the horizontal plane and phase coherence is established (the spins are all aligned along the same axis). The result is a sample magnetisation  $M_1$ . (C) The spins return to the original distribution through  $T_1$  relaxation. The loss of phase coherence is called  $T_2$  relaxation. Both processes occur simultaneously but are depicted separately in the picture.

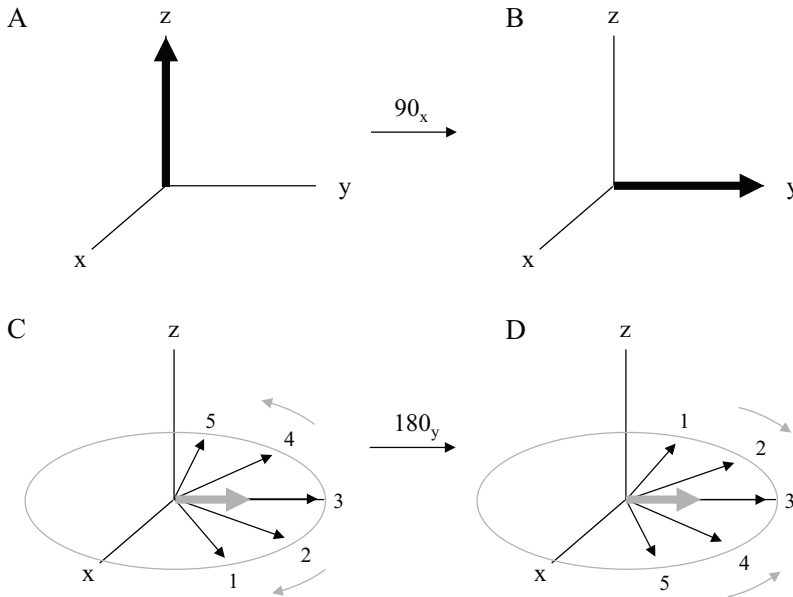


**Figure 2.2 Spin echo MRI sequence**

(A) Diagram showing the fanning out and refocussing of magnetisation in the course of a spin-echo sequence. (B) After the application of a  $90^\circ$  pulse, the original distribution is shifted into the horizontal plane. (C) The loss of phase coherence is primarily due to  $T_2^*$  effects. (D) The  $180^\circ$  pulse flips the spins in the  $xy$ -plane, and the magnetisation refocusses along the  $y$ -axis. (E) The attenuation of the net magnetisation vector is due to  $T_2$  relaxation.

This field-disturbing effect can be exploited as a source of contrast in tissue, since such magnetic field inhomogeneities typically occur at interfaces of structures with differing magnetic susceptibilities, like soft tissue and bone, or tissue and blood.  $T_2^*$  contrast is of specific importance in blood oxygenation level dependent (BOLD) imaging, which is widely used in functional MRI investigations.<sup>3</sup> The paramagnetic nature of deoxygenated blood generates magnetic field gradients in blood vessels and surrounding tissues, leading to signal loss in  $T_2^*$  weighted images. Fast  $T_2^*$  weighted imaging is performed continuously to track transient changes in the magnetic field disturbances associated with the balance between oxyhemoglobin and deoxyhemoglobin in the blood, thus providing information on local neuronal activity. The second important application of  $T_2^*$  contrast is its use in contrast enhanced MRI.<sup>4</sup> Specific exogenous (super)paramagnetic contrast agents, analogous to the tracers used in nuclear medicine, are being developed continuously in order to target specific areas or molecules, thus providing a means to map molecular events *in vivo*. Most commonly used  $T_2/T_2^*$  contrast agents are iron oxide particles, causing hypo-intensities on the corresponding images by lowering  $T_2/T_2^*$ , hence the name ‘negative’ contrast agents.

### $T_2$ and $T_2^*$ measurements

Measuring relaxation times rather than making weighted images allows the quantification of observed changes. As already described, for detection the bulk magnetisation  $M_0$  is rotated by

90° into the *xy*-plane. The ensuing loss of phase coherence due to  $T_2^*$  effects can be reversed by the application of a series of 180° RF pulses following the initial 90° RF pulse, forming the so-called Spin-Echo (SE) sequence. The restoration of coherent magnetisation between the 180° pulses is called an echo. The amplitude of this echo is only attenuated by  $T_2$  relaxation.

**(Figure 2.2)**

$T_2^*$  can be measured by means of gradient echoes. In the spin-echo sequence the 180° pulse reverses the effects of local field inhomogeneities, whereas in a gradient echo sequence the echo is generated by reversing a magnetic field gradient. The main difference between a spin echo and a gradient is that the gradient echo does not refocus the dephasing due to field inhomogeneities, and therefore the echo is weighted according to  $T_2^*$  rather than  $T_2$ . In addition to its use in  $T_2^*$  imaging, gradient echoes are commonly used in rapid imaging sequences, as the echo time can be made much shorter than in spin echo sequences.

**$T_1$**

The other relaxation time must be considered is the longitudinal relaxation time  $T_1$ , also referred to as the spin-lattice relaxation time. The mechanisms behind this relaxation are complex, but it is facilitated by the presence of microstructures (macromolecules, membranes etc.), also called the lattice, that via dipolar interactions can absorb the energy of the excited protons. This energy transfer is most efficient when the rotational correlation rate of the molecules is in the same range as the Larmor frequency. In practice this means that  $T_1$  becomes shorter as the molecular mobility decreases, but increases again for very slow molecular motion, as in solids. Both  $T_1$  and  $T_2$  reflect the properties of the physical micro-environment of water in tissue, albeit not in exactly the same way. Commonly used paramagnetic contrast agents (e.g. gadolinium or manganese-containing particles) decrease the longitudinal relaxation time  $T_1$  leading to positive contrast.

**$T_1$  measurements**

The most well-known sequence to measure  $T_1$  is the inversion recovery sequence. This sequence starts with a 180° RF pulse causing inversion of  $M_0$ , which then gradually recovers to its equilibrium. To detect the amount of magnetisation left, a 90° pulse is applied after a range of delay times. This rotates the magnetisation into the *xy*-plane, where it can be detected. **(Figure 2.3)** From the different delay times and the corresponding residual magnetisation levels,  $T_1$  can be calculated.

## Diffusion

Up to now, the translational motion of individual water molecules has not been considered. However, all molecules in a fluid are subject to Brownian movements, the extent of this motion depending on the temperature and the viscosity of the fluid. When an ensemble of molecules is followed in time, the root mean square displacement ( $x$ , m) shows a  $\sqrt{t}$  dependence:

$$x = \sqrt{2Dt} \quad [2.2]$$



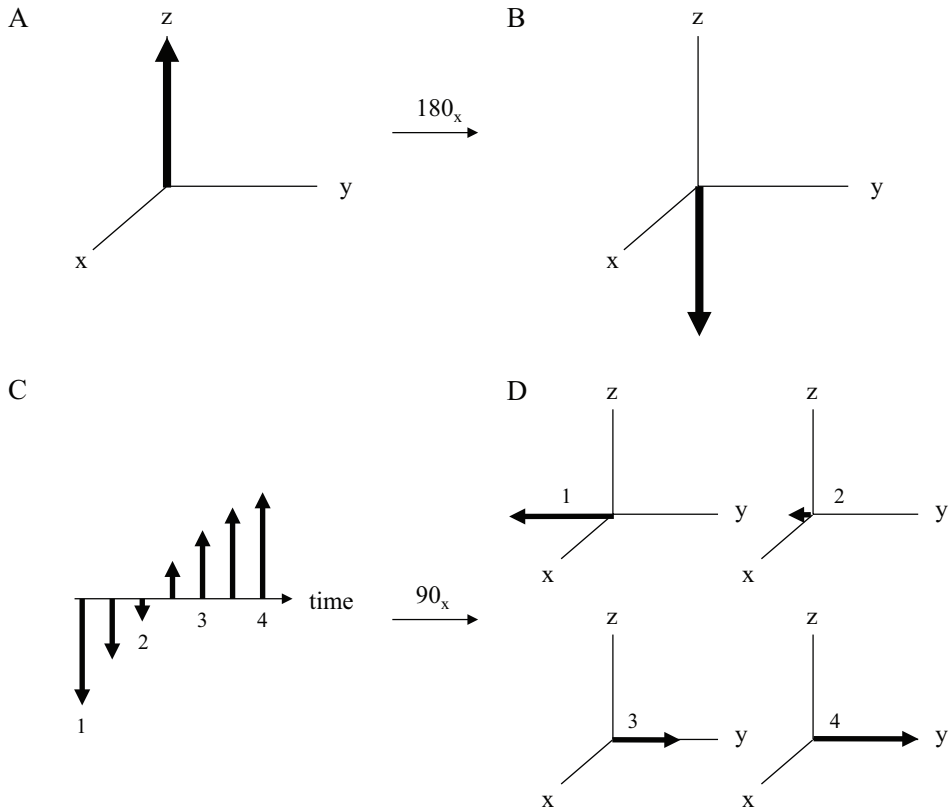


**Figure 2.3 Inversion recovery MRI sequence**

(A) Diagram showing the magnetisation changes during an inversion recovery sequence. (B) The  $180^\circ$  pulse inverts the magnetisation  $M_0$ . (C) In time, the magnetisation returns to equilibrium due to  $T_1$  relaxation. (D)  $90^\circ$  pulses are applied to detect the residual magnetisation at a number of time points. After each  $90^\circ$  pulse, a waiting time is introduced to let the magnetisation return to equilibrium, after which the next cycle of  $180^\circ$  -  $90^\circ$  pulses is performed.

where  $D$  is the bulk diffusion coefficient of the fluid ( $\text{m}^2 \text{s}^{-1}$ ),  $t$  is the displacement time (s) and  $d$  ( $= 1, 2, \text{ or } 3$ ) is the dimensionality of the diffusion displacement. Normally, the displacement distribution of all molecules is Gaussian, where the mean displacement distance increases with increasing displacement times. However, if the molecules encounter barriers to diffusion, e.g. cell membranes, these determine the maximum displacement. These boundary restrictions imply that the displacement distribution is no longer Gaussian and is going to depend on the diffusion time. As a result, the measured apparent diffusion coefficient (ADC) is smaller than the intrinsic  $D$ . This ADC value is sensitive to the number of barriers, their geometry and their permeability: in other words to the tissue microstructure.

The above is true if isotropic diffusion can be assumed, *i.e.* diffusion that exhibits no directionality. Many biological tissues have a microstructure that favors molecular motion in a certain direction. In the brain, diffusional anisotropy occurs primarily in white matter tracts, caused by the myelin sheaths and other structures surrounding the nerve fibers, which restrict diffusion perpendicular to the axonal length. The anisotropic diffusion that arises when displacement along one direction

occurs more readily than along another is defined by a diffusion tensor, and diffusion tensor imaging (DTI) is the term used for measurements of the full diffusional properties of the sample in all three dimensions.<sup>5</sup>

### Diffusion measurements

The ADC can be measured using a pulsed field gradient (PFG) experiment. In this experiment a sequence of two pulsed magnetic field gradients of equal magnitude but opposite sign and separated by an interval  $\Delta$  temporarily change the resonance frequency of the observed spins (Eqn. 2.1) as a function of their position. If the spins remain at exactly the same position, the effects of the opposing gradient pulses compensate each other. However, as soon as translational motion occurs, the gradients induced frequency shifts do not exactly compensate each other anymore and a phase shift occurs. Because diffusion is random in all directions, no net phase shift results, but phase coherence is partially lost, resulting in attenuation of the echo amplitude. (**Figure 2.4**) The amount of this attenuation is determined by the length, amplitude and separation of the gradient pulses, summarised in the so-called b factor, and by the mean translational distance travelled during the interval  $\Delta$ , which depends on the ADC. The signal intensity in a diffusion-weighted image (DWI) can therefore be described as:

$$S_b = S_0 e^{-b \cdot \text{ADC}} \quad [2.3]$$

where  $S_b$  is the DWI signal intensity and  $S_0$  is the signal without any diffusion gradients applied.

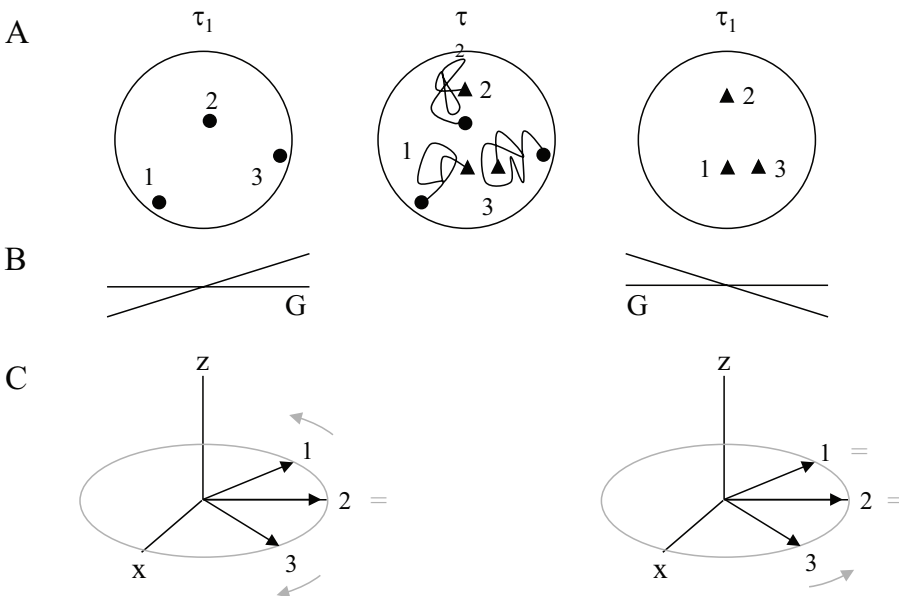


**Figure 2.4** The principle of diffusion weighted MRI

(A) Water diffusion for three different spins within a sample. (B) Two diffusion gradients are applied with opposite sign and a delay time  $\tau$  between them. (C) Diffusing spins experience different phase shifts (dependent on their position in the direction of the applied diffusion gradient) and are incompletely refocused, leading to a net loss in signal intensity

## Magnetisation Transfer Contrast

A certain fraction of protons in tissue exist in a so-called 'bound' state, *i.e.* their motion is restricted because they are part either of macromolecules, or of water molecules within the hydration layers around macromolecules. These protons possess very short  $T_2$  relaxation times ( $<100 \mu\text{s}$ ) and hence are not accessible by standard spin-echo MRI methods. With currently available small-bore technology, minimum echo times are of the order of several ms, and hence the signal from these protons has already decayed before signal acquisition. While simple models for proton relaxation behaviour predict that such a proton population will have some influence upon  $T_1$  and  $T_2$ , Wolff and Balaban<sup>6</sup> proposed the method of magnetisation transfer contrast (MTC) imaging<sup>7</sup>, as a more direct means of probing these 'bound' protons.

MTC imaging is based on an inverse Fourier relationship between  $T_2$  and the range of frequencies over which protons respond to RF excitation: protons in the 'bound' fraction possess a very short  $T_2$  and hence exhibit a broad resonance width ( $\sim 20 \text{ kHz}$ ) in the frequency domain. Conversely, bulk water protons have a long  $T_2$  with a correspondingly narrow ( $\sim 10 \text{ Hz}$ ) frequency domain resonance. **(Figure 2.5A)** This difference can be used to excite the 'bound' fraction independently from the bulk protons. If RF energy is supplied at a frequency offset from the central Larmor frequency (typically 1-5 kHz) the magnetisation in the 'bound' fraction will be reduced by saturation, while, in the absence of exchange, the bulk water pool would remain unaffected. **(Figure 2.5B)** However, on the time-scale of a typical MRI experiment there is a significant exchange of magnetisation between the two proton fractions, either by chemical exchange or by magnetic interactions. Since the 'bound' proton magnetisation has been reduced by the off-resonance irradiation, such exchange also leads to a reduction in both the magnitude of the observable bulk water magnetisation and its associated  $T_1$ . **(Figure 2.5C)** The degree of reduction depends upon both the relative sizes of the two fractions and upon the rate of magnetisation exchange between them; both of these factors may be influenced by tissue pathology.

### MTC measurements

In its most simple form, the MTC imaging experiment involves collecting an image ( $S_s$ ) which is preceded by a long ( $\sim 3 \text{ s}$ ) saturating off-resonance RF pulse, followed by a second image ( $S_0$ ) without a pre-saturation pulse.<sup>8</sup> The Magnetisation Transfer Ratio (MTR) is then quantified as: 
$$\text{MTR} = (S_0 - S_s) / S_0 \quad [2.4]$$

A high MTR signifies the presence of a significant proton pool associated with macromolecules or cellular microstructure *and* a significant exchange of magnetisation between these protons and those of the bulk water. Reduction of the MTR suggests a disruption of tissue microstructure, the most successful application of MTC in experimental neuroscience being the investigation of pathological disruption of white matter due to demyelination.

In order to reduce imaging time, selective saturation of the 'bound' fraction may also be achieved by pulsed methods whereby gradient-echo images with short TR are obtained with a low angle excitation pulse preceded by a short ( $\sim 10 \text{ ms}$ ) off-resonance pulse.<sup>9</sup> If the repetition time is sufficiently short ( $\sim 100 \text{ ms}$ ) compared to the  $T_1$  relaxation time of the 'bound' pool, an equilibrium is established after a number of cycles, resulting in substantial saturation of the 'bound' fraction.

It should be noted that unless total selective saturation of the bound pool is achieved, a situation impossible to achieve in practice, the magnitude of the MTC effect is dependent upon the duration, intensity and frequency offset of the off-resonance pulses. Caution is therefore required in the quantitative comparison of MTC imaging results obtained using differing experimental schemes.

## Concluding remarks

The combination of appropriate imaging techniques can greatly elucidate our understanding of human brain pathologies. Prior clinical application the use of suitable animal models of disease or post-mortem human brain tissue can greatly aid the development of improved MRI techniques. This experimental imaging partnership has contributed to the development of novel imaging techniques, to the promotion of better diagnostic and prognostic measures, and to elucidation of the basic mechanisms of cellular injury leading to improved therapies.

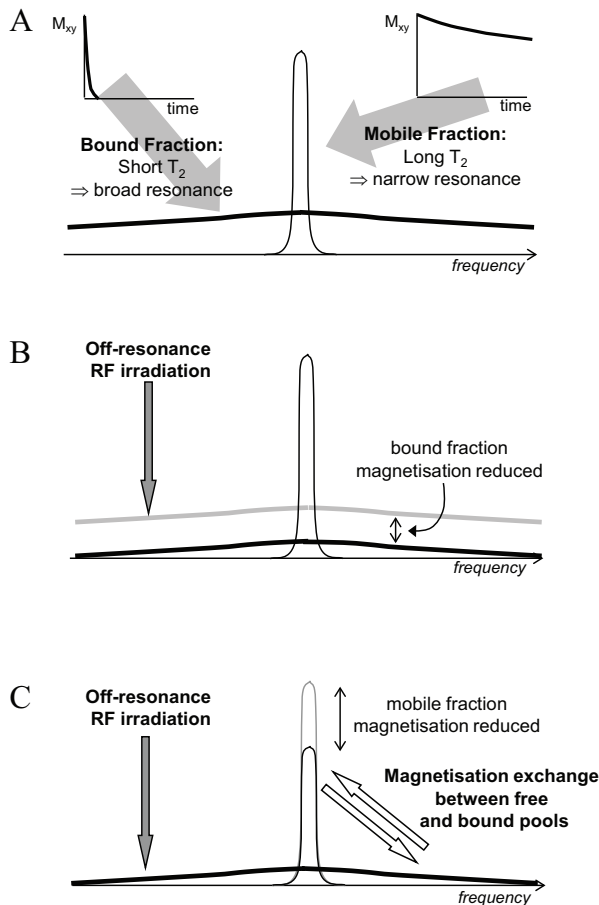


**Figure 2.5 The principles of magnetisation transfer imaging**

(A) Macromolecular-bound protons possess a very short  $T_2$  and hence a broad resonance response in the frequency domain. Mobile water protons conversely exhibit a narrow frequency domain line-width. (B) In the absence of exchange, the application of RF energy at a frequency away from resonance perturbs only the bound proton fraction, causing the magnetisation of this pool to reduce towards zero. (C) Exchange of magnetisation between free and bound protons causes a reduction in the magnetisation of the mobile pool, and hence an observable reduction in MR image intensity.

## References

1. Gadian, DG. NMR and its applications to living systems. Oxford: Oxford University Press, 1995.
2. Smith, R and Lange, R. Understanding Magnetic Resonance Imaging. Florida: CRC Press, 1999.
3. Ogawa, S, Menon, RS, Kim, SG, *et al.* On the characteristics of functional magnetic resonance imaging of the brain. *Annu Rev Biophys Biomol Struct.* 1998; 27:447-474.
4. Modo, M and Williams, SCR. MRI and novel contrast agents for molecular imaging. In: van-Bruggen N, Roberts TPL, eds. *Biomedical imaging in experimental neuroscience.* Florida: CRC Press, 2002:293-322.
5. Moseley, M, Kucharczyk, J, and Asgari, H. Anisotropy in diffusion-weighted MRI. *Magn Reson Med.* 1991; 19:321-326.
6. Wolff, SD and Balaban, RS. Magnetization transfer contrast (MTC) and tissue water proton relaxation *in vivo.* *Magn Reson Med.* 1989; 10:135-144.
7. Henkelman, RM, Stanisz, GJ, and Graham, SJ. Magnetization transfer in MRI: a review. *NMR Biomed.* 2001; 14:57-64.
8. Ordidge, RJ, Helpert, JA, Knight, RA, *et al.* Investigation of cerebral ischemia using magnetization transfer contrast (MTC) MR imaging. *Magn Reson Imaging.* 1991; 9:895-902.
9. Dousset, V, Grossman, RI, and Ramer, KN. Lesion characterization in experimental allergic encephalomyelitis and multiple sclerosis by magnetization transfer imaging. *Radiology.* 1992; 182:483-491.

## PART ONE | Native MRI contrast

# Authors have contributed to this work equally

1 Department of Radiology, Leiden University Medical Center, Leiden, the Netherlands

2 Department of Pathology, Leiden University Medical Center, Leiden, the Netherlands

3 Department of Neurology, Leiden University Medical Center, Leiden, the Netherlands

4 Department of Anatomy & Embryology, Leiden University Medical Center, Leiden, the Netherlands

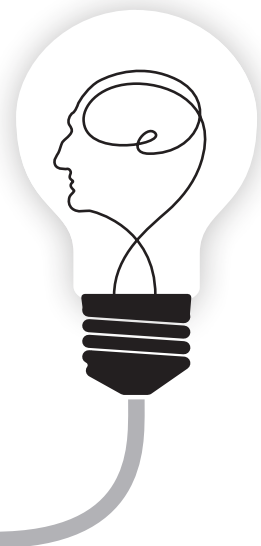
---

# Chapter 3

## MRI artifacts in human brain tissue after prolonged formalin storage

*Adapted from Magn Reson Med. 2011 Jun;65(6):1750-8*

**Rob J.A. Nabuurs**<sup>#1</sup>  
Sara van Duijn<sup>#2</sup>  
Sanneke van Rooden<sup>1</sup>  
Marion L.C. Maat-Schieman<sup>3</sup>  
Sjoerd G. van Duinen<sup>2</sup>  
Mark A. van Buchem<sup>1</sup>  
Louise van der Weerd<sup>1,4</sup>  
Remco Natté<sup>2</sup>



## Abstract

For the interpretation of magnetic resonance imaging (MRI) abnormalities in brain pathology, often *ex vivo* tissue is used. The purpose of the present study was to determine the pathological substrate of several distinct forms of MR hypo-intensities that were found in formalin-fixed brain tissue with amyloid- $\beta$  (A $\beta$ ) deposits. Samples of brain cortex were scanned using T<sub>2</sub>\*-weighted protocols at several resolutions on a 9.4T MRI scanner. High resolution MRI showed large coarse hypo-intensities throughout the cortical gray and white matter, corresponding to macroscopic discolorations and microscopic circumscribed areas of granular basophilic neuropil changes, without any further specific tissue reactions or A $\beta$  related pathology. These coarse MRI hypo-intensities were identified as localized areas of absent neuropil replaced by membrane/myelin sheath remnants using electron microscopy. Interestingly, the presence/absence of these tissue alterations was not related to amyloid deposits, but strongly correlated to the fixation time of the samples in unrefreshed formalin. These findings show that prolonged storage of formalin fixed brain tissue results in subtle histology artifacts which show on MRI as hypo-intensities that on first appearance are indistinguishable from genuine brain pathology. This indicates that post-mortem MRI should be interpreted with caution, especially if the history of tissue preservation is not fully known.



## Introduction

MR imaging of post-mortem brain tissue offers a valuable research method to study disease related changes in image contrast, because the findings can be correlated to histology.<sup>1-12</sup> High resolution *ex vivo* imaging has been a useful tool in interpreting the MRI features of many neurodegenerative disorders, including multiple sclerosis (MS), Alzheimer's disease (AD), and (sporadic) cerebral amyloid angiopathy.<sup>1-3,6-9,11,12</sup> However, the MR characteristics of the tissue rapidly change in the post-mortem situation due to tissue decomposition and chemical fixation; therefore direct translation of the findings to the clinical setting has to be done with caution.<sup>13-19</sup> Firstly, tissue decomposition occurs during the post-mortem interval (PMI), the time period between the patient's somatic death and beginning of the immersion-fixation of the tissue, which varies among subjects. Several studies have shown that an increasing PMI leads to a reduction of  $T_1$  and  $T_2$ .<sup>13,15,20</sup> A more recent study, however, suggested these findings might mainly be due to tissue dehydration or the fixative itself. When these effects were minimized, proton density,  $T_1$  and  $T_2$  values all increased with longer PMI.<sup>17</sup> Also mean diffusivity and fractional anisotropy decrease with prolonged PMI.<sup>17,21</sup>

After autopsy, brain tissue will be immersed into a solution containing a chemical fixative, most frequently being formalin also known as formaldehyde. These solutions preserve tissue by slowly diffusing into it, leading to the cross-linking of proteins and immobilization of water molecules, thereby preventing autolysis and tissue decomposition.<sup>21-23</sup> By its nature it is to be expected that this would affect MR characteristics, which indeed was confirmed by several post-mortem brain MRI studies. A reverse in gray matter (GM) / white matter (WM)  $T_1$  contrast occurs within several days of fixation, merely due to a rapid decline in the latter combined with a general decrease in both continuing at least up to three months.<sup>18</sup> Similarly,  $T_2$  relaxation declines with prolonged fixation affecting both GM and WM, reaching a stable plateau as shown by consecutively imaging up to six months fixation.<sup>13-15,18</sup>

All of the above has led to important considerations on the correct method to obtain and interpret post-mortem MR images.<sup>13,15</sup>

However, similar studies investigating the effect of long fixation periods (> 6 months) on the MR characteristics have not yet been published. Nevertheless, this question is important, especially when using rare material from tissue archives, which are stored using fixatives like formalin for periods ranging from several years up to decades. In a recent study using archival tissue with prolonged fixation times, we noticed unusually large coarse hypo-intensities, especially apparent on high resolution  $T_2^*$ -weighted images, in several brain samples regardless their pathological diagnosis. We hypothesized that these coarse hypo-intensities were the result of the extended formalin fixation period.

The purpose of the current study therefore was to investigate the occurrence of these  $T_2^*$  changes with respect to their formalin fixation time in brain samples with different pathologies. To this end, MR images were obtained of eighteen samples with fixation times ranging from 3 months to several decades. Subsequently the samples were evaluated both macroscopically and microscopically to identify the occurrence and the microscopic substrate of tissue changes due to prolonged fixation.

## Materials and Methods

### Subjects

We used brain tissue of six patients with AD, four patients with Hereditary Cerebral Hemorrhage with Amyloidosis, Dutch type (HCHWA-D), two patients with Down's Syndrome (DS), two patients with sporadic Cerebral Amyloid Angiopathy (CAA) and four control brains. (**Table 3.1**) The brain tissue had been routinely immersed in buffered 10% formalin for several weeks up to 6 months after which the wet tissue was archived in sealed plastic bags with a small excess of 10% formalin. Total fixation times varied from 4 months to 42 years. From a subset of subjects, several samples of the exact same brain had also been paraffin embedded at the beginning of their fixation process, normally within one month post-mortem. This allowed a direct comparison of structural changes with tissue from the same patients that was archived in formalin and embedded in paraffin several years later. (**Table 3.2**)

### MRI

A slice of 20x15 mm brain tissue was selected from each subject and cut into a 4-mm-thick slice using a vibratome (VT1000S, Leica). The 4-mm slice was placed in a custom made tissue holder, immersed in a proton-free fluid (Fomblin, Solvay) and positioned in a vertical small-bore 9.4T Bruker Avance 400WB MRI system, equipped with a 1 T/m actively-shielded gradient insert and Paravision 4.0 imaging software (Bruker Biospin). A 20-mm birdcage transmit/receive coil was used (Bruker BioSpin). Several 3D  $T_2^*$ -weighted gradient echo sequences were obtained with isotropic resolutions of 40 – 100 – 200 – 400  $\mu\text{m}$  with the number of signal averages respectively being 60 – 20 – 20 – 12. TE/TR = 12.26 / 75 ms, FA = 25°. With the matrix size depending on the shape of each sample, average scan time per resolution were respectively 28 hrs, 2 hrs 40 min, 20 min. and 8 min. For quantitative  $T_2^*$  measurements, 100  $\mu\text{m}$  scans were also acquired using TE = 8 – 10 – 12.26 – 15 ms.

### Histology

Following MRI, brain slices were paraffin-embedded and serially cut in 8- $\mu\text{m}$  sections. Consecutive sections were stained for general microscopic morphology (hematoxylin and eosin (HE)), for myelin (Kluver-Barrera), for iron (Perls and a modified Perls DAB)<sup>24</sup> (FEIII-DAB, FEII-DAB)<sup>25</sup>, copper (Romeis) and immunohistochemistry for A $\beta$  (Dako, 6F/3D)<sup>26</sup>, and GFAP (Dako, 6F2).<sup>27</sup> To allow correlation with MRI, sections were digitalized using a flatbed scanner (Agfa).

### Electron microscopy

Electron microscopy was performed on a subset of subjects as previously described.<sup>28</sup> (**Table 3.2**) Collection was done on copper grids instead of carbon grids. Sections were examined using a JEOL JEM-1011 electron microscope operating at 60 kV and digitalized using a MegaView III camera.

### Analysis / Scoring

Two sequential MR slices from the 3D data sets at 40  $\mu\text{m}$  resolution were examined for “coarse” hypo-intensities defined by large size (120 – 1200  $\mu\text{m}$ ), irregular contour and

**Table 3.1 Subject characteristics with corresponding macroscopic, MRI and histology scores**

Subject nr.	Age / Sex (yr)	Post mortem pathologic evaluation	Fixation period (yr)	PMI (hrs)	Macroscopic discoloration	Coarse MR Hypo-intensities	Granular neuropil changes
1	88/F	AD	0.3		Absent	Absent	Absent
2	29/M	Control	0.3		Absent	Absent	Absent
3	70/F	sCAA	0.5		Absent	Absent	Absent
4	53/M	Control	0.5		Absent	Absent	Absent
5	53/M	Control	0.5		Absent	Absent	Absent
6	71/M	sCAA	0.5		Absent	Unknown	Absent
7	49/M	DS	1	13	Absent	Absent	Absent
8	64/M	AD	6	48	Present	Present	Present
9	58/M	HCHWA-D	6	6	Present	Present	Present
10	73/M	AD	7	9	Present	Present	Present
11	65/F	AD	7	2	Present	Extensive	Present
12	50/F	HCHWA-D	9	21	Present	Extensive	Extensive
13	45/F	HCHWA-D	15		Present	Extensive	Extensive
14	90/F	AD	16		Present	Extensive	Extensive
15	52/M	HCHWA-D	17	1	Present	Extensive	Extensive
16	62/F	DS	19		Present	Extensive	Extensive
17	62/M	Control	26		Present	Extensive	Extensive
18	58/F	AD	42	14	Present	Extensive	Extensive

M = Male; F = Female; sCAA = sporadic cerebral amyloid angiopathy; DS = Down's syndrome; AD = Alzheimer's disease; HCHWA-D = hereditary cerebral hemorrhage with amyloid Dutch type; PMI = Post-mortem interval; MRI coarse hypo-intensities: Absent = 0, Present = 1-10 hypo-intensities in one image, Extensive  $\geq 10$  hypo-intensities in at least one of the two examined images. Granular neuropil changes: Absent = 0, Present = 1-4 changes per section, Extensive  $\geq 5$  changes in at least 1 of the 3 sections.

elongated to stellate shape. These coarse hypo-intensities were scored as follows: absent: 0 coarse hypo-intensities, present: 1 – 9 coarse hypo-intensities, extensive:  $\geq 10$  coarse hypo-intensities. Three HE stained sections from the same level of the two sequential MRI slices were used to correlate MR images with histology. To perform these correlations, we used Adobe Photoshop 6.0 to visually overlay digitalized histological sections to their corresponding MR images. Of each patient the same HE sections were used to score the amount of granular neuropil changes as follows: "absent" if no granular neuropil changes were found, "present" for 1 – 4 and "extensive" for  $\geq 5$  neuropil changes in at least one out of the three sections.

Subjects with similar score were combined for group analysis (Mann-Whitney) to find significant differences ( $p$ -value  $< 0.05$ ) in fixation period and age (SPSS 17).

### pH of formalin

Of five patients with widely variable fixation times the pH of the formalin around the brain slices in sealed plastic bags, was determined using a logging pH meter (Hanna, H1 98230). (**Table 3.3**)

**Table 3.2 Granular neuropil changes observed in brain tissue with short and long fixation times from within the same subject**

Subject	Age / Sex (yr)	Post-mortem diagnosis	Granular neuropil changes	
			Fixation period: < 0.5 yr	9 - 42 yr
13	45/F	HCHWA-D	-	+
15	52/M	HCHWA-D	-	+
17	62/M	Control	-	+
18	58/F	AD	-	+

**Table 3.3 pH-measurements**

Subject	Post-mortem diagnosis	Fixation period (yr)	pH
5	Control	0.5	6.62
12	HCHWA-D	9	6.11
15	HCHWA-D	17	4.98
17	Control	26	5.43
18	AD	42	5.12
Fresh formalin			7

## Results

### MRI

High resolution  $T_2^*$ -weighted images of eleven subjects showed irregularly contoured, elongated and stellate shaped hypo-intensities that were randomly distributed throughout the cortical gray matter and to a lesser degree in the white matter. (**Figure 3.1**) Their typical size (120 – 1200 $\mu$ m) and characteristic shape allowed clear distinction from possible other brain structures known to have a similar effect on  $T_2^*$ , e.g. blood vessels or small roundish hypo-intensities caused by amyloid- $\beta$  ( $A\beta$ ) plaques, especially when including their spatial orientation. (**Figure 3.4**) Based on these characteristics, we defined them as “coarse hypo-intensities” and tissue was scored according to their presence. (**Table 3.1**)

When comparing similar MR images of the same section at decreasing resolution, these coarse hypo-intensities became less pronounced and harder to recognize as such. (**Figure 3.1**) This depended on their actual size and shape being affected by partial volume effects due to increasing voxel size. High and low resolution data were compared to assess if hypo-intense voxels on low resolution scans correlated with coarse hypo-intensities at high resolution. The largest coarse hypo-intensities were also visible at the lowest isotropic resolution of 400  $\mu$ m, which is comparable to the *in vivo* MRI resolution. On quantitative  $T_2^*$  maps, areas containing coarse hypo-intensities caused a clearly noticeable decrease in  $T_2^*$ .

## Pathology

### Macroscopy

Only in brain tissue with coarse hypo-intensities on MRI, well circumscribed, white discolorations with similar size and distribution as the coarse MRI hypo-intensities were observed. (**Figure 3.2, Table 3.1**)

### Histology

Microscopically, HE sections of tissue blocks with macroscopic white discolorations showed neuropil alterations with a close spatial correlation to the coarse MRI hypo-intensities. (**Figure 3.3 and 3.4**) These neuropil alterations comprised irregular, well circumscribed areas of granular, basophilic changes usually with some tissue rarefaction. (**Figure 3.5**) The corresponding Kluver's staining within these areas was decreased with respect to surrounding cortex/white matter suggesting a lower density of myelin. Most of these areas showed birefringence under polarized light in the HE that was not seen in unstained sections or the Kluver's stain that excludes the presence of anorganic material.

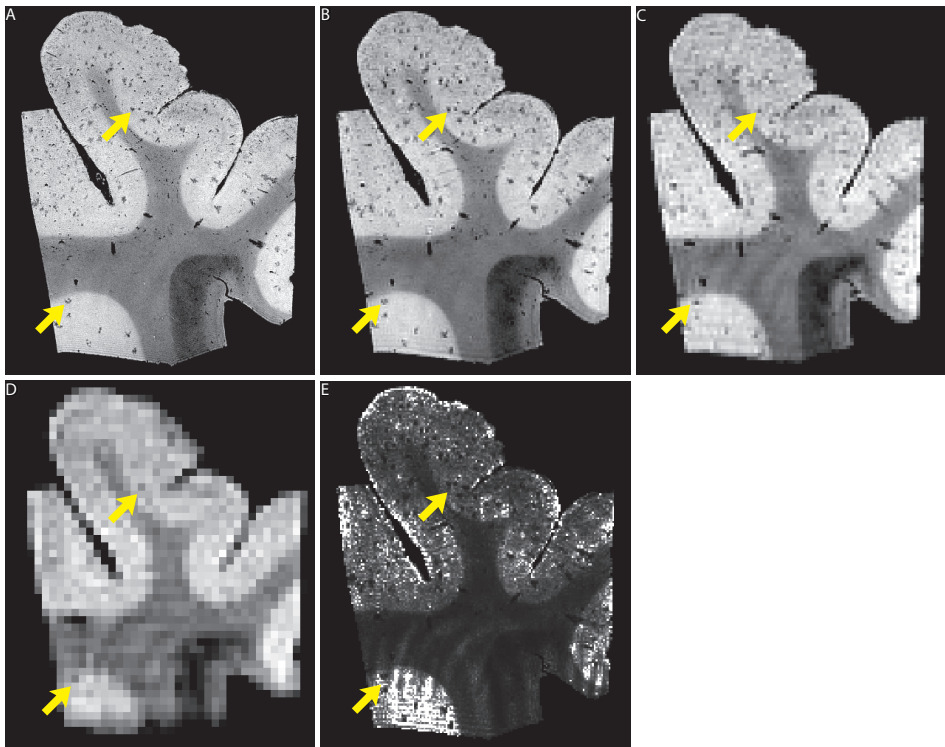


**Figure 3.1** Hypo-intensities seen on MRI

Similar  $T_2^*$ -weighted MR images of subject 14 acquired with isotropic resolution of respectively 40  $\mu\text{m}$  (A), 100  $\mu\text{m}$  (B), 200  $\mu\text{m}$  (C) and 400  $\mu\text{m}$  (D). Many coarse hypo intensities are detected in the higher resolution, but even at the lowest resolution (D) hypointense voxels are still discernible (white arrows). (E) shows the calculated  $T_2^*$  map of the section in (B) with confirming a decreased  $T_2^*$  relaxation.

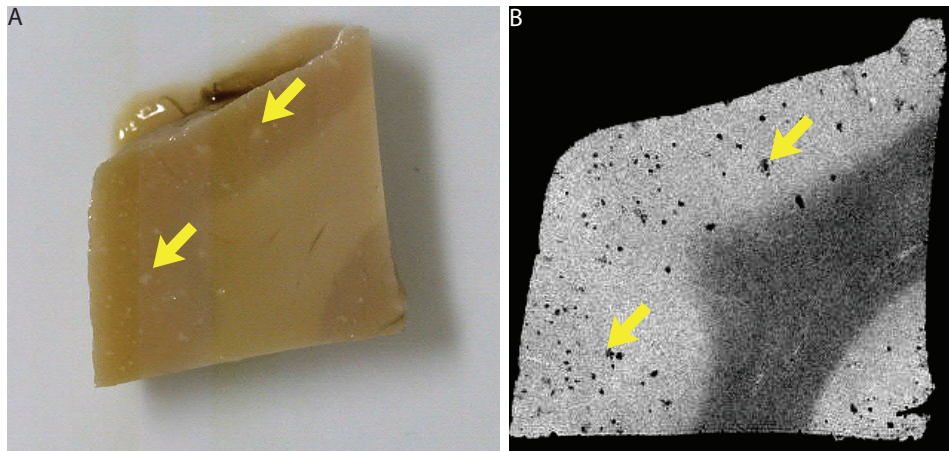


**Figure 3.2 Macroscopic correlation**

Images from subject 13 showing (A) fixated brain tissue with white discolorations (yellow arrows) and (B) high resolution (40  $\mu\text{m}$ )  $T_2^*$ -weighted MR images of the same brain tissue with coarse hypo intensities (yellow arrows).

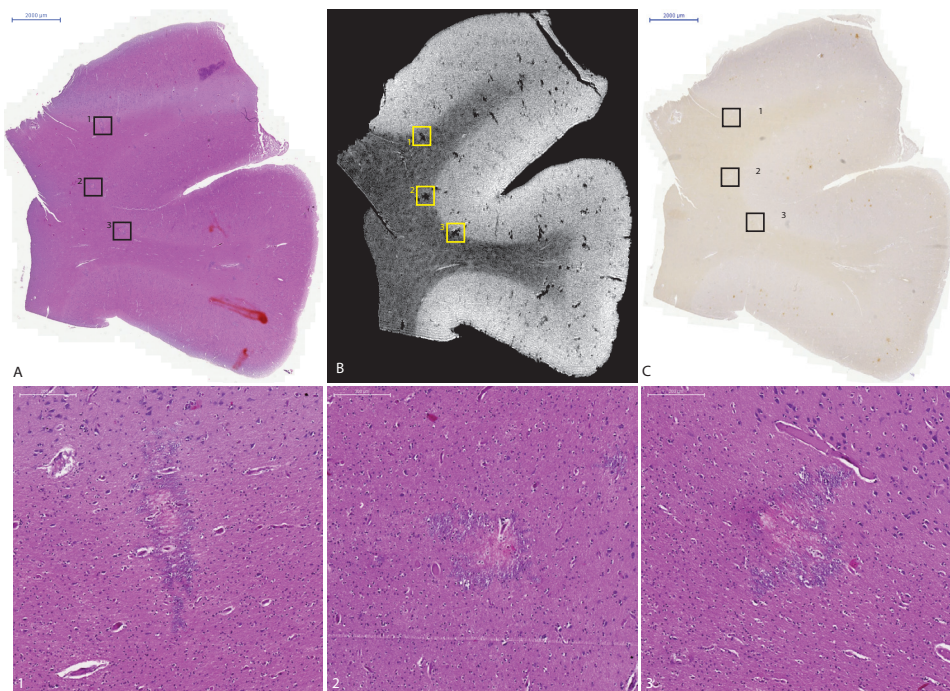


**Figure 3.3 Histological correlation with MRI hypo-intensities of subject 17**

Shown are the corresponding HE (A), MR image (B) and  $A\beta$  immunostained (C) sections of subject 17. Comparison of MR image with HE staining and  $A\beta$  staining correlating the granular neuropil changes with the The hypo-intensities seen on MRI correspond to areas of granular neuropil changes, as clearly depicted by the rectangular inserts (1-3) at 10x magnification. No  $A\beta$  deposition was observed at these locations.



The areas of basophilic granular neuropil changes were randomly distributed throughout the cortex and increasingly present in the white matter of tissue with long fixation times. These areas were found around vessels but also apart from vessels. The basophilic granular neuropil changes showed no signs of gliosis, hemorrhages or infarcts. Neurons, astrocytes, microglia and vessels were normally distributed within these areas and morphologically unaltered. Gemistocytes were not present. Furthermore, all histological (immuno)stainings for iron, copper and amyloid- $\beta$  were negative within these areas. (**Figure 3.4**)

The basophilic granular neuropil changes were not only found in AD material but also in long fixated brain tissue of controls. In contrast, these changes were not found in short fixated AD material. Apart from the coarse hypo-intensities that co-localized with neuropil degeneration, other small roundish hypo-intensities were observed on MRI that did correspond to amyloid plaques. (**Figure 3.4**)

#### *Electron microscopy*

Tissue with macroscopic white discolorations showed localized areas with absent neuropil, although vessels were often present in these spaces on one-micron-thick, epoxy embedded tissue sections stained with toluidine blue. Electron microscopy of immediately adjacent ultrathin sections showed that these areas with absent neuropil actually consisted of spaces without any neuropil or only little neuropil remnants. (**Figure 3.6**) However, in these spaces varying amounts of lamellar structures were found, which were interpreted as membrane remnants and/or swollen degenerated myelin sheaths. Outside these circumscribed areas, we observed variable splitting and swelling of myelin sheets ranging from little splitting in otherwise normal myelin sheaths around axons, up to swollen myelin sheaths lining small empty spaces within the neuropil.

#### **Relation of coarse MR hypo-intensities with fixation duration**

The presence of coarse MR hypo-intensities, macroscopic and microscopic abnormalities were scored for each subject and the results are shown in **Table 3.1** Subjects with similar scores were combined for group analysis.

With regard to coarse MR hypo-intensities, fixation periods were significantly shorter when scored "absent" compared to "present" ( $p$ -value = 0.017 /  $r$  = -0.79). Furthermore, with even longer fixation periods, the number of hypo-intensities significantly increases when comparing "present" versus "extensive" ( $p$ -value = 0.018 /  $r$  = -0.71).

Similar results were obtained when comparing groups with different scores for granular neuropil changes. While fixation periods of those scored "absent" were significantly shorter as compared to those who were scored "present" ( $p$ -value = 0.006 /  $r$  = -0.82), which was significantly shorter as compared to "extensive" cases ( $p$ -value = 0.008 /  $r$  = -0.80).

No significant differences in subject's age between groups were found for either coarse hypo intensity, histological or macroscopic score. Furthermore, no correlation was found between coarse MR hypo-intensities and presence/absence of disease regardless of type of disease.

In summary, brain tissue showed no changes when fixed for a period of one year or less in the same formalin solution, whereas changes were always present in tissue fixed for a period of 6 years or more tissue, and increasingly so with longer fixation periods.

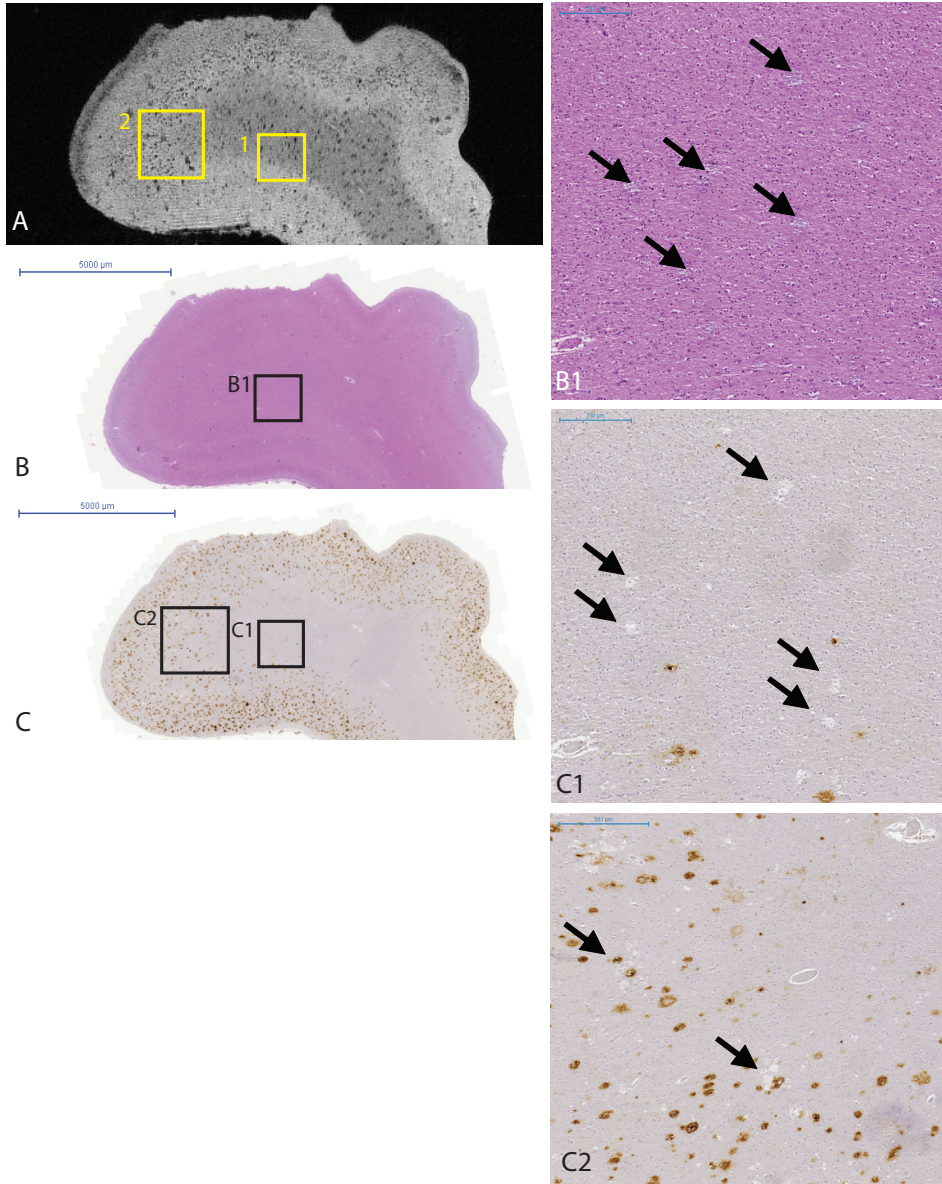


**Figure 3.4** Another example of MRI hypo-intensities due to granular neuropil alterations

A MR image (**A**) of subject 18 is shown with its corresponding HE (**B**) and A $\beta$  immunostaining (**C**). Granular neuropil changes in the white matter are observed without the presence of A $\beta$ . (**B1**) represents the 10x magnification of the HE staining showing the granular neuropil changes in the white matter. The enlarged inserts (**C1** and **C2**, with respectively 10x and 5x magnifications) highlights that these changes in the WM are not depending on A $\beta$  as *black arrows* highlight granular neuropil changes without A $\beta$  (**C1**) and A $\beta$  deposits with and without granular changes in the surrounding neuropil (**C2**).



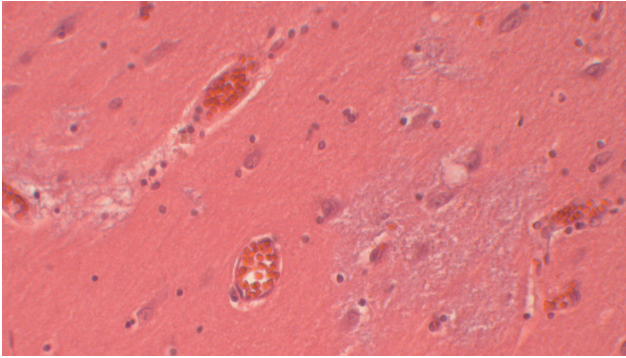


**Figure 3.5 Detailed HE staining of the granular neuropil alterations (20x)**

To test the hypothesis that prolonged formalin fixation indeed leads to histological and MR detectable changes, brain tissue from the same subject that was formalin fixed for either a short or a much longer period was compared microscopically. (**Table 3.2**) In the long-term fixed material, macroscopic white discolorations and granular neuropil changes were present, while short-term fixed material of the same subject completely lacked these findings, indeed supporting our hypothesis.

To obtain a complete picture, pH measurements were performed, because formalin solutions are known to become more acidic over time. pH measurements indeed showed increased acidity after longer periods of formalin fixation, as observed in the sealed plastic bags used for tissue storage. (**Table 3.3**)

## Discussion and Conclusion

In the present study, “coarse hypo-intensities” on post-mortem brain MRI were seen corresponding to localized areas of neuropil destruction with remnants of membranes and myelin sheaths as observed by electron microscopy. These coarse hypo-intensities are mainly detected at high-resolution MR scans. Although brain tissue from A $\beta$ -related diseases was used, the hypo-intensities were not related to deposits of iron, copper or A $\beta$  correlating with these neurological diseases. Instead, these hypo-intensities appear to be an artifact associated with the duration of fixation within the same formalin. This can be concluded from the findings that these hypo-intensities were also detected in control tissue with long fixation times, and were not found in disease-related tissue fixed for a short period.

The exact mechanism of the described storage related artifacts is not known from previous studies but formalin solutions are known to become more acidic over time.<sup>29</sup> This was confirmed by pH measurements of the formalin excess around our sealed fixed brain tissue. Possibly neuropil destruction is caused by a local increase of acidity. However, continuous exposure to formalin and/or formic acid may form many other compounds that possibly play a role in causing artifactual tissue changes.<sup>29,30</sup> We were not able to study the effect of long term fixation in regularly refreshed formalin, and we can thus not exclude prolonged immersion in formalin itself as a cause of local neuropil destruction leading to

MR hypo-intensities rather than the increasing acidity or the formation of aggressive metabolites. Post-mortem autolysis does not appear to be the cause of the artifacts we have observed.

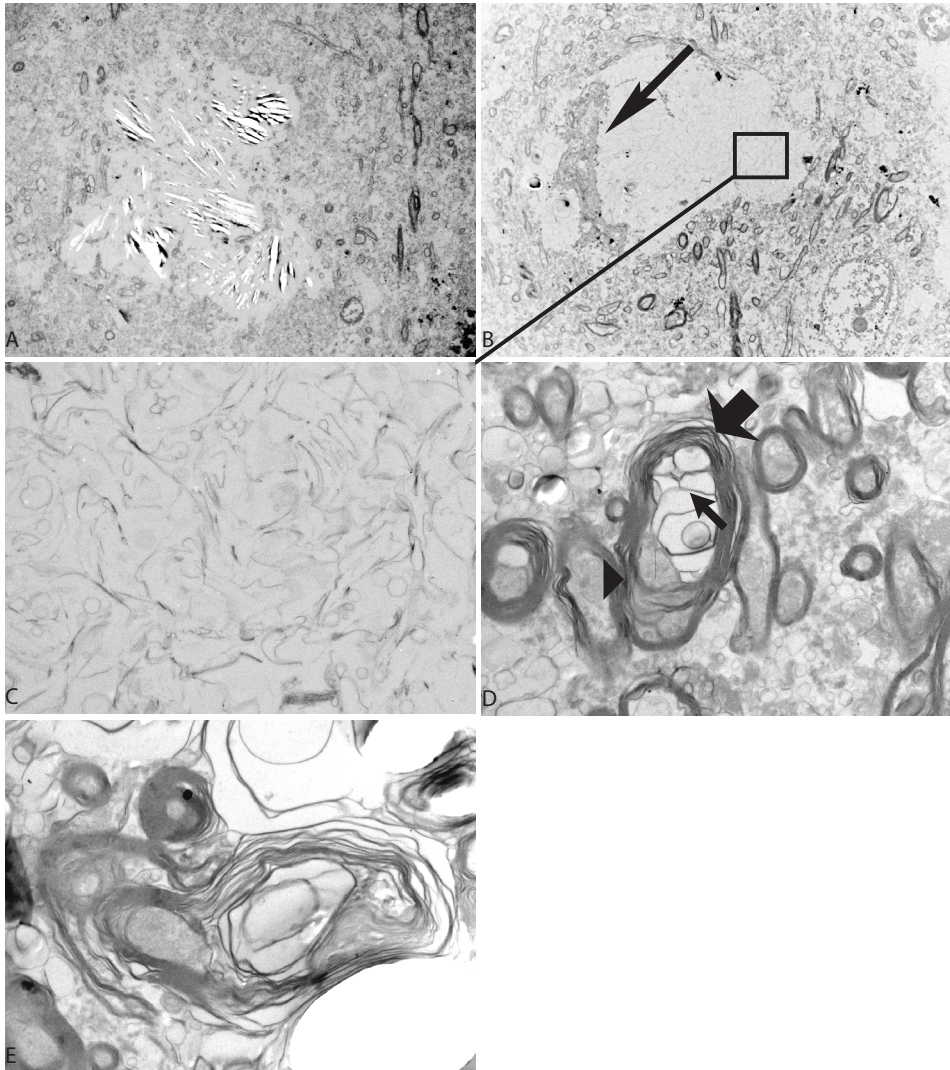


**Figure 3.6 EM examination of the neuropil**

Ultrastructure of localized areas of nearly empty spaces on semithin sections in long term formalin fixed tissue with macroscopic white discolorations. (A) These areas consisted of spaces without neuropil or only little neuropil remnants and often but not always contained a small blood vessel (1200x). (B) Circumscribed area of absent neuropil showing lamellar structures and a capillary (arrow) (1200x). (C) represents the lamellar structures in B (15000x). (D) shows myelinated axons, some with splitting of the myelin sheath. One axon (arrowhead) shows myelin splitting (large arrow) with little expansion of the spaces between the myelin sheaths (small arrow) (15000x). (E) A myelinated axon partly with intact myelin sheath and partly with myelin splitting with transition to more laminated structures with increasing spaces between the lamellae.

For this study, sufficient material fixed for a period of one to six years was lacking. Consequently, we can only conclude that neuropil artifacts occur in all tissue stored for a period of at least six years within the same formalin, whereas tissue stored for a period of one year or less showed no changes.

The coarse hypo-intensities correspond macroscopically to homogenous white discolorations in the tissue, and microscopically in 8  $\mu\text{m}$  HE sections to granular neuropil alterations with slightly less density than the surrounding neuropil. The ultrathin sections (90 nm thick) used for EM revealed that these areas represented absent neuropil with partial filling of the resulting spaces by membrane-like structures. We speculate that this degenerated membraneous/proteineous material with weak birefringence causes hypo-intensities on MRI due to its solid-state-like properties.

The low signal intensity on MRI may also result from replacement of formalin solution by proton free fluid in these relatively more empty spaces. However, a decrease in proton density would not cause a  $T_2^*$  decrease, as was observed in the  $T_2^*$  maps.

With respect to the induced MR changes, previous reports state that formalin fixation causes changes in relaxation and diffusion properties, thereby altering MR contrast, even though the exact mechanism remains unclear.<sup>16</sup> These changes in MR properties, however, occur throughout the entire sample and are partially reversible by rehydrating the sample in PBS. In contrast, the structural disruptions we found after prolonged formalin fixation are very localized and irreversible. Detected changes were furthermore not related to any of the known possible changes due to prolonged PMI as described elsewhere.<sup>13,15,17,20,21</sup> For this study brain tissue of all kinds of PMI periods was used, and no correlation was found with either the tissue changes or MRI hypo-intensities. (**Table 3.1**)

The conclusion of this study suggests that data of several earlier published studies, using post-mortem brain tissue of patients with Alzheimer's disease (AD) for MRI<sup>1-12</sup>, should be cautiously interpret. In these studies, hypo-intense spots were observed on  $T_2^*$ - or  $T_2$ -weighted scans that co-localised with dense amyloid plaques and iron accumulations.<sup>1-12</sup> However, brain tissue in these studies was collected within a short period, and fixed for a maximum period of a few months.

With regard to the detection of amyloid plaques, we also observed hypo-intense spots on MRI that corresponded to the presence of amyloid plaques. However, these did not correlate with the larger stellar shape coarse hypo-intensities. (**Figure 3.4**) The possible  $A\beta$  plaque detection indicates that the basic mechanisms for MR contrast (iron accumulation, dense protein aggregates) are still present. On ultra-high resolution scans, these different hypo-intensities can be easily distinguished. However, on scans with a lower resolution, e.g. those comparable to resolutions that can be achieved on clinical MRI systems, both forms might become indistinguishable, and based upon their size the coarse hypo-intensities due to fixation artifacts are more likely to remain visible. (**Figure 3.1**) In our study, these low resolution images were acquired at relatively short echo times; when a stronger  $T_2^*$ -weighting would be used, more hypo-intensities would be observable at these lower resolutions. Furthermore, it is important to realise that although these neuropil changes are beyond the anatomical resolution of scans with clinical resolutions, they could still be visible on such scans because their signal differs so strongly from surrounding tissue.

Other known sources for hypo-intensities on  $T_2^*$ -weighted images, like calcifications, iron deposits, microbleeds or cavernous malformations<sup>31</sup> could be easily disregarded within this study, while their presence could not be confirmed upon histology. However, especially when conducting similar *ex vivo* MR studies for either one of these pathologies using old brain material and clinically relevant resolutions, one should be aware that the described formalin fixation artifacts could possibly lead to similar hypo-intensities and thus a misinterpretation of the data.

In order to put our findings into a broader perspective, a small survey was conducted among eight other brain banks and neuropathology departments regarding their brain storage protocol. Three of these centers store their formalin-fixed brain tissue in sealed plastic bags with little excess formalin similar to the tissue used in this study, whereas four other centers store fixed brain tissue floating in formalin, two without a protocol for regularly refreshing it, one renewing formalin “when necessary” and the fourth every few years. The last center stores brains in polyethyleenglycol. How the different storage protocols affect the general tissue quality with respect to *ex vivo* MRI research after long term storage remains to be further investigated, but this small survey shows that the fixation protocol for our study is common practice among brain banks, and therefore the findings will have implications for future research on brain bank tissue.

In conclusion, our results demonstrate that fixed brain tissue stored for prolonged periods gives rise to structural tissue changes that are associated with hypo-intensities on  $T_2^*$ -weighted MR images. When brain tissue from pathology archives or brain banks is used to study (rare) disorders with *ex vivo* MRI, it is of vital importance to take the storage protocol into account and to check for the macroscopic and microscopic alterations that have been described and illustrated in this study.

## References

1. Benveniste, H, Einstein, G, Kim, KR, *et al.* Detection of neuritic plaques in Alzheimer's disease by magnetic resonance microscopy. *Proc Natl Acad Sci U S A.* 1999; 96:14079-14084.
2. Bobinski, M, de Leon, MJ, Wegiel, J, *et al.* The histological validation of post mortem magnetic resonance imaging-determined hippocampal volume in Alzheimer's disease. *Neuroscience.* 2000; 95:721-725.
3. Bronge, L, Bogdanovic, N, and Wahlund, LO. Post-mortem MRI and histopathology of white matter changes in Alzheimer brains. A quantitative, comparative study. *Dement Geriatr Cogn Disord.* 2002; 13:205-212.
4. Englund, E, Sjobeck, M, Brockstedt, S, *et al.* Diffusion tensor MRI post mortem demonstrated cerebral white matter pathology. *J Neurol.* 2004; 251:350-352.
5. Fernando, MS, O'Brien, JT, Perry, RH, *et al.* Comparison of the pathology of cerebral white matter with post-mortem magnetic resonance imaging (MRI) in the elderly brain. *Neuropathol Appl Neurobiol.* 2004; 30:385-395.
6. Geurts, JJ, Bo, L, Pouwels, PJ, *et al.* Cortical lesions in multiple sclerosis: combined post-mortem MR imaging and histopathology. *AJNR Am J Neuroradiol.* 2005; 26:572-577.
7. Gouw, AA, Seewann, A, Vrenken, H, *et al.* Heterogeneity of white matter hyperintensities in Alzheimer's disease: post-mortem quantitative MRI and neuropathology. *Brain.* 2008; 131:3286-3298.
8. House, MJ, St Pierre, TG, Kowdley, KV, *et al.* Correlation of proton transverse relaxation rates (R2) with iron concentrations in post-mortem brain tissue from alzheimer's disease patients. *Magn Reson Med.* 2007; 57:172-180.
9. Kangarlu, A, Bourekas, EC, Ray-Chaudhury, A, *et al.* Cerebral cortical lesions in multiple sclerosis detected by MR imaging at 8 Tesla. *AJNR Am J Neuroradiol.* 2007; 28:262-266.
10. Larsson, EM, Englund, E, Sjobeck, M, *et al.* MRI with diffusion tensor imaging post-mortem at 3.0 T in a patient with frontotemporal dementia. *Dement Geriatr Cogn Disord.* 2004; 17:316-319.
11. Schmierer, K, Parkes, HG, So, PW, *et al.* High field (9.4 Tesla) magnetic resonance imaging of cortical grey matter lesions in multiple sclerosis. *Brain.* 2010; 133:858-867.
12. van Rooden, S, Maat-Schieman, ML, Nabuurs, RJ, *et al.* Cerebral amyloidosis: post-mortem detection with human 7.0-T MR imaging system. *Radiology.* 2009; 253:788-796.
13. Blamire, AM, Rowe, JG, Styles, P, *et al.* Optimising imaging parameters for post mortem MR imaging of the human brain. *Acta Radiol.* 1999; 40:593-597.
14. Dawe, RJ, Bennett, DA, Schneider, JA, *et al.* Post-mortem MRI of human brain hemispheres: T2 relaxation times during formaldehyde fixation. *Magn Reson Med.* 2009; 61:810-818.
15. Pfefferbaum, A, Sullivan, EV, Adalsteinsson, E, *et al.* Post-mortem MR imaging of formalin-fixed human brain. *Neuroimage.* 2004; 21:1585-1595.
16. Shepherd, TM, Thelwall, PE, Stanisz, GJ, *et al.* Aldehyde fixative solutions alter the water relaxation and diffusion properties of nervous tissue. *Magn Reson Med.* 2009; 62:26-34.
17. Shepherd, TM, Flint, JJ, Thelwall, PE, *et al.* Post-mortem interval alters the water relaxation and diffusion properties of rat nervous tissue--implications for MRI studies of human autopsy samples. *Neuroimage.* 2009; 44:820-826.
18. Tovi, M and Ericsson, A. Measurements of T1 and T2 over time in formalin-fixed human whole-brain specimens. *Acta Radiol.* 1992; 33:400-404.
19. Yong-Hing, CJ, Obenaus, A, Stryker, R, *et al.* Magnetic resonance imaging and mathematical modeling of progressive formalin fixation of the human brain. *Magn Reson Med.* 2005; 54:324-332.
20. Nagara, H, Inoue, T, Koga, T, *et al.* Formalin fixed brains are useful for magnetic resonance imaging (MRI) study. *J Neurol Sci.* 1987; 81:67-77.
21. D'Arceuil, HE, Westmoreland, S, and de Crespigny, AJ. An approach to high resolution diffusion tensor imaging in fixed primate brain. *Neuroimage.* 2007; 35:553-565.
22. Metz, B, Kersten, GF, Hoogerhout, P, *et al.* Identification of formaldehyde-induced modifications in proteins: reactions with model peptides. *J Biol Chem.* 2004; 279:6235-6243.
23. Puchtler, H and Meloan, SN. On the chemistry of formaldehyde fixation and its effects on immunohistochemical reactions. *Histochemistry.* 1985; 82:201-204.
24. LeVine, SM. Oligodendrocytes and myelin sheaths in normal, quaking and shiverer brains are enriched in iron. *J Neurosci Res.* 1991; 29:413-419.
25. Smith, MA, Harris, PL, Sayre, LM, *et al.* Iron accumulation in Alzheimer disease is a source of redox-generated free radicals. *Proc Natl Acad Sci U S A.* 1997; 94:9866-9868.

26. Natte, R, Maat-Schieman, ML, Haan, J, *et al.* Dementia in hereditary cerebral hemorrhage with amyloidosis-Dutch type is associated with cerebral amyloid angiopathy but is independent of plaques and neurofibrillary tangles. *Ann Neurol.* 2001; 50:765-772.
27. Viale, G, Gambacorta, M, Coggi, G, *et al.* Glial fibrillary acidic protein immunoreactivity in normal and diseased human breast. *Virchows Arch A Pathol Anat Histopathol.* 1991; 418:339-348.
28. Natte, R, Yamaguchi, H, Maat-Schieman, ML, *et al.* Ultrastructural evidence of early non-fibrillar Abeta42 in the capillary basement membrane of patients with hereditary cerebral hemorrhage with amyloidosis, Dutch type. *Acta Neuropathol.* 1999; 98:577-582.
29. Matubayasi, N and Nakahara, M. Hydrothermal reactions of formaldehyde and formic acid: free-energy analysis of equilibrium. *J Chem Phys.* 2005; 122:074509.
30. Schrag, M, Dickson, A, Jiffry, A, *et al.* The effect of formalin fixation on the levels of brain transition metals in archived samples. *Biometals.* 2010.
31. Greenberg, SM, Vernooij, MW, Cordonnier, C, *et al.* Cerebral microbleeds: a guide to detection and interpretation. *Lancet Neurol.* 2009; 8:165-174.

---

## PART ONE | Native MRI contrast

- 1 Department of Radiology, C.J. Gorter Center for High Field MRI, Leiden University Medical Center, Leiden, The Netherlands
  - 2 Department of Anatomy & Embryology, Leiden University Medical Center, Leiden, The Netherlands
  - 3 Department of Neurology, Leiden University Medical Center, Leiden, The Netherlands
  - 4 Department of Pathology, Leiden University Medical Center, Leiden, The Netherlands
  - 5 Molecular Imaging Laboratories Leiden, MRI Lab, Leiden University Medical Center, Leiden, The Netherlands
-

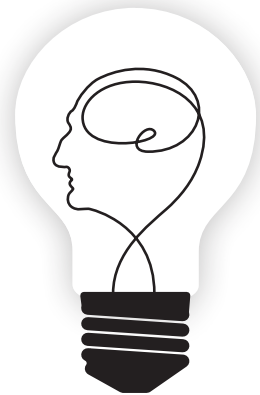


# Chapter 4

High field MRI of single histological slices using an inductively-coupled self-resonant microcoil: application to *ex vivo* samples of patients with Alzheimer's disease

*Adapted from NMR Biomed. 2011 May;24(4):351-7*

**Rob J.A. Nabuurs<sup>1,5</sup>**  
Ingrid Hegeman<sup>3</sup>  
Remco Natté<sup>4</sup>  
Sjoerd G. van Duinen<sup>3,4</sup>  
Mark A. van Buchem<sup>1</sup>  
Louise van der Weerd<sup>1,2,5</sup>  
Andrew G. Webb<sup>1</sup>



## Abstract

A simple inductively-coupled microcoil has been designed to image tissue samples placed on a microscope slide, samples which can subsequently be stained histologically. As the exact same tissue is used for MRI and histology, the two data sets can be compared without the need for complicated image registration techniques. The design can be integrated into any MRI system using existing commercial hardware. Compared to a commercial 20 mm diameter birdcage, the signal-to-noise was increased by a factor of 3.8, corresponding to a reduction in data acquisition time of ~15. An example is shown of *ex vivo* samples of patients with Alzheimer's disease, in which the co-registration of highly sensitive iron staining and focal plaques is confirmed.

## Introduction

MRI is a versatile and powerful tool to study many pathological conditions, both *in vivo* and *ex vivo*. In order to verify that changes in MRI signal intensity are due to pathology, histology remains the gold standard for determining the nature of tissue changes. It is highly challenging to co-register precisely the data from histological sections and MRI, primarily due to the deformations and shrinkage that occur when tissue is processed for histology following MR data acquisition. In addition, histological sections would ideally be cut in exactly the same orientation as the acquired MRI data, but this is in practice not feasible. To overcome these difficulties one can develop image processing algorithms to co-register the histological and MRI data by either attempting to correct for 3D deformations or the difference in spatial orientation.<sup>1</sup> However, even under the most optimal experimental conditions, the very different spatial resolution of MRI and histological sections makes direct registration a cumbersome task.

To alleviate most of these difficulties and possible errors, a straightforward solution is to obtain MR images directly from the same histological slice that is used for staining. Meadowcroft *et al.*<sup>2</sup> have designed and built a highly specialized coil setup for horizontal-bore 3T and 7T scanners, which enables direct MRI of histological sections, such as those used for standard pathology. The imaged tissue slices were afterwards subject to several histological stains, thereby showing it is a worthy addition to study and validate MR contrast changes with respect to its pathological substrate, *e.g.* within Alzheimer's disease (AD) brain tissue. The Meadowcroft coil has excellent sensitivity and performance, but requires relatively specialized expertise to construct and test, and is difficult to implement within the very restricted diameter bore of high field vertical MR magnets. A simple alternative approach would be to use a small self-resonant microcoil placed around the sample, and to inductively couple this coil to the much larger volume resonator which is standardly provided with the system. The principles of inductively coupling a larger transmit coil to a smaller self-resonant "microcoil" have been covered in many publications, with recent comprehensive signal-to-noise ratio (SNR) analyses in articles by Bilgen<sup>3</sup> and Utz<sup>4</sup>. These analyses show that the loss in sensitivity using an inductively coupled arrangement compared to using a microcoil alone is, at most, a few percent. The approach of using inductively coupled self-resonant coils for MR microscopy was first shown by Banson<sup>5</sup>, with the approach having been extended by Glover *et al.*<sup>6</sup> to show co-registered optical and MR images of epidermal cells of *Alium Cepa*.

In the following study, we have designed and characterized an inductively coupled "histological coil" for a 9.4 T vertical magnet. The coil is placed at the back of a standard microscope slide so it completely covers a 60  $\mu\text{m}$  thick tissue sample. Using these easily-produced and replaceable coils, high resolution images of histological samples can be acquired with a  $\sim 15$  fold reduction in data acquisition time compared to using a commercial resonator. After MRI, the same sample underwent staining. In this case, the samples are from *ex vivo* human brain tissue from an ongoing AD study. After MRI scanning, a double staining was performed by using a new modified Perls' 3,3'-diaminobenzidine (DAB) staining combined with immunofluorescence for amyloid  $\beta$  (A $\beta$ ).

## Materials and Methods

### RF coil design

The RF coil was constructed from pure silver 18 AWG wire, shaped into a square with dimensions 15 x 15 mm, ~20% larger than the histological slices so that areas of inhomogeneous  $B_1$  field very close to the wires do not cover the sample. (**Figure 4.1A**) For maximum SNR the microcoil should be strongly coupled to the outer birdcage coil. If the microcoil is tuned to 400 MHz, this introduces a frequency shift that could not be compensated for by re-adjusting the impedance matching capacitors of the birdcage. Therefore, the microcoil should be self-resonant at a frequency slightly different from 400 MHz. As outlined by Bilgen<sup>3</sup>, one can minimize the current in the larger coil by resonating the microcoil at a slightly lower frequency than the larger coil,

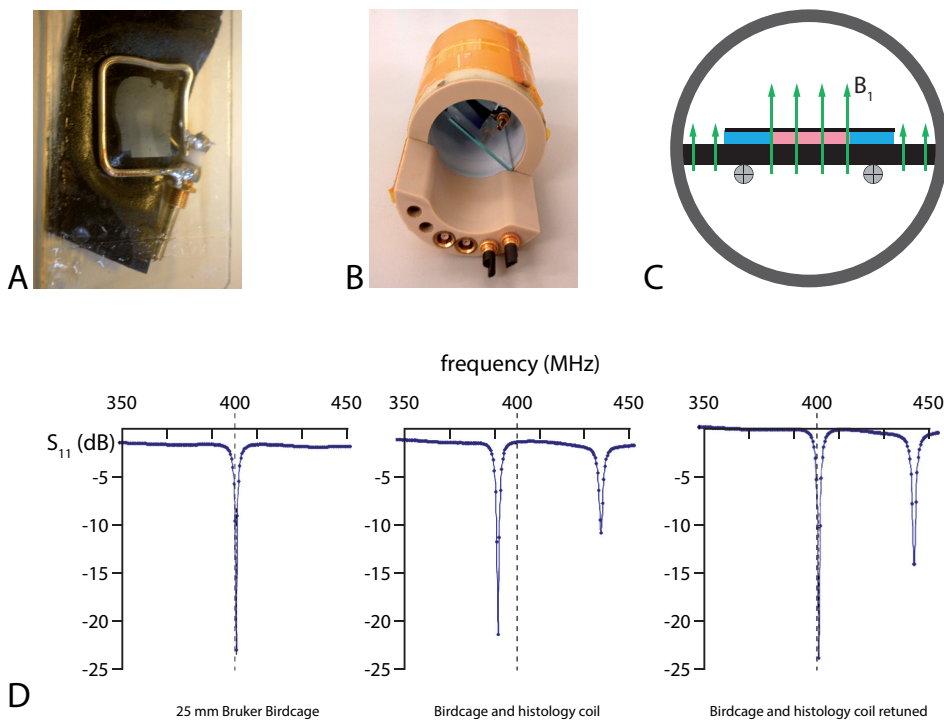


**Figure 4.1** Design of the inductively coupled microcoil

The self-resonant coil is taped onto the back of a standard 25 mm wide microscope slide such that it covers a 60  $\mu\text{m}$  thick brain section, which is mounted on the opposite side in PBS 1X (**A**). The slide is positioned in a 25 mm diameter commercial volume resonator (**B**) such it achieves the strongest coupling. Impedance matching of the histology coil is performed by using the variable capacitors of the birdcage coil (black screws). A schematic cross section of the setup is shown in (**C**) with the coil on one side of the microscope slide and the sample on the other. The arrows illustrate how the  $B_1$  field is localized due to presence of the inductively coupled coil while applying an RF pulse via the volume resonator. (**D**) Network analyzer  $S_{11}$  plots from, respectively, the commercial resonator alone (left), with the strongly coupled coil (center), and after retuning and impedance matched to 50  $\Omega$  at 400 MHz.

and then using the lower of the two split-resonances. A 1-3.5 pF non-magnetic variable capacitor (Johansson, Boonton, NY), with a DC breakdown voltage of 1 kV, was used to tune the microcoil to the resonant frequency of ~396 MHz. The coil was placed directly onto the back of a microscopic slide on which the sample had already been placed. (Figure 4.1A) Next, the slide was placed in a 25 mm standard Bruker high-pass birdcage resonator (Figure 4.1B-C), which was connected to a network analyzer (Agilent Technologies, Santa Clara, CA). The orientation of the slide was adjusted to produce the strongest coupling. The mutual inductance splits the resonance frequency into two separate peaks. The low frequency resonance was impedance matched to 50 Ohms at 400 MHz by adjusting the variable capacitors of the birdcage coil. (Figure 4.1B-D)

### Sample preparation

Tissue was obtained from The Netherlands Brain Bank (NBB), Netherlands Institute for Neuroscience, Amsterdam. All material has been collected from donors for or from whom a written informed consent for brain autopsy and the use of the material and clinical information for research purposes had been obtained by the NBB. A 12 x 12 x 10 mm formalin-fixed human brain tissue sample was resected from the neocortex and cut into 60  $\mu\text{m}$ -thick sections with a vibratome (VT1000, Leica) followed by immersion in 1X phosphate buffered saline (PBS) for at least 24 hrs to wash out any residual formalin. The tissue section was mounted on a histology slide and a drop of PBS (which had previously been placed under vacuum to reduce air bubbles) was applied to the sample to prevent dehydration. Extreme care was taken to avoid inclusion of any air bubbles by slowly lowering the coverslip, and the section was sealed with nail polish.

### MRI data acquisition

All MRI measurements were conducted on a vertical bore 9.4 T Bruker Avance 400 WB spectrometer, with a 1  $\text{Tm}^{-1}$  actively shielded gradient insert, equipped with ParaVision 5.0 software running with Topspin 2.0. Pulse width calibrations were performed with a 1 ms hermite pulse. The  $B_1$ -field homogeneity of the histology coil was evaluated using the double angle method (DAM) as described by Stollberger and Wach<sup>7</sup> in which two spin echo images were acquired with flip angles = 30° and 60°, TR = 4000 ms, TE = 6.5 ms, 4 signal averages, field of view (FOV) = 16 x 16 mm, and matrix size 64 x 64 complex data points.

Imaging experiments were performed using both gradient- and spin-echo sequences. For all sequences, a slice selection pulse was applied to excite a thickness of 2 mm. Scout gradient echo images were acquired in 1.36 minutes with a FOV of 50 x 50 mm, flip angle = 25°, TR / TE = 75 / 3 ms, matrix = [128 128] and 10 signal averages. Multiple gradient echo images were acquired with flip angle = 22.5°, TR / TE = 75 / 5 -12-19 ms, FOV = 16 x 16 mm, matrix = [256 256] and 200 signal averages resulting in a one hour scan with in-plane resolution of 62 x 62  $\mu\text{m}$ . Multiple spin-echo images were obtained in order to calculate  $T_2$ -maps, with TR / TE = 2500 / 10-20-30-40 ms, FOV = 16 x 16 mm, matrix = [128 128] and four averages, obtained in 21 minutes with 125 x 125  $\mu\text{m}^2$  resolution.

### Studies of brain tissue of patients with AD

Several previous studies have shown that the pathological hallmarks of AD, namely A $\beta$  plaques and associated iron deposition, can be detected by MR microscopy.<sup>8,9</sup> In this current study, brain samples from the entorhinal cortex of a confirmed AD patient were prepared. Multiple gradient echo images were acquired with flip angle = 22.5°, TR / TE = 75 / 15 – 25 – 35 – 45 ms, FOV = 16 x 16 mm, matrix = [400 400] and 200 averages resulting in a 1 hour 40 minutes scan with in-plane resolution of 40 x 40  $\mu\text{m}^2$ .

### Histological staining

Following MR, the same 60  $\mu\text{m}$  section was double stained using a new modified highly specific Perls' DAB to stain for iron followed by an immunofluorescence A $\beta$  staining. First the free floating section was immersed for 30 min in 100 ml of methanol with 1 ml 30% H<sub>2</sub>O<sub>2</sub> and rinsed with subsequently 96% and 70% EtOH in PBS 1X to block endogenous peroxidase. A pretreatment similar to the one described by Levine *et al.*<sup>10,11</sup> was applied at room temperature via 30 minutes of immersion in 1% NaBH<sub>4</sub> in PBS followed by 20 minutes in a mixture of 150  $\mu\text{l}$  Proteinase K (Sigma), 50  $\mu\text{l}$  Triton-X 100 and 50 ml PBS. After each step the section was briefly rinsed in PBS 1X before being placed overnight at room temperature in a solution of 7% potassium-hexacyanoferrat(II)-trihydrate and 3% HCl according to Smith *et al.*<sup>12</sup> Following rinsing in aquadest and PBS 1X the section was immersed in 100 ml 0.075% DAB (Sigma) with 50  $\mu\text{l}$  30% H<sub>2</sub>O<sub>2</sub> in PBS 1X for 10 minutes after which the reaction was stopped in aquadest.

Next, the same section was immunostained for A $\beta$  using a standard commercial monoclonal antibody immunostaining (6F/3D, DakoCytomation). One hour immersion in 85% formic acid and 30 minutes in trypsin (Type II-S, Sigma), while rinsing with aquadest and PBS 1X in between, was followed by overnight staining in 1 ml 1:10 dilution of A $\beta$ -antibody at room temperature. Secondary antibody staining consisted of 2 hours immersion with 1:100 goat-antimouse-Alexa594 (Invitrogen) for fluorescence microscopy.

### Coregistration and image analysis

Histological images were acquired using a Leica DM/RB microscope equipped with a DFC-420c CCD camera and Leica LAC software. For immunofluorescence, images were acquired in a similar fashion with a XBO xenon lamp and Texas Red filterblock N2.1. All subsequent images were taken with either a 5 or 10 x objective lens allowing automatic photomerging with Adobe Photoshop CS2 to reconstruct a larger image field. A single image was formed from the MR data by summing all the individual echoes of the MGE sequence. Finally, MR and histology data were coregistered based upon matching section outlines and structural features.

## Results

### RF coil characterization

The frequency shift when the microcoil was placed in the birdcage coil, oriented for maximum coupling, was approximately 10 MHz, as shown in **Figure 4.1D**, with a very small change in the impedance match. The birdcage coil was retuned to 400 MHz using the standard variable

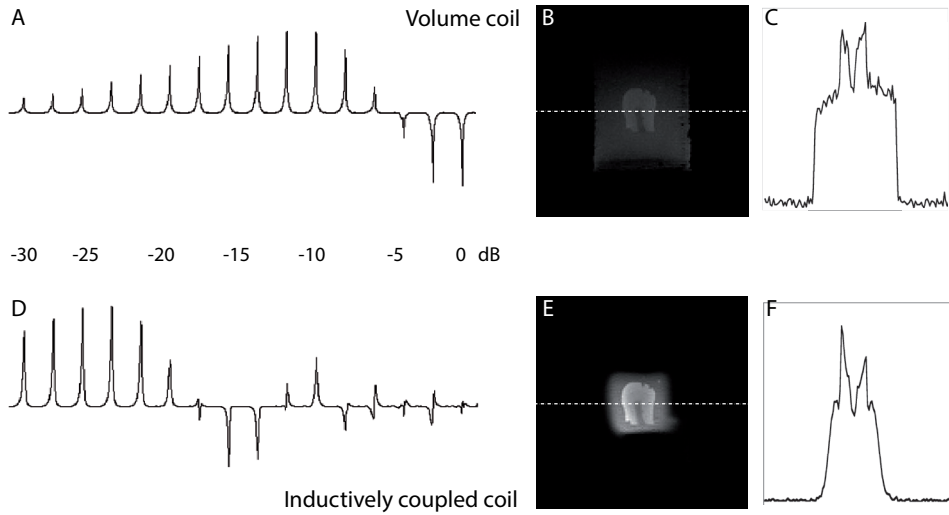


**Figure 4.2**

Pulse width calibrations (on log scale) for the commercial resonator alone (A) and with the coupled histology coil (B) showing a 12 dB reduction in power. Identical scout images obtained from a 60  $\mu\text{m}$  brain section with their corresponding profile through the horizontal center of the volume resonator without (B-C) and with the histology coil (E-F). Besides illustrating the focused B<sub>1</sub>-field, note the decreased noise in (F) compared to (C).

impedance matching capacitors, and the resulting Q of the retuned coil was almost identical to the birdcage alone. Pulse width calibrations for the 25 mm diameter volume resonator with and without the coupled microcoil showed a decrease of 12 dB in power needed for a 90° pulse when using the inductively coupled coil. (Figure 4.2A) The SNR was calculated using the MR images shown in Figure 4.2B, with a measured SNR increase of a factor 3.8 when using the coupled system, which corresponds to a reduction in imaging time of a factor of almost 15. The factor of 3.8 is very close to the expected value of 4 based upon the relative 90° pulse widths. The images in Figure 4.2B also demonstrate how the B<sub>1</sub>-field is localized when using inductively coupled coils, thereby following the concept shown in Figure 4.1C. While the PBS surrounding the brain sample is still seen beyond the edges of the coupled coil in the image acquired solely with the volume resonator, this signal is not picked up when using the coupled coil due to localization of the B<sub>1</sub> field.

The experimentally measured B<sub>1</sub>-field map shows that excitation is homogenous within the strongly coupled coil. (Figure 4.3) The homogeneity measured over a field-of-view of 80% of each of the linear dimensions of the coil showed a standard deviation of ~5% in the B<sub>1</sub>-field. Similar to a standard surface coil, this homogeneity quickly drops off at the edges of the coil. The excellent homogeneity produced by the coupled coil makes it possible to obtain accurate quantitative maps of relaxation parameters, such as T<sub>2</sub>.

Initial scans to compare the performance of the volume coil versus the coupled system clearly illustrate the gain in SNR when similar scans were obtained. Standard gradient echo images acquired with the coupled coil shows features that are not distinguishable using the volume coil alone. (Figure 4.4) Besides clearly distinguishable areas of gray (GM) and white matter (WM),

smaller structures within the GM are also visible. Similar results were obtained when using a standard multiple spin echo sequence at a slightly lower resolution. (**Figure 4.5**) Besides increased SNR and image quality, using the coupled coil allowed the calculation of more accurate  $T_2$  and  $T_2^*$  maps for obtaining quantitative measurements.

### Application to *ex vivo* human AD tissue

Previous literature has strongly suggested that in human AD brain tissue deposits of  $A\beta$ , either colocalized with iron or in the absence of any iron, can create hypointense foci upon  $T_2^*$ -weighted sequences.<sup>2,8,9,13</sup> If the spatial resolution of the MRI is sufficiently high, this allows direct correlation with histology. **Figure 4.6** shows a  $T_2^*$ -weighted MR image of a tissue section

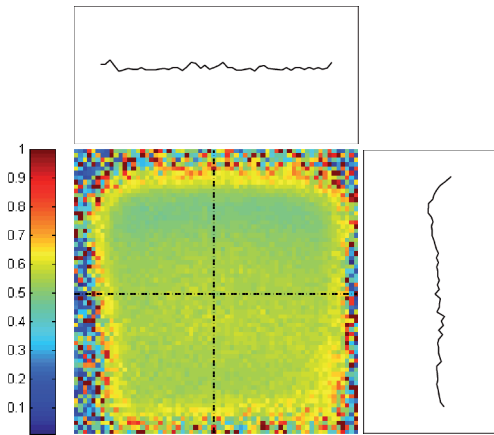
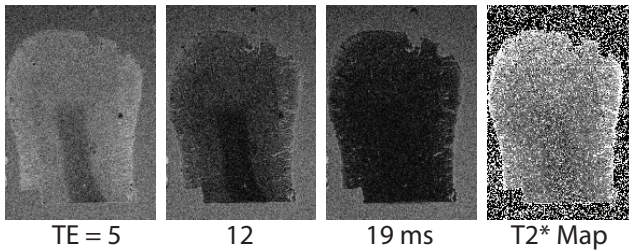


**Figure 4.3 B-field map**

Profiles through the horizontal and vertical center demonstrate the uniformity of the coil within the imaging region of a 60  $\mu\text{m}$  thick brain section.

### A. Volume resonator



### B. Inductively coupled

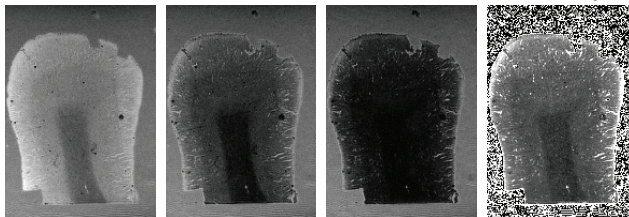
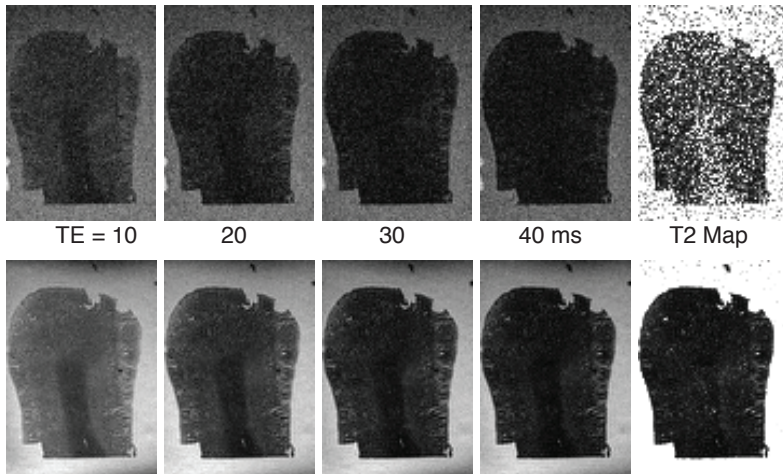


**Figure 4.4**

Multiple gradient echo images and their corresponding  $T_2^*$ -map from a 60  $\mu\text{m}$  thick brain section obtained with the volume resonator without (**A**) and with the inductively coupled histology coil (**B**).



## A. Volume resonator



## B. Inductively coupled

**Figure 4.5**

Multiple spin echo images and their corresponding  $T_2$ -map from a  $60\ \mu\text{m}$  thick brain section obtained with the volume resonator without (A) and with the inductively coupled histology coil (B).

from the entorhinal cortex of an AD patient and its corresponding histological images double stained with a modified Perls' stain for iron and immunofluorescence staining for  $A\beta$ . Registration was simply performed based upon the section's outline and structural features: the WM vasculature in particular could easily be correlated in both image modalities due to the high resolution and SNR of the MRI. When examining the complete section, WM and GM are clearly distinguishable in both modalities, in agreement with previous work<sup>2,9</sup> which ascribed the decreased WM signal intensity to an increased iron content of oligodendrocytes and myelin sheets within the WM as confirmed by our modified Perls' staining. Within the MR image, the GM shows many small hypointense foci. A similar distribution of dark brown patches in the iron staining indicated regions of high focal iron content. (Figure 4.6A-B) Furthermore, the diffuse brown background coloration within the GM on the iron stain shows a similar distribution to the reduced signal intensity on the MR image.

In order to allow a more detailed evaluation and a direct correlation between the findings on MR and histology, images were zoomed on a selected region outlined by the dashed box. (Figure 4.6C-E) As depicted by the yellow arrows, many of the MR hypointense foci indeed represent a one-to-one coregistration with these dark brown areas of high focal iron content. However, for distinct areas marked by a more diffuse brown colour, suggesting a lower iron concentration, a clear direct correlation could not be made.

When examined carefully, immunostaining for  $A\beta$  showed a high  $A\beta$  content throughout the GM with almost all deposits correlating with some degree of DAB enhancement of the Perls' staining. (Figure 4.6E) On the other hand, while most areas showing an increased iron content were surrounded or covered by  $A\beta$ , several small roundish foci did not correlate with  $A\beta$ .

According to their location and size these might be iron loaded microglia cells. Not all MR hypo-intensities could be directly correlated with either staining (**Figure 4.6**, *green arrows*), suggesting another source responsible for creating these contrast changes. Since some of these hypo-intensities can also be seen outside the tissue section, this suggests they are likely to be caused by either small impurities or tiny air bubbles.

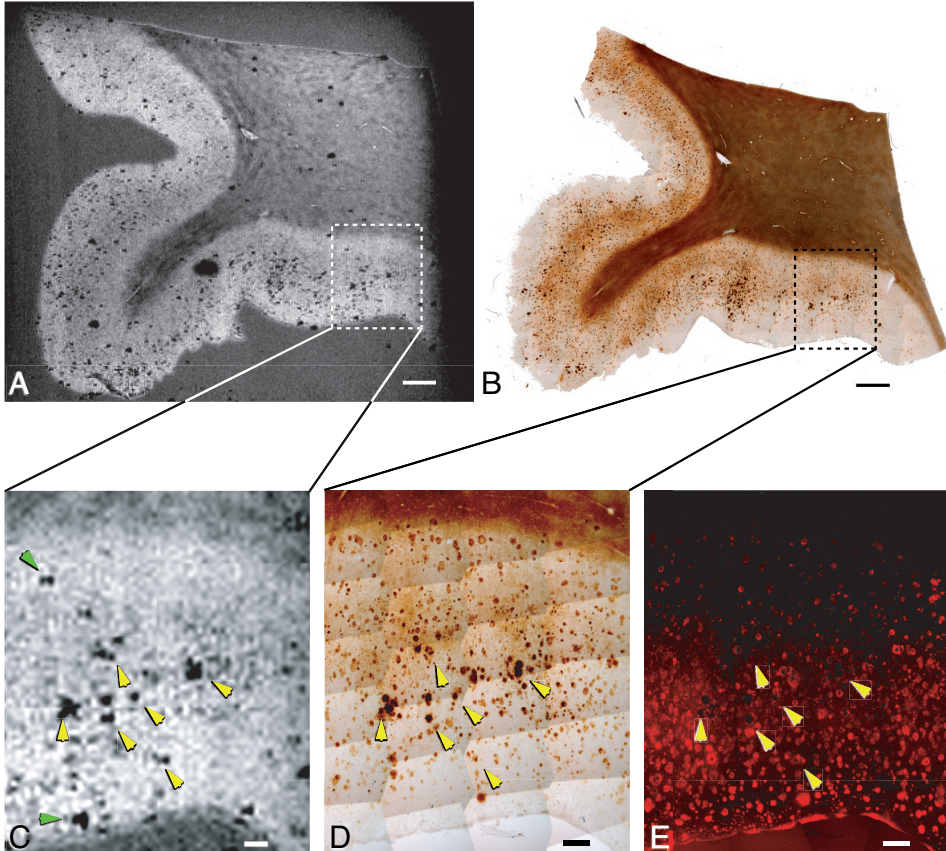


**Figure 4.6 MR microscopy of an Alzheimer's disease brain section**

(A)  $T_2^*$ -weighted image of a 60  $\mu\text{m}$  brain section of the entorhinal cortex of a known Alzheimer's disease patient. (B) Microscopy image of the same section after the new modified Perls' DAB staining for iron. Dark regions indicate higher iron concentration. For more detailed comparison a selected region was enlarged as outlined by the dashed boxes, showing respectively the  $T_2^*$ -weighted MR image (C), iron staining (D) and  $A\beta$  immunostaining (E) of the same section. Many hypointense spots within the MR images clearly coregister with focal iron accumulations (*yellow arrows*), which further colocalizes with  $A\beta$  as seen on (E). However not all hypo-intensities could be coregistered with either one of the histological stainings (*green arrows*), which might also be caused by image artifacts, like tiny air bubbles. Scale bars represent 1000  $\mu\text{m}$  in (A) and (B), and 200  $\mu\text{m}$  in (C-E).

## Discussion

The results presented here indicate that inductively coupled microcoils provide a simple and robust method to acquire high quality MR images of a single histological section in a reasonable data acquisition time. This offers an alternative approach to study various pathological conditions with MR microscopy allowing contrast changes to be easily validated by direct correlation with histology.

Compared to other approaches, these coils are easy to produce, and also to replace if needed. Made to fit around a histological section of any shape, they are broadly applicable to both horizontal and vertical bore systems, and can be impedance-matched up to frequencies well over 1 GHz. Positioned on the back of a microscopic slide, the thickness of the histological section can be varied without the need for additional hardware changes. The high resolution images obtained in this study show sufficiently high SNR such that slices thinner than the current 60  $\mu\text{m}$  should be possible to image, with even better potential correlation with standard histology.

In this study, formalin-fixed samples were cut using a vibratome and immersed in PBS several hours prior to imaging, rather than cryosectioning frozen tissue as was done in previous work.<sup>9</sup> The formalin fixation procedure is known to change MR parameters, but these are partly reversible by PBS immersion. Any extra steps in the slice preparation protocol could lead to additional differences with the *in vivo* situation, and should therefore best be avoided.<sup>9,14,15</sup>

The debate on the exact origin of MRI contrast of amyloid plaques is ongoing, but recent work by Meadowcroft *et al.* shows both dense amyloid accumulations and iron deposits appear to play a role.<sup>9</sup> Within human AD material they showed that focal iron load in amyloid plaques registered well with increased transverse relaxation rates. In contrast, in their mouse model similar effects were seen even in plaques lacking significant iron accumulation, suggesting the interaction of water with the highly compacted amyloid fibril masses as a possible cause for the increased relaxation rates. However, they also showed that the standard Perls' DAB staining is not sensitive enough to the levels of iron present, while a modified protocol was able to show minute amounts of iron even in some of these murine plaques. Applying these modified protocols to 60  $\mu\text{m}$  formalin-fixed human tissue however, high unspecific background staining hampered clear interpretation, as observed by Meadowcroft *et al.*<sup>9</sup> and our own studies (data not shown). As we were unable to exploit the more sensitive iron staining in human material, several questions remain unanswered, e.g. whether diffuse plaques have any effect upon MRI contrast at all, due either to iron or A $\beta$  deposits. Therefore, several adjustments were made to previously published modified Perls' DAB staining protocols focusing on iron accumulation within A $\beta$  deposits of AD brain tissue.<sup>10,12</sup> To lower non-iron-specific DAB enhancement, endogenous peroxidase was blocked using methanol before applying the pretreatment described by LeVine *et al.*<sup>10</sup> The Prussian blue reaction, involving binding of iron(II) containing ferrocyanide to iron(III) within the tissue, was employed using concentrations as described in Smith *et al.*<sup>12</sup> Next, the peroxidase-like H<sub>2</sub>O<sub>2</sub>-dependent oxidation of DAB used to enhance the iron staining was performed in PBS rather than in aquadest.<sup>16</sup> In our hands, the DAB enhancement was best if applied for 2 minutes. Employing our modified Perls' DAB staining on AD brain tissue resulted in similar iron plaques-like structures, as previously described by LeVine

*et al.*<sup>10</sup>, while the low unspecific background staining allows a more accurate registration with MR then described previously using the modified Perls' staining. Besides these high focal iron depositions many local iron accumulations, which had previously remained undetected, emerged from the background. **(Figure 4.6C)** The more diffuse iron staining, observed in a sublayer of the cortex, could also be detected on the corresponding MR image, in agreement with recent findings by Duyn *et al. in vivo*.<sup>17</sup> This global iron distribution should not be mistaken for unspecific background staining; in the latter case, the entire cortex would be stained, and the MRI findings would not correspond.

Although this modified staining technique improves the ability to correlate MR signal changes to focal and diffuse iron concentrations, it has a major disadvantage in that staining for amyloid by standard Thioflavin T or S is not possible, probably due to the very dark pigmentation of the iron-stained sample. Since Thioflavin T or S is an indicator of amyloid (as opposed to A $\beta$ ), a correlation between the localization of iron and amyloid is not possible. The immunofluorescence stain does detect the presence of A $\beta$ , but without the ability to discriminate between dense core amyloid and diffuse plaques containing only fibrillar A $\beta$ . Therefore, using our method we obtain much higher iron staining efficiency, but as a consequence we cannot make any statements as to whether the MR hypo-intensities correspond only to iron co-localized with a specific type of A $\beta$  deposition and/or amyloid. Nevertheless, we can conclude that almost all A $\beta$  deposits, whether diffuse plaques or amyloid, contained traces of iron detected by our modified staining, confirming the results of Meadowcroft *et al.* in human *ex vivo* brain.

**(Figure 4.6)**

## References

1. Breen, MS, Lazebnik, RS, and Wilson, DL. Three-dimensional registration of magnetic resonance image data to histological sections with model-based evaluation. *Ann Biomed Eng.* 2005; 33:1100-1112.
2. Meadowcroft, MD, Zhang, S, Liu, W, *et al.* Direct magnetic resonance imaging of histological tissue samples at 3.0T. *Magn Reson Med.* 2007; 57:835-841.
3. Bilgen, M. Inductively-overcoupled coil design for high resolution magnetic resonance imaging. *Biomed Eng Online.* 2006; 5:3.
4. Utz, M and Monazami, R. Nuclear magnetic resonance in microfluidic environments using inductively coupled radiofrequency resonators. *J Magn Reson.* 2009; 198:132-136.
5. Banson, ML, Cofer, GP, Black, R, *et al.* A probe for specimen magnetic resonance microscopy. *Invest Radiol.* 1992; 27:157-164.
6. Glover, PM, Bowtell, RW, Brown, GD, *et al.* A microscope slide probe for high resolution imaging at 11.7 Tesla. *Magn Reson Med.* 1994; 31:423-428.
7. Stollberger, R and Wach, P. Imaging of the active B<sub>1</sub> field *in vivo*. *Magn Reson Med.* 1996; 35:246-251.
8. Benveniste, H, Einstein, G, Kim, KR, *et al.* Detection of neuritic plaques in Alzheimer's disease by magnetic resonance microscopy. *Proc Natl Acad Sci U S A.* 1999; 96:14079-14084.
9. Meadowcroft, MD, Connor, JR, Smith, MB, *et al.* MRI and histological analysis of beta-amyloid plaques in both human Alzheimer's disease and APP/PS1 transgenic mice. *J Magn Reson Imaging.* 2009; 29:997-1007.
10. LeVine, SM. Iron deposits in multiple sclerosis and Alzheimer's disease brains. *Brain Res.* 1997; 760:298-303.
11. LeVine, SM. Oligodendrocytes and myelin sheaths in normal, quaking and shiverer brains are enriched in iron. *J Neurosci Res.* 1991; 29:413-419.
12. Smith, MA, Harris, PL, Sayre, LM, *et al.* Iron accumulation in Alzheimer disease is a source of redox-generated free radicals. *Proc Natl Acad Sci U S A.* 1997; 94:9866-9868.
13. van Rooden, S, Maat-Schieman, ML, Nabuurs, RJ, *et al.* Cerebral amyloidosis: post-mortem detection with human 7.0-T MR imaging system. *Radiology.* 2009; 253:788-796.
14. Pfefferbaum, A, Sullivan, EV, Adalsteinsson, E, *et al.* Post-mortem MR imaging of formalin-fixed human brain. *Neuroimage.* 2004; 21:1585-1595.
15. Shepherd, TM, Thelwall, PE, Stanisiz, GJ, *et al.* Aldehyde fixative solutions alter the water relaxation and diffusion properties of nervous tissue. *Magn Reson Med.* 2009; 62:26-34.
16. Danielisova, V, Gottlieb, M, and Burda, J. Iron deposition after transient forebrain ischemia in rat brain. *Neurochem Res.* 2002; 27:237-242.
17. Duyn, JH, van, GP, Li, TQ, *et al.* High-field MRI of brain cortical substructure based on signal phase. *Proc Natl Acad Sci U S A.* 2007; 104:11796-11801.

## PART ONE | Native MRI contrast

- 1 Department of Radiology, Leiden University Medical Center, Leiden, Netherlands
  - 2 Department of Pathology, Leiden University Medical Center, Leiden, Netherlands
  - 3 Department of Neurology, Leiden University Medical Center, Leiden, Netherlands
  - 4 Division of Image Processing (LKEB), Department of Radiology, Leiden University Medical Center, Leiden, Netherlands
  - 5 Department of Pathology, VU University Medical Center, Amsterdam, Netherlands
  - 6 Department of Anatomy & Embryology, Leiden University Medical Center, Leiden, Netherlands
  - 7 Department of Human Genetics, Leiden University Medical Center, Leiden, Netherlands
-

# Chapter 5

MR Microscopy of human A $\beta$  deposits -  
characterization of parenchymal amyloid,  
diffuse plaques and vascular amyloid

*Adapted from J Alzheimers Dis. 2013 Jan 1;34(4):1037-49*

**Rob J.A. Nabuurs<sup>1</sup>**

Remco Natté<sup>2</sup>

Fenna M. de Ronde<sup>2</sup>

Ingrid Hegeman-Kleinn<sup>3</sup>

Jouke Dijkstra<sup>4</sup>

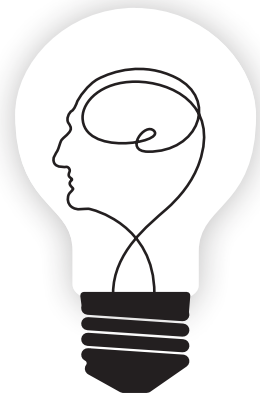
Sjoerd G. van Duinen<sup>2</sup>

Andrew G. Webb<sup>1</sup>

Annemieke J. Rozemuller<sup>5</sup>

Mark A. van Buchem<sup>1</sup>

Louise van der Weerd<sup>1,6,7</sup>



## Abstract

Cerebral deposits of amyloid-beta peptides ( $A\beta$ ) form the neuropathological hallmarks of Alzheimer's disease (AD) and cerebral amyloid angiopathy (CAA). In the brain  $A\beta$  can aggregate as insoluble fibrils present in amyloid plaques and vascular amyloid, or as diffuse plaques consisting of mainly non-fibrillar  $A\beta$ . Previously, magnetic resonance imaging (MRI) has been shown to be capable of detecting individual amyloid plaques, not only via the associated iron, but also  $A\beta$  itself has been suggested to be responsible for a decrease in the image intensity. In this current study we aim to investigate the MRI properties of the different cerebral  $A\beta$  deposits including diffuse plaques and vascular amyloid. Post-mortem 60  $\mu\text{m}$  thick brain sections of AD, CAA and Down's syndrome patients, known to contain  $A\beta$ , were studied. High resolution  $T_2^*$ - and  $T_2$ -weighted MRI scans and quantitative relaxation maps were acquired using a microcoil on a Bruker 9.4T MRI system. Specific MRI characteristics of each type of  $A\beta$  deposit were examined by co-registration of the MRI with Congo Red and  $A\beta$ -immunostainings of the same sections. Our results show that only fibrillar  $A\beta$ , present in both vascular and parenchymal amyloid, induced a significant change in  $T_2^*$  and  $T_2$  values. However, signal changes were not as consistent for all of the vessels affected by CAA, irrespective of possible dyshoric changes. In contrast, the non-fibrillar diffuse plaques did not create any detectable MRI signal changes. These findings are relevant for the interpretation and further development of (quantitative) MRI methods for the detection and follow-up of AD and CAA.



## Introduction

Diagnosis of Alzheimer's disease (AD) *in vivo* remains a problematic issue. Despite recent efforts to sharpen clinical criteria, a definitive diagnosis still requires histopathological evidence showing the cerebral presence of amyloid- $\beta$  peptides (A $\beta$ ) aggregated into amyloid plaques and neurofibrillary tangles (NFTs).<sup>1,2</sup> Although the precise role of amyloid in AD pathology is still not completely understood, accumulation of amyloid plaques is thought to precede the onset of the first clinical symptoms by up to two decades.<sup>3,4</sup> Clinical imaging techniques capable of visualizing and quantifying these early changes might enable early diagnosis.

Thus far the clinical role of magnetic resonance imaging (MRI) has been confined to depicting brain atrophy from mid-stage AD onwards.<sup>3</sup> However, clinically MRI has not been able to detect earlier pathophysiological alterations, despite preclinical evidence that showed detection of individual amyloid plaques by MRI was feasible in post mortem human brain tissue<sup>5-8</sup> as well as *ex vivo* and *in vivo* in several AD mouse models.<sup>6,9-16</sup> The high magnetic field strength, high resolution and long acquisition time used in these studies prohibit a direct translation of appropriate imaging protocols to the clinic. Though detection of individual plaques is not realistic in a clinical setting, quantitative T<sub>2</sub> and T<sub>2</sub>\* measurements could be used to detect relaxation changes associated with amyloid plaque accumulation, or associated iron deposits, even at an image resolution that is far lower than the dimensions of amyloid deposits.<sup>9,17</sup> Promising as it may be, this requires a full understanding of the MRI characteristics of all forms of A $\beta$  deposits that may be present in AD.

The most renowned type of A $\beta$  deposit in the cerebral cortex is the fibrillar plaque, which is one of the neuropathological criteria used post-mortem to confirm the diagnosis of AD. However, several other types of A $\beta$  deposits can occur in the brain. Neuropathologically, the terminology used to describe the different A $\beta$  deposits is diverse. In line with Duyckaerts *et al.* human parenchymal A $\beta$  deposits can be divided into two main subtypes based on their A $\beta$  content: diffuse plaques and focal plaques.<sup>18</sup> Although the nomenclature of the different types of focal plaques is rather heterogeneous (primitive, classic, neuritic, senile and burn-out plaques), they generally contain A $\beta$  peptides aggregated into a typical fibrillar  $\beta$ -sheet pleated conformation known as amyloid. For the remainder of this paper this type of fibrillar A $\beta$  deposits are referred to as amyloid plaques. The presence of amyloid is presumed to lead to neuronal dysfunction and even the complete loss of neurons, and correlations between amyloid plaques and clinical symptoms have been reported.<sup>18</sup>

In contrast, the so-called diffuse plaques are not specific for AD and although abundant in AD and healthy controls, they correlate poorly or not at all with dementia.<sup>19-23</sup> They are histopathologically defined as large, ill-defined patches of parenchymal deposits of A $\beta$  peptides but with hardly to no fibrillar amyloid or dystrophic neurites present.<sup>18</sup>

The formation of amyloid may also stretch along the vascular wall of leptomeningeal and parenchymal arteries and arterioles, and to a lesser extent the brain capillaries. This vascular amyloid is commonly referred to as cerebral amyloid angiopathy (CAA).<sup>18,24</sup> Although CAA is often found to co-exist with AD, it can also appear as an entity on its own leading to microbleeds and severe cerebral hemorrhages.<sup>25</sup>

Thus far, MRI studies have only examined the A $\beta$ -related MR contrast changes with respect to parenchymal amyloid plaques.<sup>6,9-16</sup> Observed contrast changes were primarily attributed to the

accumulation of iron within the plaques.<sup>9,10,12,15</sup> However, similar MRI contrast was also observed in amyloid plaques without iron, and therefore it has been hypothesized that A $\beta$  by itself contributes to the relaxation changes, presumably due to its hydrophobic nature.<sup>6,16</sup>

The aim of this study, therefore, was to study the MRI characteristics of these different types of human cerebral A $\beta$  deposits. In addition to the known induced MRI contrast changes due to the presence of amyloid plaques, we investigated the MRI characteristics of diffuse plaques and CAA in post-mortem human brain material. Ultimately, a better understanding of the MRI correlates of A $\beta$  deposits may help to interpret the observed relaxation changes in quantitative MRI of AD patients.

## Materials and Methods

### Brain samples

Brain tissue was obtained from the tissue bank of our institution and from the Netherlands Brain Bank (NBB). Several hours post-mortem, the brains were resected, serially cut in 1 cm coronal sections and stored in 4 % paraformaldehyde. Routine autopsy of the brains included histological examination for CAA- and AD-related pathology respectively according to Attems *et al.*<sup>26</sup> and Braak *et al.*<sup>27</sup> Based on autopsy-confirmed diagnosis we selected tissue from subjects suffering from diseases that are known to be associated with cerebral A $\beta$ . We selected patients with AD ( $N = 5$ ), Down's syndrome (DS) ( $N = 1$ ), CAA ( $N = 6$ ) and clinically non-demented controls ( $N = 3$ ). **(Table 5.1)** Patient anonymity was strictly maintained. All tissue samples were handled in a coded fashion, according to Dutch national ethical guidelines (Code for Proper Secondary Use of Human Tissue, Dutch Federation of Medical Scientific Societies). Previously described formalin-induced tissue artifacts that might affect MRI signal were avoided accordingly by careful visual and microscopic inspection and including material fixed for maximal 32 months.<sup>28,29</sup> **(Table 5.1)**

### Sample preparation

MR samples were prepared according to methods that have been described previously.<sup>7</sup> In short, from each subject a cortical tissue block of approximately  $12 \times 12 \times 10 \text{ mm}^3$  was resected based on known predilection sides for the different types of A $\beta$ . To study parenchymal deposits samples were obtained from a coronal section that contained a section of the hippocampus to enable imaging of the neocortex in the medial temporal lobe adjacent to the entorhinal cortex. To investigate the vascular A $\beta$  deposits, tissue blocks were obtained from occipital lobe cranial within the sulcus, since the occipital lobe is the site of predilection of CAA. Remnants of the dura were removed from the pial surface, and 60- $\mu\text{m}$ -thick tissue sections were cut with a vibratome (VT1000S, Leica, Germany). Prior to imaging, any residual formalin was washed out by immersion in phosphate buffered saline (PBS) for at least one day to partially restore transverse relaxation times.<sup>30</sup> Sections were mounted on a standard microscope slide covered with a drop of PBS to prevent dehydration.<sup>7</sup> Extreme care was taken to avoid the inclusion of any air bubbles by slowly lowering the coverslip, after which the section was sealed with nail polish.

Table 5.1 Subject characteristics and presence of A $\beta$  deposits

Subject Characteristics			Sample scoring								
No.	Age / Sex	Diagnose	Braak	Cause of death	Fixation period (months)	Normal GM	Diffuse plaques	Amyloid plaques	CAA	dysCAA	capCAA
1	23 / F	Control	0	Myocarditis	26	scored	-	-	-	-	-
2	83 / F	Control	2	Arrhythmia	26	scored	-	-	-	-	-
3	89 / F	Control	3	Myocardial infarct / Pneumonia	20	-	scored	scored	-	-	-
4	60 / F	AD	5	Cachexia / dehydration	25	-	scored	scored	-	-	-
5	77 / M	AD	6	Cachexia / dehydration	26	-	scored	scored	-	-	-
6	85 / F	AD	4	Aspiration pneumonia	26	-	scored	scored	-	-	-
7	87 / M	AD	5	Cachexia / dehydration	25	-	scored	scored	-	-	-
8	88 / F	AD	4	Unknown	17	-	scored	scored	-	-	-
9	31 / M	DS	0	Myocardial infarct	23	scored	scored	-	-	-	-
10	72 / M	sCAA	3	Intracerebral haemorrhage	32	-	-	-	scored	-	-
11	57 / M	AD / sCAA	6	Intracerebral haemorrhage	30	-	-	-	scored	scored	-
12	84 / M	sCAA	1	Pneumonia	22	-	-	-	scored	-	scored
13	61 / F	sCAA	0	Intracerebral haemorrhage	4	-	-	-	scored	-	-
14	80 / M	sCAA	2	Pneumonia	32	-	-	-	scored	scored	-
15	81 / M	sCAA	3	Haemorrhagic infarcts	5	-	-	-	scored	scored	-

Characteristics of all subjects used for this study are shown based upon clinical information and standard neuropathologic examination according to Braak criteria for thin sections.<sup>27</sup> Per subject the type of A $\beta$  deposits that were used for MRI analysis are stated as scored. A negative score does not necessarily imply they were not present but only that they were not included for that particular subject. AD = Alzheimer's disease; CAA = cerebral amyloid angiopathy; DS = Down's syndrome; sCAA = sporadic CAA; dysCAA = dystrophic CAA; capCAA = capillary CAA; GM = gray matter.

### MRI acquisition and post-processing

All MRI experiments were performed on a vertical bore 9.4 T Bruker Avance 400 WB spectrometer, equipped with a 1 Tm<sup>-1</sup> actively shielded gradient insert. As previously described, a self-resonant microcoil was placed directly on top of the sample to obtain MR images of the 60- $\mu$ m-thick tissue sections.<sup>7</sup> Multi-gradient-echo (MGE) images were acquired to assess T<sub>2</sub>\* with a repetition time (TR) = 750 ms, echo time (TE) = 4-70 ms (12 echoes with 6 ms spacing), flip angle (FA) = 30°, field of view (FOV) = 16 x 16 mm<sup>2</sup>, data matrix [400 x 400] resulting in a resolution of (40  $\mu$ m)<sup>2</sup> with a total data acquisition time of 6 hours and 40 minutes. T<sub>2</sub> effects were investigated by using a multiple spin echo sequence acquired in 4 hours and 26 minutes with TR = 2000 ms, TE = 10-100 ms (10 echoes with 10 ms spacing), FOV = 16 x 16 mm<sup>2</sup>, data matrix [200 x 200] giving a resolution of (80  $\mu$ m)<sup>2</sup>. Post-processing was performed using a voxel-wise linear regression MatLab routine (MathWorks, Natick, MA, USA) to calculate quantitative T<sub>2</sub>\* and T<sub>2</sub> maps. T<sub>2</sub>- and T<sub>2</sub>\*-weighted images were created as the sum of the third to the tenth echo image.

Despite extreme care in sample preparation, MRI hypo-intensities related to small inhomogeneities caused either by external dust particles, or tiny air bubbles were unavoidable. These artifacts were present throughout all samples, and were excluded from the analysis based on visual microscopic inspection of the sample.

### Congo Red staining for amyloid

After MRI acquisition, Congo Red staining was performed for detection of amyloid on the same control, DS and AD sections that were analyzed by MRI. After removing the coverslip, the free floating tissue section was rinsed in distilled water three times for 10 minutes each. The section was counterstained with Harris' haematoxylin and rinsed in tap water for 10 minutes. After pretreatment of 20 minutes with 3% NaCl and 0.01% NaOH in 80% EtOH, the free floating section was again immersed in the same solution for 20 minutes with 0.5% Congo Red. The section was rinsed briefly in, in turn, 96 – 80 – 70 – 0 % EtOH in distilled water and air-dried prior to mounting (Micromount). This additional rehydration step with pure distilled water reversed most non-uniform shrinkage caused by the ethanol, thereby simplifying subsequent coregistration with the MRI data. Directly thereafter the section was digitized using a bright field microscope scanner (Pannoramic MIDI, 3DHistech, Hungary). Congo Red stained amyloid was confirmed using depolarized light, under which the red stained areas gave a characteristic green birefringence.

### A $\beta$ -immunostaining

To detect all isoforms of A $\beta$ , including the diffuse plaques, a standard immunostaining procedure using a commercial monoclonal antibody (6F/3D, DakoCytomation, Denmark) was applied.<sup>31</sup> The sections that had previously undergone Congo Red staining had the coverslip removed by overnight immersion in xylene, and were rehydrated using 96 – 80 – 70 – 0 % EtOH in distilled water. During this process both Congo Red and haematoxylin were completely removed. Endogenous peroxidase activity was blocked by applying 0.3% H<sub>2</sub>O<sub>2</sub> in methanol for 20 minutes. For antigen retrieval the samples underwent 1 hour immersion in 85% formic acid, rinsing with distilled water and PBS, and 30 minutes immersion at 37 °C in 0.1% trypsin (Type II-S, Sigma) with 0.1 % CaCl<sub>2</sub> at pH 7.4. Next, the floating sections were incubated overnight with a 1:10 dilution of A $\beta$ -antibody in 1% BSA in PBS at room temperature, and rinsed three times for 10

minutes each with PBS before biotinylated RAM secondary antibodies (1:200, DakoCytomation, Denmark) in 1% BSA in PBS were added for one hour. Next, the sections were rinsed three times with PBS and incubated for 30 minutes with freshly prepared HRP-labeled avidin-biotin complex (ABC, Vector Labs, CA, USA). Enhancement was completed by 5 – 10 minutes immersion in 100 ml distilled water containing 0.075% 3,3'-diaminobenzidine (DAB) (Sigma) and 15  $\mu$ l of 30% H<sub>2</sub>O<sub>2</sub> after which the reaction was stopped in distilled water. The section was then mounted and digitized.

### Coregistration and ROI analysis

For each section, the processed images were stacked prior to co-registration with their corresponding histology using the Cyttron visualization platform (CVP, Leiden, the Netherlands) and Adobe Photoshop CS3 (Adobe). Based on evaluation by a neuropathologist (R.N.), the A $\beta$  positive areas on immunohistochemistry that were also Congo Red positive were classified as amyloid plaques. The poorly-defined larger patches of parenchymal A $\beta$  were classified as diffuse plaques based on both their morphology and the lack of Congo Red staining according to the previous nomenclature.<sup>18</sup> Further analysis included only those areas that clearly contained only a single subtype of A $\beta$  deposition. CAA-loaded vessels were selected based on their distinct vascular morphology present in the immunostaining. Areas completely devoid of any staining were classified as normal appearing gray matter (GM). Based on these classifications, T<sub>2</sub>\*- and T<sub>2</sub>-weighted images were analyzed to detect any corresponding changes in the MRI signal related to the specific A $\beta$ -deposits. Quantitative T<sub>2</sub>\* and T<sub>2</sub> relaxometry of the different parenchymal A $\beta$  deposits was assessed by region-of-interest (ROI) analyses based on the aforementioned areas using the Image J software package (National Institutes of Health, Bethesda, MA, USA). For amyloid plaques, an ROI of a single voxel was used since this corresponds best to the size of the plaques. In contrast, for the areas containing diffuse plaques, the ROI consisted of multiple voxels corresponding to the plaque's outline on histology. To assess normal-appearing GM, several ROIs of 100 voxels were selected in anatomically-similar cortical areas. Measurements across all samples were combined to calculate averages for each type of A $\beta$  deposit. Possible differences in relaxation times for each subtype were tested using a Student t-test, with p-values < 0.05 considered statistically significant.

## Results

### Parenchymal A $\beta$ deposits

All samples were taken from similar neo-cortical regions of the middle temporal lobe, and formalin fixation periods were between 3-24 months. Both diffuse and amyloid plaques were present in all samples except for two control subjects 1 and 2, and subject 9, whom only contained diffuse plaques. The distribution of both types of parenchymal A $\beta$ , however, often co-localized with each other which hampered the selection for further analysis. As we aimed to select only those areas containing a single type of deposition, diffuse and amyloid plaques could not be scored in all samples. The scored amyloid types and other characteristics of each subject are presented in **Table 5.1**.

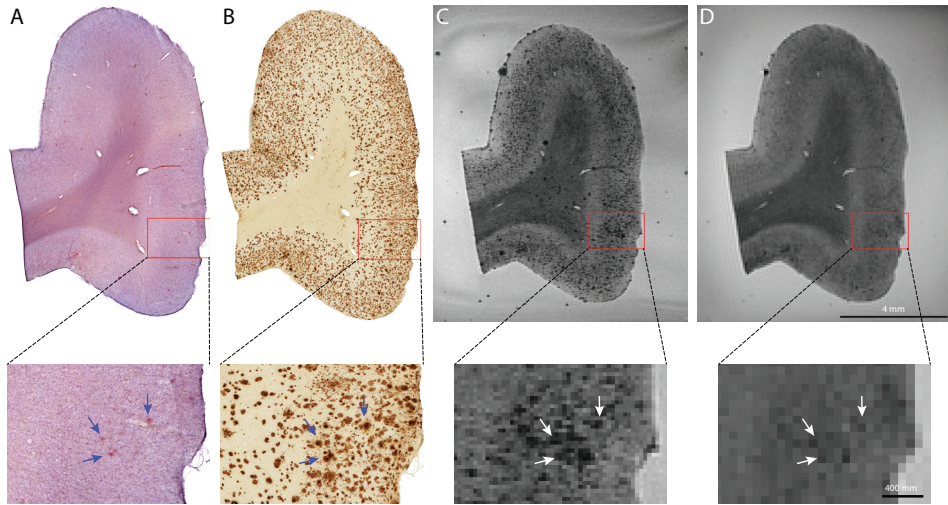


**Figure 5.1 Qualitative MRI-histology correlation**

Co-registration of (A) Congo Red and (B) A $\beta$  stained section with corresponding (C) T $_2^*$ - and (D) T $_2$ -weighted MR image from subject 4 diagnosed with Alzheimer's disease. The inhomogeneous signal in the cortex appeared to be caused by the deposition of A $\beta$  into amyloid plaques: their distribution corresponded to the hypo-intensities as detected on both types of MR images. As an example, the more detailed comparison showed several larger amyloid plaques to be co-localized with these hypo-intensities (*arrows*). Those smaller in size, or corresponding to a lesser amount of CR staining, were more difficult to discriminate. The structural layering of the GM, visible in both MR images, appeared to be independent of the A $\beta$  distribution.

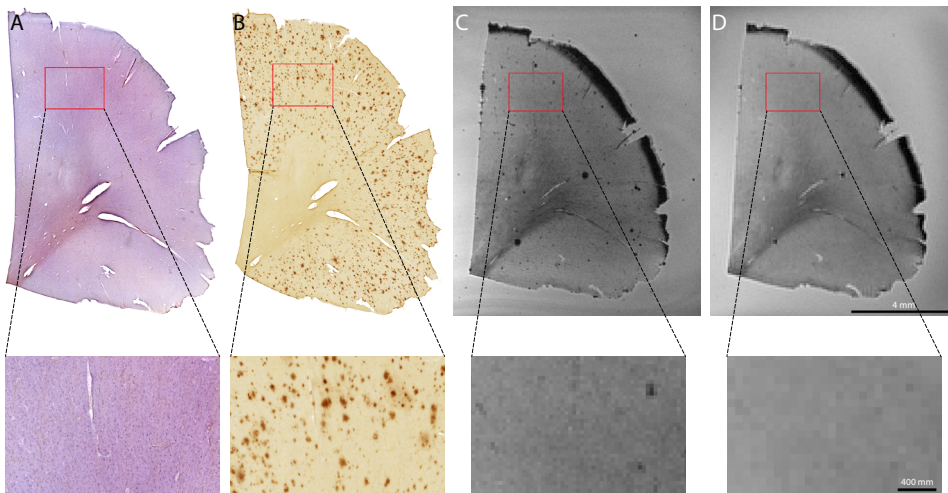


**Figure 5.2 MRI characteristics of diffuse plaques**

Co-registration of (A) Congo Red and (B) A $\beta$  stains with the corresponding (C) T $_2^*$ - and (D) T $_2$ -weighted MR images of subject 9 diagnosed with Down's syndrome. Since all A $\beta$  deposits lacked Congo Red staining, they were classified as diffuse plaques, which resulted in a relatively homogenous MR image. No A $\beta$  specific changes in MR signal intensity could be discriminated.



### T<sub>2</sub>\*- and T<sub>2</sub>-weighted MRI

On visual inspection of the T<sub>2</sub>\*- and T<sub>2</sub>-weighted scans by trained observers, only the congophilic amyloid plaques were visible as hypointense foci. (**Figure 5.1**) Congophilic amyloid plaques with smaller diameters than the MRI voxel size were less conspicuous on MRI due to the partial volume effect. In general, the signal attenuation was more pronounced on the T<sub>2</sub>\*-weighted images; however, the resolution of the T<sub>2</sub>-weighted images was four times lower than the T<sub>2</sub>\*-weighted images due to time restrictions. Despite the large amount of A $\beta$  present in the diffuse plaques, their presence did not result in any visible change in MRI contrast as compared to the surrounding GM in either sequence. This was most strikingly seen on close examination of cortical sections of subject 9, who was diagnosed with Down's syndrome, showing abundant parenchymal A $\beta$  deposits but completely lacking fibrillar amyloid. (**Figure 5.2**) MR images of normal appearing GM showed no cortical hypo-intensities apart from tissue preparation-induced artifacts. (**Figure 5.3**)

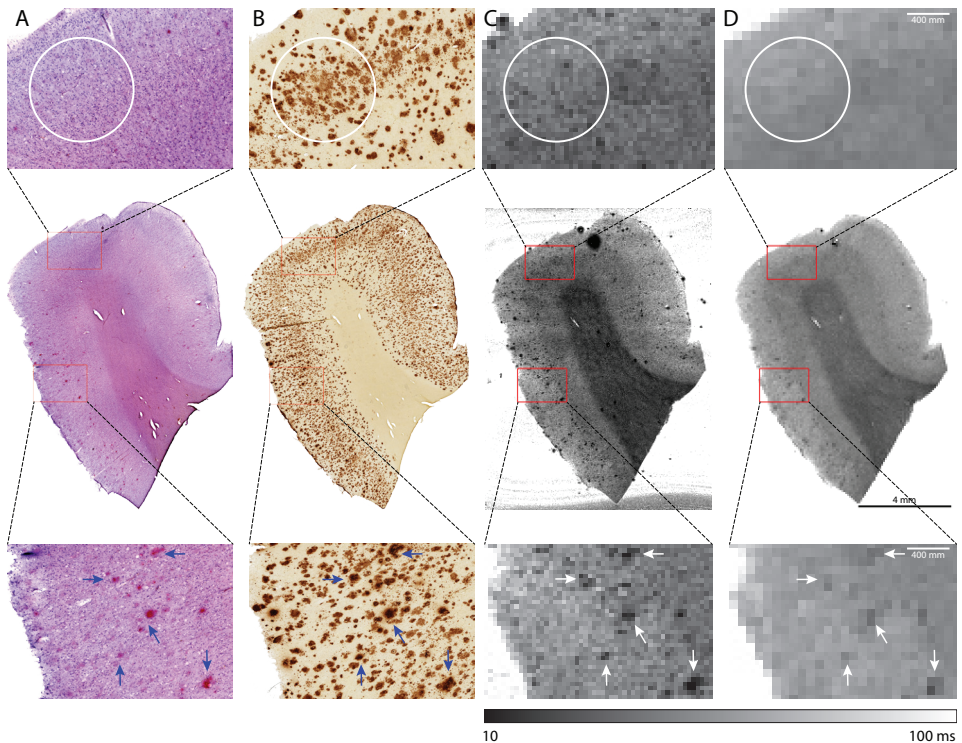


**Figure 5.3** MRI characteristics of healthy age-matched brain tissue

Co-registration of (A) Congo Red and (B) A $\beta$  stains with the corresponding (C) T<sub>2</sub>\*- weighted image and (E) T<sub>2</sub>\* map, and (E) T<sub>2</sub>-weighted image and (F) T<sub>2</sub> map of control subject 2. No inhomogeneous hypo-intensities were found within the GM since no A $\beta$  was present. Small circular hypo-intensities were observed both on and next to the section due to the inclusion of small air pockets underneath the coverslip.

### Quantitative $T_2^*$ and $T_2$ relaxation

Similar to the visual assessment, only the amyloid bearing deposits were associated with a significant decrease in  $T_2^*$  and  $T_2$  relaxation times. (**Figure 5.4**) Further quantification of these findings by ROI analysis demonstrated that cortical areas containing diffuse plaques ( $T_2 = 63.4 \pm 3.1$  ms (mean  $\pm$  SD);  $p = 0.051$ ;  $T_2^* = 47.3 \pm 6.2$  ms;  $p = 0.28$ ) were not associated with a significant difference in either  $T_2$  or  $T_2^*$  relaxation when compared to normal appearing GM ( $T_2 = 55.1 \pm 2.5$  ms;  $T_2^* = 47.5 \pm 4.7$  ms). (**Figure 5.5**) In contrast, focal amyloid-bearing deposits showed a significant reduction in  $T_2$  and particularly in  $T_2^*$  relaxation times ( $T_2 = 49.9 \pm 10.0$  ms;  $T_2^* = 17.7 \pm 6.4$  ms) when compared to normal appearing GM.

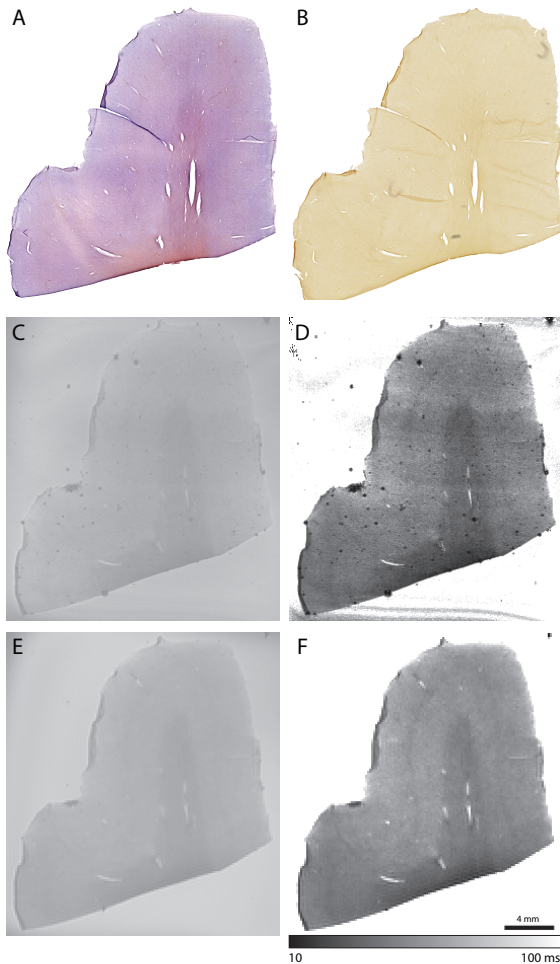


**Figure 5.4 Quantitative MRI of parenchymal A $\beta$  deposits**

Co-registration of (A) Congo Red and (B) A $\beta$  stains with corresponding quantitative (C)  $T_2^*$  and (D)  $T_2$  maps of subject 5. No signal decrease was observed corresponding to the outline of areas with A $\beta$  lacking CR positivity (*white circle*). In contrast, as an example several but not all amyloid plaques highlighted by the presence of both CR and A $\beta$  clearly resulted in hypointensities seen on the corresponding MR images (*arrows*).



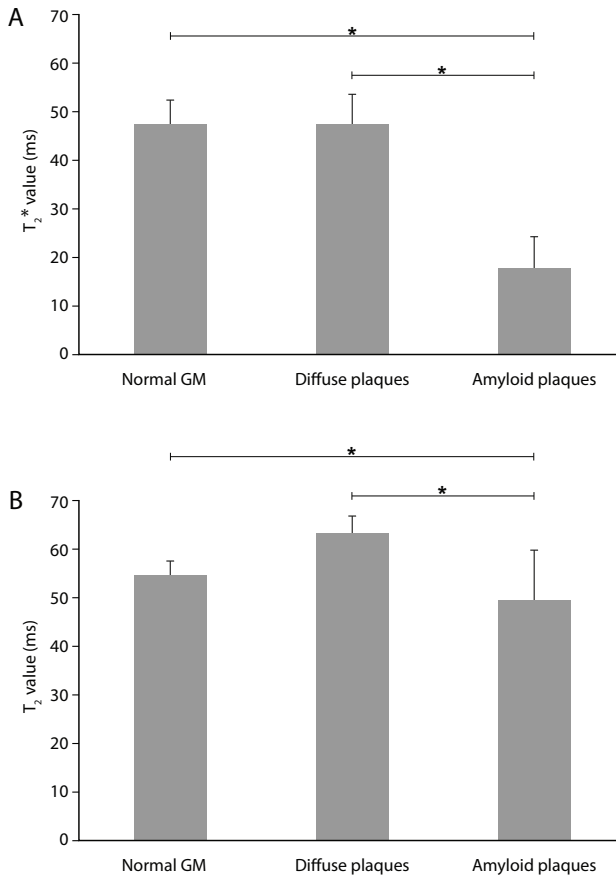


**Figure 5.5 T<sub>2</sub>\* and T<sub>2</sub> values of parenchymal A $\beta$  deposits**

Bar graphs of average (A) T<sub>2</sub>\* and (B) T<sub>2</sub> values in milliseconds (ms) resulting for ROI analyses of all samples for normal appearing GM (N = 21), diffuse plaques (N = 26) and amyloid plaques (N = 40). \*Significant difference of  $p < 0.05$  after an unpaired two-tailed Student t-test. Error bars represent the standard deviation.

### Vascular amyloid

Several subtypes of CAA were present within the subjects which, based upon the A $\beta$  immunostaining, could be classified as: a) "large vessel" CAA without, or b) "large vessel" CAA with dyschoric changes (i.e. amyloid extending outside the vascular wall into the parenchyma), or c) capillary CAA. (Table 5.1) In four subjects more than one subtype of CAA was present, while capillary CAA, which is relatively rare, was only detected in one subject. None of the selected occipital sections showed evidence of microbleeds or aneurysms that are known to often accompany CAA.

Capillary CAA did not result in any detectable MR contrast change on either the T<sub>2</sub>\*- or T<sub>2</sub>-weighted images. However, the large CAA-bearing vessels themselves were observed as hypointense structures in both scans, irrespective of accompanying dyschoric changes. (Figure 5.6) These findings were, however, not consistent for all large CAA vessels, as we also observed CAA vessels with a similar histological appearance, but without any signal attenuation on MRI. These large variations in appearance on MRI combined with the low number of subjects restricted further quantitative ROI analyses for CAA.

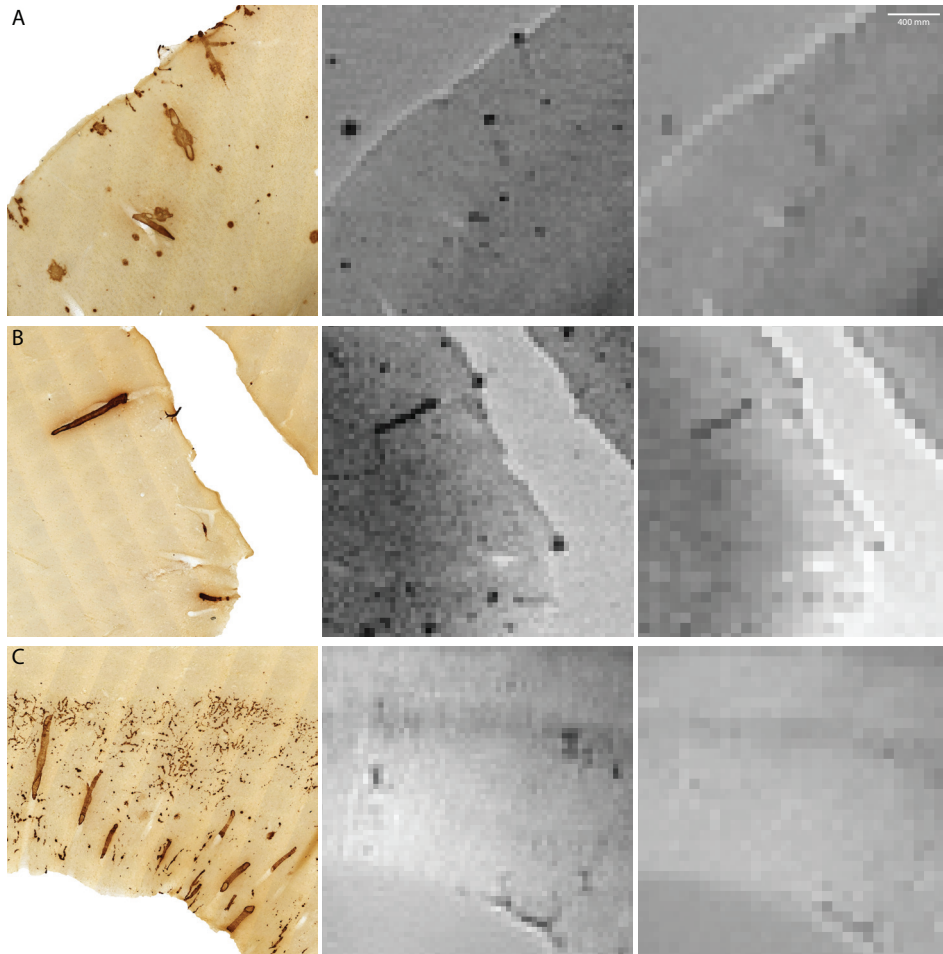


**Figure 5.6 MRI presentation of different types of CAA**

Detailed A $\beta$  immunohistochemistry with corresponding T $_2^*$ - and T $_2$ -weighted images of several types of CAA: **(A)** dyschoric CAA (subject 14); **(B)** "large vessel" CAA (subject 12); and **(C)** both capillary CAA and "large vessel" CAA (subject 13). For (A) and (B) the majority of the CAA could be correlated to similarly-shaped hypo-intense structures. In (C) neither "large vessel" nor capillary CAA were associated with a change in MRI signal intensity.

## Discussion

Previous studies have suggested that A $\beta$ , irrespective of associated iron, might induce detectable MRI contrast. Our data, however, demonstrate that the mere presence of large amounts of A $\beta$  peptides alone is not sufficient to change T $_2$  or T $_2^*$  relaxation significantly, since diffuse plaques are not associated with intensity changes on the MR images. Only when A $\beta$  is deposited in its fibrillar amyloid conformation are T $_2^*$  and T $_2$  relaxation times reduced, which can be observed as the punctuate hypo-intensities described in previous studies.<sup>5-16</sup> In addition, this study also showed that direct visualization of vascular amyloid is possible, although signal attenuation was

not observed in all CAA-affected vessels. With regard to the cerebral presence of A $\beta$ , this would imply that quantitative MRI would depict the cerebral fibrillar amyloid load rather than the amount of cerebral A $\beta$  peptides.

The current study used a magnetic field strength and spatial resolutions that are not clinically applicable; however, this study of the neocortical A $\beta$  deposits may provide background information that can support the development of future clinical (quantitative) MRI methods. Currently clinical scans do not allow the detection of individual plaques limited by the maximum resolution. We therefore did not aim to colocalize individual amyloid plaques, but tried to characterize which types of A $\beta$  deposits produce changes in MRI signal.

Diffuse plaques are hypothesized to be pathologic and are suggested to function as a seeding point for amyloid plaques. However, they are not specific for AD, they do not correlate with severity of dementia, and clinical evidence regarding their role in the pathogenesis of AD has not yet been reported.<sup>19-23</sup> In contrast, amyloid plaques are considered to be one of the definitive hallmarks of AD, and thus their presence forms one of the diagnostic criteria for AD. Any imaging technique aiming at the detection of amyloid should be sure to preclude the assignment of the A $\beta$  deposited as diffuse plaques, especially since they are often found to be present in large quantities. **(Figure 5.4)**

The current clinical standard for *in vivo* amyloid plaque detection uses [<sup>11</sup>C]-Pittsburgh-B compound (PiB) as an imaging tracer for positron emission tomography (PET). Numerous studies have demonstrated its specificity and sensitivity for plaque detection, showing that PiB binding is highly selective for fibrillar A $\beta$  deposits in AD.<sup>32</sup> However, its ability to delineate diffuse plaques and even NFTs has also been reported in a post-mortem study.<sup>33</sup> Furthermore, in cases of patients with other types of dementias, such as Parkinson's Disease Dementia, and Lewis Body Dementia, correlation of *in vivo* <sup>11</sup>C-PiB with post-mortem neuropathology showed that the high <sup>11</sup>C-PiB retention in these patients was primarily correlated to the presence of diffuse plaques.<sup>34,35</sup> Thus, in the setting of these dementias, <sup>11</sup>C-PiB PET has insufficient specificity for *in vivo* diagnosis of comorbid AD due to its inability to distinguish between diffuse and neuritic amyloid plaques.<sup>34</sup> In these cases in particular, MRI could provide additional value to confirm the presence of amyloid plaque.

In addition to investigating parenchymal A $\beta$ , this study is the first to present findings regarding MRI detection of vascular amyloid, another major site of cerebral A $\beta$  deposition. Besides being present in the vast majority of AD cases, CAA is an entity in itself and a common age-related finding at autopsy.<sup>25</sup> CAA leads to local inflammatory responses and loss of vessel wall integrity that eventually result in lobar hemorrhages, as well as complete and partial infarcts.<sup>24</sup> Thus far, only these secondary CAA-related pathologies have been reported to be detectable by MRI, but not the vascular amyloid accumulations themselves.<sup>36,37</sup> Our results showed that several CAA-affected vessels are associated with linear hypo-intensities. As these closely followed the outline of the CAA, this suggests that CAA itself in principle should be detectable with MRI.

However, not all CAA-affected vessels resulted in a similar loss of MR signal. Besides having vascular amyloid as a common denominator, various differences can be found amongst CAA.<sup>24</sup> These include not only the amount of A $\beta$  deposition but also its position within the vascular wall, vasculature fragmentation and loss of structure, formation of fibrinoid necrosis, iron accumulation and signs of hemorrhages or microaneurysms. The current study was limited as

its current setup did not allow to take these differences into account, though these might explain the variation in MRI results found within the present CAA data.

In contrast to amyloid plaques, the usual site for the development of CAA is the occipital lobe rather than the medial temporal lobe. Besides differences in clinical appearance, the spatial pattern of areas of signal loss might be used for differentiation between parenchymal and

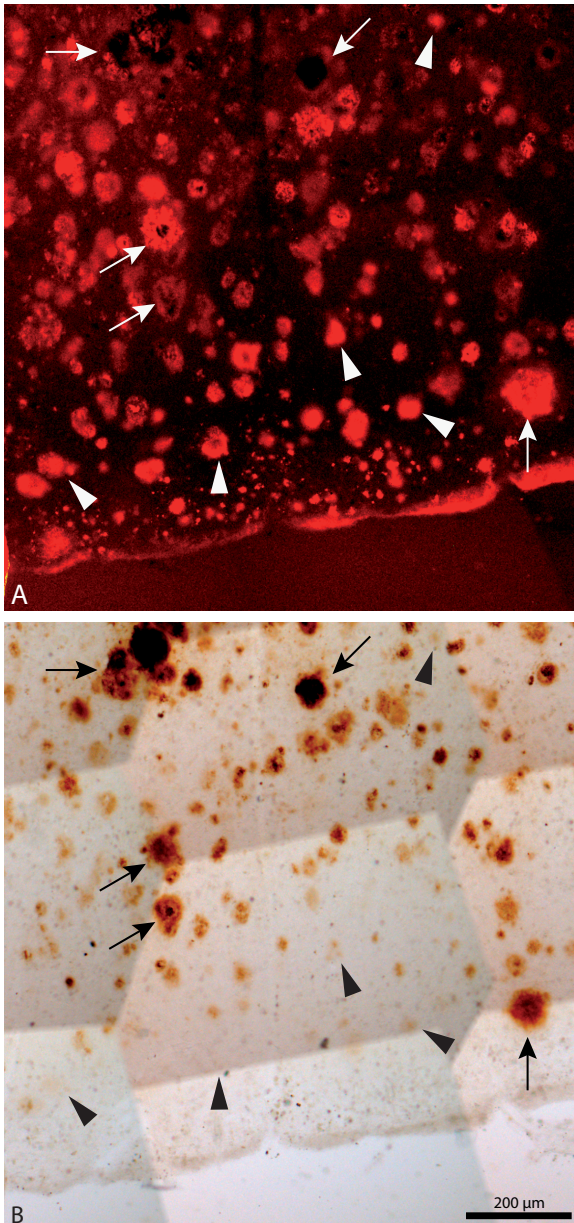


**Figure 5.7 The presence of iron within A $\beta$  deposits**

Detailed immunofluorescence against A $\beta$  (A) with corresponding 3,3'-DAB enhanced Perls' iron stain (B) (*adapted from ref. 7*). In this small cortical areas a wide variety of A $\beta$  deposits both rich (*arrows*) and low (*arrow heads*) in iron content is observed. Unable to define the diffuse plaques as the fibrillar status of each A $\beta$  deposit is unknown, therefore it remains unclear whether this might be reflected in the iron colocalization.

vascular amyloid, analogous to the different distribution seen on PiB-PET images in CAA and AD patients.<sup>38</sup> Additionally, depending on spatial resolution, the typical tubular structure of amyloid-laden vessels might be a distinctive feature of CAA.

An effort was made to assess the contribution of capillary CAA to MR signal intensity. Compared to the other types, capillary CAA is a rather rare finding but its presence correlates well with clinical symptoms such as dementia.<sup>39</sup> It was present in only one sample of all our subjects. In this sample, direct detection of amyloid on the T<sub>2</sub>(\*)-weighted MRI was hampered mainly by the small vessel size and the location of the capillary CAA within or near the stria of Gennari, a cortical layer of the occipital cortex known to result in a loss of signal using these sequences.<sup>40</sup> Further MRI studies including more capillary CAA samples will be essential to state with confidence whether capillary CAA leads to signal changes on MRI.

The possible effects of chemical fixation of tissue when acquiring post-mortem MRI data should always be taken into consideration and form an important limitation in the direct clinical translation of these types of studies.<sup>28</sup> Known effects such as altered water diffusion properties, reduced relaxation parameters and tissue changes due to prolonged fixation can be minimized by including only samples subjected to a well-defined, limited, fixation period and by thoroughly washing the sample with PBS to partially restore transverse relaxation times.<sup>28,30</sup> This cannot, however, compensate for possible effects on T<sub>2</sub>(\*) caused by protein cross-linking. In addition, tissue iron concentration are known to decrease due to prolonged formalin fixation, which influences MRI parameters.<sup>26,41</sup> Whether this iron wash-out differs between the distinct types of A $\beta$  deposits remains unknown. With regard to this study most samples were fixated for a similar period of just over two years, including the controls (**Table 5.1**), which makes it unlikely that the reported differences in MRI signal were induced by differences in fixation.

Future studies may include the use of fresh unfixed tissue as to circumvent these possible fixation effects.<sup>42</sup> The 60  $\mu$ m thick sections required for the direct one-to-one correlation as performed within this study, however, hampers the use of fresh non-frozen tissue due to technical difficulties with sectioning and mounting of the tissue.

Iron has been indicated to play an important role in the MR contrast of amyloid plaques. However, the presence of iron within the different A $\beta$  deposits remains to be further elucidated; a significant fraction of amyloid plaques have been reported not to contain any iron<sup>43</sup>, whereas several analytical microscopy studies showed a high spatial correlation between amyloid and an increase iron concentration with respect to the surrounding tissue<sup>26,44,45</sup>; only one study reported the presence of iron within vascular amyloid other than that associated with microbleeds<sup>46</sup>; and as yet no relation of iron with human diffuse plaques has been reported. The main focus of this study, however, was to investigate the MR characteristics of the different types of A $\beta$  pathology rather than to precisely unravel which constituent is responsible for the observed contrast. The potential role of iron within the non-fibrillar diffuse plaques remains an interesting one, both as a source of MRI contrast and as a neurotoxic species. In a previous study using similar sections, we showed that even within a small cortical area, the iron content was highly variable in areas with a relatively similar A $\beta$  load. (**Figure 5.7**) Whether this difference can be explained by the presence of amyloid fibrils is yet unclear, because despite several attempts using different histological stains against fibrillar amyloid, we have not been able to perform triple stainings on these thick sections.

In conclusion, direct MR microscopy of histological sections offers a valuable tool to characterize MR changes in relation to different A $\beta$  substrates. The results in this study show that both "large vessel" CAA and parenchymal amyloid cause hypo-intensities visible on T<sub>2</sub>\*- and T<sub>2</sub>-weighted MRI. In contrast, diffuse plaques do not cause any MRI signal changes. These findings provide relevant background information for the interpretation and further development of specific MRI methods for the detection and follow-up of AD and CAA.

## References

1. Dubois, B, Feldman, HH, Jacova, C, *et al.* Revising the definition of Alzheimer's disease: a new lexicon. *Lancet Neurol.* 2010; 9:1118-1127.
2. McKhann, GM, Knopman, DS, Chertkow, H, *et al.* The diagnosis of dementia due to Alzheimer's disease: recommendations from the National Institute on Aging-Alzheimer's Association workgroups on diagnostic guidelines for Alzheimer's disease. *Alzheimers Dement.* 2011; 7:263-269.
3. Frisoni, GB, Fox, NC, Jack, CR, Jr., *et al.* The clinical use of structural MRI in Alzheimer disease. *Nat Rev Neurol.* 2010; 6:67-77.
4. Jack, CR, Jr., Knopman, DS, Jagust, WJ, *et al.* Hypothetical model of dynamic biomarkers of the Alzheimer's pathological cascade. *Lancet Neurol.* 2010; 9:119-128.
5. Benveniste, H, Einstein, G, Kim, KR, *et al.* Detection of neuritic plaques in Alzheimer's disease by magnetic resonance microscopy. *Proc Natl Acad Sci U S A.* 1999; 96:14079-14084.
6. Meadowcroft, MD, Connor, JR, Smith, MB, *et al.* MRI and histological analysis of beta-amyloid plaques in both human Alzheimer's disease and APP/PS1 transgenic mice. *J Magn Reson Imaging.* 2009; 29:997-1007.
7. Nabuurs, RJ, Hegeman, I, Natte, R, *et al.* High-field MRI of single histological slices using an inductively coupled, self-resonant microcoil: application to *ex vivo* samples of patients with Alzheimer's disease. *NMR Biomed.* 2010.
8. van Rooden, S, Aat-Schieman, ML, Nabuurs, RJ, *et al.* Cerebral amyloidosis: post-mortem detection with human 7.0-T MR imaging system. *Radiology.* 2009; 253:788-796.
9. Braakman, N, Matysik, J, van Duinen, SG, *et al.* Longitudinal assessment of Alzheimer's beta-amyloid plaque development in transgenic mice monitored by *in vivo* magnetic resonance microimaging. *J Magn Reson Imaging.* 2006; 24:530-536.
10. Chamberlain, R, Reyes, D, Curran, GL, *et al.* Comparison of amyloid plaque contrast generated by T<sub>2</sub>-weighted, T<sub>2</sub>\*-weighted, and susceptibility-weighted imaging methods in transgenic mouse models of Alzheimer's disease. *Magn Reson Med.* 2009; 61:1158-1164.
11. Helpern, JA, Lee, SP, Falangola, MF, *et al.* MRI assessment of neuropathology in a transgenic mouse model of Alzheimer's disease. *Magn Reson Med.* 2004; 51:794-798.
12. Jack, CR, Jr., Garwood, M, Wengenack, TM, *et al.* *In vivo* visualization of Alzheimer's amyloid plaques by magnetic resonance imaging in transgenic mice without a contrast agent. *Magn Reson Med.* 2004; 52:1263-1271.
13. Jack, CR, Jr., Wengenack, TM, Reyes, DA, *et al.* *In vivo* magnetic resonance microimaging of individual amyloid plaques in Alzheimer's transgenic mice. *J Neurosci.* 2005; 25:10041-10048.
14. Lee, SP, Falangola, MF, Nixon, RA, *et al.* Visualization of beta-amyloid plaques in a transgenic mouse model of Alzheimer's disease using MR microscopy without contrast reagents. *Magn Reson Med.* 2004; 52:538-544.
15. Vanhoutte, G, Dewachter, I, Borghgraef, P, *et al.* Noninvasive *in vivo* MRI detection of neuritic plaques associated with iron in APP[V717I] transgenic mice, a model for Alzheimer's disease. *Magn Reson Med.* 2005; 53:607-613.
16. Wengenack, TM, Reyes, DA, Curran, GL, *et al.* Regional differences in MRI detection of amyloid plaques in AD transgenic mouse brain. *Neuroimage.* 2011; 54:113-122.
17. Ramani, A, Jensen, JH, and Helpern, JA. Quantitative MR imaging in Alzheimer disease. *Radiology.* 2006; 241:26-44.
18. Duyckaerts, C, Delatour, B, and Potier, MC. Classification and basic pathology of Alzheimer disease. *Acta Neuropathol.* 2009; 118:5-36.
19. Braak, H and Braak, E. Neuropathological staging of Alzheimer-related changes. *Acta Neuropathol.* 1991; 82:239-259.
20. Price, JL, Davis, PB, Morris, JC, *et al.* The distribution of tangles, plaques and related immunohistochemical markers in healthy aging and Alzheimer's disease. *Neurobiol Aging.* 1991; 12:295-312.
21. Thal, DR, Rub, U, Schultz, C, *et al.* Sequence of Abeta-protein deposition in the human medial temporal lobe. *J Neuropathol Exp Neurol.* 2000; 59:733-748.
22. Thal, DR, Rub, U, Orantes, M, *et al.* Phases of A beta-deposition in the human brain and its relevance for the development of AD. *Neurology.* 2002; 58:1791-1800.
23. Thal, DR, Griffin, WS, and Braak, H. Parenchymal and vascular Abeta-deposition and its effects on the degeneration of neurons and cognition in Alzheimer's disease. *J Cell Mol Med.* 2008; 12:1848-1862.
24. Thal, DR, Griffin, WS, de Vos, RA, *et al.* Cerebral amyloid angiopathy and its relationship to Alzheimer's disease. *Acta Neuropathol.* 2008; 115:599-609.
25. Attems, J. Sporadic cerebral amyloid angiopathy: pathology, clinical implications, and possible pathomechanisms. *Acta Neuropathol.* 2005; 110:345-359.



26. Attems, J, Jellinger, K, Thal, DR, *et al.* Review: sporadic cerebral amyloid angiopathy. *Neuropathol Appl Neurobiol.* 2011; 37:75-93.
27. Braak, H, Alafuzoff, I, Arzberger, T, *et al.* Staging of Alzheimer disease-associated neurofibrillary pathology using paraffin sections and immunocytochemistry. *Acta Neuropathol.* 2006; 112:389-404.
28. van Duijn, S, Nabuurs, RJ, van, RS, *et al.* MRI artifacts in human brain tissue after prolonged formalin storage. *Magn Reson Med.* 2011.
29. Pfefferbaum, A, Sullivan, EV, Adalsteinsson, E, *et al.* Post-mortem MR imaging of formalin-fixed human brain. *Neuroimage.* 2004; 21:1585-1595.
30. Shepherd, TM, Thelwall, PE, Stanisiz, GJ, *et al.* Aldehyde fixative solutions alter the water relaxation and diffusion properties of nervous tissue. *Magn Reson Med.* 2009; 62:26-34.
31. Natte, R, Maat-Schieman, ML, Haan, J, *et al.* Dementia in hereditary cerebral hemorrhage with amyloidosis-Dutch type is associated with cerebral amyloid angiopathy but is independent of plaques and neurofibrillary tangles. *Ann Neurol.* 2001; 50:765-772.
32. Ikonomic, MD, Klunk, WE, Abrahamson, EE, *et al.* Post-mortem correlates of *in vivo* PiB-PET amyloid imaging in a typical case of Alzheimer's disease. *Brain.* 2008; 131:1630-1645.
33. Lockhart, A, Lamb, JR, Osredkar, T, *et al.* PIB is a non-specific imaging marker of amyloid-beta (Abeta) peptide-related cerebral amyloidosis. *Brain.* 2007; 130:2607-2615.
34. Burack, MA, Hartlein, J, Flores, HP, *et al.* *In vivo* amyloid imaging in autopsy-confirmed Parkinson disease with dementia. *Neurology.* 2010; 74:77-84.
35. Kantarci, K, Yang, C, Schneider, JA, *et al.* Ante mortem amyloid imaging and beta-amyloid pathology in a case with dementia with Lewy bodies. *Neurobiol Aging.* 2012; 33:878-885.
36. Greenberg, SM, Vernooij, MW, Cordonnier, C, *et al.* Cerebral microbleeds: a guide to detection and interpretation. *Lancet Neurol.* 2009; 8:165-174.
37. Schrag, M, McAuley, G, Pomakian, J, *et al.* Correlation of hypo-intensities in susceptibility-weighted images to tissue histology in dementia patients with cerebral amyloid angiopathy: a post-mortem MRI study. *Acta Neuropathol.* 2009.
38. Johnson, KA, Gregas, M, Becker, JA, *et al.* Imaging of amyloid burden and distribution in cerebral amyloid angiopathy. *Ann Neurol.* 2007; 62:229-234.
39. Thal, DR, Ghebremedhin, E, Rub, U, *et al.* Two types of sporadic cerebral amyloid angiopathy. *J Neuropathol Exp Neurol.* 2002; 61:282-293.
40. Duyn, JH, van, GP, Li, TQ, *et al.* High-field MRI of brain cortical substructure based on signal phase. *Proc Natl Acad Sci U S A.* 2007; 104:11796-11801.
41. Schrag, M, Dickson, A, Jiffry, A, *et al.* The effect of formalin fixation on the levels of brain transition metals in archived samples. *Biometals.* 2010; 23:1123-1127.
42. Antharam, V, Collingwood, JF, Bullivant, JP, *et al.* High field magnetic resonance microscopy of the human hippocampus in Alzheimer's disease: quantitative imaging and correlation with iron. *Neuroimage.* 2012; 59:1249-1260.
43. Collingwood, JF, Chong, RK, Kasama, T, *et al.* Three-dimensional tomographic imaging and characterization of iron compounds within Alzheimer's plaque core material. *J Alzheimers Dis.* 2008; 14:235-245.
44. Miller, LM, Wang, Q, Telivala, TP, *et al.* Synchrotron-based infrared and X-ray imaging shows focalized accumulation of Cu and Zn co-localized with beta-amyloid deposits in Alzheimer's disease. *J Struct Biol.* 2006; 155:30-37.
45. Quintana, C, Bellefqih, S, Laval, JY, *et al.* Study of the localization of iron, ferritin, and hemosiderin in Alzheimer's disease hippocampus by analytical microscopy at the subcellular level. *J Struct Biol.* 2006; 153:42-54.
46. Schrag, M, Crofton, A, Zabel, M, *et al.* Effect of cerebral amyloid angiopathy on brain iron, copper, and zinc in Alzheimer's disease. *J Alzheimers Dis.* 2011; 24:137-149.



---

## PART ONE | Native MRI contrast

# Authors have contributed to this work equally

- 1 Department of Radiology, Leiden University Medical Center, Leiden, Netherlands
  - 2 Department of Pathology, Leiden University Medical Center, Leiden, Netherlands
  - 3 Division of Image Processing (LKEB), Department of Radiology, Leiden University Medical Center, Leiden, Netherlands
  - 4 C.S. Kubik Laboratory for Neuropathology, Massachusetts General Hospital and Harvard Medical School, Boston, Massachusetts, USA
  - 5 Department of Human Genetics, Leiden University Medical Center, Leiden, Netherlands
-

# Chapter 6

## Detection of cortical changes in Alzheimer's disease at ultra-high field MRI

*Submitted*

**Rob J.A. Nabuurs<sup>#1</sup>**

Sanneke van Rooden<sup>#1</sup>

Sara van Duijn<sup>2</sup>

Maarten J. Versluis<sup>1</sup>

Bart J. Emmer<sup>1</sup>

Michael K. Liem<sup>1</sup>

Julien R. Milles<sup>3</sup>

Andrew G. Webb<sup>1</sup>

Matthew P. Frosch<sup>4</sup>

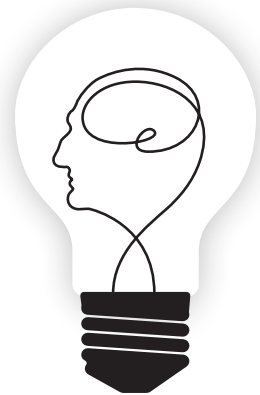
Sjoerd G. van Duinen<sup>2</sup>

Remco Natté<sup>2</sup>

Jeroen van der Grond<sup>1</sup>

Louise van der Weerd<sup>1,5</sup>

Mark A. van Buchem<sup>1</sup>



## Abstract

Non-invasive methods to detect AD (AD) *in vivo* at an early stage are important for increasing our still incomplete understanding of the pathophysiology of the disease. Recently, 7T MRI systems that generate novel susceptibility-based contrasts in the human cerebral cortex have become available. In this study we aimed to assess whether differences in cortical appearance could be observed in AD patients using 7T MRI *in vivo* and to assess the nature of these changes by a histological-radiological correlation *ex vivo*.

*In vivo* regional cortical differences between probable AD patients (n=14) and healthy control subjects (n=15), visible on 7T susceptibility-weighted (SW) images, were analyzed after defining a novel scoring method based on the cortical appearance. In addition, post-mortem MRI of confirmed AD cases (n=6) was performed to assess the histological correlates of the changes observed *in vivo* in AD patients.

Diffuse hypointense bands were frequently found in the cortex of the frontal lobes of AD patients (57%), but not in controls. Histologic correlation revealed that the pattern of the susceptibility-weighted contrast in the cortex of AD patients does not primarily co-localize with amyloid plaques or neurofibrillary tangles, but with microglia- and myelin-associated iron accumulation and with an altered myelin cytoarchitecture.

Our observation of disturbed iron accumulation and myelin architecture in AD may have important implications for future *in vivo* diagnosis of AD, but also for the understanding of the pathophysiological mechanisms underlying this disease.

## Introduction

For the definitive diagnosis of AD (AD) histological post-mortem detection of amyloid plaques and neurofibrillary tangles is required. During life, only a probable diagnosis can be made that is based primarily on clinical signs and symptoms.<sup>1</sup> However, recently it has been proposed to use biomarkers based on CSF analysis, structural MRI and amyloid imaging using PET, as supporting diagnostic criteria in research settings.<sup>2</sup>

Over the past few years, the feasibility of detecting the histological hallmarks of AD using MRI has been explored by many research groups. In general these efforts have focused on detecting individual amyloid plaques: increased iron accumulation around amyloid plaques induces a magnetic susceptibility effect, which is visible as hypointense foci on T<sub>2</sub>\*-weighted or susceptibility-weighted (SW) MRI in the cerebral cortex of transgenic AD mouse models and in human post-mortem brain slices.<sup>3-5</sup> However, these findings have not yet been convincingly replicated *in vivo* in patients, and it is doubtful whether detecting individual amyloid plaques with MRI will be possible in a clinical setting given the required high anatomical resolution, limited scanning time, and physiological motion of the patient. Furthermore, the central role of amyloid in the pathophysiology of AD remains a topic of debate. Although amyloid is still considered to be a hallmark as well as an initiating factor in the progression of the disease, there is increasing evidence that other primary or interacting causes, including changes in iron metabolism, may exist.<sup>6,7</sup>

Recent advances in human MRI systems operating at an ultra-high magnetic field strength (7 Tesla and higher) show that the increased sensitivity to susceptibility effects generates iron-based contrasts in the human brain that have not been observed at lower fields.<sup>8</sup> The aim of our study was to establish whether 7T MRI allows *in vivo* detection of differences in the cerebral cortex between probable AD patients and healthy age-matched controls. Having observed a difference, we then determined the histological substrate of the changes by comparing MRI to light- and electron microscopy (EM) of human post-mortem material of AD patients and controls.

## Materials & Methods

### ***In vivo* MRI study**

#### *Participants*

This study was approved by the institutional review board. In all cases, informed consent was obtained according to the declaration of Helsinki. Fourteen probable AD patients (mean age 76.4 years (range: 68 - 86), 9 males) and fifteen control subjects (mean age 75.1 years (range: 69 - 80), 10 males) were included. (**Table 1**) AD patients were recruited from the memory outpatient clinic of our institution. Memory outpatient clinic patients were referred to the hospital by their general practitioner or a medical specialist. Prior to the 7T MRI study these patients all underwent a routine clinical protocol, comprising a whole brain MRI (performed on a clinical 3 Tesla platform), a battery of neuropsychological tests, and a general medical and neurological examination performed by a neurologist, psychiatrist or internist-geriatrician. The diagnosis was made in a multidisciplinary consensus meeting using the National Institute

of Neurological and Communicative Disorders and Stroke and AD and Related Disorders Association (NINCDS-ADRDA) criteria for diagnosing probable AD.<sup>9</sup> Participants with the diagnosis 'probable AD', who were capable of giving informed consent and who had a Mini Mental State Examination (MMSE) of  $\geq 19$  were selected for inclusion in the 7T study, either retrospectively within one year after attending the memory clinic, or prospectively. Healthy control subjects were recruited by focused advertisements. Subjects between 69 and 80 years of age, who were living independently and had an MMSE of  $\geq 25$  and a Geriatric Depression Scale (GDS) of  $\leq 4$  were selected for inclusion. Control subjects with the following diseases were excluded: stroke, Parkinson's disease, diabetes mellitus, rheumatoid arthritis, polymyalgia rheumatica, cancer, heart failure, and chronic obstructive pulmonary disease.

#### *MRI data acquisition*

Our study was performed on a human whole-body MRI system operating at a magnetic field strength of 7 Tesla (Philips Healthcare, Best, The Netherlands) using a quadrature transmit and 16-channel receive head coil (Nova Medical, Wilmington, MA, USA). AD-related pathology spreads throughout almost the entire brain, but macroscopically typically involves the fronto-temporal association cortices.<sup>10-12</sup> Participants were scanned using a 2D flow-compensated axial  $T_2^*$ -weighted gradient-echo sequence which included the frontal lobe for detection of AD pathology with a total imaging duration of 10 minutes. Imaging parameters were: repetition time (TR)/echo time (TE) 794/25 ms, flip angle  $45^\circ$ , slice thickness 1.0 mm with a 0.1 mm interslice gap, 20 slices, 240 x 180 x 22 mm field of view, 1024x768 matrix size – resulting in an in-plane spatial resolution of 0.24 x 0.24 mm<sup>2</sup>. The bandwidth per pixel was 46 Hz, corresponding to a readout length of approximately 22 ms. Frequency and phase encoding directions were along the anterior-posterior and right-left axes, respectively. This sequence is very sensitive to image artifacts arising from resonance frequency fluctuations within the brain caused by slight patient movements, even in areas significantly away from the head, and so a navigator echo was

**Table 6.1 Characteristics of patients and controls and scoring results of the *in vivo* SWI study**

	AD (n = 14)	Controls (n = 15)	p-value
Characteristics:			
Male / female	9 / 5	10 / 5	0.893
Mean age (range, yrs)	76.4 (68 - 86)	75.1 (69 - 80)	0.497
MSME (range)	22.5 (19 - 26)	29.2 (27 - 30)	0.000
Presence of diffuse band:			
Superior frontal lobe	2 / 14 (14.3%)	0 / 15 (0%)	0.224
Middle and inferior frontal lobe	8 / 14 (57.1%)	0 / 15 (0%)	0.001
Hypo-intense foci			
Superior frontal lobe	0 / 14 (0%)	0 / 14 (0%)	-
Middle and inferior frontal lobe	0 / 14 (0%)	0 / 14 (0%)	-

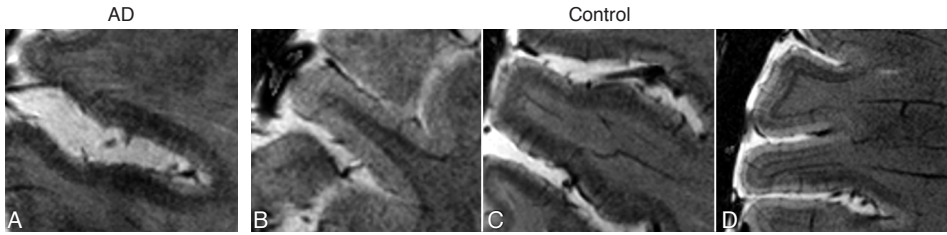


**Figure 6.1** The observed variations of *in vivo* 7T SWI appearance of the human cortex

Shown are the middle/inferior frontal brain area of an AD patient (A) and healthy elderly controls (B, C, D). A clear example of a cortical ribbon containing a hypointense diffuse band is observed in the AD patient (A). Please note the blurring of the edges of the layers. (B) shows an example of a cortical ribbon containing one regular layer with higher signal intensity than the adjacent WM. In (C) a cortical ribbon is shown containing two well-defined layers. (D) shows a cortical ribbon containing three well-defined layers.

included to correct for these artifacts.<sup>13</sup> Shimming up to third order was performed using an image based shimming approach.<sup>14</sup> Phase images were unwrapped by high-pass filtering with a 92x92 kernel size. SW images were constructed by applying four phase mask multiplications.<sup>15</sup> Whole brain imaging at this high spatial resolution ( $0.24 \times 0.24 \times 1 \text{ mm}^3$ ) however would result in an impractically long imaging duration, particularly for AD patients.<sup>13</sup> Since susceptibility artifacts induced by the temporal bone hampered the imaging of the temporal lobe, the final imaging volume focused on the frontal lobe, which is less prone to atrophy than the temporal lobe, but is known to accumulate high amyloid loads<sup>16</sup>, to have a lower metabolic rate<sup>17</sup>, and to have an altered resting state network connectivity in AD.<sup>18</sup>

#### Image analysis

Based on previous 7T MRI studies of the human cortex in post-mortem brain specimens of AD patients<sup>4</sup> and *in vivo* imaging of healthy volunteers<sup>19</sup> we developed a scoring method to capture the appearance of the cortex on SW images. We defined a normal cortex based on the following criteria: **a)** a cortical ribbon containing one homogeneous layer with a higher signal intensity as compared to the adjacent white matter (WM), **b)** a cortical ribbon containing two well-defined, homogeneous layers, with the superficial layer demonstrating a higher signal intensity compared to the deepest layer (the layer adjacent to the WM) and the WM, or **c)** a cortical ribbon with three layers: the same layers as previously described separated by a third thin layer with a lower signal intensity than the other two layers. (**Figure 6.1**) Abnormal cortex was classified as a deviation from the normal patterns described above, showing the presence of well-defined foci of signal loss (hypointense foci) and/or more diffuse areas with lower signal intensity in the superficial layer as compared to the adjacent WM (a diffuse band). (**Figure 6.1**) Features were scored as present or absent per subject in several predefined gyri of the frontal lobe. (**Table 6.1**) Uniform window settings were used for all images. Images were scored by two neuroradiologists (B.E. and M.L.) who were blinded for the diagnosis in a consensus reading.

#### Statistics

A Mann-Whitney U-test was used to assess differences in age and MMSE, and a chi-square test was used to assess differences in gender between AD and control groups. For each feature

Table 6.2 Post-mortem subject characteristics and SWI analysis

Subject characteristics			9.4 T SWI analysis						
No.	Age / Sex	Diagnose	Cause(s) of death	Braak	Amyloid	Homogenous with cortical layers	Diffuse band	Hypo-intense foci	Clouds
1	83 / F	Control	Arrhythmia	II	0	Yes	-	-	-
2	93 / F	Control	Acute death	I	A	Yes	-	-	-
3	89 / F	Control	Myocardial infarct / Pneumonia	III	A	No	+	+	+
4	77 / M	AD	Cachexia / dehydration by advanced dementia syndrome	VI	C	No	+	+	-
5	85 / F	AD	Aspiration pneumonia by advanced dementia syndrome	IV	C	No	+	-	+
6	87 / F	AD	Respiratory tract infection / cerebrovascular accident	VI	C	No	+	-	+
7	87 / M	AD	Cachexia / dehydration by advanced dementia syndrome	V	C	No	+	+	-
8	87 / F	AD	Sepsis	V	C	No	-	-	+
9	88 / F	AD	Unknown	IV	C	No	+	-	+

Characteristics are based on clinical information and standard neuropathologic examination according to the Braak criteria for tau and amyloid pathology.<sup>20</sup> The scoring indicates the presence (+) or absence (-) of the different patterns on the corresponding SW images. *F* = female; *M* = male.



(hypointense foci and/or a diffuse band), a Fisher's exact test was performed per brain region. Positive and negative predictive values of the features to detect AD were calculated per brain region. All statistical analyses were performed with the Statistical Package of Social Sciences (SPSS 17.0.1; SPSS, Chicago, Ill).

## Post-mortem MRI study

### *Study design*

To investigate the histological substrates responsible for the observed *in vivo* MRI changes at 7T, we applied similar scan methods on post-mortem material of AD patients and controls using a vertical-bore 9.4 T system (Bruker Biospin, Ettlingen, Germany). For each sample high-resolution (isotropic 40  $\mu\text{m}$  voxels) images were acquired, as well as images with a similar resolution (isotropic 200  $\mu\text{m}$  voxels) as were used in the *in vivo* study. The lower resolution MR images were acquired to help translation between the *in vivo* and *ex vivo* MR data sets. The high-resolution MR images helped to identify the particular MR images that matched best with the 8- $\mu\text{m}$  thick histological sections.

### *Sample preparation*

Brain tissue was obtained from the tissue bank of the Department of Pathology at our institution and from the Netherlands Brain Bank (NBB, Netherlands Institute for Neuroscience, Amsterdam). Following a post-mortem interval of <19 hours, brains were resected and stored in 4% paraformaldehyde. At both institutions brain tissue was examined histologically for the presence of AD-related pathology and scored using the Braak classification.<sup>20</sup> Based on availability six samples with a clinical diagnosis of AD by histological confirmation were selected, as well as three age-matched non-demented controls. (**Table 6.2**) Patient anonymity was strictly maintained. All tissue samples were handled in a coded fashion, according to Dutch national ethical guidelines (Code for Proper Secondary Use of Human Tissue, Dutch Federation of Medical Scientific Societies). To avoid formalin-induced artifacts in the MR images only material fixed for a period of between three months and two years was used.<sup>21</sup> From each subject one tissue block of approximately 4 x 15 x 15 mm<sup>3</sup> was resected from the medial temporal lobe using a vibratome (VT1000S, Leica, Germany). Care was taken to ensure that the samples were resected with a similar gyral orientation. Residual formalin was washed out by placing the samples in phosphate buffered saline (PBS) for >24 hours to partially restore MR relaxation parameters.<sup>22</sup> For MRI, each sample was placed in a customized tissue container and immersed in a proton-free fluid (Fomblin LC08, Solvay). Air was removed by application of a vacuum for several minutes.<sup>21</sup>

### *Post-mortem MRI*

Scans were acquired on a 9.4 Tesla vertical bore MRI system, equipped with a 1 T/m actively-shielded gradient insert and Paravision 5.0 imaging software (Bruker Biospin, Ettlingen, Germany). A 20-mm diameter birdcage transmit/receive coil was used to acquire T<sub>2</sub>\*-weighted 3D gradient echo images with TR = 75 ms; TE = 22.5 ms; flip angle = 25° at either 200  $\mu\text{m}$  isotropic resolution with 20 signal averages, or 40  $\mu\text{m}$  isotropic resolution with 28 signal averages. The average scan time per resolution was approximately 40 minutes (200  $\mu\text{m}$

resolution) or 25 hours (40  $\mu\text{m}$  resolution), with minor differences between samples of slightly different sizes. To create SW images comparable to *in vivo* scans, the 200  $\mu\text{m}$  resolution phase images were unwrapped using a k-space Hanning filter with a width set to 50% of the image size.<sup>23</sup> Final SW images were reconstructed from the original images by four phase mask multiplications.<sup>15</sup> All data processing was performed with MatLab (MathWorks, Natick, MA).

#### *Post-mortem image analysis*

For assessment of *ex vivo* SW images we used the same criteria as were used *in vivo* for defining normal and abnormal cortex (hypointense bands and hypointense foci). In addition, since the *ex vivo* images showed increased anatomical detail compared to the *in vivo* scans (due to the absence of physiological motion), a third category of abnormal cortex could be added, namely diffuse areas with low signal intensity, not extending parallel to the cortical surface (as in healthy tissue) but instead expanding locally in an irregular fashion throughout the cortex, a feature which we have termed “clouds” (**Suppl. Figure 6.1**). Window settings were optimized for each sample based on the WM and gray matter (GM) histogram. The 200  $\mu\text{m}$  SW images were scored blinded for diagnosis by a neuroradiologist (M.v.B) and MR-microscopy expert (L.v.d.W) in a consensus reading.

#### *Histology and electron microscopy*

All brain samples were paraffin-embedded and serially cut into 8- $\mu\text{m}$  thick sections. Tissue morphology was assessed by standard hematoxylin-eosin (HE) staining. Iron was detected using a 3'3-diaminobenzidine-tetrahydrochloride (DAB) enhanced Perls' staining protocol for light microscopy and EM which has shown to be the most sensitive to detect iron-positive structures in paraffin-embedded human AD brain tissue.<sup>24,25</sup> Consecutive sections were (co-)stained for amyloid-beta ( $\text{A}\beta$ ), paired helical filament-tau (AT8), myelin (protolipid-protein (PLP)), microglia (CD68 and HLA-DR) and activated astrocytes (GFAP). (**Suppl. Table 6.1**) Endogenous peroxidase was blocked by 30 minutes of incubation in methanol with 0.02%  $\text{H}_2\text{O}_2$ . After these pre-treatments, non-specific binding was minimized by incubation with 10% fetal calf serum (DakoCytomation). Labeling was visualized by DAB staining (DakoCytomation). All sections were digitized with a microscope scanner (Panoramic, 3DHistotech, Hungary) for global and microscopic evaluation. To assess co-localization of cellular iron with CD68, HLA-DR or GFAP-positive cells, sections stained for iron as described above were subsequently treated according to the previously described immunohistochemical procedures except for using an Alexa647-labeled secondary anti-mouse antibody for immunofluorescence. (**Suppl. Table 6.1**) Co-localization of these antigens with iron was assessed using a confocal fluorescence microscope (LSM 510, Zeiss, Germany). Iron-stained ultrathin (100 nm) sections were examined by electron microscopy (JEM-1011, JEOL, Germany) to assess the exact localization of the cortical iron in the neuropil.

#### *Histology-MRI correlation*

The digitized histological sections were matched with their corresponding high-resolution (40  $\mu\text{m}$ ) MR images by visual comparison of the contour and vascular architecture of each section. The corresponding low-resolution SW image that matched best with the histological section

could then be identified directly since the two SW image datasets are inherently co-registered. To assess the histological substrate of the cortical changes observed on MR images, the digitized histological sections were first inspected at low magnification (2x) alongside the corresponding low-resolution SW image. Subsequently, these areas were further analyzed microscopically at higher magnification (40x) to look for the microscopic changes underlying the MR. All observations were independently verified by three neuropathologists (R.N., S.v.D., M.F.).

## Results

The characteristics of the participants for *in vivo* MRI are shown in **Table 6.1**. No difference in age ( $p = 0.497$ ) or gender ( $p = 0.893$ ) was found between patient and control groups. Scores for global cognitive functioning (MMSE score) were significantly higher in controls (29.2 points; range 27-30) than in patients with AD (22.5 points, range 19-26),  $p < 0.001$ . 7T SW images of the frontal lobe of probable AD patients ( $n=14$ ) were visually compared to those of control subjects ( $n=15$ ).

We developed a scoring method to rate the cortical appearance based on previous 7T observations in normal brain and post-mortem observations in AD patients, distinguishing normal-appearing cortical patterns with one or more homogeneous layers from hypo-intense foci or hypointense diffuse bands. (**Figure 6.1**) Clear *in vivo* differences between AD patients and controls were seen in terms of the presence of diffuse hypointense bands on the SW images. (**Table 6.1** and **Figure 6.2**)

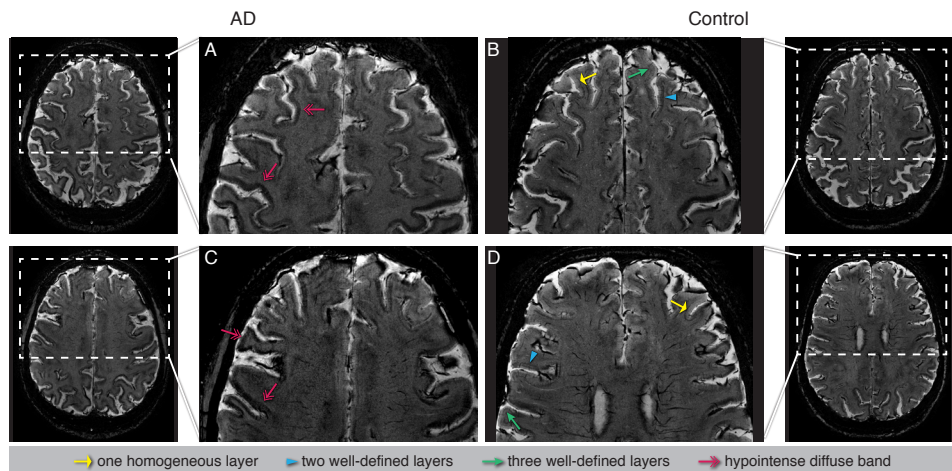


**Figure 6.2** *In vivo* cortical differences seen on SWI in AD patients versus age-matched control subjects

Regional distribution of the observed variations of *in vivo* 7T SWI appearance as presented in Figure 6.1, shown in an AD patient and a control subject. The left two columns (**A** and **C**) show an AD patient and the right two columns (**B** and **D**) a control subject. The upper row (**A** and **B**) shows the superior frontal region, the lower row (**C** and **D**) the middle and inferior frontal region. In the AD patient a diffuse band is seen in both regions of the frontal lobe and the double arrows show several locations containing this band whereas in the control subject this diffuse band is absent and a regular layer (arrow), two-well defined layers (arrowhead) and three-well defined layers (small arrow) could be detected.

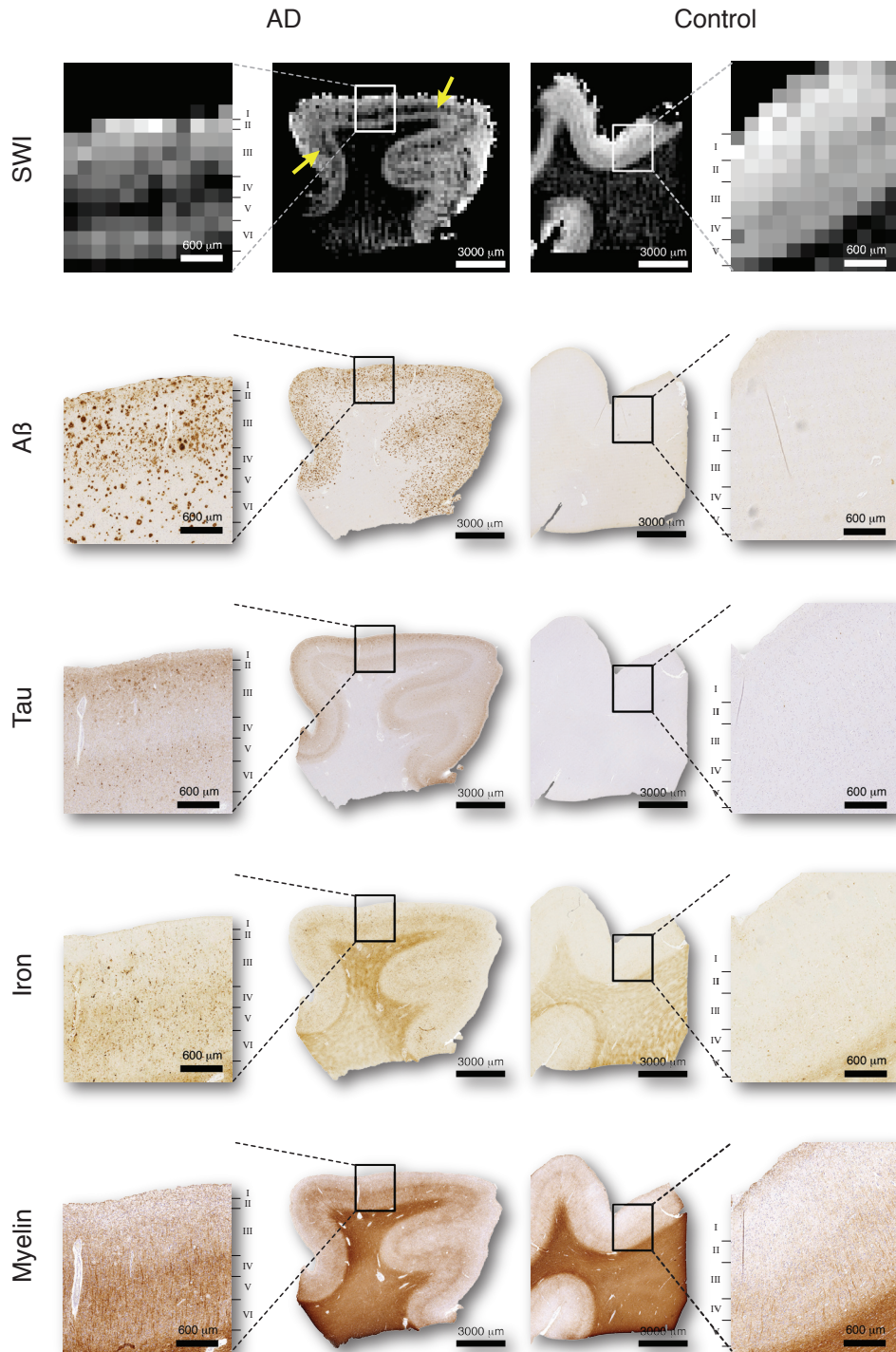


**Figure 6.3 Comparison of post-mortem SWI with histology**

The SWI image of the AD patient (Table 6.2 subject 7) showed a midcortical hypointense band (*yellow arrows*) in addition to several focal hypo-intensities, as opposed to a clear homogenous cortex as seen in the control subject (Table 6.2 subject 1). For detailed evaluation similar regions of interest of the cortex are shown alongside each corresponding main image and the cortical layers have been assigned accordingly. Neither the cortical distribution of A $\beta$  or tau matched the hypointense band. Tau typically showed a band-like pattern in cortical layers II – III and V, and so is not co-localized in the layer corresponding to MR signal decrease. Both iron and myelin correlated with the observed pattern of band-like hypo-intensities, including a diminished staining in the inner cortical layers V and VI. As compared to the control, the iron staining of the AD subject showed an increase in cellular deposits and diffuse iron within the neuropil, mainly centered around cortical layer IV spreading to both sides with overlap in layers III and IV. The myelin distribution visualized by the PLP-immunostaining showed a similar pattern of increased staining in the AD subject resulting from a denser network of thin myelinated fibers. Similar to previous reports, in the AD patient the cortex also contained several small roundish areas devoid of myelinated fibers suggesting the presence of amyloid plaques based on their morphological appearance.<sup>29</sup>

Within the frontal lobe, these patterns were found in the middle and inferior frontal gyri in eight out of 14 patients, whereas these diffuse bands were not observed in any of the control subjects. In these frontal gyri, the diffuse hypointense band was significantly more prevalent in AD patients as compared to controls ( $p = 0.001$ ), with positive predictive and negative values of 100% and 71%, respectively. In the superior frontal gyrus, a similar hypointense band was observed in only two out of the 14 AD patients and in none of the control subjects: there was no significant difference between the two groups ( $p = 0.224$ ). For this specific cortical region, corresponding positive and negative predictive values were 100% and 55%, respectively. Foci of signal loss were not observed in the frontal lobe in either AD patients or control subjects. Post-mortem cerebral cortex samples of six AD cases and three age-matched controls were scanned with a similar SWI protocol as for the *in vivo* MRI. Two of the controls showed a normal cortex. The control subject with an abnormal cortex revealed AD-type pathology (Braak stage III), despite the absence of an ante-mortem clinical AD diagnosis. We therefore discuss the findings in this case separately.

In all post-mortem AD samples (six out of six), an abnormal cortex was observed on SW images. **(Table 6.2)** Hypointense bands were observed in five out of six AD cases, and in the control with Braak III. Due to the lack of physiological movements, the *ex vivo* images that were acquired with a similar resolution as the *in vivo* images provided more anatomical detail, and demonstrated that the hypointense bands did not cover the full width of the cortex, but were located centrally in the cortex. **(Figure 6.3)** Hypointense foci were observed in two out of six AD cases, and in the one control specimen with Braak III. In addition to the scoring criteria defined for the *in vivo* scans, in these post-mortem samples a third category of cortical disturbance could be observed, consisting of cloud-like areas of low signal intensity with less alignment along, and more expansion through, the cortical layers (four out of six AD cases, and in the control subject with Braak III). **(Suppl. Figure 6.1)**

Comparing radiological and histological data of the same sample, the epicenter of the hypointense bands and clouds observed on the *ex vivo* MR images could be localized in cortical layer IV. Subsequently, we assessed which of the histological markers (A $\beta$ , tau, iron, and myelin) showed a similar distribution over the cortical layers to the hypointense bands and clouds. We observed that the hypointense bands and clouds on MRI co-localized with areas characterized by an increased presence of iron and changes in myelin structure. **(Figure 6.3)**



Only cortices that were scored as abnormal on SW images demonstrated these accentuated local patterns for iron and myelin on histological examination. Interestingly, no co-localization was observed between the hypointense bands and clouds on MRI and areas staining for A $\beta$  or tau. Tau pathology typically affected cortical layers II – III and V. A $\beta$  staining was present to an equal extent across all cortical layers. Microscopically, some of the hypointense foci observed on the *ex vivo* images corresponded to large amyloid plaques, but these focal signal voids barely contributed to the observed hypointense cortical bands. (Suppl. Figure 6.2)

Since the pattern of the abnormalities observed on MRI corresponded best with the patterns observed on iron and myelin-stained tissue, we examined these stainings in more detail. Microscopically, using higher magnification, four different types of iron accumulation were observed in the cortex: 1) diffuse neuropil deposition associated with myelinated fibers, 2) dense stellate cytoplasmic iron accumulation in microglial cells, 3) a dense thin line of perinuclear iron accumulation in oligodendroglial and microglial cells, and 4) iron associated with amyloid plaques. (Figure 6.4)

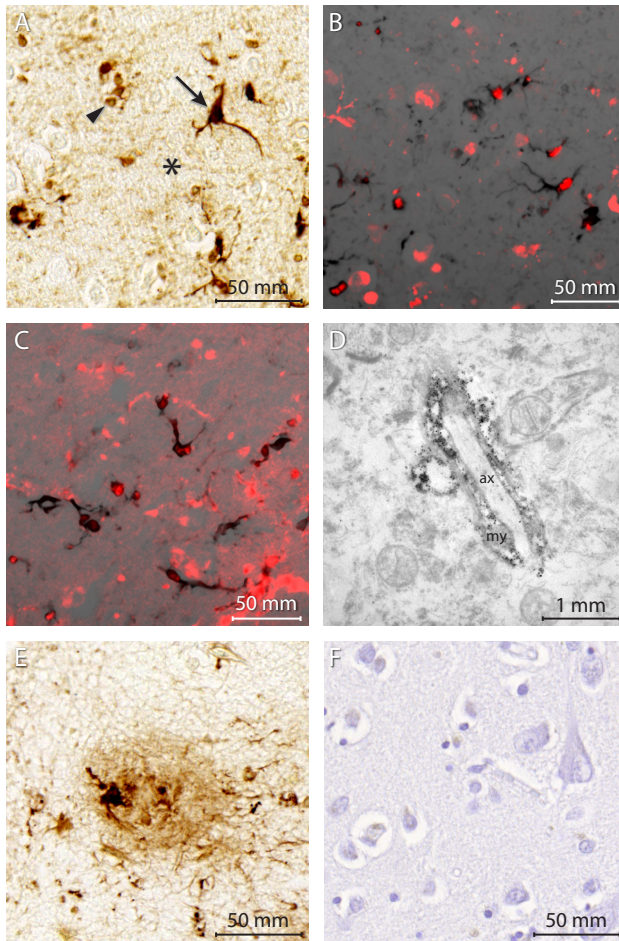


**Figure 6.4 Characterization of intracortical iron distribution in AD brain tissue**

Shown are the different types of cellular and neuropilar intracortical iron in the medial temporal lobe of an AD patient (Table 6.2 subject 7). (A) Indicated by the brown color due to the modified 3'3-DAB enhanced Perls' iron staining, iron is present as perinuclear (*arrow head*) and stellate cellular deposits (*arrow*), and as diffuse iron spread throughout the neuropil (*asterix*). Morphologically the cellular iron was attributed to oligodendro- or microglia cells. The latter was further verified by the colocalization of iron (black) with (B) CD68 (*red*) and (C) HLA-DR (*red*) immunostaining. As indicated by both stainings, even in close proximity to these iron-bearing microglia, several microglia were present that were completely devoid of iron. (D) Ultrastructurally, as shown by EM, neuropil iron was found to be located in the myelin sheets folded around an axon. (E) A example of iron found associated with an amyloid plaque. (F) The negative iron staining of a consecutive section did not result in any DAB enhancement, thereby confirming specificity of the iron stain. (*axon, ax*; *myelin sheet, my*)

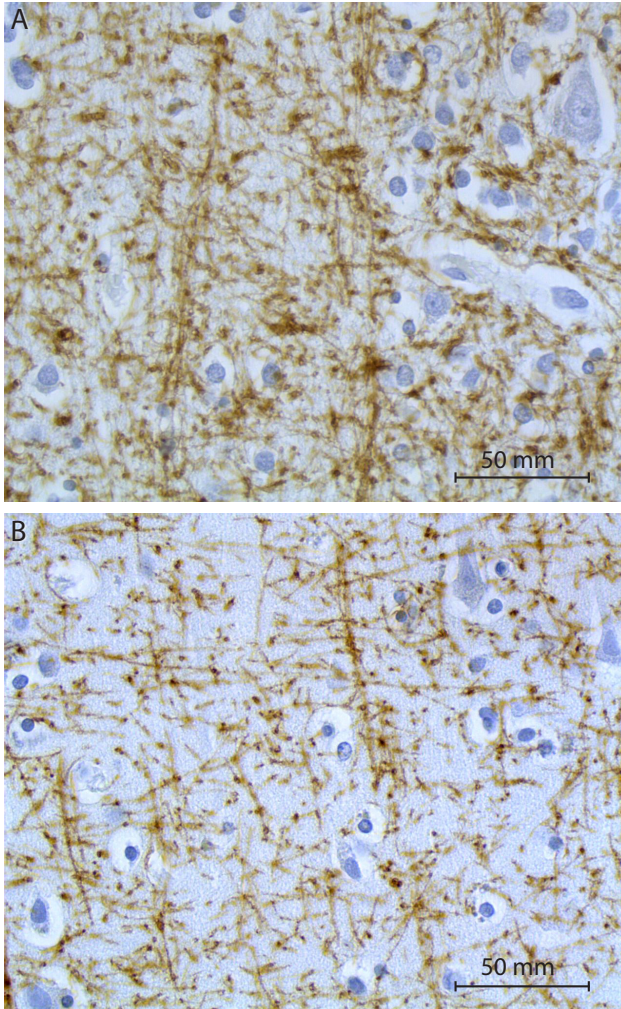


**Figure 6.5 Structural alterations of intracortical myelin**

In addition to the observed differences in myelin highlighted by Figure 6.3, this figure presents a more detailed comparison of the intracortical myelin of the medial temporal lobe of (A) an AD patient (Table 6.2 subject 4) and (B) a non-demented age-matched control (Table 6.2 subject 1). Shown are midcortical regions (layer IV) with a comparable orientation assessed by a PLP-immunostaining (*brown*). At this higher magnification, the intracortical myelin in the AD subjects was characterized by an accentuated PLP staining due to changes in myelin structure comprising fragmentation, increased segmental tortuosity and bead-like varicosities. As a result the PLP staining of the AD cortex appeared disorganized with loss of individually discernable fibers and orientation when compared to the cortex of the control subjects.

All four types of iron deposits were more abundant in the subjects with an abnormally appearing cortex on post-mortem MRI, including the control subject with Braak III. The first three types of iron deposits were localized differently in the cortical layers: neuropil iron accumulation was centered in layer IV, extending into layers III and V of the cortex; stellate glial aggregates were most abundant in the middle cortical layers (layers III and IV), but were also present to a lesser extent in the deep cortical layers (layers V and VI), and perinuclear glial iron accumulation was most abundant in layers V and VI, followed by layers IV and III. (Figure 6.3) In addition, increased microglial and neuropil iron accumulations were also observed in areas characterized by cloud-like hypo-intensities on MRI. EM analysis revealed that the diffuse iron in the neuropil was located predominantly in oligodendrocytic myelin sheaths. (Figure 6.4D)

The association of iron with myelin sheaths in the neuropil led us to examine the cortical myelin in more detail using a PLP staining. Interestingly, the intensity of myelin staining also showed a

colocalization with the low signal intensity bands and clouds on MRI. (**Figure 6.3**) Histologically, these areas were characterized by an accentuated PLP staining due to changes in myelin structure comprising fragmentation, increased segmental tortuosity and bead-like varicosities, centralized in layer IV, but extending to layers III and V in the AD patients. (**Figure 6.3** and **6.5**) Furthermore, as expected, small round plaque-like areas that were devoid of any myelin fibers were observed in cortical areas containing a high number of A $\beta$  deposits.

## Discussion

Using 7T MRI we observed striking differences *in vivo* in the frontal cortex between AD patients and age-matched controls. In patients with probable AD we found a disturbance of the layered structure of the cortex. Previous studies in healthy subjects demonstrated that cortical lamination at 7T reflects intracortical myeloarchitecture<sup>8,19,26</sup>, and this normal pattern of cortical lamination was attributed to differences in myelin-associated iron and myelin lipids in the different cortical layers.<sup>19</sup> Our current study shows that in AD patients the cortical areas of altered SW contrast co-localize with areas of increased microglia- and myelin-associated iron accumulation and also with changes in myelin cytoarchitecture. However, our data also demonstrate that the pattern of the changes observed on MRI does not correspond to the pattern of amyloid deposits. These observations are not in line with the previous assumption, mostly based on animal experiments, that T<sub>2</sub>\*-weighted and SW imaging contrast in AD primarily reflects the presence of iron associated with amyloid plaques.<sup>3-5,19</sup> Our observations of disturbed iron accumulation and myelin architecture have important implications for *in vivo* diagnosis of AD, and also for the understanding of the pathophysiological mechanisms underlying this disease.

According to the amyloid hypothesis oligomeric forms of A $\beta$  are the trigger for a cascade of events that ultimately results in dementia. However, there is increasing evidence that a range of other etiological factors have an important impact on this cascade, presumably by interacting with the A $\beta$  aggregates or by subsequent cellular changes which follow it.<sup>6,11,27</sup> In our study, we found a close correlation between SW MRI contrast changes, myelin changes and increased iron accumulation in cortices with AD pathology. Interestingly, changes in iron metabolism and myelin breakdown have both been mentioned as potential upstream mechanisms for AD.<sup>11,27</sup> Iron and myelin are closely associated in the brain. Seventy percent of the brain's iron is located in oligodendrocytes. Maturation of oligodendrocytes and myelin synthesis are both dependent on the availability of iron.<sup>11,28</sup> During demyelination processes in disease, as well as during normal myelin turnover, iron is assumed to be released from myelin into the brain tissue.<sup>11</sup> Our observation of increased iron in microglial cells (which have an important phagocytic role) in areas of altered myelin structure suggests that the observed MRI changes are a reflection of increased demyelination.

Cortical demyelination has been observed previously in AD, but mainly as areas of focal myelin loss in the immediate vicinity of amyloid plaques.<sup>29,30</sup> We also observed this pattern of myelin loss in our samples, but it was much less prominent than the more diffuse changes in myelin structure (increased fragmentation, tortuosity, and bead-like varicosities) which we report here.



To our knowledge, these findings have not been reported before in human AD, but strikingly similar myelin alterations were recently discovered in a mouse model of AD.<sup>31</sup> Apart from its role in myelin metabolism, iron is an important upstream and downstream modulator of several molecular pathways in AD. Recently it was demonstrated that APP plays a physiological role in preventing iron-mediated oxidative stress in the brain.<sup>32</sup> In AD, zinc accumulation in amyloid plaques and loss of soluble tau interfere with APP's ferroxidase activity, causing increased neuronal iron accumulation. Furthermore, there is evidence that APP processing through the amyloidogenic and non-amyloidogenic pathways is affected by iron.<sup>32,33</sup> Finally, experimental data have demonstrated that iron may accelerate A $\beta$  oligomerization.<sup>34</sup> Based on these observations, it has been suggested that iron could be an important biomarker of AD.<sup>35,36</sup>

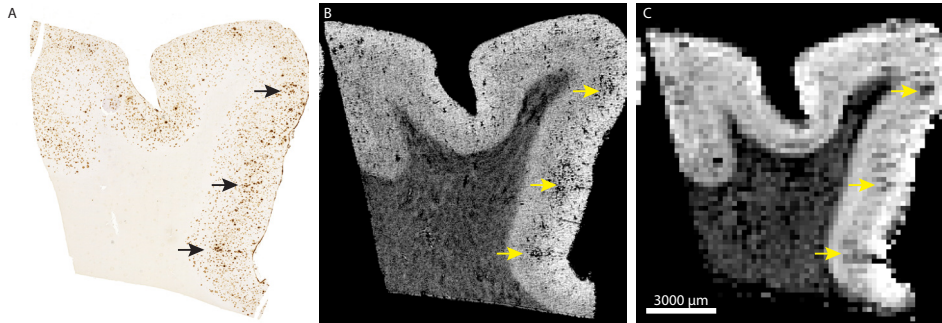
The data presented here show convincing evidence that the cortical myelin cytoarchitecture and iron distribution are disturbed in AD patients. Although these changes might not be central to the pathogenesis of AD, the ability to visualize them by MRI creates a putative novel biomarker with the potential to reflect an as yet underappreciated change that may accompany the progression of AD. However, our data are preliminary since they have been generated in a limited number of patients and healthy controls, and cover only a limited part of the brain. Post-mortem, we observed these changes in SWI contrast in all patients with confirmed AD. *In vivo*, we observed these changes in cortical appearance only in a sub-set of patients; one reason for this discrepancy may be that the patients have been included based on a clinical diagnosis (NINCDS-ADRDA criteria), which is known to have a limited diagnostic accuracy (77 - 85%).<sup>37</sup> Further studies, comprising larger patient series and additional controls populations of patients with different types of dementia are required to assess the potential of the cortical changes we observed to constitute true diagnostic biomarkers for AD. There are many other important and related questions, such as whether the presence of cortical changes is associated with reduced cognitive function, whether the changes appear early in the course of AD, and whether the frontal lobes are the best regions in which to detect these early changes. Additional *in vivo* and post-mortem research on the correlation between ultra-high field MRI and pathology will allow us to further elucidate the role of iron and myelin in the pathogenesis of AD. Overall, the analysis of the cortical changes via visual inspection and simple scoring criteria, without the need for quantitative measurements or sophisticated image processing techniques, makes the proposed method very attractive as a diagnostic and research tool in a clinical setting.

## References

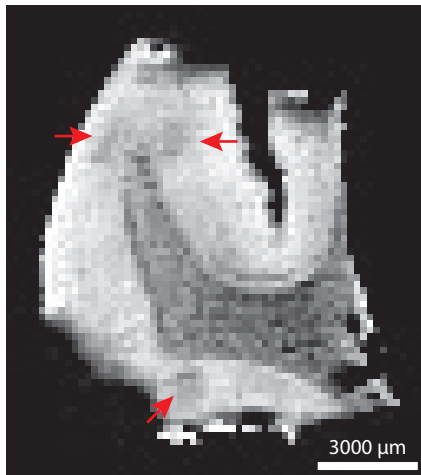
1. Montine, TJ, Phelps, CH, Beach, TG, *et al.* National Institute on Aging-Alzheimer's Association guidelines for the neuropathologic assessment of AD: a practical approach. *Acta Neuropathol.* 2012; 123:1-11.
2. Jack, CR, Jr., Knopman, DS, Jagust, WJ, *et al.* Hypothetical model of dynamic biomarkers of the Alzheimer's pathological cascade. *Lancet Neurol.* 2010; 9:119-128.
3. Chamberlain, R, Wengenack, TM, Poduslo, JF, *et al.* Magnetic resonance imaging of amyloid plaques in transgenic mouse models of AD. *Curr Med Imaging Rev.* 2011; 7:3-7.
4. van Rooden, S, Maat-Schieman, ML, Nabuurs, RJ, *et al.* Cerebral amyloidosis: post-mortem detection with human 7.0-T MR imaging system. *Radiology.* 2009; 253:788-796.
5. Meadowcroft, MD, Connor, JR, Smith, MB, *et al.* MRI and histological analysis of beta-amyloid plaques in both human AD and APP/PS1 transgenic mice. *J Magn Reson Imaging.* 2009; 29:997-1007.
6. Fjell, AM and Walhovd, KB. Neuroimaging results impose new views on AD—the role of amyloid revised. *Mol Neurobiol.* 2012; 45:153-172.
7. Karran, E, Mercken, M, and De, SB. The amyloid cascade hypothesis for AD: an appraisal for the development of therapeutics. *Nat Rev Drug Discov.* 2011; 10:698-712.
8. Fukunaga, M, Li, TQ, van, GP, *et al.* Layer-specific variation of iron content in cerebral cortex as a source of MRI contrast. *Proc Natl Acad Sci U S A.* 2010; 107:3834-3839.
9. McKhann, G, Drachman, D, Folstein, M, *et al.* Clinical diagnosis of AD: report of the NINCDS-ADRDA Work Group under the auspices of Department of Health and Human Services Task Force on AD. *Neurology.* 1984; 34:939-944.
10. Alves, L, Correia, AS, Miguel, R, *et al.* AD: a clinical practice-oriented review. *Front Neurol.* 2012; 3:63.
11. Bartzokis, G. AD as homeostatic responses to age-related myelin breakdown. *Neurobiol Aging.* 2011; 32:1341-1371.
12. Duyckaerts, C, Delatour, B, and Potier, MC. Classification and basic pathology of Alzheimer disease. *Acta Neuropathol.* 2009; 118:5-36.
13. Versluis, MJ, Peeters, JM, van Rooden, S, *et al.* Origin and reduction of motion and f0 artifacts in high resolution T2\*-weighted magnetic resonance imaging: application in AD patients. *Neuroimage.* 2010; 51:1082-1088.
14. Schar, M, Kozerke, S, Fischer, SE, *et al.* Cardiac SSFP imaging at 3 Tesla. *Magn Reson Med.* 2004; 51:799-806.
15. Haacke, EM, Xu, Y, Cheng, YC, *et al.* Susceptibility weighted imaging (SWI). *Magn Reson Med.* 2004; 52:612-618.
16. Rowe, CC and Villemagne, VL. Brain Amyloid Imaging. *J Nucl Med.* 2011.
17. Langbaum, JB, Chen, K, Lee, W, *et al.* Categorical and correlational analyses of baseline fluorodeoxyglucose positron emission tomography images from the AD Neuroimaging Initiative (ADNI). *Neuroimage.* 2009; 45:1107-1116.
18. Rombouts, SA, Barkhof, F, Goekoop, R, *et al.* Altered resting state networks in mild cognitive impairment and mild AD: an fMRI study. *Hum Brain Mapp.* 2005; 26:231-239.
19. Duyn, JH, van, GP, Li, TQ, *et al.* High-field MRI of brain cortical substructure based on signal phase. *Proc Natl Acad Sci U S A.* 2007; 104:11796-11801.
20. Braak, H, Alafuzoff, I, Arzberger, T, *et al.* Staging of Alzheimer disease-associated neurofibrillary pathology using paraffin sections and immunocytochemistry. *Acta Neuropathol.* 2006; 112:389-404.
21. van Duijn, S, Nabuurs, RJ, van, RS, *et al.* MRI artifacts in human brain tissue after prolonged formalin storage. *Magn Reson Med.* 2011.
22. Shepherd, TM, Thelwall, PE, Stanisz, GJ, *et al.* Aldehyde fixative solutions alter the water relaxation and diffusion properties of nervous tissue. *Magn Reson Med.* 2009; 62:26-34.
23. Wang, Y, Yu, Y, Li, D, *et al.* Artery and vein separation using susceptibility-dependent phase in contrast-enhanced MRA. *J Magn Reson Imaging.* 2000; 12:661-670.
24. Meguro, R, Asano, Y, Odagiri, S, *et al.* Nonheme-iron histochemistry for light and electron microscopy: a historical, theoretical and technical review. *Arch Histol Cytol.* 2007; 70:1-19.
25. van Duijn, S, Nabuurs, RJ, van Duinen, SG, *et al.* Comparison of histological techniques to visualize iron in paraffin-embedded brain tissue of patients with AD. *J Histochem Cytochem.* 2013; 61:785-792.
26. Cohen-Adad, J, Polimeni, JR, Helmer, KG, *et al.* T(2)\* mapping and B(0) orientation-dependence at 7 T reveal cyto- and myeloarchitecture organization of the human cortex. *Neuroimage.* 2012; 60:1006-1014.
27. Herrup, K. Reimagining AD—an age-based hypothesis. *J Neurosci.* 2010; 30:16755-16762.
28. Todorich, B, Pasquini, JM, Garcia, CI, *et al.* Oligodendrocytes and myelination: the role of iron. *Glia.* 2009; 57:467-478.

29. Mitew, S, Kirkcaldie, MT, Halliday, GM, *et al.* Focal demyelination in AD and transgenic mouse models. *Acta Neuropathol.* 2010; 119:567-577.
30. Serrano-Pozo, A, William, CM, Ferrer, I, *et al.* Beneficial effect of human anti-amyloid-beta active immunization on neurite morphology and tau pathology. *Brain.* 2010; 133:1312-1327.
31. Chen, H, Epelbaum, S, and Delatour, B. Fiber Tracts Anomalies in APPxPS1 Transgenic Mice Modeling AD. *J Aging Res.* 2011; 2011:281274.
32. Duce, JA, Tsatsanis, A, Cater, MA, *et al.* Iron-export ferroxidase activity of beta-amyloid precursor protein is inhibited by zinc in AD. *Cell.* 2010; 142:857-867.
33. Lei, P, Ayton, S, Finkelstein, DI, *et al.* Tau deficiency induces parkinsonism with dementia by impairing APP-mediated iron export. *Nat Med.* 2012; 18:291-295.
34. Roberts, BR, Ryan, TM, Bush, AI, *et al.* The role of metallobiology and amyloid-beta peptides in AD. *J Neurochem.* 2012; 120 Suppl 1:149-166.
35. Collingwood, J and Dobson, J. Mapping and characterization of iron compounds in Alzheimer's tissue. *J Alzheimers Dis.* 2006; 10:215-222.
36. Zhu, WZ, Zhong, WD, Wang, W, *et al.* Quantitative MR phase-corrected imaging to investigate increased brain iron deposition of patients with Alzheimer disease. *Radiology.* 2009; 253:497-504.
37. Jobst, KA, Barnetson, LP, and Shepstone, BJ. Accurate prediction of histologically confirmed AD and the differential diagnosis of dementia: the use of NINCDS-ADRDA and DSM-III-R criteria, SPECT, X-ray CT, and Apo E4 in medial temporal lobe dementias. *Oxford Project to Investigate Memory and Aging. Int Psychogeriatr.* 1998; 10:271-302.
38. Natte, R, Maat-Schieman, ML, Haan, J, *et al.* Dementia in hereditary cerebral hemorrhage with amyloidosis-Dutch type is associated with cerebral amyloid angiopathy but is independent of plaques and neurofibrillary tangles. *Ann Neurol.* 2001; 50:765-772.

## Supplemental

**Supplemental Figure 6.1 Cortical hypointense clouds on post-mortem SW images**

Examples of “cloud” hypo-intensities (red arrows) on the post-mortem low resolution SW images corresponding to Table 6.2 subject 2. These represent a third category of abnormal cortex consisting of diffuse areas with low signal intensity, not extending parallel to the cortical surface but expanding locally in an irregular fashion throughout the cortex.

**Supplemental Figure 6.2 Focal hypo-intensities on post-mortem SW images**

Correlation of A $\beta$  plaques (A) with focal hypo-intensities on the post-mortem high (B) and low (C) resolution SW images corresponding to Table 6.2 subject 4. Similar to previous studies, areas that contain a high amount of large dense core A $\beta$  plaques (arrows) typically co-localized with many focal hypo-intensities on the high resolution (isotropic 40  $\mu$ m voxels) SW images. On the corresponding lower resolution SW images (isotropic 200  $\mu$ m voxels), however, only some focal hypo-intensities remained discernible, mainly due to partial voluming effects. In general, these focal signal voids contributed to a very small degree to the observed hypointense cortical bands.

**Supplemental Table 6.1 Applied immunohistochemistry procedures including primary and secondary antibodies and additional pretreatments**

Primary antibody (source)	(dilution)	Secondary antibody (dilution)	Pre-treatment	Ref.
Anti-human A $\beta$ (6F/3D, DakoCytomation, Glostrup, Denmark)	1:20	#	1:200 †	38
Anti-PHF-tau monoclonal mouse (AT8, Innogenetics, Ghent, Belgium)	1:2000	#	1:200	
Anti-protolipid protein (PLP) monoclonal mouse (Serotec)	1:2000	#	1:200	
Anti-human CD68 monoclonal mouse (KP1, DakoCytomation, Glostrup, Denmark)	1:50	#	1:200 ‡	
		¥	1:100 ‡	
Anti-human HLA-DR monoclonal mouse (Dakocytomation, Glostrup Denmark)	1:30	#	1:200 ‡	
		¥	1:100 ‡	
Anti-human GFAP monoclonal mouse (6F2, DakoCytomation, Glostrup, Denmark)	1:1000	#	1:200 ‡	
		¥	1:100 ‡	

# Biotinylated rabbit anti-mouse (DakoCytomation, Glostrup, Denmark) followed by ABC (Vector) prior to DAB-enhancement

¥ Goat anti-mouse Alexa Fluor 647 (Invitrogen)

† Formic acid + Trypsin

‡ Steamed for 20 minutes in citrate buffer (pH 6)

## **PART TWO** | Development of Molecular Imaging strategies

1 Department of Radiology, Leiden University Medical Center, the Netherlands

2 Department of Anatomy & Embryology, Leiden University Medical Center, the Netherlands

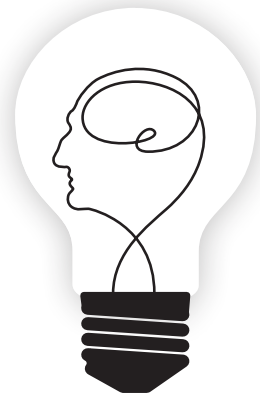
---

# Chapter 7

## MR-based molecular imaging of the brain: the next frontier

*Adapted from AJNR Am J Neuroradiol. 2010 Oct;31(9):1577-83*

Maaïke E. de Backer<sup>1</sup>  
**Rob J.A. Nabuurs<sup>1</sup>**  
Mark A. van Buchem<sup>1</sup>  
Louise van der Weerd<sup>1,2</sup>



## Abstract

In the foreseeable future the molecular imaging field could greatly assist neuroradiologists. Reporter molecules provide information on specific molecular or cellular events that could not only aid diagnosis, but potentially differentiate between different stages of disorders and treatments. In order to accomplish this, reporter molecules literally need to pass a barrier, the blood-brain barrier, which is designed to repel non-essential molecules from the brain. Although this is not a trivial task, several transport systems could be tricked into guiding molecules into the brain.

The non-invasive nature in conjunction with a wide availability makes MRI particularly suitable for longitudinal neurological imaging studies. This review explains the principles of MR contrast, delineates different types of reporter molecules and describes strategies to transport reporters into the brain. It also discusses recent advances in MR hardware, pulse sequences, the development of (targeted) reporter probes and future directions of the MR neuroimaging field.



## Introduction

Anatomical images have always been the center of gravity in the daily work of radiologists. They provide the basis of many diagnoses supplemented by physiological magnetic resonance data or metabolic profiling if necessary. Despite the sophistication of these techniques and the wealth of information that can be obtained, the diagnostic information often remains non-specific and evidence regarding the nature of the underlying disease commonly remains circumstantial. In contrast to generic contrast agents used in the clinic, the 'molecular imaging' (MI) field uses reporter molecules tailored for *in vivo* detection of specific molecular or cellular events. Formally, MI encompasses techniques that directly or indirectly monitor and record the spatiotemporal distribution of molecular or cellular processes for biochemical, biologic, diagnostic, or therapeutic applications.<sup>1,2</sup> (**Table 7.1**) The technique is widely used in pre-clinical research and is on the verge of entering the clinical arena. It enables radiologists to add molecular or cellular information to their array of diagnostic tools, which will have a tremendous effect on the diagnosis of neurological disorders, where invasive diagnostic techniques like biopsies can rarely be used.<sup>3,4</sup> Radiologists may even be able to detect "pre-disease" or "pre-symptomatic states" when molecular and cellular changes arise before they lead to anatomical or functional disturbances. Following an early diagnosis, MI could closely monitor the effectiveness of therapeutic interventions.

MR imaging is already the imaging technique of choice for neuroradiologists and MR imaging systems are widely available. In principle one could collect anatomical and physiological information and report the location of reporter molecules in a patient during a single MR imaging session. For these reasons this review focuses on MR-based MI of the brain, explaining the principles of MR reporter molecules, describing strategies to target them to the brain and reviewing the state of the art in CNS MI.

## Brain targeting

An important feature of the brain that sets it apart from other organs in terms of MI is the presence of the blood-brain barrier (BBB), a selective barrier to the CNS that impedes the influx of most compounds from blood to brain. (**Figure 7.1A**) It permits the passage of metabolic compounds and ions to maintain neuronal function, while shielding off possible harmful compounds. The effective barrier results from the selective permeability of tight junctions between endothelial cells, although the underlying layers and cell types also exhibit great influence on its function and permeability. The endothelial cells in the cerebral vasculature differ from normal endothelial cells in having low pinocytotic activity, abundant mitochondria, fewer fenestrations and specialized junctions to adjacent cells; all these features play a role in the impermeability of the BBB.<sup>5</sup>

The BBB is generally regarded as a bottleneck for MI imaging of the brain, as it severely hinders the delivery of reporter probes to the brain. Designing reporter molecules such that they may cross the barrier is not trivial, although a good understanding of BBB physiology has resulted in several delivery strategies.<sup>6</sup> With paracellular transport sealed off, transmembrane transport

**Table 7.1 Definitions**

Molecular imaging	<i>In vivo</i> imaging of the spatiotemporal distribution of molecular or cellular processes.
Cellular imaging	<i>In vivo</i> imaging of the spatiotemporal distribution of cellular processes.
Contrast agent, label	Chemical functional group that allows visualization by an appropriate imaging technique. For example, Gd chelates or iron oxides are MR contrast agents, <sup>18</sup> F atoms are PET contrast agents, and fluorophores are optical contrast agents.
Nanoparticle	Molecules in the 10-1000 nanometer range that serve as an imaging platform. Examples include SPIO particles, liposomes, dendrimers and quantum dots.
Reporter probe, Reporter molecule	A molecule or nanoparticle that is used to image particular biological processes. The molecule or nanoparticle is a composite of a contrast agent and targeting moiety.
Reporter cell	A cell that contains a contrast agent.
Reporter gene	A gene that encodes for a protein that (directly or indirectly) is easy to assay. Reporter genes are linked to genes of interest to study expression levels.

through endothelial cells is the only way to gain access to the brain. Several strategies to transport MI probes across the BBB can be followed, exploiting different endogenous transport systems: passive diffusion, carrier-mediated transport, receptor-mediated endocytosis and adsorptive endocytosis.<sup>7-10</sup> (**Figure 7.1B**)

Small molecules such as oxygen and carbon dioxide readily diffuse into the brain, but the BBB is quite restrictive for other compounds. Nevertheless, small non-charged lipophilic compounds may be engineered to passively enter the brain.<sup>11</sup> However, lipophilic compounds have major drawbacks, including enhanced uptake and retention by peripheral tissues, complicating the compound biodistribution and pharmacokinetics.<sup>12</sup> In practical terms, lipophilic compounds are generally not soluble in aqueous solutions. Organic solvents are usually excluded from *in vivo* experiments for toxicity reasons, while others that are in clinical use, such as DMSO, reduce the integrity of the BBB, which clearly is not desirable for non-invasive imaging purposes.<sup>13</sup> Metabolites such as glucose, amino acids, nucleosides and neurotransmitters are transported into the brain by carrier-mediated transport through proteins in the plasma membrane of endothelial cells that catalyze bidirectional transport (blood to brain and *vice versa*).<sup>14</sup> These pumps operate on both sides of the cell to maintain a nutritional balance. Reporter molecules that mimic the structure of a nutrient could trick the transport system to gaining entrance to the brain, although efflux pumps on the luminal (blood) side may impede this effort.<sup>15</sup> Positron emission tomography (PET) has extensively employed this strategy, e.g. by using fluorodeoxyglucose as a glucose analog.<sup>16</sup>

Larger reporter probes may target internalizing receptors, resulting in receptor-mediated endocytosis: following complex formation of the probe and the receptor, the complex is internalized, transported to the abluminal (brain) side of endothelial cells and released into the brain. The insulin receptor and transferrin receptor are well-known examples.<sup>8</sup> This transport mechanism is suitable for the translocation of macromolecules and nanoparticles and is therefore particularly interesting for MI.<sup>7</sup> A prerequisite for this mechanism is a receptor-binding ligand, such as a molecular mimic of an endogenous ligand or an antibody against the receptor of interest. Evidently, the ligand should be conjugated to a contrast agent or an MR imaging-detectable nanoparticle to be able to visualize it using MR imaging.

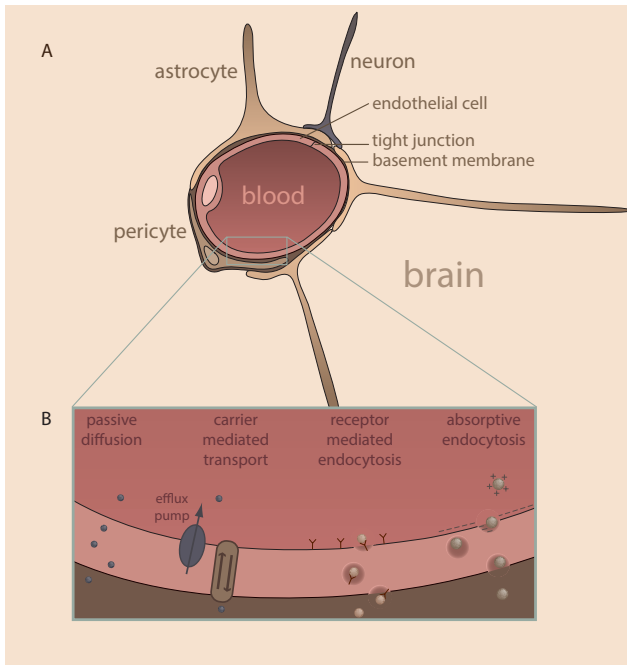


**Figure 7.1 Blood-brain barrier**  
**(A)** Schematic representation of the blood-brain barrier (BBB) and **(B)** transport mechanisms for BBB passage (see text for details).

Compounds may also be internalized by non-specific interactions with the cell surface. Cationized albumin, for example, interacts with the anionic cell surface of the endothelial cells, and is then internalized via adsorptive endocytosis.<sup>8</sup> This is a general internalization mechanism that is not specific for endothelial cells, so with regard to MI this strategy is not very useful, as reporter probes would be internalized by a range of cell types, resulting in a high non-specific background signal.

It is possible to disrupt the BBB temporarily to gain access to the brain, e.g. through osmotic pressure (mannitol). A method that appears relatively safe is the injection of microbubbles into the bloodstream followed by focused local ultrasound exposure causing cavitation, leading to BBB disruption.<sup>17</sup> Such methods may be used for preclinical studies, but will not be suitable for clinical use of targeted probes, except perhaps for image-guided drug delivery.

## Generating MR Contrast

Whatever the object of interest is, the reporter system used to visualize it should contain an MR imaging-visible contrast agent. An overview of these agents is provided here below and in **Table 7.2**. Iron oxide particles (SPIO, CLIO and MION) are composed of iron oxide crystals with polymer coatings and are often biodegradable. They are synthesized in different forms and sizes, ranging from 300 nm to 1.6  $\mu\text{m}$  in diameter, and each size category exhibits different pharmacodynamical behavior and relaxation effects.<sup>18</sup> All iron oxide particles possess relatively large (negative) magnetic susceptibilities, thereby reducing  $T_2$  and  $T_2^*$  relaxation times, resulting

**Table 7.2 MR contrast**

MR Contrast agent	Examples	Predominant effect	MR sensitivity	Notes
T <sub>1</sub> agent	Gd <sup>3+</sup> , Mn <sup>2+</sup> chelates	T <sub>1</sub>	++	Gd is chelated for toxicity reasons
T <sub>2</sub> agent	SPIO, USPIO MION, CLIO	T <sub>2</sub>	++++	Large range of sizes
CEST; paraCEST	Amino acids, sugars; Eu-DOTA	saturation transfer	++	Pre-clinical stage
Heteronuclei	<sup>19</sup> F, <sup>31</sup> P	“Hot spot” imaging	+	Negligible background signal

in signal voids or hypointense regions in T<sub>2</sub>- or T<sub>2</sub>\*-weighted MR images. The fact that SPIOs cause ‘negative contrast’ could make them difficult to distinguish from imaging artifacts or other susceptibility sources. To overcome this disadvantage, imaging sequences are being developed that produce positive contrast using SPIOs, although the generated contrast is still non-specific and cannot be exclusively attributed to the presence of iron oxide particles.<sup>19</sup> Some SPIOs are approved by the FDA, making them popular choices for cellular and molecular imaging, although their relatively large size makes them less useful for targets that are not easily accessible, as in neurological applications.

Paramagnetic agents (e.g. Gd) have small positive magnetic susceptibilities that cause a modest decrease of relaxation times, particularly T<sub>1</sub>, resulting in ‘positive contrast’ on T<sub>1</sub>-weighted images.<sup>20</sup> The positive contrast effect of paramagnetic contrast agents is much weaker than the negative contrast effect of SPIOs. Sensitivity could be enhanced by conjugating multiple Gd-containing chelates to a single probe, such as a dendrimer or protein, but the design of large complexes is always a trade-off between sensitivity and molecular weight. The larger (and ‘brighter’) contrast agents are synthesized, the more difficulties they will encounter to cross the BBB. A special class of paramagnetic contrast agents is encompassed by ‘smart’ or ‘responsive’ contrast agents. Their relaxation properties significantly change in response to local physiological changes, e.g. in pH, temperature or enzyme activity.<sup>21,22</sup> Paramagnetic agents are small and generally easy to conjugate to probes of interest, which makes them suitable for neuro-imaging, although they remain relatively insensitive.

Chemical Exchange Saturation Transfer (CEST) is contrast mechanism that has been developed over the past decade and is based on magnetization transfer through proton exchange.<sup>23</sup> CEST agents contain exchangeable protons with a resonance frequency different from bulk water. Upon selective irradiation of this frequency, magnetization is transferred to bulk water through chemical exchange, causing a decrease in the signal intensity of bulk water. The contrast can thus be switched ‘on’ (by presaturation of the CEST protons) or ‘off’ (no presaturation). The efficacy of CEST agents depends on the exchange rate and frequency difference between the exchangeable ‘CEST protons’ and bulk water and can be improved by the incorporation of lanthanide ions (PARACEST).<sup>24</sup> CEST probes can be engineered to work at different excitation frequencies, which potentially allows us to study interactions of cells labeled with different CEST agents.<sup>25</sup>

Contrast agents described thus far are detected indirectly, in the sense that they affect the relaxation properties of water protons. Their effect is registered in the final proton image. A more direct approach is heteronuclear MR imaging. In principle any nucleus with a non-zero magnetic spin and a large enough 'magnetic sensitivity' could be used. Fluorine ( $^{19}\text{F}$ ) is a popular choice in the MI field, as it exhibits favorable MR characteristics with a spin- $\frac{1}{2}$ , a magnetic sensitivity close to that of proton and 100% natural abundance. Moreover, there are hardly any endogenous fluorine-containing molecules, so fluorine-based reporter molecules do not suffer from background signal. Compared with proton imaging, however, the fluorine signal will be rather low; fluorine probes accumulate at most in the millimolar range, whereas the water concentration *in vivo* is roughly 40 mol/l. The design of fluorine-based probes is very variable, ranging from low-MW molecules with covalently bound fluorine atoms to perfluorocarbon molecules measuring hundreds of nanometers.<sup>26-28</sup> Low-MW fluorine probes may be designed to accumulate in the brain, where they could take full advantage of the 'hot spot imaging' principle if they locally agglomerate to sufficiently high concentrations.

## Reporter Systems

MR-based MI is used to detect a wide range of biological events, which can be classified in three categories (with some overlap between them). Firstly, the presence of specific *molecules*, such as receptors, can be imaged (see "*Detecting molecules*"). Secondly, specific *cells*, such as stem cells after transplantation (see "*Detecting cells*"), can be traced, and thirdly, the expression of specific *genes* (see "*Reporter genes*") can be visualized.

### Detecting molecules

Molecular reporter probes come in many shapes and sizes, but their principal components are a targeting molecule and a contrast agent. The probe should be targeting a unique hallmark of the biological process of interest. Popular target choices are receptors, enzymes and cytokines, which are often expressed to much higher levels in pathologies. Once a target is chosen, one needs to select a complementary ligand that binds the target with high affinity and specificity. Natural ligands, such as receptor agonists, can be used, or specific ligands, such as antibodies or peptides, can be developed.

Reporter probes are synthesized in a wide range of sizes and can be divided in low-MW probes and large MW probes or nanoparticles. (**Figure 7.2**) Low-MW probes are based on drugs, metabolites or inhibitors, in which single atoms or small functional groups are substituted with a contrast moiety. For neurological MI applications, low-MW probes most likely find their way to the brain via passive diffusion or carrier-mediated transport. A beautiful example is the small fluorine-containing reporter probe developed by Higuchi *et al.*<sup>27</sup> This molecule targets amyloid plaques, one of the hallmarks of Alzheimer's disease (AD) and was intravenously injected into transgenic AD mice. (**Figure 7.3A-C**) Using a combination of  $^{19}\text{F}$  and  $^1\text{H}$  MRI, Higuchi showed the presence of this probe in the brain of these mice, presumably bound to amyloid plaques. High-MW reporter probes (with MWs over 5 kDa and diameters ranging from a few to hundreds of nm) are based on proteins or nanoparticles to which contrast agents and ligands are

conjugated. Some nanoparticles, such as SPIOs or perfluorocarbon particles, generate contrast themselves (see section “Generating MR contrast”), while others (such as liposomes and dendrimers) simply supply a crosslinking platform. There is a trend in the field to construct

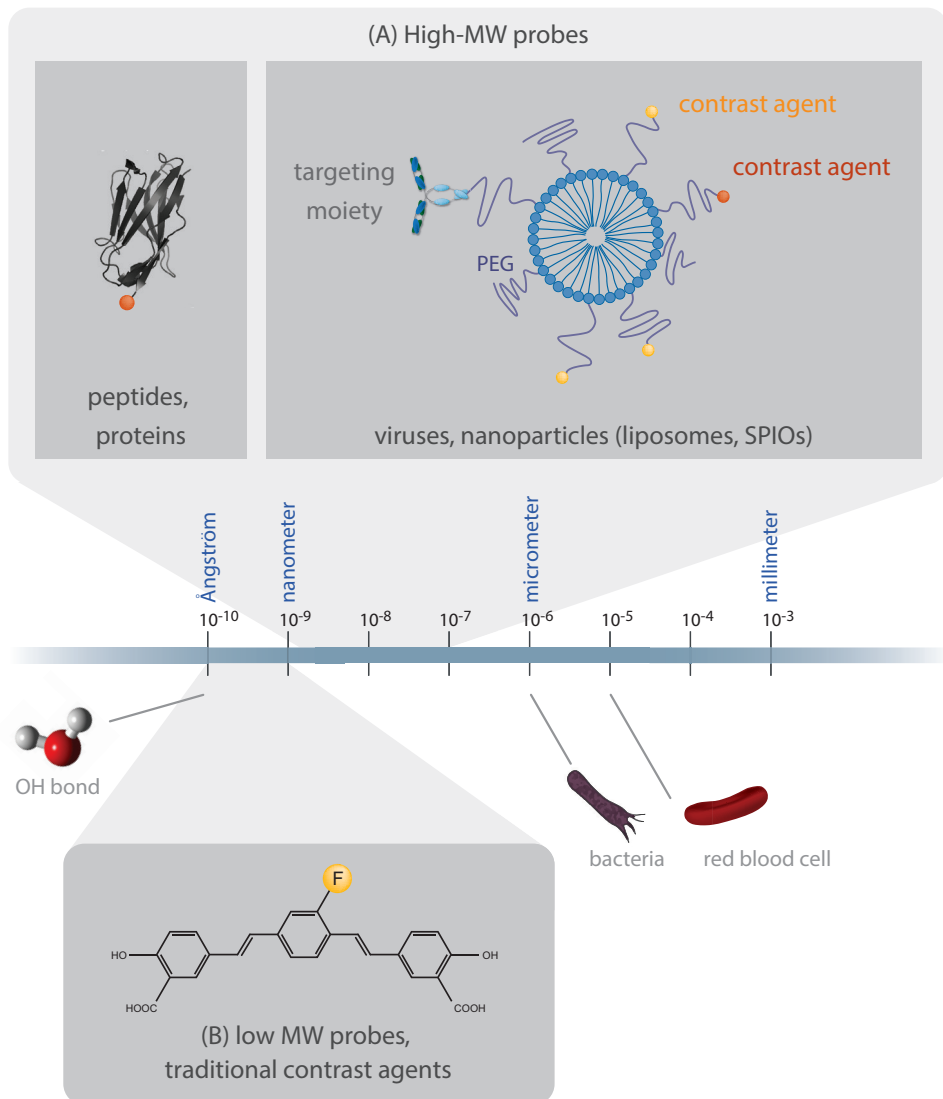


**Figure 7.2 Reporter probes and their orders of magnitude**

The actual size of reporter molecules ranges from a several Ångströms ( $10^{-10}$ m) to hundreds of nanometers. **(A)** High-MW biomolecules (not drawn to scale), such as peptides or antibodies, that have target affinity could directly be labeled with a contrast agent. Reporter molecules based on liposomes or SPIO particles, tens to hundreds of nanometers in size, are conjugated to targeting moieties and contrast agents. **(B)** Low-MW reporter probes are small molecules that contain contrast-generating labels. They fall in the low nanometer range. The figure shows reporter probe FSB that is able to cross the blood brain barrier and bind to amyloid plaques. It is labeled with  $^{19}\text{F}$  for MR imaging.<sup>27</sup>

nanoparticles that contain multiple types of contrast agents, which can be visualized by different imaging modalities.<sup>29</sup> This concept, referred to as multimodality imaging, combines the strengths of different imaging techniques, such as sensitive PET tracers with high resolution MR images. For example, Kircher *et al.* set out to aid neurosurgeons visualizing brain tumor margins.<sup>30</sup> They synthesized a long-circulating multimodality reporter molecule, composed of an iron-oxide nanoparticle and a near-infrared fluorochrome and injected this into rats bearing gliosarcoma that expressed green fluorescent protein. MR imaging confirmed that microglia had sequestered the nanoparticle and displayed the tumor as hypointense regions in T<sub>2</sub>-weighted images. Subsequent optical imaging allowed discrimination of tumors from brain tissue, which ultimately could be used by surgeons during surgery.

### Detecting cells

Instead of visualizing reporter molecules, it is also possible to label intact cells, allowing cell tracking and gaining knowledge on cell behavior, such as migration patterns of immune cells following immunotherapy or stem cell survival following transplantation.

Evidently, cells should remain viable and functional after the labeling procedure. Cellular contrast agents should ideally remain within the desired cell type and not dilute with cell division to enable reliable longitudinal studies.<sup>31,32</sup> SPIO particles are by far the most used MR contrast agents used for MR cell tracking. However, a particular confound is that the MR image cannot distinguish viable cells from non-viable cells. Additionally, due to susceptibility effects, hypointense regions in MR images are significantly larger than the actual cluster of labeled cells, which could lead to misinterpretations of the iron source. MR imaging-based cell tracking does not exclusively lean on SPIO particles; Gd-based approaches benefiting from positive contrast have also been demonstrated, although substantial amounts of lanthanide-based contrast agents are required to affect MR images, which increases toxicity issues.<sup>33</sup> Phosphorous and fluorine imaging have the advantage of a low background and can often be performed in a quantitative manner, but they too suffer from sensitivity issues. Finally, CEST imaging is emerging as a very useful technique, especially in reporter gene imaging.<sup>34</sup>

Cell labeling can be performed *in vitro*, after which the labeled cells are implanted or the contrast agent may be injected systemically, which is then taken up by phagocytotic cells.<sup>35</sup> Many cell types readily take up contrast agents via phagocytosis, but non-phagocytic cells (including stem cells) can be labeled via transfection agents, fluid phase pinocytosis, encapsulation, receptor-mediated uptake or magneto-electroporation, amongst others.<sup>31,32</sup> Cells that have been labeled for CNS application include neural stem cells, oligodendrocyte precursors and macrophages.<sup>36-38</sup> Tracking neuronal stem cells empowers us to study the best way to administer the cells (intravenous *versus* intraparenchymal transplantation), estimate the dose (how many cells to use), assess the survival rate, evaluate their migration patterns, check if they find their target site and home, and optimize the therapeutic time window.<sup>32,39</sup> To illustrate this, Hoehn *et al.* transplanted SPIO-labeled stem cells into the contralateral hemisphere of a mouse displaying ischaemic stroke.<sup>37</sup> T<sub>2</sub>\*-weighted MR images showed the migration of these cells across the brain from the implantation site to the edge of an ischaemic lesion. (**Figure 7.3D-F**) This example demonstrates the possibility to follow cells in real time, which may be used to study the therapeutic potential of stem cells in the future.

## Reporter genes

The previous two sections focused on reporting specific molecules or cells; this section addresses imaging gene function, which in contrast to cell tracking, exclusively reports on viable cells. Reporter gene imaging is a technique in which gene products (i.e. reporter proteins) are imaged *in vivo*.<sup>40,41</sup> Essentially, a reporter gene is transcribed to mRNA, which in turn is translated into a reporter protein (which are far more abundant in the cell than DNA or RNA). A good reporter protein must be easy to assay and must not normally be expressed in the cells of interest or, when encoding for endogenous proteins, must be expressed at much higher levels than normal. The gene of interest is unlikely to encode an MR-visible protein, although the protein of interest may interact with exogenous reporter molecules.<sup>42</sup> Often, the gene of interest is teamed up with a reporter gene. These genes can be engineered such that they are both driven by the same promoter. Upon activation of this promoter (which can be conditional or tissue-specific, for example), the expression of both genes is simultaneously enhanced; imaging the reporter protein thus 'reports' on the expression of the gene of interest. The reporter protein may produce endogenous contrast or may be imaged via exogenous reporter molecules.<sup>42</sup>

Reporter gene imaging is currently in a preclinical stage, but its potential is enormous. One could monitor gene expression, track cells in normal and abnormal development, map dynamic protein interactions and check cell transplantation therapy. Taking this one step further, one could follow the effects of gene therapy, in which cells are genetically modified to produce a therapeutic effect.<sup>40,42</sup> Reporter gene imaging is commonly used in the nuclear and optical imaging field, with green fluorescent protein<sup>43</sup> and luciferase<sup>44</sup> as prominent examples, but MR imaging starts claiming a place on stage as well, by virtue of its non-invasive nature and whole-body coverage.

Needless to say, for MR reporter gene imaging, the reporter protein needs to be MR detectable and common strategies are outlined in recent reviews.<sup>40,42,45</sup> Reporter genes may encode for artificial proteins, which are detectable by CEST imaging (**Figure 7.3G-I**)<sup>34</sup>, but most MR reporter systems are based on the accumulation of iron, circumventing the administration of exogenous contrast agents. When reporter genes overexpress proteins such as ferritin<sup>46,47</sup>, the transferrin receptor<sup>48</sup> or MagA<sup>49</sup> at high levels, they cause a local build-up of iron, which leads to enhanced negative contrast in T<sub>2</sub>- or T<sub>2</sub>\*-weighted images. This principle has been demonstrated by Genove *et al.*<sup>47</sup>, who visualized gene expression using genetically modified replication-defective adenovirae carrying the genes for the light-chain or heavy-chain subunits of ferritin. They injected the adenovirae into the striatum of a living mouse, which lead to the local overexpression of ferritin and the accumulation of endogenous iron. This resulted in enhanced negative contrast in T<sub>2</sub>-weighted MR images, which was visible for weeks.

The field of MR reporter gene imaging is developing at a steady pace, but before it becomes a mainstream clinical tool it has to overcome several issues. The efficiency of gene transfer is currently very modest, which in combination with low MR sensitivity, makes MR reporter imaging a challenge. Reporter gene imaging (in combination with gene therapy) often uses viral based vectors to package genes, and a delivery device to pass them to the target organ. In this respect the method is not strictly non-invasive. Current applications of reporter gene imaging are therefore mostly confined to small animal models, although clinical applications are anticipated in the future, most likely as a tool to visualize gene therapy.



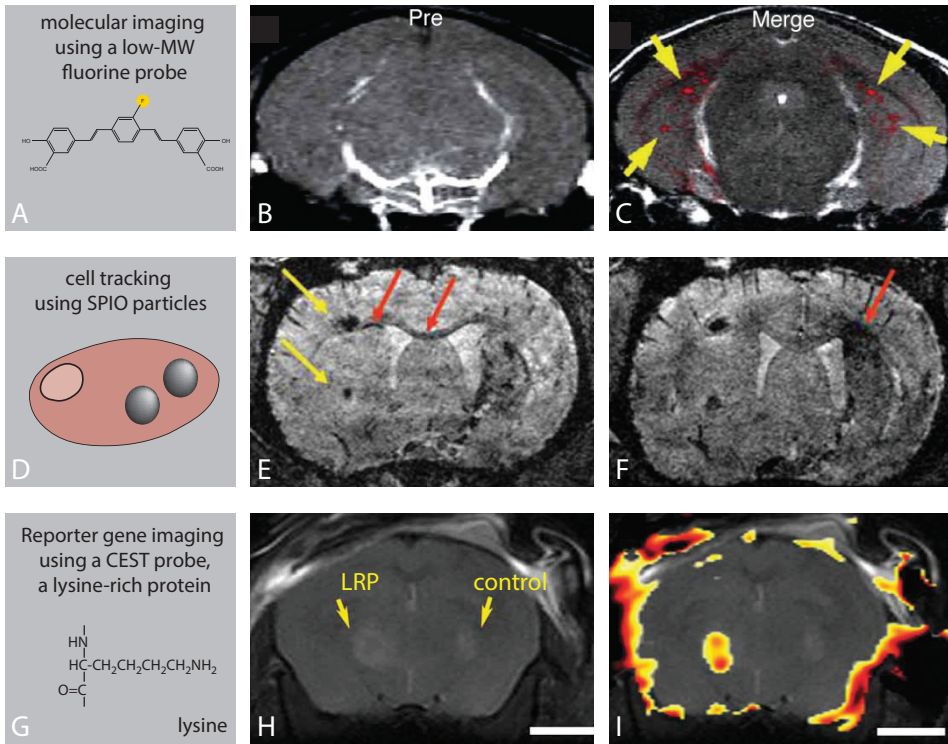


**Figure 7.3** *In vivo* examples of molecular neuroimaging using MRI

(A–C) MR images of transgenic mice displaying symptoms of AD. (A) A fluorine containing reporter probe with affinity for senile plaques was intravenously injected and imaged by  $^{19}\text{F}$  and  $^1\text{H}$  MRI. (B) Proton MR image before injection of the reporter probe; (C) merged proton and fluorine image after injection of the reporter probe, indicating the anatomical locations of the reporter molecule in the brain.<sup>27</sup> (D–F) Cellular imaging of migrating stem cells in a mouse model of ischaemic stroke. (E) Stem cells were labeled with ultra-small SPIO particles and transplanted into the contralateral hemisphere. (F) They migrate from the implantation sites along the corpus callosum towards the ischaemic border zone.<sup>37</sup> (G–I) *In vivo* reporter gene imaging using CEST reporter proteins. The left hemisphere of a mouse brain was injected with glioma cells expressing LRP (lysine rich protein, a CEST agent); the right hemisphere was injected with control tumor cells. (H) Anatomical MR image of the brain; (I) CEST signal intensity-difference map superimposed on the anatomical image, indicating the LRP-expressing tumor xenograft.<sup>34</sup>

## Current developments

The field of molecular imaging is developing in several directions. Imaging modalities perform better, molecular biologists construct ingenious reporter genes and transgenic mice, while chemists improve contrast agents and create multimodal reporter molecules.<sup>20,50</sup>

There is a continuous effort to increase the field strengths of human scanners, and these high-field magnets are making their way into the clinic. The most commonly used clinical scanners operate at field strengths of 1.5 Tesla, while 3 Tesla is regarded as high-field, but ultra-high field magnets at 7 Tesla are also used for patient studies. As the MR signal is proportional to the magnetic field strength, using high-field scanners improves the sensitivity and enhances the signal to noise ratio, improving anatomical and functional imaging.<sup>51</sup> A higher magnetic field

also increases the spectral resolution, which is an additional benefit for  $^1\text{H}$ -MR spectroscopy and CEST-based imaging. Unfortunately high-field magnets do not come without expense: increased magnetic susceptibility effects, field inhomogeneity and energy deposition pose worries and technical challenges, but these are partly overcome by using optimized coils, fast and parallel imaging and refocusing flip angles.<sup>52,53</sup>

With regard to molecular imaging, high-field scanners are able to detect lower concentrations of reporter molecules, which decreases toxicity issues. This is particularly the case for iron oxide-based particles, heteronuclear contrast agents and CEST agents. On the other hand, the current lanthanide-based contrast agents do not perform as well at high fields, and their relaxation behavior should be significantly improved.<sup>20</sup> Regardless of the field strength there is a continuous effort to tailor and improve pulse sequences, such as ultrafast imaging sequences and creating positive contrast for SPIO particles.<sup>19</sup>

## Outlook

The road to MR-based MI has been a long one. MR-based contrast agents are inherently far less sensitive than radiotracers, which makes them more likely to fail due to sensitivity or toxicity problems. Nevertheless, the advantage of providing anatomical, physiological and molecular or cellular information during a single examination is so great that research in this area is booming.

In the near future we anticipate that fluorine-based reporter molecules in conjunction with MR imaging at high(er) fields holds great promise, combining “hot spot imaging” and sensitivity. In contrast to fluorine-based radiotracers, MR reporter probes are relatively long-lived and could be imaged at a regular basis while avoiding excessive ionizing radiation. While BBB research is in fifth gear, MI imaging of the brain is already in use for pathologies with a (possible) compromised BBB, such as cerebrovascular diseases, inflammatory conditions and gliomas. Without the need to cross the BBB, this approach could take full advantage of current developments in the field.

Also, alternative therapies for neurological disorders, such as gene therapy and stem cell transplantation, are active areas of research and we expect that MI will play an essential role in the development of these therapies, for example by tracing labeled stem cells or by developing a common platform for treatment and diagnostics. Examples for this common approach are already known from cancer research, where liposomal particles have been used that target tumor sites, contain anti-cancer drugs and MRI-visible contrast agents to monitor the treatment response.

Many radiologists may regard MI as science fiction, but they should be aware that this field develops at a fast pace. Although currently most research is applied in animal models, the first radiological studies in humans have already been performed. It is generally believed that MI based on radiological techniques will be introduced in the clinical arena within the next few years. However, the clinical implementation of MR-based MI will only occur when academic radiologists are actively involved in research programs in which they master data collection and interpretation of MI images. This could be achieved by providing MI courses to residents,

organizing postgraduate courses for radiologists and by creating MI fellowships. Radiologists could also assist (bio)chemists in the development of reporter probes to advance clinical applications. Seeing that MI is on the brink of leaping to the clinic, radiologists should prepare themselves now to join that jump in the near future.

## References

1. Thakur, M and Lentle, BC. Report of a summit on molecular imaging. *Radiology*. 2005; 236:753-755.
2. Weissleder, R and Mahmood, U. Molecular imaging. *Radiology*. 2001; 219:316-333.
3. Hammoud, DA, Hoffman, JM, and Pomper, MG. Molecular neuroimaging: from conventional to emerging techniques. *Radiology*. 2007; 245:21-42.
4. Herholz, K, Coope, D, and Jackson, A. Metabolic and molecular imaging in neuro-oncology. *Lancet Neurology*. 2007; 6:711-724.
5. Hawkins, BT and Davis, TP. The blood-brain barrier/neurovascular unit in health and disease. *Pharmacological Reviews*. 2005; 57:173-185.
6. Neuwelt, E, Abbott, NJ, Abrey, L, *et al.* Strategies to advance translational research into brain barriers. *Lancet Neurology*. 2008; 7:84-96.
7. Barbu, E, Molnar, E, Tsibouklis, J, *et al.* The potential for nanoparticle-based drug delivery to the brain: overcoming the blood-brain barrier. *Expert Opin Drug Deliv*. 2009; 6:553-565.
8. de Boer, AG and Gaillard, PJ. Drug targeting to the brain. *Annual Review of Pharmacology and Toxicology*. 2007; 47:323-355.
9. Pardridge, WM. Blood-brain barrier delivery. *Drug Discovery Today*. 2007; 12:54-61.
10. Tosi, G, Costantino, L, Ruozi, B, *et al.* Polymeric nanoparticles for the drug delivery to the central nervous system. *Expert Opin Drug Deliv*. 2008; 5:155-174.
11. Abraham, MH. The factors that influence permeation across the blood-brain barrier. *European Journal of Medicinal Chemistry*. 2004; 39:235-240.
12. Banks, WA. Characteristics of compounds that cross the blood-brain barrier. *BMC Neurol*. 2009; 9 Suppl 1:S3.
13. Broadwell, RD, Salzman, M, and Kaplan, RS. Morphologic effect of dimethyl sulfoxide on the blood-brain barrier. *Science*. 1982; 217:164-166.
14. Ohtsuki, S and Terasaki, T. Contribution of carrier-mediated transport systems to the blood-brain barrier as a supporting and protecting interface for the brain; importance for CNS drug discovery and development. *Pharmaceutical Research*. 2007; 24:1745-1758.
15. Tsuji, A. Small molecular drug transfer across the blood-brain barrier via carrier-mediated transport systems. *NeuroRx: The Journal of the American Society for Experimental NeuroTherapeutics*. 2005; 2:54-62.
16. Reivich, M, Kuhl, D, Wolf, A, *et al.* The [<sup>18</sup>F]fluorodeoxyglucose method for the measurement of local cerebral glucose utilization in man. *Circ Res*. 1979; 44:127-137.
17. Kinoshita, M, McDannold, N, Jolesz, FA, *et al.* Targeted delivery of antibodies through the blood-brain barrier by MRI-guided focused ultrasound. *Biochemical and Biophysical Research Communications*. 2006; 340:1085-1090.
18. Bulte, JWM and Kraitchman, DL. Iron oxide MR contrast agents for molecular and cellular imaging. *NMR in Biomedicine*. 2004; 17:484-499.
19. Cunningham, CH, Arai, T, Yang, PC, *et al.* Positive contrast magnetic resonance imaging of cells labeled with magnetic nanoparticles. *Magnetic Resonance in Medicine: Official Journal of the Society of Magnetic Resonance in Medicine / Society of Magnetic Resonance in Medicine*. 2005; 53:999-1005.
20. Caravan, P. Strategies for increasing the sensitivity of gadolinium based MRI contrast agents. *Chemical Society Reviews*. 2006; 35:512-523.
21. Querol, M and Bogdanov, A. Amplification strategies in MR imaging: activation and accumulation of sensing contrast agents (SCAs). *Journal of Magnetic Resonance Imaging: JMRI*. 2006; 24:971-982.
22. Sosnovik, DE and Weissleder, R. Emerging concepts in molecular MRI. *Current Opinion in Biotechnology*. 2007; 18:4-10.
23. Ward, KM, Aletras, AH, and Balaban, RS. A new class of contrast agents for MRI based on proton chemical exchange dependent saturation transfer (CEST). *J Magn Reson*. 2000; 143:79-87.
24. Woods, M, Woessner, DE, and Sherry, AD. Paramagnetic lanthanide complexes as PARACEST agents for medical imaging. *Chemical Society Reviews*. 2006; 35:500-511.
25. McMahon, MT, Gilad, AA, DeLiso, MA, *et al.* New "multicolor" polypeptide diamagnetic chemical exchange saturation transfer (DIACEST) contrast agents for MRI. *Magn Reson Med*. 2008; 60:803-812.
26. Ahrens, ET, Flores, R, Xu, H, *et al.* *In vivo* imaging platform for tracking immunotherapeutic cells. *Nature Biotechnology*. 2005; 23:983-987.
27. Higuchi, M, Iwata, N, Matsuba, Y, *et al.* <sup>19</sup>F and <sup>1</sup>H MRI detection of amyloid beta plaques *in vivo*. *Nature Neuroscience*. 2005; 8:527-533.

28. Ruiz-Cabello, Js, Walczak, P, Kedziorek, DA, *et al.* *In vivo* "hot spot" MR imaging of neural stem cells using fluorinated nanoparticles. *Magnetic Resonance in Medicine: Official Journal of the Society of Magnetic Resonance in Medicine / Society of Magnetic Resonance in Medicine.* 2008; 60:1506-1511.
29. McCarthy, JR and Weissleder, R. Multifunctional magnetic nanoparticles for targeted imaging and therapy. *Adv Drug Deliv Rev.* 2008; 60:1241-1251.
30. Kircher, MF, Mahmood, U, King, RS, *et al.* A multimodal nanoparticle for preoperative magnetic resonance imaging and intraoperative optical brain tumor delineation. *Cancer Res.* 2003; 63:8122-8125.
31. Long, CM and Bulte, JW. *In vivo* tracking of cellular therapeutics using magnetic resonance imaging. *Expert Opin Biol Ther.* 2009; 9:293-306.
32. Politi, LS, Bacigaluppi, M, Brambilla, E, *et al.* Magnetic-resonance-based tracking and quantification of intravenously injected neural stem cell accumulation in the brains of mice with experimental multiple sclerosis. *Stem Cells.* 2007; 25:2583-2592.
33. Modo, M, Cash, D, Mellodew, K, *et al.* Tracking transplanted stem cell migration using bifunctional, contrast agent-enhanced, magnetic resonance imaging. *Neuroimage.* 2002; 17:803-811.
34. Gilad, AA, McMahon, MT, Walczak, P, *et al.* Artificial reporter gene providing MRI contrast based on proton exchange. *Nat Biotechnol.* 2007; 25:217-219.
35. Hoehn, M, Himmelreich, U, Kruttwig, K, *et al.* Molecular and cellular MR imaging: potentials and challenges for neurological applications. *Journal of Magnetic Resonance Imaging: JMRI.* 2008; 27:941-954.
36. Bulte, JW, Zhang, S, van, GP, *et al.* Neurotransplantation of magnetically labeled oligodendrocyte progenitors: magnetic resonance tracking of cell migration and myelination. *Proc Natl Acad Sci U S A.* 1999; 96:15256-15261.
37. Hoehn, M, Wiedermann, D, Justicia, C, *et al.* Cell tracking using magnetic resonance imaging. *J Physiol.* 2007; 584:25-30.
38. Syková, E and Jendelová, P. Migration, fate and *in vivo* imaging of adult stem cells in the CNS. *Cell Death and Differentiation.* 2007; 14:1336-1342.
39. Kraitchman, DL, Gilson, WD, and Lorenz, CH. Stem cell therapy: MRI guidance and monitoring. *J Magn Reson Imaging.* 2008; 27:299-310.
40. Gilad, AA, Winnard, PT, van Zijl, PCM, *et al.* Developing MR reporter genes: promises and pitfalls. *NMR in Biomedicine.* 2007; 20:275-290.
41. Massoud, TF, Singh, A, and Gambhir, SS. Noninvasive molecular neuroimaging using reporter genes: part I, principles revisited. *AJNR American Journal of Neuroradiology.* 2008; 29:229-234.
42. So, PW, Parkes, HG, and Bell, JD. Application of magnetic resonance methods to studies of gene therapy. *Progress in Nuclear Magnetic Resonance Spectroscopy.* 2007; 51:49-62.
43. Yeh, E, Gustafson, K, and Boulianne, GL. Green fluorescent protein as a vital marker and reporter of gene expression in *Drosophila*. *Proceedings of the National Academy of Sciences of the United States of America.* 1995; 92:7036-7040.
44. Gould, SJ and Subramani, S. Firefly luciferase as a tool in molecular and cell biology. *Analytical Biochemistry.* 1988; 175:5-13.
45. Gilad, AA, Ziv, K, McMahon, MT, *et al.* MRI reporter genes. *Journal of Nuclear Medicine: Official Publication, Society of Nuclear Medicine.* 2008; 49:1905-1908.
46. Cohen, B, Ziv, K, Plaks, V, *et al.* MRI detection of transcriptional regulation of gene expression in transgenic mice. *Nat Med.* 2007; 13:498-503.
47. Genove, G, DeMarco, U, Xu, H, *et al.* A new transgene reporter for *in vivo* magnetic resonance imaging. *Nat Med.* 2005; 11:450-454.
48. Weissleder, R, Moore, A, Mahmood, U, *et al.* *In vivo* magnetic resonance imaging of transgene expression. *Nat Med.* 2000; 6:351-355.
49. Zurkiya, O, Chan, AW, and Hu, X. MagA is sufficient for producing magnetic nanoparticles in mammalian cells, making it an MRI reporter. *Magn Reson Med.* 2008; 59:1225-1231.
50. Aime, S, Castelli, DD, Crich, SG, *et al.* Pushing the sensitivity envelope of lanthanide-based magnetic resonance imaging (MRI) contrast agents for molecular imaging applications. *Acc Chem Res.* 2009; 42:822-831.
51. Willinek, WA and Kuhl, CK. 3.0 T neuroimaging: technical considerations and clinical applications. *Neuroimaging Clin N Am.* 2006; 16:217-28, ix.
52. Nakada, T. Clinical application of high and ultra high-field MRI. *Brain Dev.* 2007; 29:325-335.
53. Trattnig, S, Pinker, K, Ba-Ssalamah, A, *et al.* The optimal use of contrast agents at high field MRI. *Eur Radiol.* 2006; 16:1280-1287.

## PART TWO | Development of Molecular Imaging strategies

1 Department of Human Genetics, Leiden University Medical Center, Leiden, Netherlands

2 Department of Radiology, Leiden University Medical Center, Leiden, Netherlands

3 Department of Molecular Cell Biology, Utrecht University, Utrecht, Netherlands

4 Department of Pathology, Leiden University Medical Center, Leiden, Netherlands

5 Department of Neurology, Leiden University Medical Center, Leiden, Netherlands

6 Department of Pharmacology, Leiden-Amsterdam Center for Drug Research, Leiden University, Netherlands

# Chapter 8

Transmigration of amyloid- $\beta$  specific heavy chain antibody fragments across the *in vitro* blood-brain barrier

*Adapted from Neuroscience 2011 Sept;190:37-42*

Kim S. Rutgers<sup>1</sup>

**Rob J.A. Nabuurs<sup>2</sup>**

Sjoerd A. van den Berg<sup>1</sup>

Geert J. Schenk<sup>6</sup>

Maarten Rotman<sup>1</sup>

C. Theo Verrips<sup>3</sup>

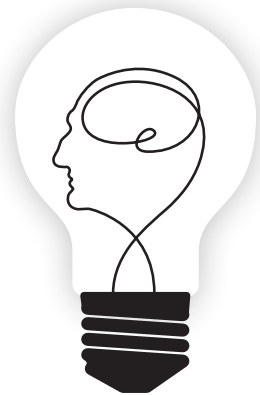
Sjoerd G. van Duinen<sup>4,5</sup>

Marion L. Maat-Schieman<sup>5</sup>

Mark A. van Buchem<sup>2</sup>

A. Bert G. de Boer<sup>6</sup>

Silvère M. van der Maarel<sup>1</sup>



## Abstract

Previously selected amyloid- $\beta$  recognizing V<sub>H</sub>H affinity binders derived from the Camelid heavy chain antibody repertoire were tested for their propensity to cross the blood-brain barrier (BBB) using an established *in vitro* BBB co-culture system. Of all tested V<sub>H</sub>H, ni3A showed highest transmigration efficiency which is, in part, facilitated by a 3 amino acid substitution in its N-terminal domain. Additional studies indicated that the mechanism of transcellular passage of ni3A is by active transport. As V<sub>H</sub>H ni3A combines the ability to recognize amyloid- $\beta$  and to cross the BBB, it has potential as a tool for non-invasive *in vivo* imaging and as efficient local drug targeting moiety in patients suffering from cerebral amyloidosis such as Alzheimer's disease and cerebral amyloid angiopathy.



## Introduction

Alzheimer's disease (AD) is the most prevalent form of dementia and clinically characterized by an irreversible process of cognitive decline.<sup>1</sup> Cerebral amyloid angiopathy (CAA), is the main cause of non-hypertensive intracerebral hemorrhage in the elderly.<sup>2</sup> AD and CAA share amyloid beta (A $\beta$ ) accumulation and aggregation as one of their primary neuropathologic characteristics.<sup>3,4</sup> Furthermore, a definitive diagnose can only be made with certainty by post-mortem histological analysis of brain tissue. Ideally, treatment of AD and CAA patients has to be started before significant cognitive loss has occurred. However, this requires novel diagnostic methods, ideally non-invasive, allowing the early detection of these diseases. Therefore, several classical antibodies, targeted at A $\beta$ , have been developed for detection and treatment of cerebral amyloidosis, but their utilization *in vivo* has been hampered by their size which prevents them from crossing the blood-brain barrier (BBB) effectively.

*Camelidae* co-express unusually shaped antibodies which are devoid of light chains next to their conventional immunoglobulin repertoire. These antibodies, referred to as heavy chain antibodies (HCAb), are composed of two identical heavy chains. Their antigen-binding properties are therefore only defined by the variable domains of these heavy chains (V<sub>H</sub>H). Interestingly, these V<sub>H</sub>H by themselves are fully capable of antigen binding.<sup>5</sup>

V<sub>H</sub>H have a molecular mass of ~15 kDa with affinities similar to those achieved with conventional antibodies.<sup>6</sup> V<sub>H</sub>H rapidly pass the renal filter, resulting in a rapid tissue penetration and fast blood clearance.<sup>7</sup> Moreover, it was demonstrated that they can cross the BBB: V<sub>H</sub>H FC5 binds to human cerebromicrovascular endothelial cells (HCEC) and transmigrates across an *in vitro* human BBB model.<sup>8</sup> Therefore, V<sub>H</sub>H are considered to have potential as tools for early non-invasive diagnosis using targeted contrast agents and delivery of therapeutic agents in patients with neurodegenerative disorders.

Targeted drug delivery and non-invasive early diagnosis using targeted contrast agents in neurodegenerative disorders are complicated by the regulated interface created by the BBB. The BBB's primary function is to maintain homeostasis of the brain and protect it against undesirable compounds and cells. For the identification of compounds that can cross the BBB the availability of *in vitro* BBB (co)-culture systems is imperative. Previously, we reported on an *in vitro* BBB co-culture system consisting of bovine brain capillary endothelial cells (BCEC) and newborn rat astrocytes. This established BBB model has been studied thoroughly and was shown to mimic the BBB *in vitro*, having small paracellular permeability, expression of various transporters and a relatively high transendothelial electrical resistance (TEER).<sup>9</sup>

In a previous study, we described a panel of V<sub>H</sub>H which we selected against A $\beta$  by phage display.<sup>10</sup> As a first step toward *in vivo* application, we here analyzed their propensity to cross the BBB *in vitro* and the influence of three specific amino acid substitutions on this crossing ability. The combination of both properties, that is, the ability to cross the BBB and to recognize A $\beta$ , would render these V<sub>H</sub>H promising tools for non-invasive *in vivo* imaging and efficient local drug targeting in patients with AD or CAA.

## Materials and Methods

### **V<sub>H</sub>H used in this study**

The V<sub>H</sub>H used in this study were described previously.<sup>10</sup> V<sub>H</sub>H ni3A, ni8B and va2E are selected against A $\beta$ . V<sub>H</sub>H ni3A and ni8B are derived from a non-immune library; va2E is selected from an immune library created after immunisation with post-mortem cerebral blood vessels of a Hereditary Cerebral Hemorrhage With Amyloidosis – Duchtype (HCHWA-D) patient. V<sub>H</sub>H FC5 encoding mRNA and amino acid sequences are deposited in the GenBank no. AF441486 and no. AAL58846, respectively and was produced synthetically.

### **Subcloning and Production**

The V<sub>H</sub>H genes were subcloned into the pUR5850VSV production vector.<sup>11</sup> Thereafter, the V<sub>H</sub>H were produced in *E. coli* and purified from the periplasmic supernatants as described earlier.<sup>12</sup> To test the necessity of the presence of three atypical amino acids in the N-terminus (framework 1; FR1) of ni3A for its ability to cross the BBB, a chimeric V<sub>H</sub>H 3A2E was constructed by PCR amplification of FR1 of ni3A and the region starting from complementarity determining region 1 (CDR1) until FR4 of va2E, and subsequent cloning of the chimeric PCR product into the pUR5071myc and pUR5850VSV vectors. All vectors were sequence verified (LGTC, Leiden, Netherlands). Production was performed as described previously.<sup>12</sup>

The open reading frame of the similarly sized control protein alpha-synuclein (SNCA) was PCR amplified from human brain cDNA, cloned, sequence verified and its encoded product was produced in the pET28 production system (Novagen, Madison, WI, USA). Primer sequences are available upon request. All proteins were purified using Talon metal affinity resin (Clontech, Palo Alto, CA, USA) according to the instructions of the manufacturer.

### **Immunohistochemistry**

Frozen brain tissue sections (8  $\mu$ m) from the neocortex of neuropathologically confirmed HCHWA-D, AD patients and non-demented controls were rinsed in PBS, fixed with ice-cold acetone for 10 min, incubated with peroxidase blocking reagent (Dako Cytomation) for 20 min, washed in PBS and incubated with the anti-A $\beta$  V<sub>H</sub>H (20 ng/ $\mu$ l) in 1% BSA/PBS overnight in a wet chamber. Thereafter, the sections were rinsed with PBS and incubated with mouse-anti-VSV for 1 hour and EnVision<sup>®</sup> system labelled Polymer-Hrp anti-Mouse (Dako Cytomation) for 30 min. Detection was performed with Liquid DAB<sup>+</sup> Substrate Chromogen System (Dako Cytomation). In addition, hematoxylin counterstaining was performed and the sections were dehydrated and mounted in micromount mounting medium (Surgipath, Richmond, IL, USA). 6E10 (Covance, Princeton, New Jersey, USA) was used as a positive control for A $\beta$  staining.

### ***In vitro* blood-brain barrier system**

The *in vitro* BBB model was prepared as described before.<sup>9,13</sup> Briefly, brain capillaries were isolated from cortices of bovine brain, acquired at a slaughterhouse (de Boer, Nieuwerkerk a/d IJssel, The Netherlands). The capillary fraction was prepared by homogenization, captured by percolation with nylon meshes and subsequently digested by enzymes. Astrocytes were isolated from cortices of brains of newborn Wistar rats (Harlan B.V., Zeist, the Netherlands) and used

for co-culture purposes and the preparation of astrocyte conditioned medium. Brain capillaries were cultured on collagen and fibronectin coated culture flasks in 50% astrocyte conditioned medium to brain capillary endothelial cells (BCEC). The astrocytes were seeded on the bottom of the filter. Two days later the BCEC were passaged on collagen coated Transwell polycarbonate filters (surface area: 0.33cm<sup>2</sup>, pore size: 0.4 μm, Corning Costar, Cambridge, MA, USA) and cultured to tight monolayers in 50% astrocyte conditioned medium in 5 days.

### ***In vitro* blood-brain barrier transport**

Transport studies were performed after 10 days of seeding and subsequently 5 days of seeding on the filters in DMEM+ 10% fetal calf serum (Bio Whittaker Europe, Verviers, Belgium) at 37°C. Transport studies were initiated by adding 10 μg V<sub>H</sub>H to the upper chamber of the *in vitro* BBB system. 60 μl aliquots were taken from the bottom chamber at 5 – 15 – 30 – 60 and 90 min. As a control a protein with the same size as a V<sub>H</sub>H (SNCA) was used. Membrane integrity was monitored with transendothelial electrical resistance (TEER) measurements, which was shown before to be a reliable and sensitive method to rule out paracellular BBB permeability.<sup>9</sup> The threshold was set at a resistance of 400 Ohm x cm<sup>2</sup>. After 120 min the cells were washed 3 times 300μl DMEM+S, harvested and lysed with MPER (Pierce Biotechnology, Rockford, IL, USA). For determination of the amount of V<sub>H</sub>H/protein that transmigrated across the model, 25 μl aliquots collected from the bottom chamber were immobilized on a Ni-NTA HisSorb 96-well plate (QIAGEN Benelux, Venlo, The Netherlands) diluted in 1% BSA with a final volume of 200 μl, at 4°C overnight. Plates were washed 4 times with PBS 0.05% Tween (PBST) and incubated with anti-*c-myc* / anti-VSV monoclonal antibody diluted in 1% BSA for 1 hour at room temperature. After washing, plates were incubated with polyclonal Rabbit anti-Mouse Immuno globulins conjugated with HRP (DakoCytomation). Plates were washed and detection was performed by adding 100 μl OPD (3,7 mM o-phenyldiamine, 50 mM Na<sub>2</sub>HPO<sub>4</sub>·H<sub>2</sub>O, 25 mM citric acid) supplemented with 0.01% H<sub>2</sub>O<sub>2</sub> to the wells. When the reaction was clearly visible, 50 μl 1M H<sub>2</sub>SO<sub>4</sub>/well was added to stop the reaction. The extinction at 490 nm was measured utilizing a Biotec synergy HT plate reader. Statistical analyses were performed by unpaired 2 tailed t-test comparing target V<sub>H</sub>H to control for each time point (**Figure 8.3**) or 2-way ANOVA followed by a Bonferonni post hoc test (**Figure 8.4**) using GraphPad Prism version 5.00 for Windows (GraphPad Software, San Diego California USA). Threshold value for statistical significant differences was set at 5%.

## Results

### **Subcloning and purification of specific V<sub>H</sub>H**

Two independent V<sub>H</sub>H clones, ni3A and ni8B respectively (**Figure 8.1B**), were chosen for this study.<sup>10</sup> These V<sub>H</sub>H were subcloned into the pUR5850-VSV production vector. Ni3A has an unexpected intrinsic efficiency in crossing the BBB. (see below, **Figure 8.3**) In order to investigate the necessity of the presence of three, for V<sub>H</sub>H unusual amino acid residues in the N-terminus of ni3A, [R15-D-G-D], with respect to crossing the BBB, chimaeric V<sub>H</sub>H 3A2E was constructed. 3A2E consists of the N-terminus from ni3A fused, at the boundary between FR1 and CDR1, with

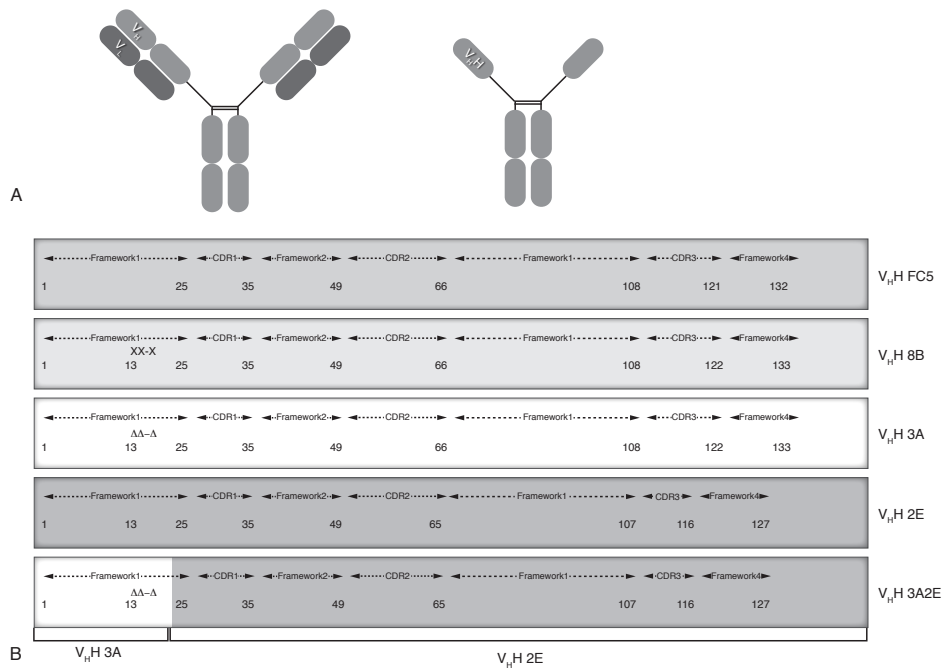


**Figure 8.1 Overview single and chimaeric  $V_H$ H constructs**

(A) Schematic representation of a conventional IgG with two heavy and two light chains (*left*) and a Camelid heavy chain IgG (*right*). The variable domains, including the  $V_H$ H domains used in this study are indicated. (B) Schematic representation of the  $V_H$ Hs used for the different experiments. First (top to bottom) the monovalent  $V_H$ Hs FC5 (*grey*), 8B (*less grey*), 3A (*white*), and 2E (*dark grey*) are shown. 8B and 3A differ 3 amino acids in framework 1, 13, 14 and 16, depicted with XX-X and  $\Delta\Delta\Delta$ , respectively. 2E is an unrelated  $V_H$ H that differs from ni3A and ni8B. At the bottom the chimaeric  $V_H$ H 3A2E, used to investigate the influence of the three unusual amino acids ( $\Delta\Delta\Delta$ ) of 3A on the transport, is depicted. 3A2E consists of amino acids 1-16 of 3A and amino acids 17-127 of 2E.

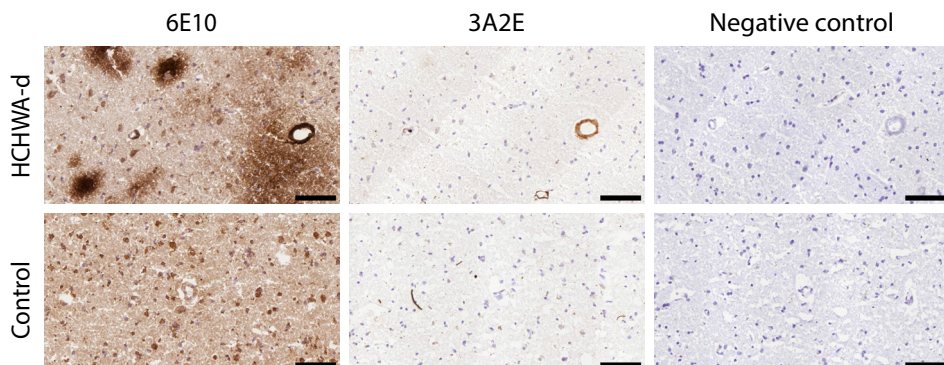


**Figure 8.2 Immunohistochemistry using chimaeric  $V_H$ H 3A2E**

Shown are adjacent neocortical cryosections of confirmed AD, HCHWA-D and control subjects stained with a commercial anti-A $\beta$  antibody (6E10), chimaeric 3A2E or its negative control. 3A2E retains its functionality of recognizing preferentially vascular A $\beta$ . On adjacent sections 6E10 showed the presence of large parenchymal deposits, only partially detected by 3A2E within the AD subject and completely lacking upon HCHWA-D tissue. Both control and negative control staining showed no non-specific staining patterns. Scale bar = 100  $\mu$ m.

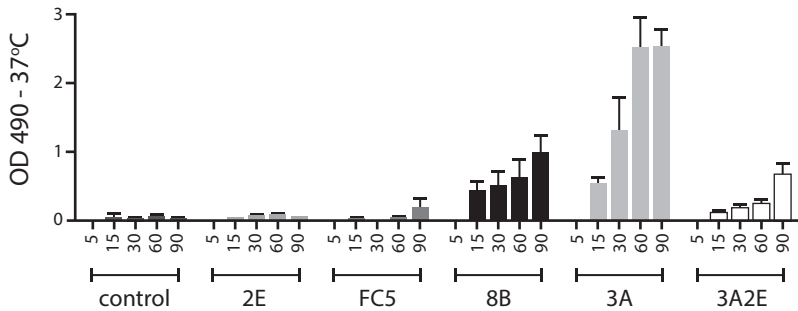


**Figure 8.3 Transmigration of V<sub>H</sub>Hs across the *in vitro* BBB system**

Transmigration of the control (SNCA) protein and V<sub>H</sub>Hs 2E, FC5, 8B, 3A and the chimaeric V<sub>H</sub>H 3A2E at 37°C. Measurements were taken 5 – 15 – 30 – 60 – 90 minutes after addition of the V<sub>H</sub>H samples to the system. Data is represented as OD490 at consecutive time points. \* $p < 0.05$  compared to the control, trending  $p$  values are noted in the graph. V<sub>H</sub>H 8B and V<sub>H</sub>H 3A demonstrate significant transport across the *in vitro* BBB. In addition, the chimaeric V<sub>H</sub>H 3A2E shows transport relative to the control and native 2E V<sub>H</sub>H.

the C-terminus of va2E and therefore also contains these unusual amino acid residues. V<sub>H</sub>H va2E also recognizes A $\beta$  but was selected from a different phage display library.<sup>10</sup> After production in *E. coli* the pure V<sub>H</sub>H were isolated from the periplasmic fraction and purified by immobilized metal affinity chromatography on Talon beads. An overview of the single and chimaeric V<sub>H</sub>H constructs is shown in **Figure 8.1**.

### Immunohistochemistry

Frozen brain tissue sections of AD, DS and HCHWA-D patients showed specific A $\beta$  staining of 3A2E indicating that the A $\beta$  recognizing propensity of va2E was preserved in this chimaeric molecule (HCHWA-D and control sections are shown in **Figure 8.2**). The specificity of the A $\beta$  staining was confirmed by the absence of staining in control brain tissue sections and an identical staining pattern was obtained with the commercially available A $\beta$  antibody, 6E10 in all patients. In contrast to 6E10, only vascular staining was observed with 3A2E, equal to ni3A and ni8B, as previously described.<sup>10</sup>

### *In vitro* blood-brain barrier transport

V<sub>H</sub>H ni3A, ni8B and FC5 were assessed for their ability to transmigrate across the BBB *in vitro*. While FC5 was previously described to cross the BBB as it was selected for this propensity, we didn't anticipate that ni3A showed higher transmigration velocity than FC5.<sup>8</sup> Yet, the transmigration rate of ni3A and ni8B was significantly higher compared to FC5 (respectively  $p < 0.01$  and  $p = 0.02$ ). (**Figure 8.3**)

Although V<sub>H</sub>H ni3A differs by 3 amino acids in its N- terminus from ni8B but has furthermore identical CDRs, a significantly higher transmigration velocity was observed by ni3A ( $p < 0.05$ ). In order to elucidate the capacity of ni3A to cross the BBB system with high efficiency, two additional V<sub>H</sub>H were tested: V<sub>H</sub>H va2E and chimaeric V<sub>H</sub>H 3A2E. The difference in crossing efficiency between va2E and the unrelated control protein of similar molecular weight (SNCA) did not reach statistical significance ( $p = 0.22$ ). Chimaeric V<sub>H</sub>H 3A2E has the same FR1 as ni3A

and the 2E-specific C-terminus. Chimaeric V<sub>H</sub>H 3A2E displayed a significantly higher transmigration rate compared to 2E ( $p=0.002$ ), indicating that the 3 amino acids subtracted from ni3A facilitate the crossing efficiency of V<sub>H</sub>H. At 4°C there was no significant passage of the V<sub>H</sub>H ni3A, indicating that the transmigration of ni3A is by active transport. (Figure 8.4) Time as well as temperature was a significant determinant of transport speed, as was determined by 2-way ANOVA (time  $p=0.01$  and temperature  $p<0.01$ , respectively), confirming the temperature dependency of the transport of V<sub>H</sub>H ni3A. In all experiments TEER was measured to rule out paracellular BBB permeability.<sup>9</sup>

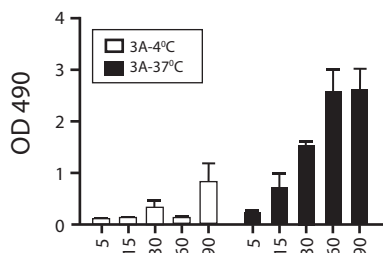


**Figure 8.4 Energy-dependence transmigration of ni3A across the in vitro BBB**

Measurements were taken 5 – 15 – 30 – 60 – 90 minutes after addition of the samples to the system at 4°C and 37°C. Data is represented as OD490 at consecutive time points. \*= $p<0.05$  compared to the control, trending  $p$  values are noted in the graph. Transport of 3A is time and temperature dependent, as determined by 2-way ANOVA. Significance of the separate time points was determined by Bonferonni post hoc test.

## Discussion

The availability of effective treatment for neurodegenerative disorders like AD and CAA is currently lacking but dearly needed. This lack of available therapy is partly based on our poor understanding of the pathogenesis of these diseases. The absence of reliable and sensitive biomarkers that permit studying cerebral amyloidosis in its early phases has certainly contributed to this situation. Cerebral A $\beta$  accumulation and aggregation is one of the primary neuropathologic characteristics of AD and CAA and is assumed to play a key role in the pathogenesis of these diseases. Consequently A $\beta$  is considered to be an important biomarker of cerebral amyloidosis.<sup>3,4</sup> Recently, molecular imaging techniques have been developed that permit detection of brain amyloidosis *in vivo*. Currently, positron emission tomography (PET) using amyloid-binding radiotracer compounds are being used for detecting cerebral amyloidosis in patients worldwide.<sup>14-16</sup> However, these agents detect both vascular and parenchymal A $\beta$ , and are thus not well suited to differentially recognize AD and CAA. Therefore, the development of imaging moieties that can be used to differentiate between vascular and parenchymal amyloid in living patients could help detecting CAA and/or AD *in vivo*.

Previously we reported V<sub>H</sub>H which differentially recognize vascular and parenchymal A $\beta$  deposition.<sup>10</sup> In this study we assessed the ability of these recently selected V<sub>H</sub>H for their ability to serve as imaging moieties and vehicles for tissue targeting. These V<sub>H</sub>H have the potential to serve as delivery vectors for efficient local drug targeting and for diagnostic purposes. It is believed that V<sub>H</sub>H have advantages to serve as imaging agents and/or transport moieties behind the BBB as they may overcome some of the current hurdles to transmigrate over the regulated interface created by the BBB.<sup>7,17</sup> In this study, an established *in vitro* co-culture model of the

BBB was used to test different A $\beta$  recognizing V<sub>H</sub>H for their ability to cross the BBB. Previously it was shown that in order to acquire a high quality *in vitro* co-culture model of the BBB one needs an optimal isolation method of bovine brain capillaries, and specific culture procedures for primary bovine BCEC and rat-astrocytes.<sup>9</sup> The co-culture systems used in this study are superior to other transport systems with respect to paracellular permeability and the maintenance of influx and efflux.<sup>18</sup>

As V<sub>H</sub>H FC5 was previously reported to cross the BBB *in vitro*, we compared the crossing efficiency of FC5 to V<sub>H</sub>H ni3A selected against A $\beta$ . To our great surprise, ni3A showed higher transmigration efficiency than FC5 at 37°C. It was reported previously that transport of FC5 across the *in vitro* BBB was by uptake and transcytosis via clathrin-coated vesicles, via a temperature and energy dependent receptor-mediated endocytosis (RME).<sup>19</sup> The first step towards elucidation of the mechanism behind the ni3A transport was to test the energy dependence of this transport. An experimental observation that would support active transport is temperature dependence because energy consumption and active transport processes are minimal at 0–4°C while functioning normally at 37°C.<sup>20</sup> Although energy dependence can also be observed for passive diffusion<sup>21,22</sup>, the temperature dependency by which a compound will diffuse through a medium is neglectable according to the formula:

$$D = D_0 e^{-EA/RT} \quad [8.1]$$

(where  $D$  is the diffusion coefficient,  $D_0$  is the “frequency factor,”  $EA$  is the activation energy,  $R$  is the gas constant and  $T$  is thermodynamic, or absolute, temperature (i.e. in Kelvins)).<sup>23</sup> Thus the influence of temperature on diffusion is minimal since the difference between 4°C (=277 kelvin) and 37°C (=310 kelvin) has a neglect influence on the diffusion coefficient of compounds. Therefore transport of ni3A at 4°C and 37°C was compared to investigate temperature and energy dependence. At 4°C there was barely passage of ni3A. This indicates temperature and energy dependence and suggests that the mechanism of transcellular passage of ni3A is by active transport.

Ni3A passes the system with the highest efficiency compared to all other V<sub>H</sub>H tested. Because ni3A is only three amino acids different from ni8B in FR1, and they present different crossing efficiencies, we hypothesized that those amino acid residues could potentially be key for the crossing propensity. It is interesting to note that these three amino acid diversion of ni3A is a special feature that is not present in any germline V<sub>H</sub>H gene. In order to test this hypothesis, V<sub>H</sub>H 3A2E was constructed, a chimaeric V<sub>H</sub>H in which we combined FR1 of ni3A with the carboxyterminus (CDR1-FR4) of va2E. This affinity binder va2E was selected against A $\beta$  from an immune library<sup>10</sup> and showed no crossing ability.

*In vitro* BBB passage of va2E was significantly and positively facilitated by the replacement of the three ni3A-specific amino acids. Although the unique amino acids in ni3A are not sufficient for efficient transmigration we conclude that they positively affect the transmigration rate. Apparently, a combination of N-terminal amino acid substitutions and other ni3A and ni8B-specific downstream sequences allow ni3A to outperform other V<sub>H</sub>H in its transmigration efficacy. In support, chimaeric 3A2E and ni8B, both having only one of these features, show intermediate transmigration efficiencies. The reason for the effect of the three amino acids remains to be elucidated. From numerous studies on enhancement of drug transport, it is known that positively charged amino acids can increase the BBB permeability and transport

into the brain.<sup>24</sup> Ni3A has 18 positively charged amino acids and ni8B 17, this could be a reason for the enhanced transport. Further analysis of the tertiary structure and the interaction between the different molecules is necessary to determine the exact nature of the higher transport rate of ni3A.

In conclusion, in this study V<sub>H</sub>H ni3A shows in addition to a high affinity for A $\beta$ , the ability to cross the BBB *in vitro*. This transport is temperature sensitive and facilitated by three unique amino acids. Ni3A has potential as *in vivo* imaging agent and local drug targeting moiety. Further studies will need to focus on its mechanism of transmigration and its application *in vivo*.



## References

1. Alzheimer, A, Stelzmann, RA, Schnitzlein, HN, et al. An English translation of Alzheimer's 1907 paper, "Über eine eigenartige Erkrankung der Hirnrinde". *Clin Anat.* 1995; 8:429-431.
2. Revesz, T, Holton, JL, Lashley, T, et al. Sporadic and familial cerebral amyloid angiopathies. *Brain Pathol.* 2002; 12:343-357.
3. Hardy, J and Selkoe, DJ. The amyloid hypothesis of Alzheimer's disease: progress and problems on the road to therapeutics. *Science.* 2002; 297:353-356.
4. van Duinen, SG, Castano, EM, Prelli, F, et al. Hereditary cerebral hemorrhage with amyloidosis in patients of Dutch origin is related to Alzheimer disease. *Proc Natl Acad Sci U S A.* 1987; 84:5991-5994.
5. Hamers-Casterman, C, Atarhouch, T, Muyldermans, S, et al. Naturally occurring antibodies devoid of light chains. *Nature.* 1993; 363:446-448.
6. Zhang, J, Tanha, J, Hirama, T, et al. Pentamerization of single-domain antibodies from phage libraries: a novel strategy for the rapid generation of high-avidity antibody reagents. *J Mol Biol.* 2004; 335:49-56.
7. Harmsen, MM, Van Solt, CB, Fijten, HP, et al. Prolonged *in vivo* residence times of llama single-domain antibody fragments in pigs by binding to porcine immunoglobulins. *Vaccine.* 2005; 23:4926-4934.
8. Muruganandam, A, Tanha, J, Narang, S, et al. Selection of phage-displayed llama single-domain antibodies that transmigrate across human blood-brain barrier endothelium. *FASEB J.* 2002; 16:240-242.
9. Gaillard, PJ, Voorwinden, LH, Nielsen, JL, et al. Establishment and functional characterization of an *in vitro* model of the blood-brain barrier, comprising a co-culture of brain capillary endothelial cells and astrocytes. *Eur J Pharm Sci.* 2001; 12:215-222.
10. Rutgers, KS, van Remoortere, A, Van Buchem, MA, et al. Differential recognition of vascular and parenchymal beta amyloid deposition. *Neurobiol Aging.* 2009.
11. van Koningsbruggen, S, de Haard, H, de Kievit, P, et al. Llama-derived phage display antibodies in the dissection of the human disease oculopharyngeal muscular dystrophy. *J Immunol Methods.* 2003; 279:149-161.
12. Kazemier, B, de Haard, H, Boender, P, et al. Determination of active single chain antibody concentrations in crude periplasmic fractions. *J Immunol Methods.* 1996; 194:201-209.
13. Gaillard, PJ and de Boer, AG. 2B-Trans technology: targeted drug delivery across the blood-brain barrier. *Methods Mol Biol.* 2008; 437:161-175.
14. Klunk, WE, Engler, H, Nordberg, A, et al. Imaging brain amyloid in Alzheimer's disease with Pittsburgh Compound-B. *Ann Neurol.* 2004; 55:306-319.
15. Small, GW, Kepe, V, Ercoli, LM, et al. PET of brain amyloid and tau in mild cognitive impairment. *N Engl J Med.* 2006; 355:2652-2663.
16. Verhoeff, NP, Wilson, AA, Takeshita, S, et al. In-vivo imaging of Alzheimer disease beta-amyloid with [11C]SB-13 PET. *Am J Geriatr Psychiatry.* 2004; 12:584-595.
17. Muyldermans, S, Cambillau, C, and Wyns, L. Recognition of antigens by single-domain antibody fragments: the superfluous luxury of paired domains. *Trends Biochem Sci.* 2001; 26:230-235.
18. Prieto, P, Baird, AW, Blaauboer, BJ, et al. The assessment of repeated dose toxicity *in vitro*: a proposed approach. The report and recommendations of ECVAM workshop 56. *Altern Lab Anim.* 2006; 34:315-341.
19. Abulrob, A, Sprong, H, Van Bergen en, HP, et al. The blood-brain barrier transmigrating single domain antibody: mechanisms of transport and antigenic epitopes in human brain endothelial cells. *J Neurochem.* 2005; 95:1201-1214.
20. Sugano, K, Kansy, M, Artursson, P, et al. Coexistence of passive and carrier-mediated processes in drug transport. *Nat Rev Drug Discov.* 2010; 9:597-614.
21. Lei, YD, Wania, F, Shiu, WY, et al. HPLC-based method for estimating the temperature dependence of n-octanol-water partition coefficients. *Journal of Chemical and Engineering Data.* 2000; 45:738-742.
22. Tanaka, M, Fukuda, H, and Nagai, T. Permeation of Drug Through A Model Membrane Consisting of Millipore Filter with Oil. *Chemical & Pharmaceutical Bulletin.* 1978; 26:9-13.
23. Crank, J. The mathematics of diffusion. 2nd ed. Oxford: Oxford Press, 1975:414.
24. Pardridge, WM. Blood-brain barrier delivery. *Drug Discov Today.* 2007; 12:54-61.

## PART TWO | Development of Molecular Imaging strategies

# Authors have contributed to this work equally

1 Department of Radiology, Leiden University Medical Center, Leiden, Netherlands;

2 Department of Human Genetics, Leiden University Medical Center, Leiden, Netherlands;

3 Nuclear Medicine & PET Research, Radionuclide Center, Free University Medical Center, Amsterdam, Netherlands;

4 Department of Neurology, Massachusetts General Hospital and Harvard Medical School, Charlestown, MA, USA;

5 Department of Anatomy & Embryology, Leiden University Medical Center, Leiden, Netherlands

# Chapter 9

*In vivo* detection of amyloid- $\beta$  deposits using heavy chain antibody fragments in a transgenic mouse model for Alzheimer's disease

*Adapted from PLoS ONE 2012;7(6):e38284*

**Rob J.A. Nabuurs<sup>#1</sup>**

Kim S. Rutgers<sup>#2</sup>

Mick M. Welling<sup>1</sup>

Athanasios Metaxas<sup>3</sup>

Maaïke E. de Backer<sup>1</sup>

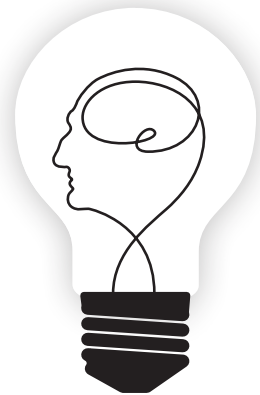
Maarten Rotman<sup>2</sup>

Brian J. Bacskai<sup>4</sup>

Mark A. van Buchem<sup>1</sup>

Silvère M. van der Maarel<sup>2</sup>

Louise van der Weerd<sup>1,2,5</sup>



## Abstract

This study investigated the *in vivo* properties of two heavy chain antibody fragments ( $V_HH$ ), ni3A and pa2H, to differentially detect vascular or parenchymal amyloid- $\beta$  ( $A\beta$ ) deposits characteristic for Alzheimer's disease and cerebral amyloid angiopathy.

Blood clearance and biodistribution including brain uptake were assessed by bolus injection of radiolabeled  $V_HH$  in APP/PS1 mice or wildtype littermates. In addition, *in vivo* specificity for  $A\beta$  was examined in more detail with fluorescently labeled  $V_HH$  by circumventing the blood-brain barrier via direct application or intracarotid co-injection with mannitol.

All  $V_HH$  showed rapid renal clearance (10–20 min). Twenty-four hours post-injection  $^{99m}Tc$ -pa2H resulted in a small yet significant higher cerebral uptake in the APP/PS1 animals. No difference in brain uptake were observed for  $^{99m}Tc$ -ni3A or DTPA( $^{111}In$ )-pa2H, which lacked additional peptide tags to investigate further clinical applicability. *In vivo* specificity for  $A\beta$  was confirmed for both fluorescently labeled  $V_HH$ , where pa2H remained readily detectable for 24 hours or more after injection. Furthermore, both  $V_HH$  showed affinity for parenchymal and vascular deposits, this in contrast to human tissue, where ni3A specifically targeted only vascular  $A\beta$ . Despite a brain uptake that is as yet too low for *in vivo* imaging, this study provides evidence that  $V_HH$  detect  $A\beta$  deposits *in vivo*, with high selectivity and favorable *in vivo* characteristics, making them promising tools for further development as diagnostic agents for the distinctive detection of different  $A\beta$  deposits.

## Introduction

Besides neurofibrillary tangles, Alzheimer's disease (AD) is characterized by cerebral deposition of  $\beta$ -amyloid (A $\beta$ ) in so-called senile or diffuse plaques.<sup>1</sup> Similar vascular deposits of A $\beta$  associated with cerebral amyloid angiopathy (CAA) lead to loss of vessel wall integrity increasing the risk of brain haemorrhages.<sup>2</sup> Present in 30% of the non-demented population over 60 years of age, CAA co-exists in 90% of the AD patients and forms an important complication in the development of immunotherapeutic strategies.<sup>3-5</sup> Although, the exact role of A $\beta$  regarding the underlying pathogenesis remains unsolved, accumulation is believed to start 20–30 years prior to clinical onset.<sup>6,7</sup> Distinctive *in vivo* detection of the different A $\beta$  deposits therefore renders important knowledge regarding early diagnosis and preventive therapy development.

Currently, a gross differentiation can only be made based on the occipital predilection of CAA, while existing PET ligands, like <sup>11</sup>C-PiB, target A $\beta$  in its fibrillar amyloid form rather than specific vascular or parenchymal types of A $\beta$  deposits.<sup>8</sup>

Previously, we have selected heavy chain antibody fragments with high affinity specific for either CAA or all types of human A $\beta$  deposits.<sup>9</sup> Derived from the Camelid heavy chain antibody repertoire, which completely lack light chains, their single N-terminal domain (V<sub>H</sub>H) is fully capable of antigen binding with affinities comparable with those of conventional antibodies.<sup>10,11</sup> Blood-brain barrier (BBB) passage was shown to be favorable in an *in vitro* assay<sup>12</sup>; therefore, this study assessed the *in vivo* characteristics of two distinct A $\beta$  targeting V<sub>H</sub>H, ni3A and pa2H, for their potential use to differentially detect AD and CAA. First, pharmacologic behaviour and biodistribution were examined after administration of radiolabeled V<sub>H</sub>H into a transgenic AD/CAA mouse model. Secondly, fluorescently labeled V<sub>H</sub>H were administered after the BBB was circumvented to evaluate their ability to specifically bind A $\beta$  deposits *in vivo*.

## Materials and Methods

### Production of ni3A and pa2H

V<sub>H</sub>H ni3A and pa2H were selected from respectively a non-immune or an immune library created after immunisation with post-mortem brain parenchyma of a patient with Down's syndrome. V<sub>H</sub>H were subcloned and produced as previously reported including a myc- or VSV-tag for detection and a his-tag for purification.<sup>9</sup> Similarly, pa2H free of any additional peptide tags was commercially produced by overexpression in yeast (BAC, Leiden, the Netherlands).

### Animal studies

All studies were performed using 12 – 16 month old transgenic mice or wildtype littermates from a colony set up using the APP<sup>swe</sup>/PS1<sup>dE9</sup> strain (APP/PS1) (JAX), known to accumulate vascular and parenchymal A $\beta$  deposits<sup>13</sup>, and have been approved by the institutional Animal Ethics Committee (DEC) at the Leiden University Medical Center, permit number 09132. Besides standard genotyping, after each experiment amyloid pathology was confirmed by standard Thioflavin T staining.

## Human material

Human brain tissue was obtained of AD/CAA patients or controls as confirmed by neuropathological examination in agreement with the guidelines of the ethics committee of the LUMC. Patient anonymity was strictly maintained. All tissue samples were handled in a coded fashion, according to Dutch national ethical guidelines (Code for Proper Secondary Use of Human Tissue, Dutch Federation of Medical Scientific Societies).

## Murine specificity of the selected V<sub>H</sub>H

To evaluate appropriate use of the APP/PS1 mouse model, murine cryosections (10µm) were stained according previous protocols<sup>9,12</sup> with in addition a standard anti-mouse-to-mouse kit (ARK, Dako Cytomation). Final preparations were analyzed with an automated Panoramic MIDI microscope (3DHistech).

## Biodistribution and clearance

### *Radiolabeling*

V<sub>H</sub>H were labeled according to two different protocols. First, his-tagged V<sub>H</sub>H were labeled directly with technetium-99m (<sup>99m</sup>Tc) using a previously published protocol.<sup>14</sup> Briefly, 20 µl of V<sub>H</sub>H in PBS solution (450-500 ng/µl) was added to 8 µl of an aseptic mixture of 950 mg/l Sn(Cl)<sub>2</sub>·2H<sub>2</sub>O and 2 g/l Na<sub>4</sub>P<sub>2</sub>O<sub>7</sub>·10H<sub>2</sub>O (Technescan PYP, Covidien, Petten, the Netherlands) in saline. After addition of 4 µl of 10 mg/ml of KBH<sub>4</sub> (crystalline, Sigma Chemical Co, St. Louis, MO) in 0.1 M NaOH, and 100 µl of Na[<sup>99m</sup>TcO<sub>4</sub>] solution (approximately 200-700 MBq/ml, Technekow, Covidien, Petten, the Netherlands) the mixture was gently stirred at room temperature for at least 30 min before use. Analysis of the labeling solution, referred to as <sup>99m</sup>Tc-V<sub>H</sub>H, yielded a radiochemical purity of >95% without detectable unreduced or free <sup>99m</sup>TcO<sub>4</sub>.<sup>15</sup>

Secondly, untagged V<sub>H</sub>H were chelated for indium-111 (<sup>111</sup>In) using diethylene triamine penta-acetic acid (DTPA). Untagged pa2H was chelated in a total volume of 1.0ml with 20-fold molecular excess of p-SCN-Bn-DTPA (Macrocyclics, Dallas, TX) at pH 8.5 in phosphate buffer for 5 hr at 37.5°C and purified by dialysis using phosphate buffered saline (PBS). <sup>111</sup>In chloride (25µl, 111 MBq/ml, Covidien, the Netherlands) was added to DTPA-pa2H conjugate (0.1ml) in 0.25 M ammonium acetate buffer (0.8 ml) at pH 5.5 and incubated for 1 hr at room temperature. The reaction was quenched with 50mM ethylene diamine tetra-acetic acid (EDTA) (50 µl) to chelate residual non-bound <sup>111</sup>In and the radiolabeled antibody was then purified using a Sephadex™ G-25 column (PD 10; GE Healthcare) eluted with PBS. Radiochemical purity assessed by instant thin layer chromatography (ITLC) yielded a purity of >95%.

### *Biodistribution and brain uptake*

To study the biodistribution, animals were injected intravenously with 0.2 ml radiolabeled V<sub>H</sub>H diluted with saline (5-10 MBq/ml, 10µg/ml). At different intervals (t = 3 - 6 - 24hrs) post-injection APP/PS1 (n=4) and wildtype animals (n=4) were sacrificed (Euthanasol, AST Pharma). Similar biodistribution experiments using untagged DTPA(<sup>111</sup>In)-pa2H were only performed at 24 hours post-injection for APP/PS1 (n=6) and wildtype mice (n=6). Blood was collected via cardiac puncture, and various organs were removed, including the brain, which was divided into the cerebrum and cerebellum. All were weighed and counted for radioactivity (Wizard<sup>2</sup>, Perkin Elmer). After decay

correction, radioactivity was expressed as the percentage of the total injected dose of radioactivity per gram tissue (%ID/g). Blood/cerebrum ratios were calculated to correct for possible confounding effects accountable by residual blood. Similarly, muscle/cerebrum determined target-to-non-target ratios. Differences were regarded significant when  $p \leq 0.05$  using an unpaired one or two tailed t-test. Experiments at  $t = 24$ hrs were repeated twice using  $^{99m}\text{Tc}$ -pa2H.

#### *Blood clearance and analysis*

Simultaneously, blood half-life was examined by collecting 5  $\mu\text{l}$  tail samples at several time points between 3–90 minutes post-injection of radiolabeled V<sub>H</sub>H into transgenic or wildtype mice ( $n=4-6$ ). Combined with the cardiac blood samples corresponding half-lives were calculated using GraphPad Prism.

Similarly, 10  $\mu\text{l}$  samples obtained at 10 and 90 minutes post-injection were mixed with 90  $\mu\text{l}$  heparin (34 U/ml saline) and 900  $\mu\text{l}$  PBS. Centrifugation for 10 minutes at 7,000 rpm separated plasma from the cell pellet. Radioactivity was measured separately to determine the blood distribution of radiolabeled V<sub>H</sub>H over time.

#### *Specificity of radiolabeled pa2H*

A $\beta$  specificity of pa2H-his after  $^{99m}\text{Tc}$ -radiolabeling was tested by quantitative competition autoradiography. Human and murine brain cryosections (20  $\mu\text{m}$ ) were blocked with 1% bovine serum albumin (BSA)/PBS at 37°C for 1 hour followed by similar application of the labeling solution, which was diluted to 1  $\mu\text{g}/\text{ml}$  by 1%BSA/PBS with or without additional 1 hour pre-incubation with excess monomeric or fibrillar A $\beta_{1-40}$  (rPeptide) at 37°C. Fibrils were produced using existing protocols.<sup>16</sup>

After rinsing 3 times with PBS, radioactivity was counted for 15 minutes by a gamma camera (Toshiba GCA7100/UI). A similar region of interest was fitted for each scintigram to assess binding of  $^{99m}\text{Tc}$ -pa2H-his with 0.1 ml of diluted labeling solution as a reference. Binding was expressed as the % of radioactivity compared to the section without any competitor. Experiments were performed in triplicate.

### ***In vivo A $\beta$ targeting by V<sub>H</sub>H***

#### *Fluorescent labeling*

Tagged V<sub>H</sub>H were fluorescently labeled with Alexa Fluor 594 protein labeling kit (Molecular Probes, Invitrogen) according to the manufacturer's guidelines, except using only half of the recommended amount of dye. Briefly spun to remove possible aggregates, extensive dialysis removed excess free label. The labeling degree and protein concentration (200–600 ng/ $\mu\text{l}$ ) were determined using the Nanodrop ND1000 (Isogen Life Sciences). Protein integrity was confirmed by mass spectrometry.

#### *Immunofluorescence using V<sub>H</sub>H-Alexa594*

To examine whether the fluorescent labeling affected antigen recognition, human and murine cryosections (10  $\mu\text{m}$ ) were rinsed with PBS, fixed in ice-cold acetone for 10 minutes before overnight incubation with V<sub>H</sub>H- Alexa594 in 1% BSA/PBS in a wet chamber. Washed 3 x 5 minutes with PBS, sections were mounted and analyzed using a fluorescence microscope (Leica DMR5500B).

### *In vivo* A $\beta$ imaging by topical application

Four APP/PS1 animals received permanent cranial windows to allow serial *in vivo* imaging of the brain by multiphoton microscopy. Animals were anaesthetized using 2% isoflurane gas inhalation, and the exposed skull was partly replaced by a round glass coverslip glued into place using Krazyglue<sup>®</sup> according to previous surgical protocols.<sup>17,18</sup> Prior to fixation of the cranial window, a drop of 40-60  $\mu$ l of V<sub>H</sub>H-Alexa594 (275-400 ng/ $\mu$ l) was applied directly onto the exposed brain for 30 minutes and briefly rinsed with PBS. Colocalization with the A $\beta$  deposits was based either upon their typical green autofluorescence or by intraperitoneal injections of Methoxy-X04 one day prior surgery.<sup>16</sup> Animals were imaged immediately following surgery, which was typically less than 90 minutes after beginning of the procedure, and re-imaged under isoflurane anaesthesia (2%) for several days to study the washout. Images were acquired with a Bio-Rad 1024 multiphoton microscope equipped with a Ti:Sapphire laser (Mai Tai, Spectra Physics) and external photodetectors (Hamamatsu Photonics). Areas were imaged to approximately 200  $\mu$ m deep in 5  $\mu$ m steps with a 20x objective (UMPlanFI, NA=0.95; Olympus). Maximum intensity projections were reconstructed using ImageJ.

### *Specific in vivo* A $\beta$ binding after BBB disruption

A systemic approach to study the *in vivo* behaviour of the V<sub>H</sub>H throughout a larger area within the brain involved intracarotid infusion (60  $\mu$ l/min) of 100  $\mu$ l pa2H-*his*-Alexa594 along with 600  $\mu$ l 15% mannitol selectively into the right carotic artery to disrupt the BBB.<sup>19</sup> At  $t = 2$  and 24 hours post-injection, transgenic (n=9) and wildtype animals (n=3) were euthanized (Euthanasol, AST Pharma), and perfused with 4% paraformaldehyde (PFA). Resected brains were stored in

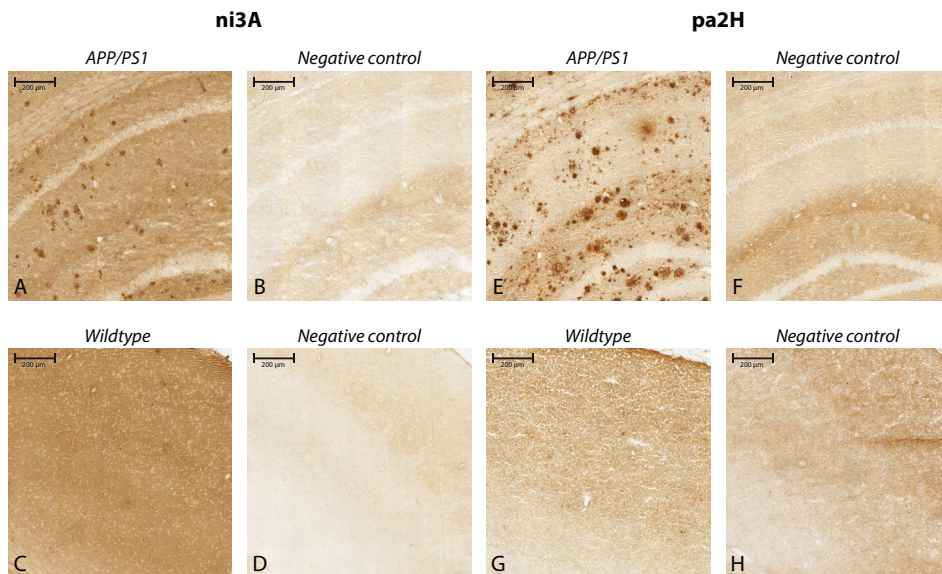


**Figure 9.1 Immunostaining on murine APP/PS1 sections using ni3A and pa2H**

The upper panels (A - D) show 10x magnifications of the resulting staining with cryosections of aged APP/PS1 mouse brain tissue including negative controls, while the lower panels (E - H) show similar staining performed with wildtype littermates.



4% PFA with 10% sucrose for 4 hours followed by overnight fixation in 4% PFA with 30% sucrose. Next, the brains were snap frozen and sectioned completely to obtain consecutive 30 µm thick cryosections. Besides standard Thioflavin T staining for amyloid, adjacent sections were immunostained for Aβ (6F/3D, DakoCytomation)<sup>20</sup> with 1:100 goat-antimouse-Alexa488 (Invitrogen) to assess colocalization. Images obtained by a Leica DM5500B microscope were merged using Adobe Photoshop CS3.

## Results

### Murine specificity of the selected V<sub>H</sub>H

Immunostained brain sections of aged APP/PS1 and wildtype littermates using tagged V<sub>H</sub>H ni3A and pa2H were made to assess their capacity to selectively recognize different types of deposits. (**Figure 9.1**) Pa2H stained positive for all forms of Aβ depositions. In this transgenic mouse model, ni3A did not show selective affinity for vascular Aβ; both vascular and parenchymal Aβ depositions were clearly labeled. Compared to ni3A, equivalent staining protocols with pa2H resulted in higher specificity for Aβ combined with a low unspecific background binding. For neither V<sub>H</sub>H specific affinity was detected within the brain sections of wildtype animals.

### Biodistribution and clearance

#### *Biodistribution and brain uptake*

The distribution of a bolus injection of radiolabeled tagged ni3A and pa2H over time is shown in **Table 9.1** and **9.2**. No significant differences in organ uptake between wildtype and transgenic animals were found, except for the brain uptake of <sup>99m</sup>Tc-pa2H after 24 hours. Although the amount was low (0.038 %I.D./g), cerebral uptake was 40% higher in the transgenic animals. The cerebrum/blood ratio did not differ, indicating that this difference was not caused by different V<sub>H</sub>H concentrations within the blood pool. For the cerebellum similar results were found. Repeated experiments for this particular endpoint resulted in similar findings.

To investigate whether these findings were not confounded by either the non-specific radiolabeling procedure or the presence of additional peptide tags, the biodistribution experiment was repeated with untagged DTPA(<sup>111</sup>In)-pa2H. (**Table 9.2**) With this labeling protocol, we no longer observed a significantly higher cerebral uptake in amyloid-bearing mice. Regardless of the tag, the majority of radiolabeled V<sub>H</sub>H was excreted via the kidneys. Cellular involvement as shown by distinctive hepatic clearance or splenic activity was low. In comparison to <sup>99m</sup>Tc-ni3A, <sup>99m</sup>Tc-pa2H showed about 3 times higher clearance via liver and spleen. Also, the clearance rate for <sup>99m</sup>Tc-pa2H was lower, independent of genotype. However, within the first 3 hours <sup>99m</sup>Tc-ni3A resulted in a higher general organ uptake, with exception of the aforementioned liver and spleen.

#### *Blood clearance and analysis*

Blood clearance of the tagged <sup>99m</sup>Tc-V<sub>H</sub>H consisted of a fast and a slow component. (**Figure 9.2A**) In general, the majority of the radiolabeled V<sub>H</sub>H was cleared from the blood with a half-life of 10–20 minutes (**Table 9.3**). The actual half-life of the slow component of <sup>99m</sup>Tc- V<sub>H</sub>H could

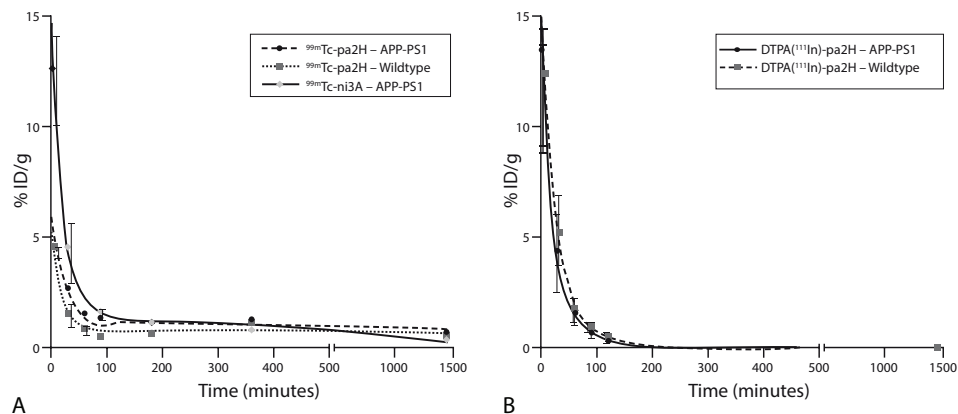


**Figure 9.2 Blood clearance**

These graphs represent the blood half lives of tagged  $^{99m}\text{Tc}$ -ni3A and -pa2H (A), and untagged DTPA( $^{111}\text{In}$ )-pa2H (B) in APP/PS1 mice and wildtype littermates. Data is shown as percentage of injected dose per gram of blood (%ID/g) over time. Based upon this plot the clearance is suggested to respectively consist of a fast and a slow phase, or only a single phase.

**Table 9.1. Biodistribution of  $^{99m}\text{Tc}$ -ni3A in mice**

Tissue / organ	t = 3 hr		t = 6 hr		t = 24 hr	
	Wildtypes	APP/PS1	Wildtypes	APP/PS1	Wildtypes	APP/PS1
blood	1.202 ± 0.379	1.146 ± 0.131	0.778 ± 0.048	0.808 ± 0.115	0.451 ± 0.073	0.363 ± 0.051
heart	0.525 ± 0.129	0.508 ± 0.109	0.347 ± 0.049	0.337 ± 0.127	0.252 ± 0.041	0.216 ± 0.014
lungs	0.850 ± 0.184	0.819 ± 0.208	0.659 ± 0.184	0.743 ± 0.301	0.375 ± 0.113	0.291 ± 0.055
liver	1.078 ± 0.235	1.000 ± 0.293	1.078 ± 0.188	1.223 ± 0.424	0.568 ± 0.149	0.488 ± 0.164
kidneys	15.531 ± 2.986	15.192 ± 3.075	10.266 ± 1.657	14.294 ± 4.337	9.089 ± 6.152	9.901 ± 1.158
spleen	0.590 ± 0.257	0.531 ± 0.084	0.792 ± 0.144	0.753 ± 0.291	0.397 ± 0.056	0.465 ± 0.234
muscle	0.171 ± 0.075	0.120 ± 0.069	0.111 ± 0.088	0.086 ± 0.022	0.043 ± 0.007	0.048 ± 0.008
cerebrum	0.035 ± 0.009	0.035 ± 0.007	0.031 ± 0.007	0.035 ± 0.008	0.018 ± 0.003	0.019 ± 0.001
cerebellum	0.073 ± 0.031	0.063 ± 0.009	0.098 ± 0.009	0.096 ± 0.014	0.029 ± 0.005	0.026 ± 0.002
cerebrum/ blood ratio	0.030 ± 0.003	0.030 ± 0.004	0.040 ± 0.010	0.043 ± 0.004	0.040 ± 0.001	0.053 ± 0.008 *
cerebrum/ muscle ratio	0.242 ± 0.142	0.335 ± 0.116	0.407 ± 0.270	0.428 ± 0.171	0.422 ± 0.029	0.403 ± 0.100

A bolus injection of 2  $\mu\text{g}$   $^{99m}\text{Tc}$ -ni3A was administered intravenously into 12 – 14 month old APP/PS1 mice or their wild type littermates. At three time points after injection the animals were sacrificed and various tissues and entire organs were removed, weighed and counted for radioactivity. Values are expressed as a percentage of the injected dose per gram tissue (mean ± SD). \* =  $P < 0.05$  wildtype mice compared to APP/PS1 mice.

only be calculated with limited accuracy, since the half-life was longer than the blood sampling period. In line with the above biodistribution, six hours post-injection, the blood levels of <sup>99m</sup>Tc-pa2H were remarkably higher compared to earlier time points, which is characteristic for a second passage. Within the first 90 minutes about 80% of the <sup>99m</sup>Tc-V<sub>H</sub>H remained within the blood plasma, indicating that no significant cellular uptake occurred. (Table 9.4)

In contrast to tagged <sup>99m</sup>Tc-V<sub>H</sub>H, the blood clearance of untagged DTPA(<sup>111</sup>In)-pa2H was mono-exponential, with a similar rapid clearance within 20 minutes, but without a slow component. (Figure 9.2B)

#### Specificity of <sup>99m</sup>Tc-pa2H

After radiolabeling of the tagged pa2H its specificity for A $\beta$  was unaffected, as shown by scintigraphic analysis; binding of <sup>99m</sup>Tc-pa2H was higher in those sections including A $\beta$ . (Table 9.5) Furthermore, binding was significantly ( $p < 0.001$ ) reduced when the tracer was pre-incubated with either monomeric or fibrillar A $\beta$ .

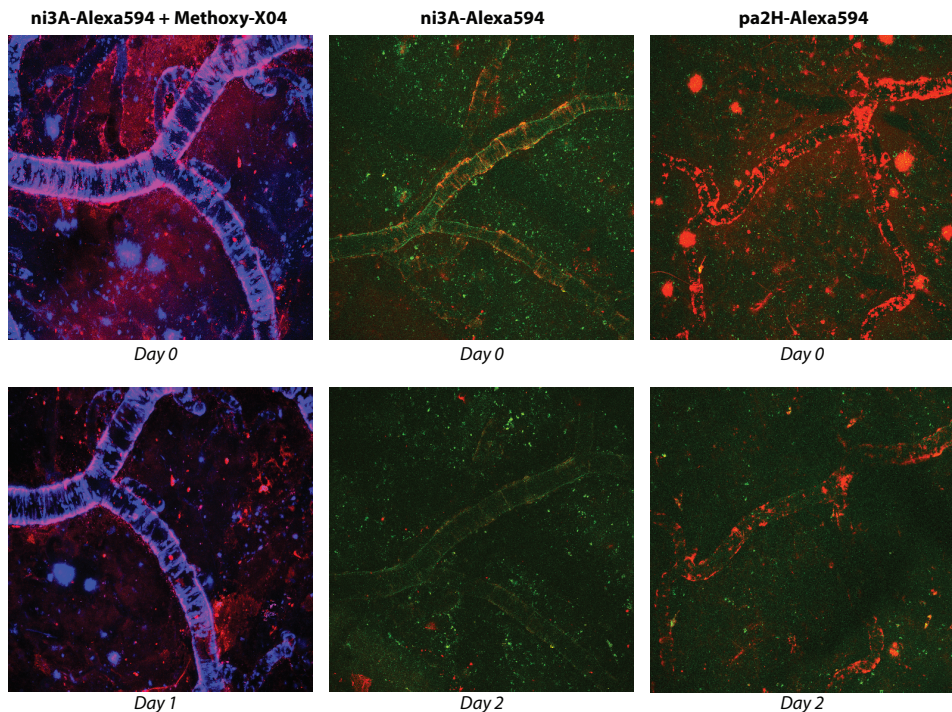


**Figure 9.3** *In vivo* A $\beta$  imaging after direct brain application

Topical application of ni3A- or pa2H-Alexa594 (red) as visualized over time by intravital multiphoton microscopy in APP/PS1 mice clearly shows the specific *in vivo* labeling of different A $\beta$  deposits. In the **left**, vascular and parenchymal A $\beta$  deposits, detected by prior labeling with Methoxy-X04 (blue), colocalize with ni3A-Alexa594 (red) directly following topical application. One day later, labeling of the plaques has diminished to almost none with some residual left bound to CAA. With interpretation hampered by Methoxy-X04, **middle** images show a similar experiment. Colocalization with A $\beta$  deposits based upon autofluorescence (green) gave comparable results and almost complete wash out after two days. Pa2H-Alexa594 (red), as shown in the **right** images, remains bound to vascular A $\beta$  even two days after application, when the plaques remained undetected. All images are maximum intensity projections of a 3D cortical volume with a field of view 615 x 615  $\mu$ m.

Table 9.2. Biodistribution of radiolabeled pa2H in mice

Tissue / organ	<sup>99m</sup> Tc-pa2H					
	t = 3 hr		t = 6 hr		t = 24 hr	
	Wildtypes	APP/PS1	Wildtypes	APP/PS1	Wildtypes	APP/PS1
blood	0.566 ± 0.003	0.654 ± 0.015	1.009 ± 0.054	1.244 ± 0.123	0.575 ± 0.084	0.696 ± 0.049
heart	0.273 ± 0.121	0.240 ± 0.017	0.623 ± 0.101	0.763 ± 0.031	0.367 ± 0.059	0.393 ± 0.007
lungs	0.843 ± 0.256	0.537 ± 0.010	0.930 ± 0.242	1.088 ± 0.035	0.620 ± 0.160	0.622 ± 0.031
liver	2.615 ± 0.796	1.866 ± 0.016	3.014 ± 1.021	3.392 ± 1.932	1.450 ± 0.402	1.161 ± 0.470
kidneys	9.243 ± 1.787	6.241 ± 0.530	14.306 ± 4.105	15.612 ± 1.042	9.824 ± 2.810	8.608 ± 0.738
spleen	1.515 ± 0.503	1.319 ± 0.060	6.498 ± 1.623	6.258 ± 0.208	3.584 ± 1.381	1.747 ± 0.100
muscle	0.356 ± 0.379	0.054 ± 0.006	0.174 ± 0.022	0.347 ± 0.026	0.102 ± 0.023	0.113 ± 0.018
cerebrum	0.014 ± 0.003	0.017 ± 0.001	0.033 ± 0.005	0.044 ± 0.004	0.027 ± 0.004	0.038 ± 0.002 *
cerebellum	0.023 ± 0.001	0.026 ± 0.001	0.054 ± 0.016	0.067 ± 0.001	0.030 ± 0.007	0.045 ± 0.000 *
cerebrum/blood ratio	0.025 ± 0.005	0.026 ± 0.003	0.033 ± 0.004	0.035 ± 0.004	0.047 ± 0.003	0.055 ± 0.008
cerebrum/muscle ratio	0.083 ± 0.081	0.309 ± 0.067	0.190 ± 0.007	0.177 ± 0.135	0.270 ± 0.032	0.346 ± 0.377
Wildtypes						
APP/PS1						
Wildtypes						
APP/PS1						

A bolus injection of 2 µg radiolabeled pa2H was administered intravenously into 12 – 14 month old APP/PS1 mice or their wildtype littermates. At three or one time points after injection of radiolabeled pa2H respectively with or without additional peptide tags, the animals were sacrificed and various tissues and entire organs were removed, weighed and counted for radioactivity. Values are expressed as a percentage of the injected dose per gram tissue (mean ± SD). \* = P<0.05 wildtype mice compared to APP/PS1 mice.

### ***In vivo* A $\beta$ targeting by V<sub>H</sub>H**

#### *In vivo* A $\beta$ imaging by topical application

After direct application onto the exposed mouse brain, fluorescent V<sub>H</sub>H were followed up for at least 48 hours by *in vivo* multiphoton microscopy. (**Figure 9.3**) Specific *in vivo* labeling of A $\beta$  plaques by ni3A-Alexa594 was initially confirmed by colocalization with Methoxy-X04, a known *in vivo* amyloid targeting fluorophore. Beside possible binding competition with the V<sub>H</sub>H, Methoxy-X04 hampered good validation due to signal cross-over into the red channel. However, colocalization based on the typical autofluorescence patterns of the different A $\beta$  deposits resulted in similar findings. Selectivity was confirmed by lack of nonspecific background signal. Although both V<sub>H</sub>H were capable of targeting A $\beta$  *in vivo*, only pa2H-Alexa594 was detectable after two days, mainly bound to vascular amyloid.

#### *Specific in vivo* A $\beta$ binding after BBB disruption

Based on the above findings, co-injections of pa2H-Alexa594 with mannitol were done in the right carotid artery to selectively open the BBB in the ipsilateral hemisphere to study the *in vivo* characteristics throughout the brain. Two hours post-injection, fluorescence was detected in the right hemisphere, co-localizing with A $\beta$ . (**Figure 9.4**) Even within the deeper brain structures, no nonspecific binding was observed. A $\beta$  related fluorescent signal remained detectable for at least 24 hours post-injection. Without BBB disruption or within wildtype littermates, no apparent A $\beta$  labeling could be detected.

#### *Immunofluorescence using V<sub>H</sub>H-Alexa594*

Selectivity for specific A $\beta$  deposits was not altered after fluorescent labeling of the V<sub>H</sub>H, since on human sections, ni3A-Alexa594 selectively stained vascular A $\beta$  and pa2H-Alexa594 stained both parenchymal and vascular A $\beta$ . (**Figure 9.5**) On murine material all A $\beta$  deposits were stained by both fluorescent V<sub>H</sub>H.

**Table 9.3** Blood half lives of radiolabeled V<sub>H</sub>H

V <sub>H</sub> H	genotype	Fast t <sub>1/2</sub>			Slow t <sub>1/2</sub>		
		(min)	(95% C.I.)	%	(min)	%	(95% C.I.)
<sup>99m</sup> Tc-ni3A	APP/PS1	14.71	(8.65 - 49.13)	89.7	580	10.3	(101.8 - ∞)
	Wildtype	ND		ND	ND	ND	
<sup>99m</sup> Tc-pa2H	APP/PS1	21.89	(14.24 - 39.38)	79.8	2562	20.2	(975.0 - ∞)
	Wildtype	10.78	(7.27 - 20.76)	87.1	5861	12.9	(969.3 - ∞)
DTPA( <sup>111</sup> In)-pa2H	APP/PS1	19.69	12.63 - 44.60	100	-	-	
	Wildtype	15.83	9.30 - 53.37	100	-	-	

Half lives were determined by fitting a one or a two phase exponential decay model based on blood obtained from both tail vein and cardiac puncture at several time points after intravenous bolus injection of 2  $\mu$ g radiolabeled V<sub>H</sub>H in 12 - 14 month old APP/PS1 mice and wildtype littermates, as depicted in **Figure 9.2**. Please note that DTPA(<sup>111</sup>In)-pa2H was produced without any additional peptide tags.

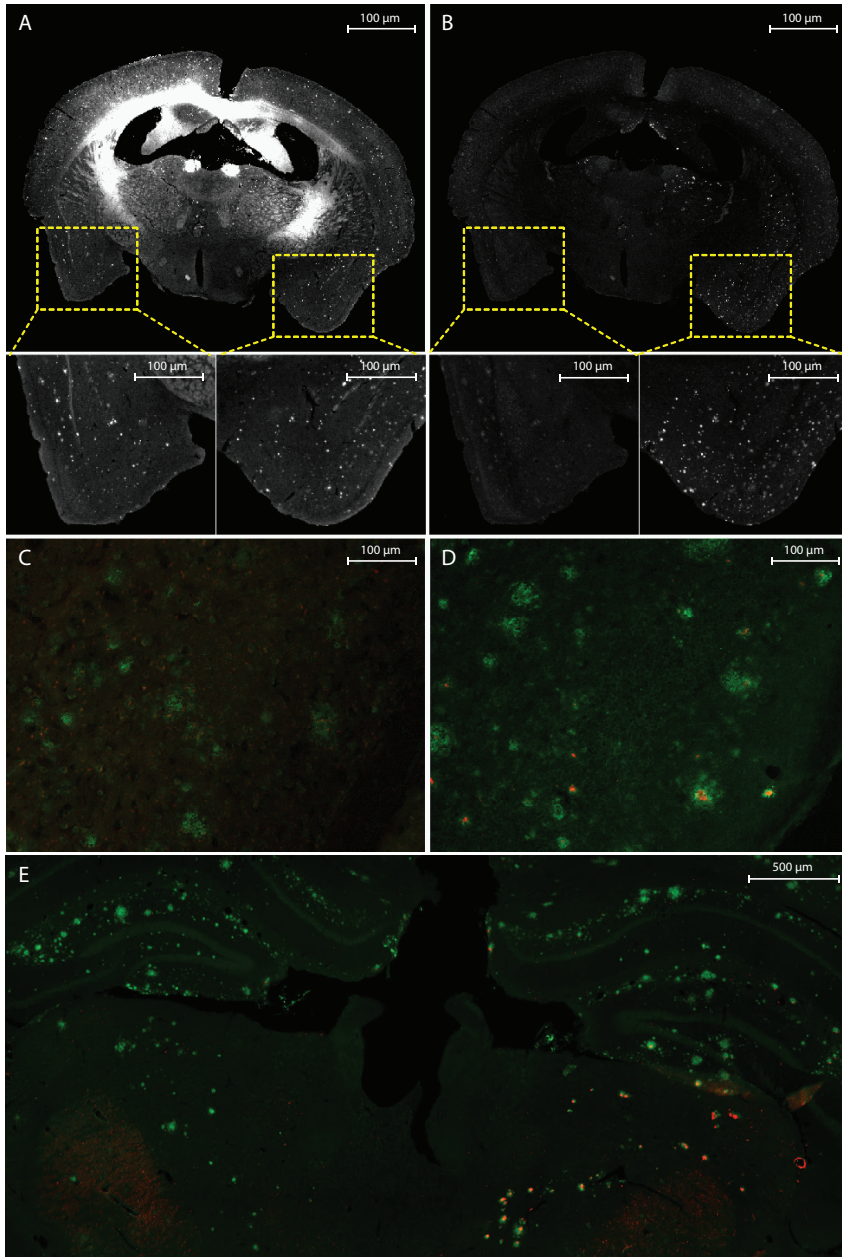


**Figure 9.4 Specific *in vivo* A $\beta$  binding after BBB disruption**

After disruption of the BBB using a co-injection of 15% mannitol with pa2H-Alexa594 into the right carotid artery of an aged APP/PS1 mouse sacrificed 2hrs post injection, amyloid plaques are clearly depicted in both hemispheres using a Thioflavin T (ThT) staining (A), while the pa2H-Alexa594 signal is only detected in the right hemisphere (B). More careful examination shows all Alexa594 signal colocalizes with ThT in the right hemisphere, while in the left only some autofluorescence can be detected. Furthermore, immunofluorescence anti-A $\beta$  staining of the plaques using Alexa488 within the left hemisphere (C) results only in green signal, while within the right hemisphere (D) the red signal from pa2H-Alexa594 nicely colocalizes within the plaques. Experiments performed in a similar setting but sacrificed 24hrs post-injection, showed similar results with pa2H-Alexa594 still nicely corresponding to the green labeling of the anti-A $\beta$  staining within the right hemisphere (E).



**Table 9.4. Blood distribution of <sup>99m</sup>Tc-pa2H**

Sample	Time p.i. (min)	Fraction	APP/PS1		Wildtype	
			(%)	sd	(%)	sd
<sup>99m</sup> Tc-pa2H	10	Plasma	88,9	6,2	80,3	5,2
		Cell Pellet	11,1		19,7	
	90	Plasma	83,6	8,7	72,0	8,2
		Cell Pellet	16,4		28,0	

At different time point after bolus injection of <sup>99m</sup>Tc-pa2H blood collected from the tail vein of 12-14 month old APP/PS1 mice or wildtype littermates. Separated into the cell pellet and plasma, samples were counted for radioactivity. Fractions are expressed in percentage of total activity at that time point. No significant differences were calculated using a student t-test ( $p < 0.05$ ).

**Table 9.5. Quantitative autoradiography**

Brain tissue	Binding of <sup>99m</sup> Tc-VHH <i>ng (± sd)</i>	Competition binding	
		Monomeric A $\beta$	Fibrillar A $\beta$
		<i>ng (± sd)</i>	<i>ng (± sd)</i>
APP/PS1	98.8 (± 20,7)*	60.1 (± 22.2)	31.4 (± 14.3)
Wildtype	86.4 (± 14.8)	56.4 (± 19.5)	27.1 (± 12.5)
AD human	190.1 (± 73.5)*	81.4 (± N.D.)	42.3 (± 29.2)
Control human	102.3 (± 30.2)	27.2 (± N.D.)	49.9 (± 17.4)

Differences in radioactivity were measured after application of 1  $\mu$ g <sup>99m</sup>Tc-pa2H to human and murine APP/PS1 brain sections. \*Statistical difference ( $p < 0.05$ ) between either murine or human control versus A $\beta$  bearing sections.

## Discussion

In this study, we assessed two previously described V<sub>H</sub>H for their potential to cross the blood-brain barrier and distinctively detect vascular and parenchymal A $\beta$  deposits *in vivo*.

### Specific detection of parenchymal and vascular amyloid in APP/PS1 mice

Both V<sub>H</sub>H stained positive for A $\beta$  upon APP/PS1 brain sections confirming appropriate use of this transgenic model. *In vivo* binding to parenchymal and vascular A $\beta$  was confirmed when the BBB was circumvented. Signal remained detectable for at least 24 hours while *in vivo* pa2H showed a high affinity combined with a low off-rate. However, previously shown selectivity for solely vascular A $\beta$  in human post-mortem brain sections by ni3A was not observed within this mouse model. (Figure 9.1, 9.3 and 9.5) Fluorescent or radiolabeling prior *in vivo* application did not affect their specificity. The unique specific reactivity of ni3A for vascular amyloid deposition on human brain material is not yet completely understood.<sup>9</sup> Known differences in morphology and composition of human and murine A $\beta$  deposits might help to understand ni3A's specific reactivity.<sup>21,22</sup> Human plaques consist of discontinuous patches with decreased density and random fibrillar orientation within the amyloid core; murine plaques are generally built up by long organized fibrils, resulting in densely packed amyloid plaques with a relatively large core.<sup>23</sup>

Besides morphological differences, posttranslational modifications of A $\beta$  differ from mouse to man leading to alterations of the A $\beta$  molecule itself.<sup>21,24,25</sup> Differences in metal ion content are known to influence the tertiary structure.<sup>26,27</sup> Previous epitope mapping revealed that ni3A has no other cross reaction but to A $\beta$ <sub>1-42</sub>,<sup>9</sup> which is highly abundant in parenchymal and vascular deposits in both humans and APP/PS1 mice. Altogether, this leads to the conclusion that the selective reactivity of ni3A must depend on the structural presentation of A $\beta$ <sub>1-42</sub>, in which case murine parenchymal plaques probably show structural similarities to human CAA.

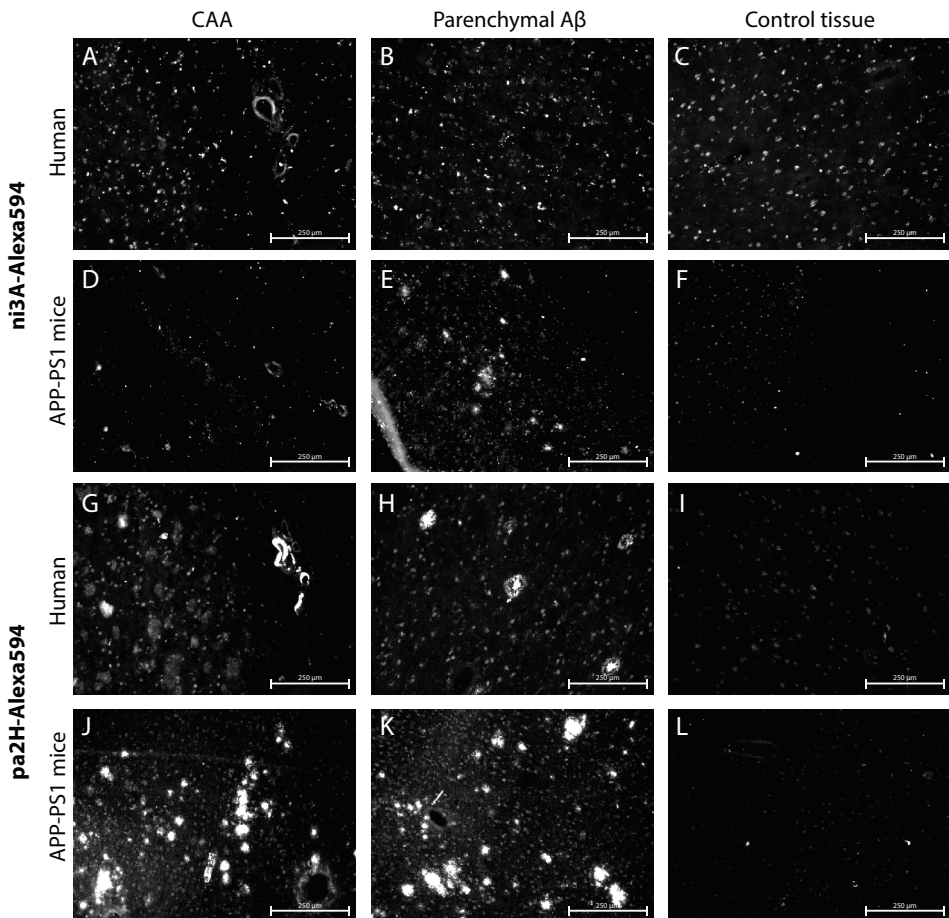


**Figure 9.5 Immunofluorescence with V<sub>H</sub>H-Alexa594**

Shown are the results of immunofluorescence staining with ni3A- and pa2H-Alexa594 on cryosections of APP/PS1 murine and human AD/CAA brain tissue, including wildtype or healthy controls. Both V<sub>H</sub>H stain positive for CAA in all sections (**A,D,G,J**). Only ni3A-Alexa594 stained negative for human parenchymal A $\beta$  (**B**), while pa2H stained positive for several types of parenchymal A $\beta$  deposits (**G,H,J,K**) in both humans and mice. In either human or murine control tissue no such staining patterns were observed (**C,F,I,L**).



### ***In vivo* blood-brain barrier passage**

Previous *in vitro* data suggested that our V<sub>H</sub>H actively migrated across the BBB in a more efficient way than FC5, a V<sub>H</sub>H specifically selected to pass the BBB.<sup>12</sup> However, the *in vivo* experiments resulted only in a small cerebral uptake of the tagged <sup>99m</sup>Tc-pa2H at 24 hours after intravenous administration, and the current brain uptake levels were insufficient to assess the uptake kinetics *in vivo* with for example SPECT imaging. (data not shown) Additional experiments with untagged DTPA(<sup>111</sup>In)-pa2H further confirmed the current limitations as hardly any cerebral uptake was observed with this labeling protocol. The increased brain uptake for <sup>99m</sup>Tc-pa2H compared to DTPA(<sup>111</sup>In)-pa2H may be due to the slower blood clearance for <sup>99m</sup>Tc-pa2H. The observed fast blood clearance and relatively high renal retention for the V<sub>H</sub>H in this study is in line with previous reports<sup>28,29</sup>, and typical for peptides and proteins smaller than the filtering threshold of the glomerular membrane (<60kDa).<sup>30</sup> However, in general, a short blood residential time effectively reduces the blood-to-brain transfer.

*In vivo* studies with the BBB crossing V<sub>H</sub>H FC5 demonstrated 4 %ID/g brain uptake, which is much higher than our findings.<sup>31</sup> This discrepancy may be due to the lower dose that we used, but several other factors may also play a part. For FC5 it is known it uses receptor-mediated endocytosis via the α(2,3)-sialoglycoprotein.<sup>32</sup> For our V<sub>H</sub>H, *in vitro* active transport mechanisms are involved, but the specific receptors are as yet unknown.<sup>12</sup> Possibly, the *in vivo* BBB passage may be limited by the availability of these receptors in our mouse model.

To improve BBB penetration for the amyloid-targeting V<sub>H</sub>H, one could increase the blood circulation time by multimerization or by conjugating the V<sub>H</sub>H to an albumin-targeting moiety or V<sub>H</sub>H.<sup>33,34</sup> An alternative approach would be to incorporate the V<sub>H</sub>H into a BBB-targeting nanoparticle. Recently, several nanoparticle carrier systems have been developed for brain delivery of therapeutics that would also be suitable for loading with V<sub>H</sub>H.<sup>35</sup>

### **Diagnostic and therapeutic value of V<sub>H</sub>H**

In general, V<sub>H</sub>H constitute many unique characteristics that make them interesting tools for either diagnostics or therapeutics. Compared to conventional monoclonal antibodies or Fab', V<sub>H</sub>H express a similar unique level of specificity and affinity, but because of their single domain, production and modification is relatively easy and cost-efficient.<sup>29</sup>

Currently used amyloid-targeting ligands, like <sup>11</sup>C-PiB recognize amyloid plaques rather than Aβ. In contrast, we already showed that V<sub>H</sub>H may be more specific to a certain sub-types of Aβ accumulation.<sup>9</sup> Further selection may allow the *in vivo* detection of the full range of Aβ aggregates from oligomers to dense core plaques to CAA.

Besides diagnostics, several V<sub>H</sub>H have shown their potential therapeutic value *in vitro*, preventing aggregation of amyloid fibrils, oligomeric forms of Aβ and polyA-binding protein nuclear 1.<sup>36-39</sup> In the latter case, even complete clearance of existing aggregates was reported. Whether V<sub>H</sub>H evaluated in this study possess similar abilities is currently under investigation. However, within the data presented here, we observed that several Aβ plaques, as detected by their autofluorescence, could no longer be seen two days after V<sub>H</sub>H application. (**Figure 9.3**)

Whereas current passive immunotherapies targeting A $\beta$  are hampered by unwanted immunogenic side effects, repetitive administration of V<sub>H</sub>H has shown to be non-immunogenic.<sup>4,40</sup> Furthermore, their selective binding to different A $\beta$  species, like ni3A's specific binding for CAA, could shift A $\beta$  brain efflux in the favored direction, which could be used to tailor anti-A $\beta$  therapy to further reduce therapy-induced complications, e.g. CAA related microbleeds.<sup>4,5,41</sup> These initial *in vivo* studies to investigate whether A $\beta$  specific V<sub>H</sub>H can be exploited as diagnostic tools show promising results for further development. Although capable of strong specific binding *in vivo* with low unspecific background binding and favorable wash-out, issues regarding higher brain uptake and clearance need to be addressed in the future.

## References

1. Duyckaerts, C, Delatour, B, and Potier, MC. Classification and basic pathology of Alzheimer disease. *Acta Neuropathol.* 2009; 118:5-36.
2. Smith, EE and Greenberg, SM. Beta-amyloid, blood vessels, and brain function. *Stroke.* 2009; 40:2601-2606.
3. Weller, RO, Preston, SD, Subash, M, et al. Cerebral amyloid angiopathy in the aetiology and immunotherapy of Alzheimer disease. *Alzheimers Res Ther.* 2009; 1:6.
4. Jicha, GA. Is passive immunization for Alzheimer's disease 'alive and well' or 'dead and buried'? *Expert Opin Biol Ther.* 2009; 9:481-491.
5. Greenberg, SM, Bacskai, BJ, and Hyman, BT. Alzheimer disease's double-edged vaccine. *Nat Med.* 2003; 9:389-390.
6. Jack, CR, Jr., Knopman, DS, Jagust, WJ, et al. Hypothetical model of dynamic biomarkers of the Alzheimer's pathological cascade. *Lancet Neurol.* 2010; 9:119-128.
7. Frisoni, GB, Fox, NC, Jack, CR, Jr., et al. The clinical use of structural MRI in Alzheimer disease. *Nat Rev Neurol.* 2010; 6:67-77.
8. Johnson, KA, Gregas, M, Becker, JA, et al. Imaging of amyloid burden and distribution in cerebral amyloid angiopathy. *Ann Neurol.* 2007; 62:229-234.
9. Rutgers, KS, van, RA, van Buchem, MA, et al. Differential recognition of vascular and parenchymal beta amyloid deposition. *Neurobiol Aging.* 2009.
10. Hamers-Casterman, C, Atarhouch, T, Muyldermans, S, et al. Naturally occurring antibodies devoid of light chains. *Nature.* 1993; 363:446-448.
11. Harmsen, MM and De Haard, HJ. Properties, production, and applications of camelid single-domain antibody fragments. *Appl Microbiol Biotechnol.* 2007; 77:13-22.
12. Rutgers, KS, Nabuurs, RJ, van den Berg, SA, et al. Transmigration of beta amyloid specific heavy chain antibody fragments across the *in vitro* blood-brain barrier. *Neuroscience.* 2011.
13. Jankowsky, JL, Slunt, HH, Ratovitski, T, et al. Co-expression of multiple transgenes in mouse CNS: a comparison of strategies. *Biomol Eng.* 2001; 17:157-165.
14. Welling, MM, Paulusma-Annema, A, Balter, HS, et al. Technetium-99m labelled antimicrobial peptides discriminate between bacterial infections and sterile inflammations. *Eur J Nucl Med.* 2000; 27:292-301.
15. Welling, MM, Korsak, A, Gorska, B, et al. Kit with technetium-99m labelled antimicrobial peptide UBI 29-41 for specific infection detection. *Journal of Labelled Compounds & Radiopharmaceuticals.* 2005; 48:683-691.
16. Klunk, WE, Bacskai, BJ, Mathis, CA, et al. Imaging Abeta plaques in living transgenic mice with multiphoton microscopy and methoxy-X04, a systemically administered Congo red derivative. *J Neuropathol Exp Neurol.* 2002; 61:797-805.
17. Skoch, J, Dunn, A, Hyman, BT, et al. Development of an optical approach for noninvasive imaging of Alzheimer's disease pathology. *J Biomed Opt.* 2005; 10:11007.
18. Robbins, EM, Betensky, RA, Domnitz, SB, et al. Kinetics of cerebral amyloid angiopathy progression in a transgenic mouse model of Alzheimer disease. *J Neurosci.* 2006; 26:365-371.
19. Wadghiri, YZ, Sigurdsson, EM, Wisniewski, T, et al. Magnetic resonance imaging of amyloid plaques in transgenic mice. *Methods Mol Biol.* 2005; 299:365-379.
20. Natte, R, Maat-Schieman, ML, Haan, J, et al. Dementia in hereditary cerebral hemorrhage with amyloidosis-Dutch type is associated with cerebral amyloid angiopathy but is independent of plaques and neurofibrillary tangles. *Ann Neurol.* 2001; 50:765-772.
21. Duyckaerts, C, Potier, MC, and Delatour, B. Alzheimer disease models and human neuropathology: similarities and differences. *Acta Neuropathol.* 2008; 115:5-38.
22. Guntert, A, Dobeli, H, and Bohrmann, B. High sensitivity analysis of amyloid-beta peptide composition in amyloid deposits from human and PS2APP mouse brain. *Neuroscience.* 2006; 143:461-475.
23. van Groen, T, Kiliaan, AJ, and Kadish, I. Deposition of mouse amyloid beta in human APP/PS1 double and single AD model transgenic mice. *Neurobiol Dis.* 2006; 23:653-662.
24. Bussiere, T, Bard, F, Barbour, R, et al. Morphological characterization of Thioflavin-S-positive amyloid plaques in transgenic Alzheimer mice and effect of passive Abeta immunotherapy on their clearance. *Am J Pathol.* 2004; 165:987-995.
25. Richardson, JA and Burns, DK. Mouse models of Alzheimer's disease: a quest for plaques and tangles. *ILAR J.* 2002; 43:89-99.

26. Adlard, PA and Bush, AI. Metals and Alzheimer's disease. *J Alzheimers Dis.* 2006; 10:145-163.
27. Leskovicjan, AC, Lanzirrotti, A, and Miller, LM. Amyloid plaques in PSAPP mice bind less metal than plaques in human Alzheimer's disease. *Neuroimage.* 2009; 47:1215-1220.
28. Gaiakam, LO, Huang, L, Cavellers, V, et al. Comparison of the biodistribution and tumor targeting of two 99mTc-labeled anti-EGFR nanobodies in mice, using pinhole SPECT/micro-CT. *J Nucl Med.* 2008; 49:788-795.
29. Huang, L, Muylrdemans, S, and Saerens, D. Nanobodies(R): proficient tools in diagnostics. *Expert Rev Mol Diagn.* 2010; 10:777-785.
30. Behr, TM, Goldenberg, DM, and Becker, W. Reducing the renal uptake of radiolabeled antibody fragments and peptides for diagnosis and therapy: present status, future prospects and limitations. *Eur J Nucl Med.* 1998; 25:201-212.
31. Muruganandam, A, Tanha, J, Narang, S, et al. Selection of phage-displayed llama single-domain antibodies that transmigrate across human blood-brain barrier endothelium. *FASEB J.* 2002; 16:240-242.
32. Abulrob, A, Sprong, H, Van Bergen en, HP, et al. The blood-brain barrier transmigrating single domain antibody: mechanisms of transport and antigenic epitopes in human brain endothelial cells. *J Neurochem.* 2005; 95:1201-1214.
33. Coppieters, K, Dreier, T, Silence, K, et al. Formatted anti-tumor necrosis factor alpha V<sub>H</sub>H proteins derived from camelids show superior potency and targeting to inflamed joints in a murine model of collagen-induced arthritis. *Arthritis Rheum.* 2006; 54:1856-1866.
34. Tijnk, BM, Laeremans, T, Budde, M, et al. Improved tumor targeting of anti-epidermal growth factor receptor Nanobodies through albumin binding: taking advantage of modular Nanobody technology. *Mol Cancer Ther.* 2008; 7:2288-2297.
35. Koffie, RM, Farrar, CT, Saidi, LJ, et al. Nanoparticles enhance brain delivery of blood-brain barrier-impermeable probes for *in vivo* optical and magnetic resonance imaging. *Proc Natl Acad Sci U S A.* 2011; 108:18837-18842.
36. Chartier, A, Raz, V, Sterrenburg, E, et al. Prevention of oculopharyngeal muscular dystrophy by muscular expression of Llama single-chain intrabodies *in vivo*. *Hum Mol Genet.* 2009; 18:1849-1859.
37. Dumoulin, M, Last, AM, Desmyter, A, et al. A camelid antibody fragment inhibits the formation of amyloid fibrils by human lysozyme. *Nature.* 2003; 424:783-788.
38. Lafaye, P, Achour, I, England, P, et al. Single-domain antibodies recognize selectively small oligomeric forms of amyloid beta, prevent Abeta-induced neurotoxicity and inhibit fibril formation. *Mol Immunol.* 2009; 46:695-704.
39. Verheesen, P, de, KA, van, KS, et al. Prevention of oculopharyngeal muscular dystrophy-associated aggregation of nuclear polyA-binding protein with a single-domain intracellular antibody. *Hum Mol Genet.* 2006; 15:105-111.
40. Stijlemans, B, Conrath, K, Cortez-Retamozo, V, et al. Efficient targeting of conserved cryptic epitopes of infectious agents by single domain antibodies. African trypanosomes as paradigm. *J Biol Chem.* 2004; 279:1256-1261.
41. Klunk, WE, Lopresti, BJ, Ikonovic, MD, et al. Binding of the positron emission tomography tracer Pittsburgh compound-B reflects the amount of amyloid-beta in Alzheimer's disease brain but not in transgenic mouse brain. *J Neurosci.* 2005; 25:10598-10606.

---

## PART TWO | Development of Molecular Imaging strategies

1 Department of Radiology, Leiden University Medical Center, Leiden, Netherlands

2 Department of Bioorganic Synthesis, Leiden Institute of Chemistry, Leiden University, Leiden, Netherlands

3 Radionucleotide Laboratory, Free University, Amsterdam, Netherlands

4 Division of Drug Delivery Technology, Leiden Academic Center for Drug Research, Leiden University, Netherlands

5 Department of Human Genetics, Leiden University Medical Center, Leiden, Netherlands

---

# Chapter 10

## Polyfluorinated bis-styrylbenzenes as amyloid- $\beta$ plaque binding ligands

*adapted from Bioorg Med Chem 2014, doi: 10.1016/j.bmc.2014.02.054*

**Rob J.A. Nabuurs<sup>1</sup>**

Varsha V. Kapoerchan<sup>2</sup>

Athanasios Metaxas<sup>3</sup>

Sanne de Jongh<sup>1</sup>

Maaïke de Backer<sup>1</sup>

Mick M. Welling<sup>1</sup>

Wim Jiskoot<sup>4</sup>

Albert D. Windhorst<sup>3</sup>

Hermen S. Overkleeft<sup>2</sup>

Mark A. van Buchem<sup>1</sup>

Mark Overhand<sup>2</sup>

Louise van der Weerd<sup>1,5</sup>



## Abstract

Detection of cerebral  $\beta$ -amyloid ( $A\beta$ ) by targeted contrast agents remains of great interest to aid the *in vivo* diagnosis of Alzheimer's disease (AD). Bis-styrylbenzenes have been previously reported as potential  $A\beta$  imaging agents. To further explore their potency as  $^{19}\text{F}$  MRI contrast agents we synthesized several novel fluorinated bis-styrylbenzenes and studied their fluorescent properties and amyloid- $\beta$  binding characteristics. The compounds showed a high affinity for  $A\beta$  plaques on murine and human brain sections. Interestingly, competitive binding experiments demonstrated that they bound to a different binding site than chrysamine G. Despite their high  $\log P$  values, many bis-styrylbenzenes were able to enter the brain and label murine amyloid *in vivo*. Unfortunately initial post-mortem  $^{19}\text{F}$  NMR studies showed that these compounds as yet do not warrant further MRI studies due to the reduction of the  $^{19}\text{F}$  signal in the environment of the brain.



## Introduction

Alzheimer's disease (AD) is the predominant form of dementia in the aging population. The disease is marked by neuronal degeneration associated with deposits of tau proteins in intraneuronal neurofibrillary tangles (NFTs) and of amyloid- $\beta$  ( $A\beta$ ) peptides in extracellular amyloid plaques.<sup>1</sup> Although the precise role of amyloid in AD pathology is still not completely understood, accumulation of amyloid plaques is thought to precede the onset of the first clinical symptoms by up to two decades.<sup>2,3</sup> A clinical imaging technique capable of visualizing and quantifying these early changes thus may enable early diagnosis and better understanding of the pathophysiology.

Over the past years progress has been made in the development of  $A\beta$ -targeting imaging ligands suitable for visualization by positron emission tomography (PET), single positron emission tomography (SPECT), fluorescence microscopy or magnetic resonance imaging (MRI).

For clinical use, the [ $^{11}\text{C}$ ]-benzothiazole derivative Pittsburgh compound B (PiB, **1**, **Figure 10.1**) is the best characterized *in vivo* PET radiotracer. However, as the short half-life of  $^{11}\text{C}$  limits its use to medical centers with an on-site cyclotron, alternatives are desired. Therefore, several longer-lived  $^{18}\text{F}$  radiofluorinated derivatives have been designed, like flutemetamol (**2**)<sup>4</sup>, florbetapir (**3**) and florbetaben(**4**)<sup>5</sup>, of which the first two recently have been the first to be admitted for commercial use with the last one expected to follow soon thereafter.<sup>6,7</sup> Despite the inherent high sensitivity of PET, the development of  $A\beta$ -targeted imaging probes suitable for clinical MRI remains attractive as this would lower the threshold for performing amyloid scans given the wider availability of MRI systems as compared to PET systems, the lack of ionizing irradiation and the lower costs involved in performing clinical MRI as compared to PET. Furthermore, such agents could be used in one scan session comprising a comprehensive structural and functional scan protocol as well as a scan to detect the molecular imaging tracers, whereas one PET examination only provides one biomarker.

Based on congo red (**5**), several bis-styrylbenzenes have been reported to show strong  $A\beta$  binding affinities and serve as potential backbones for *in vivo* PET or SPECT imaging probes, like **6** (chrysamine G), **7** (X-34)<sup>8</sup>, **8** (ISB)<sup>9</sup> and **10** (Methoxy-X04)<sup>10</sup> (**Figure 10.1** and **Scheme 10.1**). The styrylbenzene backbone has also been explored for the development as an MRI contrast agent. The initial breakthrough came with the design of compound **9** (FSB), which was specifically designed for *in vivo* detection of  $A\beta$  using  $^{19}\text{F}$  MRI.<sup>11</sup> Since normal biological tissue completely lacks fluorine,  $^{19}\text{F}$  MRI would allow direct imaging of the amyloid binding compound, without any endogenous background signal ('hot spot imaging'). Initial *in vivo* animal studies with compound **9** showed promising results. Unfortunately,  $^{19}\text{F}$  MRI *in vivo* experiments suffer from the inherently low sensitivity of MRI with a detection limit in the micromolar to millimolar range depending merely on the voxel size and magnetic field strength. As initial  $^{19}\text{F}$  compound only carried a single fluorine atom this makes  $^{19}\text{F}$  MRI a technical challenge requiring long acquisition times. The incorporation of multiple magnetically equivalent  $^{19}\text{F}$  atoms could aid with respect to this aspect, as the spin of each individual  $^{19}\text{F}$  nucleus directly adds to the MR signal. The study therefore aimed to further exploit the bis-styrylbenzene backbone as a specific amyloid- $\beta$  targeting MR contrast agent by increasing the number of fluorine atoms positioned to maintain favorable NMR characteristics as well as solubility.

Synthesized compounds were evaluated with respect to their A $\beta$  binding and specificity, and their fluorescent properties. Partition coefficients (logP) were determined to assess hydrophobicity. Compounds were injected systemically in transgenic AD mice to determine BBB passage and affinity for amyloid plaques *in vivo*. For the most promising compound, *in vitro* and post-mortem  $^{19}\text{F}$  NMR studies were performed.

## Design

Previously Flaherty *et al.* have designed a similar series of polyfluorinated compounds, based on a bis-styrylbenzene structure with either a non-substituted core with fluorine substitutions on the outer rings, or four  $^{19}\text{F}$  atoms on the inner ring with a polar substituent on the outer ring.<sup>12</sup> These compounds were found to target A $\beta$  *in vivo*. As was already proven for Methoxy-X04

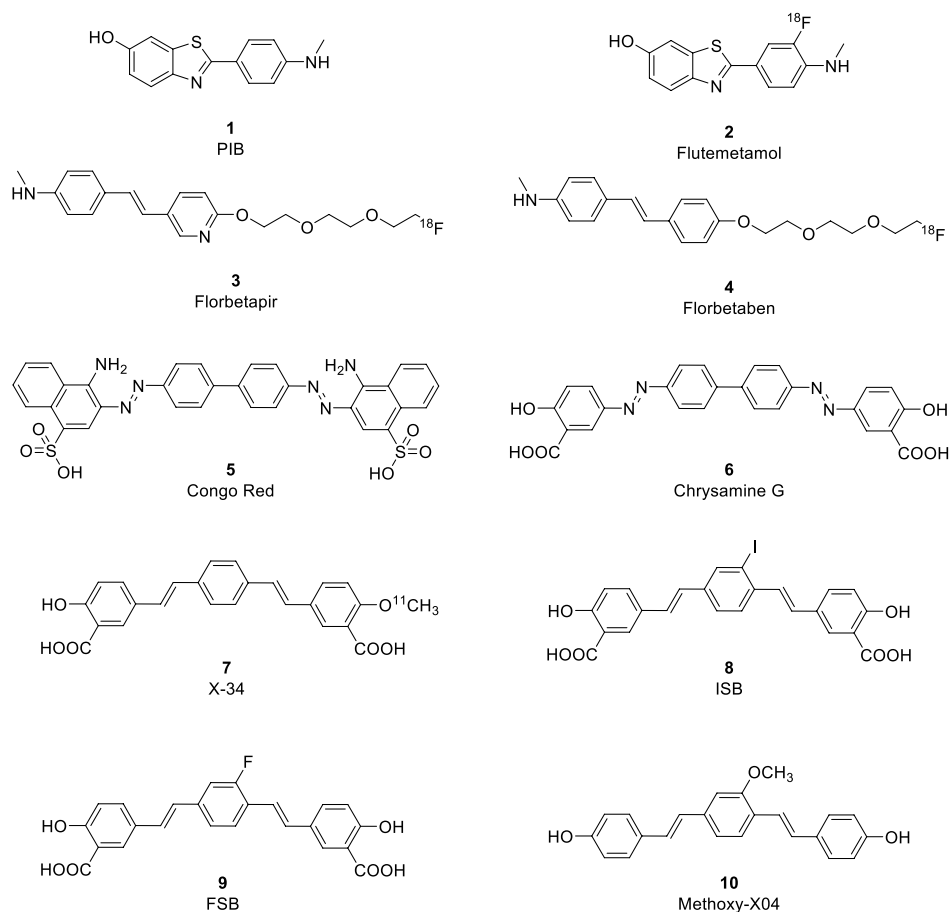
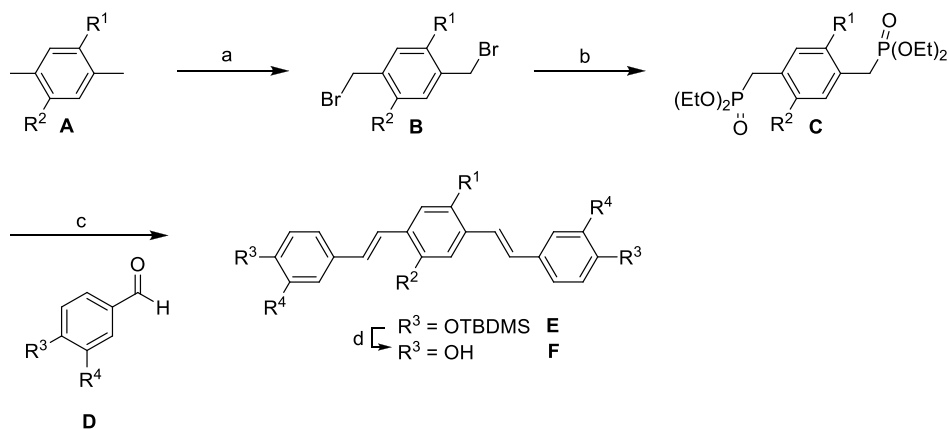


Figure 10.1 Previously reported amyloid- $\beta$  binding ligands

Scheme 10.1 General synthesis route of envisioned fluorinated bis-styrylbenzenes



	$\text{R}^1$	$\text{R}^2$	$\text{R}^3$	$\text{R}^4$
10 (Methoxy-X04)	OMe	H	OH	H
11	OMe	OMe	OH	H
12	OMe	H	$\text{CH}_2\text{OH}$	H
13	OMe	H	$\text{CF}_3$	H
14	OMe	H	$\text{OCF}_3$	H
15	OMe	H	$\text{CF}_2\text{CF}_2\text{H}$	H
16	OH	H	$\text{CF}_3$	H
17	OH	H	$\text{OCF}_3$	H
18	OH	H	$\text{CF}_2\text{CF}_2\text{H}$	H
19	$\text{CF}_3$	H	OH	H
20	$\text{OCH}_2\text{CF}_3$	H	OH	H
21	$\text{O}(\text{CH}_2)_3\text{CF}_3$	H	OH	H
22	$\text{OC}(\text{CF}_3)_3$	H	OH	H
23	OH	H	OMe	$\text{CF}_3$
24	OMe	H	OMe	$\text{CF}_3$

Reagents and conditions: **a**) N-bromosuccinimide, benzoyl peroxide,  $\text{CCl}_4$ , reflux, 16 h. **b**) Triethyl phosphite, 150 °C, 16 h. **c**) 1. KOtBu or NaH, THF, -10 or 0 °C, 20 min. then D, rt, 16 h. **d**) tetra-n-butylammonium fluoride, THF, 0 °C, rt, 16 h.

(**10**), acidic functional groups are not required for high affinity  $\text{A}\beta$  binding, with the apparent  $K_d$ 's of these fluorinated compounds being  $\sim 300$  fold lower compared to **9**. Despite their ability to label amyloid *in vivo*, however, the Flaherty compounds are very hydrophobic, and therefore their solubility and blood-brain barrier (BBB) passage are likely to limit their full potential as a  $^{19}\text{F}$  MRI agent. Furthermore, positioning of the  $^{19}\text{F}$  group directly on the planar backbone may have a detrimental effect on its relaxometry following binding, while it has been suggested that in addition to the inherent sensitivity of MRI also  $^{19}\text{F}$  relaxivity plays an important role in the

detection, due to a reduction of the transverse relaxation time ( $T_2$ ) caused by binding to amyloid, or by a hydrophobic environment like brain tissue.<sup>13</sup> Therefore, we set out to extend the existing bis-styrylbenzene library by adding one or more polar moieties to improve solubility and increase the number of (magnetically equivalent) fluorine atoms positioned such to maintain favorable NMR characteristics.

As a starting point, Methoxy-X04 (**10**) was chosen.<sup>10</sup> With an affinity for A $\beta$  in the nanomolar range ( $K_i = 26.8$  nM), this fluorescent small molecule is frequently used for intravital microscopy studies as it has high affinity for A $\beta$  plaques *in vivo* following intravenous or intraperitoneal injection.<sup>14</sup> We designed a series of bis-styrylbenzenes with incorporating multiple preferably magnetically equivalent fluorine atoms (**11 – 24**) or additional minor modifications. (**Scheme 10.1**)

Compounds **11 – 24** are accessible from the general synthesis route given in **Scheme 10.1**, with the key building blocks being a diphosphonate (**C**) and an aromatic aldehyde (**D**). Substituted p-xylene (**A**) is subjected to radical bromination to yield dibromide (**B**). This dibromide is then treated with triethyl phosphite in an Arbuzov reaction to give diphosphonate (**C**). A Horner-Wadsworth-Emmons (HWE) reaction between diphosphonate (**C**) and an aldehyde (**D**) yields the (E, E)-bis-styrylbenzene (**E**). If necessary, an additional deprotection step with TBAF is carried out to remove the silyl protecting groups (only in the cases where the final compounds have hydroxyl substituents). Independently, a similar synthesis route for the design of NFT and amyloid probes based on styrylbenzenes was recently published by Boländer *et al.*<sup>15</sup>

The building blocks needed for the synthesis of compounds **10 – 24** are depicted in **Figure 10.2**, and were synthesized or commercially available. (For synthesis of all building blocks, see **Appendix I**).

## Results and Discussion

### Fluorescent properties

All synthesized compounds are expected to have fluorescent properties based on their conjugated ring structures. We therefore determined excitation and emission wavelengths of 300 nM solutions and the corrected emission intensities were compared to that of Methoxy-X04. (**Table 10.1**)

It has been reported that binding to amyloid may have a significant effect on fluorescence properties<sup>16</sup>, and therefore the fluorescence was also measured in the presence of synthetic A $\beta$  fibrils. The parent compound **10** showed the highest intrinsic fluorescence with a 10-fold increase in the presence of amyloid fibrils. A similar increase was typically only observed for those compounds that only had minor modifications on the outer rings. Several previously reported A $\beta$ -targeting fluorophores have shown a clear red-shifted emission spectrum following binding.<sup>17,18</sup> Some of our compounds showed a similar red-shift; though resulting in multiple emission peaks in the spectrum. (**Figure 10.3**) This observation suggests the presence of multiple binding sites, similar to what has previously been reported, for example for Thioflavin.<sup>19</sup>

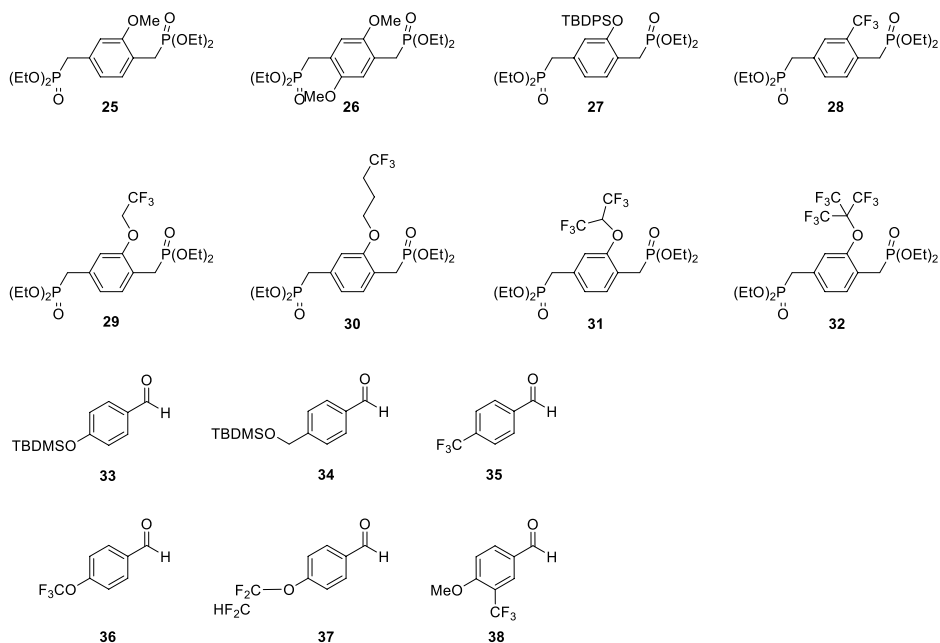


Figure 10.2 Structures of the building blocks 25-38

### Qualitative assessment of human and murine amyloid plaques binding

Fluorescence microscopy was used for a qualitative assessment of the amyloid-binding properties. A concentration series of each compound (1 – 10 – 100  $\mu$ M) was applied to brain slices of APP/PS1 mice and human AD patients. At 100  $\mu$ M all compounds, except **11** and **21**, showed characteristic staining of amyloid plaques on both human and murine sections. At the lower concentrations, however, clear differences in affinity were found. (**Table 10.1** and **Figure 10.4**) Amyloid plaques in humans and mice differ in composition and compactness.<sup>20</sup> This is likely the reason that all compounds showed higher affinity for murine plaques as they were visible even after staining with 1  $\mu$ M concentration, whereas compounds **19** – **21** and **23** – **24** showed no detectable amyloid plaques in the human sections at this concentration. To illustrate these differences, **Table 10.1** and **Figure 10.4** highlight the results of the 10  $\mu$ M staining on human sections and the 1  $\mu$ M concentration used to stain the murine sections. In general, planarity is considered one of the criteria for binding to A $\beta$  plaques.<sup>21</sup> The introduction of an additional substitution on the middle ring, which disturbs the planar conformation, has a detrimental effect on the binding affinity, as virtually no binding was seen using **11**. Although previous studies have reported possible interaction of styrylbenzenes with NFTs<sup>15</sup>, for none of our compounds NFTs staining was observed in the human AD cortex at these concentrations. Furthermore, with no background staining in either human or murine control brain sections this suggested their specificity to amyloid. As stated in the previous paragraph, the fluorescence intensity with and without amyloid fibrils differed significantly for the various compounds. Therefore, the fluorescence intensity in the presence of fibrils was calculated and expressed relative to the intensity of Methoxy-X04 (**10**). (**Table 10.1**)

Table 10.1 Fluorescent and binding characteristics

Compound	MW	Ex vivo A $\beta$ binding <sup>a</sup>		$\lambda_{\text{em}}^{\text{b}}$	$\lambda_{\text{ex}}^{\text{b}}$	Fluorescence intensity <sup>c</sup>	Fluorescence intensity on binding to fibrillar A $\beta^{\text{d}}$	Increase on binding to fibrillar A $\beta$	K <sub>i</sub>
	(da)	Human	Murine	(all $\pm$ 1nm)	(all $\pm$ 1nm)	(%)			(nM)
10	344,403	+	+	372	451	100	100	9.8	24.2
11	374,429	-	-	<i>n.d.</i>	<i>n.d.</i>	<i>n.p.</i>	<i>n.p.</i>	<i>n.p.</i>	<i>n.d.</i>
12	372,456	+	++	360	436	63	26	4.1	<i>n.d.</i>
13	448,400	+	++	356	471	9	1	~1	<i>n.d.</i>
14	480,399	+	++	354	456	31	3	~1	<i>n.d.</i>
15	544,433	+	++	354	456	10	1	~1	<i>n.d.</i>
16	434,374	++	++	351	464	6	2	3.6	<i>n.d.</i>
17	466,372	++	++	331	458	17	13	7.4	<i>n.d.</i>
18	530,407	++	++	325	487	7	<i>n.d.</i>	<i>n.d.</i>	<i>n.d.</i>
19	382,375	-	++	354	466	18	19	10.7	244
20	412,401	-	+	360	450	16	7	4.1	39.3
21	440,454	-	-	360	465	5	2	4.3	56.4
22	548,397	++	++	355	472	21	38	17.8	84.48
23	494,426	-	++	355	472	17	2	~1	<i>n.d.</i>
24	508,452	-	++	355	494	37	4	~1	<i>n.d.</i>

<sup>a</sup> Staining of amyloid plaques in human (10  $\mu\text{M}$ ) and APP-PS1 murine (1  $\mu\text{M}$ ) was scored whether the compound stained less (-), similar (+) or more (++) for amyloid plaques in comparison to 10. <sup>b</sup> ExEm wavelength maxima were determined of 300 nM solutions. <sup>c</sup> Fluorescence intensity was calculated relative to 10. <sup>d</sup> Fluorescence intensity was calculated relative to intensity of 10 after binding to fibrillar A $\beta$ . *n.d.* = not detected; *n.p.* = not performed

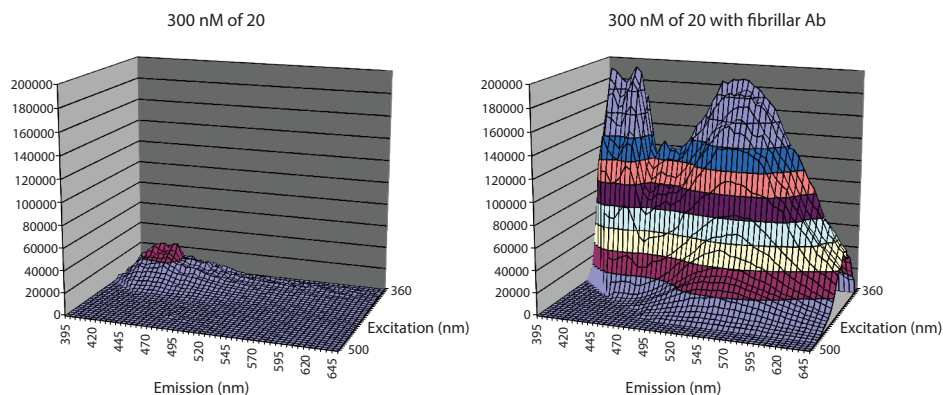


**Figure 10.3** Excitation and emission spectra of compound **22**

Shown are the excitation/emission spectra of compound **22** to illustrate possible effects on the fluorescent properties following binding of amyloid.

Assuming that the fluorescence yield in the presence of synthetic A $\beta$  is representative for that in the presence of amyloid plaques, the data in **Figure 10.4** can be interpreted as follows. Despite having a lower fluorescent intensity for the bound compound, compounds **16 – 18** and **22** labeled more human amyloid, thus suggesting an improved binding compared to Methoxy-X04. Similar analysis of the stained APP/PS1 sections revealed the affinity of all compounds, except **11** and **21**, to be significantly higher than that of our lead compound Methoxy-X04 ( $K_d$  26.8 nM). Compounds **13** and **15** were found to have the most efficient binding properties for murine amyloid plaques. With the lowest fluorescent intensity after binding to amyloid, being 100 x less than Methoxy-X04, the murine amyloid plaques nonetheless appeared very bright.

#### Affinity for synthetic amyloid- $\beta$ fibrils

A competition assay with [ $^3$ H]chrysamine G (**6**) was used to determine the binding inhibition coefficient ( $K_i$ ) for the compounds. Based on this assay reproducible results could only be obtained for those compounds with a hydroxyl substituent on the outer rings. (**Figure 10.5**) The *ex vivo* stainings clearly showed that many of the other compounds show affinity for amyloid, implying that these compounds probably use different binding sites than chrysamine G. Even the provided  $K_i$  values for compounds **19 – 23** only reflect competition against the [ $^3$ H] chrysamine G binding sites, and therefore most likely underestimate the overall affinity of these compounds for synthetic A $\beta$  fibrils.

#### LogP values

The blood-brain barrier (BBB) is a tight layer of endothelial cells in the wall of cerebral blood vessels that limits the passage of blood compounds into the brain. It is traditionally stated that for optimal passive BBB passage, compounds should preferably have moderately hydrophobicity (logD or logP 2.0 - 3.5) however a number of successful radiopharmaceuticals do not meet this requirement.<sup>22</sup> Therefore LogP or LogD should be considered carefully as selection criterion,

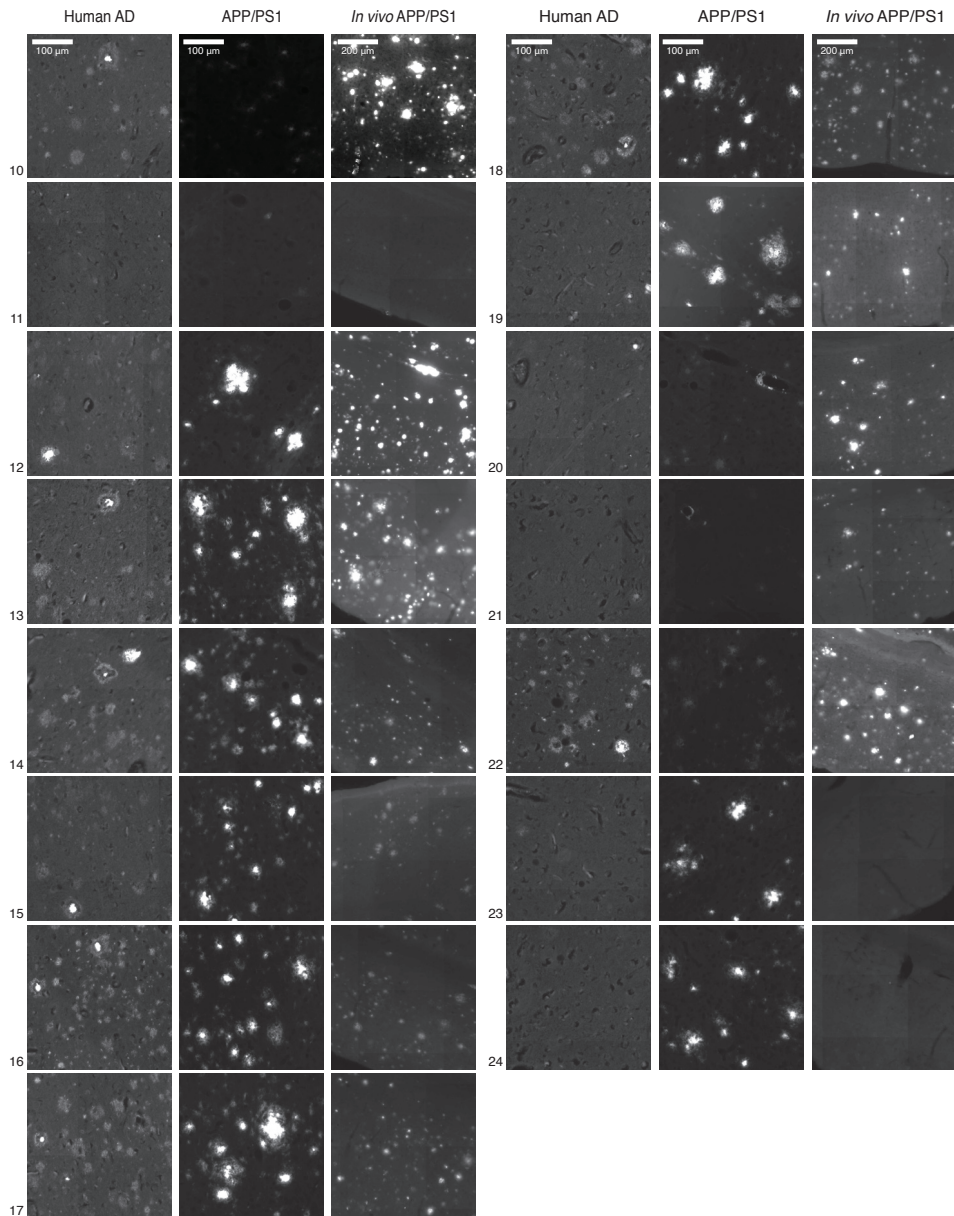


**Figure 10.4 Staining for murine and human amyloid plaques**

Shown paraffin embedded 8 μm thick human AD sections are stained using 10 μM, whereas APP/PS1 murine sections are stained using 1 μM to best depict the differences in amyloid staining between the different compounds. Thirty micrometer thick murine APP/PS1 sections following *in vivo* administration are shown with two times less magnification to allow visualization of a larger cortical region. All images were digitized using the same settings.



but it is a valid parameter for selection nonetheless when applied within one series of compounds. For each of our compounds **10** – **24**, logP values were determined with an HPLC-based method according to Benhaim *et al.*<sup>23-25</sup> The found logP values are shown in **Table 10.2**. The limitation of this method is that logP values > 7 cannot be measured reliably. Not surprisingly, many of the compounds actually do show logP values > 7, which is a logical consequence of the fact that Methoxy-X04 (**10**) itself already has a logP value of 5.05 and that the introduction of fluorine makes the molecules more hydrophobic.

### ***In vivo* amyloid plaque labeling in transgenic AD mice**

To assess the ability of the compounds to pass the BBB *in vivo* and subsequently bind to amyloid, solutions of each compound were injected intravenously in living transgenic APP/PS1 mice that had extensive cerebral amyloid plaques. The mice were sacrificed, their brains were removed and post-mortem sections were studied using the same fluorescence microscopy set-up as for the stained brain sections. *In vivo* labeling of amyloid plaque was observed for almost all compounds, except **11**, **23** and **24**, showing their ability to pass the BBB. (**Figure 10.4** and **Table 10.2**) Apparently, a high logP value does not necessarily prohibit BBB passage. Some compounds, particularly **13**, showed a comparable signal intensity after intravenous injection compared to Methoxy-X04, despite having a 100-fold lower fluorescence yield. This suggests that these compounds have a high affinity and/or cross the BBB more efficiently than Methoxy-X04.

**Table 10.2** LogP values and *in vivo* amyloid labeling

Compound	logP (calc) <sup>a</sup>	logP (determined)	<i>In vivo</i> amyloid labeling
10	5.55	4.84	+
11	5.46	5.00	-
12	5.53	4.99	+
13	9.06	>7	+
14	8.44	>7	+
15	10.04	>7	+
16	8.74	6.18	+
17	8.12	>7	+
18	9.72	>7	+
19	6.74	5.64	+
20	6.82	5.25	+
21	7.37	5.79	+
22	10.22	>7	+
23	8.57	7.17	-
24	8.89	>7	-

<sup>a</sup>LogP values were calculated used web-based methods: [www.molinspiration.com](http://www.molinspiration.com) and <http://intro.bio.umb.edu/111-112/OLLM/111F98/jlogp/test.html>. The ability to label amyloid plaques in the brains of APP-PS1 mice following intravenous injection were scored absent (-) or present (+).

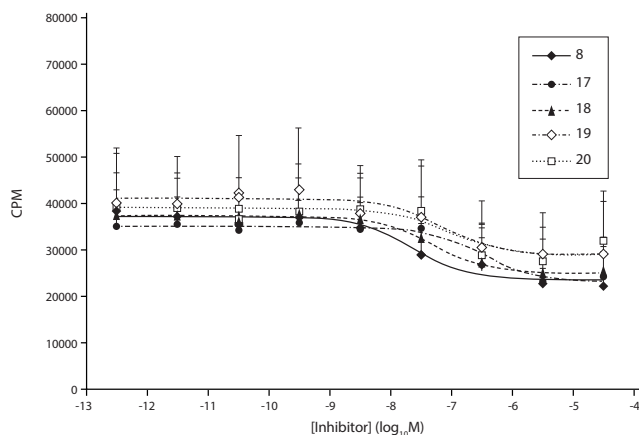


**Figure 10.5 Binding competition with chrysamine G**

Non-linear fitting to assess affinity for synthetic amyloid- $\beta$  fibrils by a competition assay with [ $^3\text{H}$ ]chrysamine G.

### *In vitro* and post-mortem fluorine NMR

Based on the above experiments, compounds **13** and **22** were identified as the most promising leads, based on favorable binding, and positive staining after intravenous injection *in vivo* indicating good BBB passage. Initial  $^{19}\text{F}$  NMR studies were only conducted with compound **22**, which had the highest number of magnetically equivalent  $^{19}\text{F}$  atoms. NMR spectra were acquired for 1.92 mM of **22** with or without an excessive amount of fibrillar A $\beta$ . Binding to fibrillar amyloid did not result in significant line broadening of the NMR spectrum. (**Figure 10.6A**) The NMR spectrum corresponding to compound **22** mixed with homogenized APP/PS1 brain, however, revealed a small chemical shift of 0.03 ppm and a severe reduction in  $T_2$  as observed by the line broadening of the peak. As suggested previously, most likely the lipophilic environment of the brain tissue itself results in a reduced relaxation time and thereby signal loss.<sup>13</sup>

Finally, 30  $\mu\text{mol/kg}$  of **22** was injected intravenously in APP/PS1 mice. The brains were removed after 24 hours and a  $^{19}\text{F}$  NMR spectrum was obtained of the brain homogenate. No  $^{19}\text{F}$  signal was observed, although antemortem intravital microscopy showed clear labeling of cerebral amyloid. (**Figure 10.6B-C**)

The severe attenuation of the  $^{19}\text{F}$  NMR signal due the hydrophobic nature of both the fluorinated compounds as well as the brain itself seemed to hampered the detection of the  $^{19}\text{F}$  signal in the mouse brain. This is contrary to the initial publication of a  $^{19}\text{F}$  amyloid ligand by Higuchi *et al.*<sup>11</sup>, but in agreement with the findings of Amatsubo *et al.*<sup>13</sup> Our design balanced between the planarity needed for amyloid binding and free rotation for the fluorine groups to maintain favourable NMR characteristics, however, this data still suggests that the hydrophobic interaction between the brain and the  $^{19}\text{F}$  groups are responsible for line broadening. As recently pointed out *in vivo* by Yanagisawa *et al.* this problem might be overcome by the use of a polyethylene glycol (PEG) linker to attach the fluorine groups further away from the amyloid binding core.<sup>26</sup>

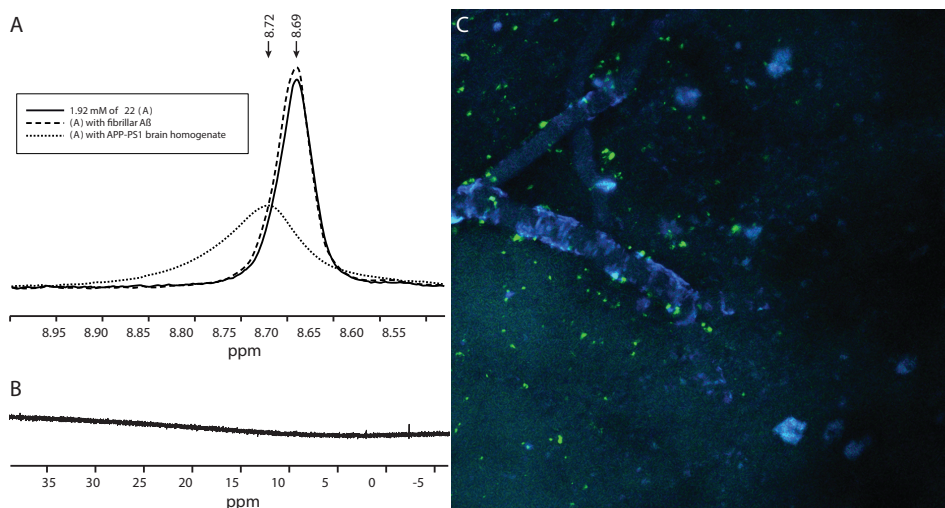


**Figure 10.6** *In vitro* and post-mortem  $^{19}\text{F}$  NMR analyses of compound **22**

(A) shows the NMR spectra corresponding to 1.92 mM of compound **22** in solution without (-) or with the presence of 22  $\mu\text{M}$  fibrillar A $\beta$  (- -) or mixed with a homogenized aged APP/PS1 mouse brain. All spectra are relative to trifluoroacetic acid set at 0 ppm. In (B) shows a NMR spectra of a homogenized APP/PS1 mouse brain made 24 hours post-injection of 30  $\mu\text{mol}/\text{kg}$  of dissolved **22**. The corresponding intravital microscopic image presented in (C) clearly shows the antemortem labeling of cerebral amyloid (blue) in both vasculature as well as parenchymal amyloid plaques. Image dimensions are 615 x 615  $\mu\text{m}$ .

## Summary and conclusion

In this work, a series of 15 analogs of Methoxy-X04 (**10**) with various number of fluorine atoms has been synthesized and evaluated for their A $\beta$  binding properties and ability to pass the BBB. The incorporation of suitably placed fluoro substitutions could improve the current (MRI) contrast agents for the diagnosis of Alzheimer's disease. It was concluded that the introduction of a second substitution on the inner ring was not well tolerated, whereas single bulky modifications on both the outer and inner rings were well tolerated. Despite the observed high logP values brain entry did not seem to be inhibited for most compounds. Based on all findings, compounds **13** and **22** were considered most promising for the development of A $\beta$  imaging agents. However, the post-mortem NMR results leave us to conclude that there seems to be no role for these compounds as MR imaging agents for the diagnosis of AD. To our opinion it remains doubtful whether the incorporation of other fluorine moieties or higher field magnetic field strength will help to overcome these hurdles next to those set by the inherent relatively low sensitivity of  $^{19}\text{F}$  MRI in combination with known cerebral A $\beta$  concentrations.

Nevertheless, this study expands the existing knowledge on bis-styrylbenzenes as amyloid targeting agents in general and creates opportunities for their application as fluorescent amyloid ligands for preclinical optical imaging. Recent advances in fluorine chemistry create further opportunities to radiolabel compounds of our series with  $^{18}\text{F}$ .<sup>27,28</sup> These compounds might provide additional information regarding accumulation of cerebral amyloid, especially since we have found that our series of compounds bind to a distinct binding site.

## Materials and Methods

### Preparation of A $\beta$ <sub>1-40</sub> fibrils

A $\beta$  fibrils were prepared by stirring a 0.5 mg/ml solution of A $\beta$  peptide (1-40) (RPeptide, Bogart, GA) at 37 °C for 3 days, which resulted in a cloudy solution. The presence of fibrils was confirmed by the appearance of an emission peak at 482 nm (excitation 440 nm) upon addition of a 5  $\mu$ M solution in PBS of Thioflavin T (Sigma, Germany) to a small amount of fibrils. Aliquots of 10  $\mu$ L were transferred to Eppendorf vials and stored at -80 °C until the assay was to be performed.

### Fluorescence spectra

All compounds were dissolved in DMSO at 0.3 mM and diluted to 300nM with 9:1 PBS:ethanol. Fluorescence spectra were measured on a Varian Cary Eclipse fluorescence spectrophotometer to obtain peak excitation and emission wavelengths, which were used to select the correct fluorescence filter settings for further microscopic evaluation. All measurements were carried out at 20 °C and in triplicate. 3D fluorescence spectra were obtained by adding 500  $\mu$ L of the dissolved compounds to previously prepared A $\beta$  aliquots. After manual shaking for 30 sec, 300  $\mu$ L samples were measured (Infinity M1000, Tecan, Switzerland).

### Staining of human and transgenic AD brain sections

Stock solutions of 3 mM in DMSO were diluted to 1 – 10 – 100  $\mu$ M in 2:3 PBS:ethanol and sonicated for 15 minutes. Paraffin sections (8  $\mu$ m) of the medial temporal lobe cortex of human AD subject that was assigned as Braak IV, 14 months old transgenic murine APP/PS1 brain and age-matched control cortices were deparaffinized prior to staining for 10 minutes in absolute darkness. After gently rinsing with tap water, sections were placed in 0.1 % NaOH in 80% ethanol for 2 minutes, air dried and coverslipped using Aqua / Polymount. Fluorescence of the stained sections was analyzed using a whole microscopic slide scanner (Pannoramic MIDI, 3DHitech, Hungary) with a DAPI filter cube (Ex 365 nm; Em 445/50 nm) using the same intensity setting throughout all experiments.

### *In vivo* A $\beta$ plaque labeling in transgenic AD mice

Twelve-to-fourteen-month-old APP/PS1 mice or age-matched wildtype animals (n=2 per compound) were injected intravenously with 0.05 M dissolved in 1:1 DMSO:Cremophor diluted with PBS to a total volume of 200  $\mu$ L, resulting in a total dose of 30 $\mu$ mol/kg. One day after injection, animals were sacrificed using 200  $\mu$ L Euthanasol (AST Pharma) prior to transcardial perfusion with 4% paraformaldehyde in PBS. Brains were removed and cryoprotected in 4% PFA with 10% sucrose for 4 hours followed by immersion in 4% PFA with 30% sucrose overnight. Snap-frozen brains were cryosectioned (30  $\mu$ m) and fluorescence images were analyzed as described above.

### Competition binding assay

Competition binding experiments were conducted at room temperature, in a final volume of 1 ml assay buffer (150 mM Tris-HCl, 20% ethanol, pH 7.0). Compounds were dissolved as 3 mM stock solutions in DMSO, sonicated for 15 min, and used in a final concentration range of 30

$\mu\text{M}$  to  $30\text{ pM}$ .  $10\ \mu\text{l}$  of unlabeled test compounds was combined with  $890\ \mu\text{l}$  of assay buffer and  $50\ \mu\text{l}$  of  $100\ \text{nM}$  [ $^3\text{H}$ ]-chrysamine G stock (specific activity  $33.8\ \text{Ci/mmol}$ ). The mixture was sonicated for  $10\ \text{min}$ , and the assay was subsequently started by the addition of  $50\ \mu\text{l}$  synthetic  $\text{A}\beta_{1-40}$  fibrils, to achieve final concentrations of  $5\ \text{nM}$  [ $^3\text{H}$ ]chrysamine G and  $50\ \text{nM}$  fibrils. Nonspecific binding was determined in the presence of  $1\ \mu\text{M}$  Methoxy-X04. Incubations were terminated after  $1\ \text{h}$  via filtration through Whatman GF/B filters (pre-soaked in binding buffer), using a 48-well Brandel harvester. The filters were washed two times with  $3\ \text{ml}$  of ice-cold binding buffer ( $\text{pH}\ 7.0$ ), and radioactivity was determined by liquid scintillation spectrometry in  $5\ \text{ml}$  of Optiphase-HiSafe 3, at an efficiency of  $40\ \%$ .

$K_i$  values were determined by nonlinear regression analysis using the equation:  $\log\text{EC}_{50} = \log[10^{\wedge}\log K_i * (1 + \text{Radioligand} / \text{NM} / \text{HotKd} / \text{NM})]$  where  $K_d = 200\ \text{nM}$ , and radioligand =  $5\ \text{nM}$ . (GraphPad Software Inc., San Diego, CA)

### Procedure for logP determinations

LogP determinations were performed using literature procedures.<sup>23</sup> The measurements were performed on a Jasco HPLC-system (detection simultaneously at  $214$  and  $254\ \text{nm}$ ) coupled to a Perkin Elmer Sciex API 165 mass instrument with a custom-made Electrospray Interface (ESI). An analytical Gemini  $\text{C}_{18}$  column (Phenomenex,  $50 \times 4.60\ \text{mm}$ ,  $3\ \mu\text{m}$ ) was used in combination with buffers A) phosphate buffer of  $\text{pH} = 7.0$  ( $0.02\ \text{M}\ \text{Na}_2\text{HPO}_4$  adjusted to  $\text{pH} = 7.0$  with phosphoric acid) and B)  $0.25\ \%$  octanol in methanol.

Of all compounds to be evaluated, stock solutions of  $0.5\ \text{mg/ml}$  were prepared in methanol. These stock solutions were then diluted with water, making sure that the volume percentage of water was such that the compounds did not precipitate (max  $40\ \%$  water). A  $0.25\ \text{mg/ml}$  solution of  $\text{NaNO}_3$  in water was used as a non-retaining compound to determine the dead time of the system. For calibration purposes known compounds were taken from the literature. Of these compounds,  $0.25\ \text{mg/ml}$  solutions in either  $75\ \%\ \text{H}_2\text{O}/\text{MeOH}$  or  $50\ \%\ \text{H}_2\text{O}/\text{MeOH}$  were made.

For each sample, a series of four isocratic runs was performed, (for instance  $55, 60, 65, 70\ \%$  B), and the retention times (from UV-detection at  $214\ \text{nm}$ ) thus obtained were converted to the retention factor  $k'$  according to the formula  $k' = (t_R - t_0) / t_0$ , with  $t_R$  being the retention time of the compound and  $t_0$  being the retention time of  $\text{NaNO}_3$ . The retention factors were extrapolated to  $0\ \%$  B, yielding  $k'_w$ . As there is a linear relationship between  $\log P$  and  $\log k'_w$ , plotting  $\log P$  values of known compounds (**Table 10.3**) against obtained  $\log k'_w$  values in this system yields a calibration curve. From this curve,  $\log P$  values of unknown compounds can be calculated from their  $k'_w$  values.

### *In vitro* $^{19}\text{F}$ NMR analyses

To investigate the possible effect on its NMR properties caused by either binding to amyloid or the lipophilic environment of the brain several samples were prepared similar to the protocol described previously.<sup>13</sup> The *in vitro*  $^{19}\text{F}$  NMR analyses were performed using a Bruker DMX400 NMR spectrometer (Bruker, Germany). All samples were diluted with  $10\ \%\ \text{D}_2\text{O}$  in  $0.1\ \text{M}$  PBS with one EDTA-free protease inhibitor tablet (Complete Mini, Roche Diagnostics) added to every  $10\ \text{ml}$ . Aliquots ( $500\ \mu\text{l}$ ) of only the solvent, the solvent containing  $22\ \mu\text{M}$  of aggregated  $\text{A}\beta$  or the

brain homogenate were added to 20  $\mu\text{l}$  of 0.05 M of **22** in 1:1 DMSO:Cremophor to achieve a final concentration of 1.92 mM of compound **22**. The mixtures were transferred to a standard 5 mm NMR tube. NMR spectra were obtained using a single pulse sequence with a 22,573 Hz spectral width (SW) and 100 scans. The chemical shifts of the  $^{19}\text{F}$  NMR signals were identified by setting the reference trifluoroacetic acid (TFA) at 0 ppm.

### Post-mortem $^{19}\text{F}$ NMR in APP/PS1 mice

Twelve-to-fourteen-month-old APP/PS1 mice ( $n=2$ ) received an intravenous injection with 0.05 M of compound **22** dissolved in 1:1 DMSO:Cremophor diluted with PBS to a total volume of 200  $\mu\text{l}$  to achieve a total dose of 30  $\mu\text{mol}/\text{kg}$ . Prior injection the animals underwent cranial window surgery.<sup>14</sup> Twenty four hours post injection the animals underwent *in vivo* multiphoton microscopy (LSM 710 MP, Carl Zeiss, Germany) operating at 750 nm to validate the presence and labeling of cerebral amyloid. After perfusion the resected brain was snap frozen and prepared for NMR similar to the above brain homogenates. A similar fluorine NMR spectrum was obtained using a single pulse sequence with a 94340 Hz SW and 1200 scans.

**Table 10.3 Reference logP values**

compound	logP
resorcinol	0.8
p-nitroaniline	1.39
phenol	1.46
m-nitrophenol	2
2-naphthol	2.7
naphthalene	3.37

Based on known literature values, the logP of several reference compounds yield a required calibration curve to determine the logP values of our compounds.<sup>21-23</sup>

## Synthetic Procedures

### General

Reagents and solvents were used as provided, unless stated otherwise. 4-trifluoromethylbenzaldehyde (**35**), 4-trifluoromethoxybenzaldehyde (**36**), 4-(1,1,1,2,2-tetrafluoroethyl)benzaldehyde (**37**), 3-trifluoromethyl-4-methoxybenzaldehyde (**38**) (**Figure 10.2**) were purchased at standard suppliers. The other building blocks were prepared following literature procedures (see **Appendix I**). THF was distilled over  $\text{LiAlH}_4$  prior to use. Reactions were carried out under inert conditions and ambient temperature, unless stated otherwise. Prior to performing a reaction, traces of water were removed from the starting materials by repeated coevaporation with anhydrous 1,4-dioxane or anhydrous toluene. These solvents were stored over 4 Å molsieves. Reactions were monitored by thin layer chromatography on aluminum coated silica sheets (Merck, silica 60 F254), using visualization either with iodine, or spraying with a solution of 25 g  $(\text{NH}_4)_2\text{MoO}_4$ , 10 g  $(\text{NH}_4)_4\text{Ce}(\text{SO}_4)_4$  in 100 ml  $\text{H}_2\text{SO}_4$  and 900 ml  $\text{H}_2\text{O}$ , or a

solution of 20% H<sub>2</sub>SO<sub>4</sub> in ethanol, followed by charring at ~150 °C. Column chromatography was carried out with silica gel (Screening Devices bv, 40-63 µm particle size, 60 Å), using technical grade solvents. NMR spectra were recorded at 298K on a Bruker AV400 using deuterated solvents. All carbon spectra are proton-decoupled. Chemical shifts (δ) are given in ppm, in <sup>13</sup>C spectra relative to the solvent peaks of CDCl<sub>3</sub> (77.0 ppm), CD<sub>3</sub>OD (49.0 ppm), DMF-d<sub>7</sub> (29.76 ppm), acetone-d<sub>6</sub> (29.9 ppm) or DMSO-d<sub>6</sub> (39.51 ppm), in <sup>1</sup>H spectra relative to the solvent peak of tetramethylsilane (0.0 ppm), CD<sub>3</sub>OD (3.31 ppm), DMF-d<sub>7</sub> (2.75 ppm), acetone-d<sub>6</sub> (2.05 ppm) or DMSO-d<sub>6</sub> (2.50 ppm), in <sup>19</sup>F spectra relative to the solvent peak of TFA (0 ppm). Coupling constants are given in Hz. IR spectra were recorded on a Perkin Elmer Paragon 1000 FT-IR Spectrometer. High resolution mass spectra were recorded by direct injection (2 µL of a 2 µM solution in H<sub>2</sub>O/MeCN; 50/50; v/v and 0.1% formic acid) on a mass spectrometer (Thermo Finnigan LTQ Orbitrap) equipped with an electrospray ion source in positive mode (source voltage 3.5 kV, sheath gas flow 10, capillary temperature 250 °C) with resolution R = 60000 at m/z 400 (mass range m/z = 150-2000) and dioctylphthalate (m/z = 391.28428) as a "lock mass". The high resolution mass spectrometer was calibrated prior to measurements with a calibration mixture (Thermo Finnigan). It should be noted that, with the exception of compound **9** (data not shown) and only certain intermediates ionized correctly, none of the target compounds provided useful (HR)MS data.

LC-MS analysis was performed on a Finnigan Surveyor HPLC system with a Gemini C<sub>18</sub> 50 × 4.6 mm column (3 micron, Phenomenex, Torrance, CA, USA) (detection at 200-600 nm), coupled to a Thermo Finnigan LCQ Advantage Max mass spectrometer (Breda, The Netherlands) with electrospray ionization (ESI; system 1), with as eluents (A): H<sub>2</sub>O; (B): MeCN and (C): 1% aq. TFA.

#### **General procedure A: Horner-Wadsworth-Emmons reaction with NaH**

The diphosphonate (0.83 mmol) was dissolved in THF (2.6 ml) and cooled to 0 °C. NaH (60% wt. dispersion in mineral oil, 0.17 g, 4.17 mmol) was added and the mixture stirred for 30 min at 0 °C. The aldehyde (2.08 mmol) was dissolved in THF and added to the reaction mixture, which was subsequently stirred for 16 h at rt. After cooling and quenching with water, the mixture was extracted three times with EtOAc and the combined organic layers were washed with sat. aq. NaHCO<sub>3</sub>, dried (Na<sub>2</sub>SO<sub>4</sub>), filtered and concentrated. The crude product was subjected to column chromatography to yield the pure product.

#### **General procedure B: Horner-Wadsworth-Emmons reaction with KOtBu**

The diphosphonate (0.95 mmol) was dissolved in THF (20 ml) and cooled to -10 °C. KOtBu (0.30 g, 2.45 mmol) was added and the black mixture stirred for 20 min. A solution of the aldehyde (2.37 mmol) in THF (6 ml) was added and the reaction stirred at room temperature for 16 h. The reaction was cooled to 0 °C, quenched with water and extracted five times with EtOAc. The combined organic layers were dried (Na<sub>2</sub>SO<sub>4</sub>), filtered and concentrated. The crude product was subjected to column chromatography to yield the pure product.

#### **General procedure C: silyl deprotection**

A solution of protected bis-styrylbenzene (0.63 mmol) in THF (2 ml) was cooled to 0 °C and TBAF (1 M in THF, 3.14 ml, 3.14 mmol) was added. The blood-red solution was stirred for 16 h after

which water was added and the reaction mixture was extracted with EtOAc. To the aqueous layer 1 M HCl was added, followed by two times extracting with EtOAc. The combined organic layers were dried ( $\text{Na}_2\text{SO}_4$ ), filtered and concentrated. The pure product was obtained by column chromatography (0 → 25% EtOAc/light petroleum).

#### **(E, E)-1-methoxy-2,5-bis(4-hydroxy)styrylbenzene; Methoxy-X04 (10)**

Methoxy-X04 was prepared according to general procedures **A** and **C**, using diphosphonate **25** and aldehyde **33**. Physical data corresponded to those reported by Klunk *et al.*<sup>10</sup>

#### **(E, E)-1,4-dimethoxy-2,5-bis(4-hydroxy)styrylbenzene (11)**

Following general procedure **A**, diphosphonate **26** (0.34 g, 0.78 mmol) was reacted with aldehyde **33** (0.46 g, 1.9 mmol). A bright yellow solid was isolated (221 mg) by column chromatography (10 → 30% EtOAc/light petroleum) of which 100 mg was purified by preparative HPLC (40:60 → 20:80 of 20 mM  $\text{NH}_4\text{OAc}/\text{MeOH}$ ), to yield 22 mg (0.059 mmol, 8%) of compound **11**.

$^1\text{H}$  NMR ( $\text{CD}_3\text{OD}$ , 400 MHz):  $\delta$  7.43 (d,  $J$  = 8.6 Hz, 4H); 7.33 (d,  $J$  = 16.5 Hz, 2H); 7.27 (s, 2H); 7.19 (d,  $J$  = 16.5 Hz, 2H); 6.82 (d,  $J$  = 8.6 Hz, 4H); 3.93 (s, 6H).  $^{13}\text{C}$  NMR ( $\text{CD}_3\text{OD}$ , 100 MHz):  $\delta$  158.5; 152.6; 130.9; 129.7; 128.9; 127.6; 121.1; 116.6; 109.9; 56.8. IR (neat): 3359.6; 1605.3; 1515.7; 1495.6; 1463.6; 1435.4; 1408.7; 1260.0; 1196.0; 1171.8; 1022.4; 958.3; 849.6; 819.7; 790.1; 685.9; 551.0; 521.6. LC-MS retention time: 8.99 min (10 → 90% MeCN, 15 min run).

#### **(E, E)-1-methoxy-2,5-bis(4-hydroxymethyl)styrylbenzene (12)**

Following general procedure **A**, diphosphonate **25** (0.2 g, 0.5 mmol) was reacted with aldehyde **34** (0.31 g, 1.25 mmol). The crude product was subjected to column chromatography (0 → 2% EtOAc/light petroleum) to yield the intermediary bis-TBDMS protected styrylbenzene (0.28 g, 0.48 mmol, 96%) as a bright yellow solid.  $^1\text{H}$  NMR ( $\text{CDCl}_3$ , 400 MHz):  $\delta$  7.58 (d,  $J$  = 8.1 Hz, 1H); 7.51 (d,  $J$  = 6.1 Hz, 2H); 7.49 (d,  $J$  = 6.3 Hz, 2H); 7.44 (s, 1H); 7.34-7.28 (m, 4H); 7.16-7.13 (m, 2H); 7.13-7.09 (m, 2H); 7.03 (d,  $J$  = 1.4 Hz, 1H); 4.75 (d,  $J$  = 2.4 Hz, 4H); 3.95 (s, 3H); 0.95 (s, 9H); 0.95 (s, 9H); 0.11 (s, 6H); 0.11 (s, 6H).  $^{13}\text{C}$  NMR ( $\text{CDCl}_3$ , 100 MHz):  $\delta$  157.0; 141.0; 140.7; 137.9; 136.7; 136.0; 128.7; 128.4; 128.1; 126.4; 126.4; 126.4; 126.0; 122.7; 119.3; 108.6; 64.9; 64.8; 55.6; 26.0; 18.4; -5.2. IR (neat): 2953.7; 2927.5; 2855.3; 1593.8; 1553.7; 1515.3; 1458.3; 1421.9; 1377.6; 1248.7; 1206.0; 1084.2; 1037.1; 1005.7; 967.3; 837.4; 773.9; 668.1; 504.2. The bis-TBDMS protected (E, E)-styrylbenzene (0.27 g, 0.46 mmol) was treated with TBAF according to general procedure **C**. Compound **12** was obtained by column chromatography (50% EtOAc/light petroleum → 10% MeOH/EtOAc) as a bright yellow solid (0.14 g, 0.37 mmol, 79%).

$^1\text{H}$  NMR ( $\text{DMF-d}_7$ , 400 MHz):  $\delta$  7.68 (d,  $J$  = 8.0 Hz, 1H); 7.59 (d,  $J$  = 8.1 Hz, 2H); 7.55 (d,  $J$  = 8.1 Hz, 2H); 7.49 (d,  $J$  = 16.6 Hz, 1H); 7.39-7.34 (m, 4H); 7.31 (d,  $J$  = 5.0 Hz, 2H); 7.28 (d,  $J$  = 4.9 Hz, 1H); 7.25-7.21 (m, 2H).  $^{13}\text{C}$  NMR ( $\text{DMF-d}_7$ , 100 MHz):  $\delta$  157.7; 142.6; 142.3; 138.8; 137.2; 136.6; 129.0; 128.9; 128.4; 127.4; 126.8; 126.8; 126.6; 126.0; 122.9; 119.7; 109.3; 63.8; 55.6. IR (neat): 1592.0; 1557.6; 1515.8; 1455.9; 1418.0; 1340.0; 1269.9; 1243.7; 1211.9; 1158.1; 1112.4; 1034.2; 1011.7; 956.3; 825.7; 624.2.

#### **(E, E)-1-methoxy-2,5-bis(4-trifluoromethyl)styrylbenzene (13)**

Following general procedure **A**, diphosphonate **26** (0.20 g, 0.5 mmol) was reacted with aldehyde



**35** (0.22 g, 1.25 mmol). After work-up, the crude product was purified by column chromatography (0 → 1% EtOAc/light petroleum) and the compound **13** was obtained as a bright yellow solid (80 mg, 0.18 mmol, 36%).

<sup>1</sup>H NMR (acetone-d<sub>6</sub>, 400 MHz): δ 7.82 (d, *J* = 8.2 Hz, 2H); 7.79 (d, *J* = 8.5 Hz, 2H); 7.76-7.69 (m, 5H); 7.66 (d, *J* = 16.7 Hz, 2H); 7.43 (s, 2H); 7.38 (d, *J* = 16.4 Hz, 2H); 7.29 (dd, *J* = 8.1 Hz, *J* = 1.3 Hz, 1H); 4.00 (s, 3H). <sup>13</sup>C NMR (acetone-d<sub>6</sub>, 100 MHz): δ 158.5; 143.0; 142.4; 139.3; 132.1; 128.3; 128.3; 127.9; 127.9; 127.8; 126.7; 126.5; 126.5; 126.5; 120.7; 110.3; 56.1. <sup>19</sup>F NMR (acetone-d<sub>6</sub>, 375 MHz): δ 12.70 (s, 3F); 12.65 (s, 3F). IR (neat): 1608.4; 1464.0; 1420.1; 1323.6; 1246.5; 1158.5; 1116.6; 1105.9; 1065.5; 1036.4; 1014.1; 967.0; 954.2; 866.5; 848.8; 829.9; 759.2; 744.8; 622.2; 593.3; 508.4.

#### **(*E*, *E*)-1-methoxy-2,5-bis(4-trifluoromethoxy)styrylbenzene (14)**

Following general procedure **A**, diphosphonate **25** (0.20 g, 0.5 mmol) was reacted with aldehyde **36** (0.24 g, 1.25 mmol). After work-up, the product **14** was obtained by column chromatography (0 → 1.5% EtOAc/light petroleum) as a bright yellow solid (83 mg, 0.17 mmol, 35%).

<sup>1</sup>H NMR (CDCl<sub>3</sub>, 400 MHz): δ 7.56 (d, *J* = 8.0 Hz, 1H); 7.54-7.50 (m, 4H); 7.44 (d, *J* = 16.5 Hz, 1H); 7.19 (t, *J* = 7.8 Hz, 4H); 7.14-7.10 (m, 2H); 7.09-7.05 (m, 2H); 7.01 (d, *J* = 1.3 Hz, 1H); 3.94 (s, 3H). <sup>13</sup>C NMR (CDCl<sub>3</sub>, 100 MHz): δ 157.2; 137.7; 136.7; 135.9; 127.7; 127.5; 127.2; 126.6; 125.9; 124.1; 121.2; 121.1; 119.4; 108.5; 55.5. <sup>19</sup>F NMR (CDCl<sub>3</sub>, 375 MHz): δ 19.80 (s, 3F); 19.79 (s, 3F). IR (neat): 1593.1; 1557.6; 1510.2; 1421.9; 1254.6; 1199.8; 1159.4; 1104.9; 1034.0; 1015.7; 962.2; 921.6; 838.6; 673.8; 620.1; 530.0; 505.9.

#### **(*E*, *E*)-1-methoxy-2,5-bis(4-{1,1,2,2-tetrafluoroethyl})styrylbenzene (15)**

Following general procedure **A**, diphosphonate **25** (0.20 g, 0.5 mmol) was reacted with aldehyde **37** (0.28 g, 1.25 mmol). After work-up, compound **15** was isolated by column chromatography (0 → 7.5% EtOAc/light petroleum) as a yellow solid (0.14 g, 0.25 mmol, 50%).

<sup>1</sup>H NMR (CDCl<sub>3</sub>, 400 MHz): δ 7.56 (d, *J* = 7.3 Hz, 1H); 7.55-7.49 (m, 4H); 7.33 (d, *J* = 16.5 Hz, 1H); 7.24-7.16 (m, 4H); 7.13-7.04 (m, 4H); 7.01 (d, *J* = 2.3 Hz, 1H); 6.07-5.76 (m, 2H); 3.94 (s, 3H). <sup>13</sup>C NMR (CDCl<sub>3</sub>, 100 MHz): δ 157.1; 148.5; 148.2; 137.7; 136.4; 135.6; 129.2; 128.7; 127.9; 127.8; 127.6; 127.5; 127.2; 126.6; 125.8; 122.4; 121.9; 121.8; 121.8; 121.7; 119.4; 119.1; 116.7; 116.4; 116.2; 115.5; 110.2; 108.7; 108.1; 107.7; 107.3; 55.5. <sup>19</sup>F NMR (CDCl<sub>3</sub>, 375 MHz): δ -10.5 (s, 4F); -59.06 (t, *J* = 5.5 Hz, 2F); -59.20 (t, *J* = 5.5 Hz, 2F). IR (neat): 1510.5; 1463.9; 1421.9; 1392.9; 1302.4; 1274.0; 1195.2; 1115.4; 1035.7; 1015.7; 961.8; 837.0; 784.1; 766.2; 709.4; 623.3; 600.0; 544.1.

#### **(*E*, *E*)-1-hydroxy-2,5-bis(4-trifluoromethyl)styrylbenzene (16)**

Following general procedure **B**, diphosphonate **27** (0.85 g, 1.34 mmol) was reacted with aldehyde **35** (0.59 g, 3.36 mmol). After work-up, the crude product was purified by column chromatography (0 → 6% EtOAc/light petroleum) and product **16** was obtained as a bright yellow solid (0.2 g, 0.48 mmol, 36%).

<sup>1</sup>H NMR (CD<sub>3</sub>OD, 400 MHz): δ 7.67-7.52 (m, 10H); 7.21 (d, *J* = 16.5 Hz, 1H); 7.14 (d, *J* = 2.2 Hz, 2H); 7.07 (dd, *J* = 8.1 Hz, *J* = 1.5 Hz, 1H); 7.02 (d, *J* = 1.6 Hz, 1H). <sup>13</sup>C NMR (CD<sub>3</sub>OD, 100 MHz): δ 156.2; 142.7; 141.9; 138.6; 131.7; 129.2; 127.8; 127.8; 127.5; 127.4; 127.2; 126.9; 126.2; 126.2; 126.1; 126.1; 125.0; 119.5; 114.3. <sup>19</sup>F NMR (CD<sub>3</sub>OD, 375 MHz): δ 14.98 (s, 3F); 14.91 (s, 3F). IR (neat):

1611.5; 1428.3; 1319.9; 1163.2; 1107.4; 1066.6; 1014.2; 967.4; 956.5; 872.2; 831.8; 757.9; 750.6; 624.8; 592.8; 507.7.

#### **(*E, E*)-1-hydroxy-2,5-bis(4-trifluoromethoxy)styrylbenzene (17)**

Following general procedure **B**, diphosphonate **27** (0.99 g, 1.56 mmol) was reacted with aldehyde **36** (0.74 g, 3.91 mmol). The crude product was purified by column chromatography (0 → 8% EtOAc/light petroleum) and product **17** was obtained as a bright yellow solid (0.47 g, 1.01 mmol, 65%).

<sup>1</sup>H NMR (CD<sub>3</sub>OD, 400 MHz): δ 7.63 (d, *J* = 5.8 Hz, 2H); 7.61 (d, *J* = 5.6 Hz, 2H); 7.48 (d, *J* = 16.5 Hz, 1H); 7.40-7.34 (m, 1H); 7.27-7.18 (m, 5H); 7.12 (d, *J* = 3.2 Hz, 2H); 7.07 (dd, *J* = 8.1 Hz, *J* = 1.5 Hz, 1H); 7.02 (d, *J* = 1.6 Hz, 1H). <sup>13</sup>C NMR (CD<sub>3</sub>OD, 100 MHz): δ 156.7; 149.7; 149.4; 149.4; 139.2; 139.0; 138.1; 133.0; 130.8; 129.0; 128.8; 128.1; 127.9; 127.7; 126.0; 125.4; 122.3; 122.2; 121.6; 119.7; 114.4. <sup>19</sup>F NMR (CD<sub>3</sub>OD, 375 MHz): δ 18.85 (s, 6F). IR (neat): 1604.3; 1557.6; 1515.8; 1505.7; 1269.9; 1158.4; 1099.9; 1015.6; 967.6; 928.0; 839.2; 676.6; 624.0; 525.1.

#### **(*E, E*)-1-hydroxy-2,5-bis(4-{1,1,2,2-tetrafluoroethyl})styrylbenzene (18)**

Following general procedure **B**, diphosphonate **27** (0.74 g, 1.17 mmol) was reacted with aldehyde **37** (0.65 g, 2.92 mmol). After work-up, the crude product was subjected to column chromatography (0 → 10% EtOAc/light petroleum) to yield product **18** as a bright yellow solid (0.27 g, 0.5 mmol, 43%).

<sup>1</sup>H NMR (CD<sub>3</sub>OD, 400 MHz): δ 7.61 (d, *J* = 5.3 Hz, 2H); 7.59 (d, *J* = 5.2 Hz, 2H); 7.56 (d, *J* = 8.1 Hz, 1H); 7.48 (d, *J* = 16.6 Hz, 1H); 7.25-7.19 (m, 5H); 7.12 (d, *J* = 5.5 Hz, 2H); 7.08 (dd, *J* = 7.9 Hz, *J* = 1.7 Hz, 1H); 7.02 (d, *J* = 1.5 Hz, 1H); 6.46-6.14 (m, 2H). <sup>13</sup>C NMR (CD<sub>3</sub>OD, 100 MHz): δ 156.6; 149.2; 139.2; 138.4; 137.6; 130.4; 128.8; 128.6; 128.1; 128.0; 127.9; 125.6; 125.4; 123.0; 123.0; 119.7; 114.3.

#### **(*E, E*)-1-trifluoromethyl-2,5-bis(4-hydroxy)styrylbenzene (19)**

Following general procedure **A**, diphosphonate **28** (0.37 g, 0.83 mmol) was reacted with aldehyde **33** (0.49 g, 2.1 mmol). After work-up, the crude product was purified by column chromatography (0 → 4% EtOAc/light petroleum) and the intermediary bis-TBDMS protected styrylbenzene was obtained as a bright yellow solid (0.36 g, 0.59 mmol, 71%). <sup>1</sup>H NMR (CDCl<sub>3</sub>, 400 MHz): δ 7.77-7.72 (m, 2H); 7.61 (d, *J* = 8.1 Hz, 1H); 7.44-7.37 (m, 4H); 7.31 (dd, *J* = 16.1 Hz, *J* = 1.8 Hz, 1H); 7.11 (d, *J* = 16.3 Hz, 1H); 7.05 (d, *J* = 16.0 Hz, 1H); 7.00-6.92 (m, 1H); 6.88-6.81 (m, 4H). <sup>13</sup>C NMR (CDCl<sub>3</sub>, 100 MHz): δ 156.0, 155.9, 136.5, 135.0; 131.7, 130.3, 130.2, 129.6, 129.0, 128.1, 127.9, 126.9, 125.0, 123.8, 122.0, 120.4, 29.7, 25.7, -4.4. <sup>19</sup>F NMR (CDCl<sub>3</sub>, 375 MHz): δ 18.17 (s, 3F). IR (neat): 1598.9; 1508.0; 1471.8; 1327.9; 1314.0; 1251.5; 1170.0; 1154.7; 1131.4; 1115.5; 1102.1; 1051.1; 962.1; 938.5; 906.8; 834.5; 778.2; 700.2; 667.7; 660.3; 638.4; 554.5; 534.7.

The bis-TBDMS protected styrylbenzene (0.34 g, 0.54 mmol) was treated with TBAF according to general procedure **C**, and following column chromatography (0 → 30% EtOAc/light petroleum), the impure product was purified by HPLC (CN column, 35:65 → 10:90 of 0.2% aq. TFA/MeOH) and product **19** was obtained as a yellow solid (83 mg, 0.22 mmol, 40%).

<sup>1</sup>H NMR (CD<sub>3</sub>OD, 400 MHz): δ 7.81 (d, *J* = 8.2 Hz, 1H); 7.73 (s, 1H); 7.70 (d, *J* = 8.5 Hz, 1H); 7.42 (d, *J* = 8.0 Hz, 2H); 7.38 (d, *J* = 8.0 Hz, 2H); 7.23 (d, *J* = 16.0 Hz, 1H); 7.14 (t, *J* = 16.9, 2H); 6.99 (d, *J* =

16.3 Hz, <sup>1</sup>H); 6.80 (dd, *J* = 7.8 Hz, *J* = 3.5 Hz, 4H).

<sup>13</sup>C NMR (CD<sub>3</sub>OD, 100 MHz): δ 159.1; 158.9; 138.3; 136.2; 133.3; 131.1; 130.2; 130.0; 129.3; 129.2; 128.4; 128.0; 127.5; 125.0; 124.9; 124.7; 124.7; 124.6; 124.6; 121.7; 116.7; 116.6. <sup>19</sup>F NMR (CD<sub>3</sub>OD, 375 MHz): δ 17.64 (s, 3F). IR (neat): 1605.0; 1512.1; 1441.0; 1313.9; 1257.1; 1239.9; 1199.4; 1171.9; 1153.6; 1108.8; 1079.5; 1049.9; 959.8; 869.9; 837.2; 812.7; 671.7; 552.7; 522.1.

#### **(*E, E*)-1-(2,2,2-trifluoroethoxy)-2,5-bis(4-hydroxy)styrylbenzene (20)**

Following general procedure **B**, dipshosphonate **29** (0.45 g, 0.95 mmol) was reacted with aldehyde **33** (0.56 g, 2.37 mmol). After work-up, the crude product was subjected to column chromatography (0 → 5% EtOAc/light petroleum) and the bis-TBDMS protected styrylbenzene was obtained as a bright yellow solid (0.4 g, 0.63 mmol, 66%). <sup>1</sup>H NMR (CDCl<sub>3</sub>, 400 MHz): δ 7.59-7.51 (m, 4H); 7.43 (d, *J* = 16.5 Hz, <sup>1</sup>H); 7.31 (d, *J* = 7.7 Hz, <sup>1</sup>H); 7.69 (d, *J* = 8.0 Hz, <sup>1</sup>H); 7.24 (d, *J* = 16.4 Hz, <sup>1</sup>H); 7.18 (d, *J* = 16.3 Hz, <sup>1</sup>H); 7.10-7.06 (m, 2H); 7.00 (dd, *J* = 8.6 Hz, *J* = 2.0 Hz, 4H); 4.56 (q, *J* = 8.2 Hz, *J* = 8.1 Hz, 2H); 1.16 (s, 18H); 0.38 (s, 6H); 0.38 (s, 6H). <sup>13</sup>C NMR (CDCl<sub>3</sub>, 100 MHz): δ 155.6; 155.5; 154.7; 137.9; 131.8; 131.0; 130.3; 129.3; 128.6; 127.7; 126.7; 126.7; 125.8; 121.0; 120.4; 120.3; 120.1; 110.7; 67.2; 66.8; 66.5; 66.1; 29.7; 25.6; -4.4. <sup>19</sup>F NMR (CDCl<sub>3</sub>, 375 MHz): δ 3.80 (t, *J* = 8.1 Hz, 3F).

The bis-TBDMS protected styrylbenzene (0.4 g, 0.63 mmol) was treated with TBAF according to general procedure **C**. After work-up, the crude product was purified by column chromatography (0 → 25% EtOAc/light petroleum) and product **20** was obtained as a bright yellow solid (0.127 g, 0.31 mmol, 49%).

<sup>1</sup>H NMR (CD<sub>3</sub>OD, 400 MHz): δ 7.51 (d, *J* = 8.1 Hz, <sup>1</sup>H); 7.40-7.29 (m, 4H); 7.20 (d, *J* = 16.5 Hz, <sup>1</sup>H); 7.13 (dd, *J* = 8.1 Hz, *J* = 1.0 Hz, <sup>1</sup>H); 7.05 (d, *J* = 16.5 Hz, <sup>1</sup>H); 7.03 (d, *J* = 16.3 Hz, <sup>1</sup>H); 7.00 (d, *J* = 1.1 Hz, <sup>1</sup>H); 6.87 (d, *J* = 16.3 Hz, <sup>1</sup>H); 6.81-6.75 (m, 4H); 4.48 (q, *J* = 8.3 Hz, *J* = 8.3 Hz, 2H). <sup>13</sup>C NMR (CD<sub>3</sub>OD, 100 MHz): δ 157.8; 157.6; 155.5; 138.9; 130.4; 130.0; 129.7; 129.5; 128.6; 128.5; 127.2; 125.7; 121.5; 120.0; 116.2; 116.2; 111.4; 67.4; 67.0; 66.7. <sup>19</sup>F NMR (CD<sub>3</sub>OD, 375 MHz): δ 6.89 (t, *J* = 7.5 Hz, 3F). IR (neat): 3331.9; 1606.2; 1515.7; 1505.9; 1455.8; 1427.9; 1238.9; 1169.7; 1118.3; 964.1; 828.9; 667.9; 617.9; 518.9.

#### **(*E, E*)-1-(4,4,4-trifluorobutoxy)-2,5-bis(4-hydroxy)styrylbenzene (21)**

Following general procedure **B**, dipshosphonate **30** (0.50 g, 1 mmol) was reacted with aldehyde **33** (0.59 g, 2.5 mmol). After work-up, the crude product was purified by column chromatography (0 → 2% EtOAc/light petroleum) and the bis-TBDMS protected styrylbenzene was obtained as a bright yellow solid (0.3 g, 0.46 mmol, 46%). <sup>1</sup>H NMR (CDCl<sub>3</sub>, 400 MHz): δ 7.53 (d, *J* = 8.1 Hz, <sup>1</sup>H); 7.38 (d, *J* = 8.4 Hz, 4H); 7.28 (d, *J* = 16.5 Hz, <sup>1</sup>H); 7.12-7.05 (m, 2H); 7.03 (d, *J* = 16.2 Hz, <sup>1</sup>H); 6.95 (d, *J* = 1.1 Hz, <sup>1</sup>H); 6.92 (d, *J* = 16.3 Hz, <sup>1</sup>H); 6.86-6.80 (m, 4H); 4.13 (t, *J* = 6.0 Hz, 2H); 2.46-2.31 (m, 2H); 2.20-2.10 (m, 2H); 0.99 (s, 18H); 0.21 (s, 12H). <sup>13</sup>C NMR (CDCl<sub>3</sub>, 100 MHz): δ 155.9; 155.6; 155.4; 137.9; 131.3; 130.6; 128.7; 128.3; 127.7; 127.6; 126.5; 126.5; 126.1; 120.9; 120.4; 120.3; 119.6; 109.6; 66.6; 31.1; 30.8; 29.4; 25.7; 22.4; 22.3; 18.2; -4.4. <sup>19</sup>F NMR (CDCl<sub>3</sub>, 375 MHz): δ 11.39 (t, *J* = 10.9 Hz, 3F). IR (neat): 1599.9; 1508.7; 1471.7; 1250.8; 1166.6; 1153.9; 1027.7; 908.7; 833.2; 798.6; 779.1; 700.5; 661.8; 623.5; 531.4; 504.4.

The silylated bis-styrylbenzene (0.3 g, 0.46 mmol) was deprotected according to general procedure **C**. After work-up, the crude product was purified using column chromatography (10 → 22.5% EtOAc/light petroleum) and product **21** was obtained as a bright yellow solid (0.12 g, 0.27 mmol, 58%).

<sup>1</sup>H NMR (CD<sub>3</sub>OD, 400 MHz): δ 7.50 (d, *J* = 8.1 Hz, 1H); 7.38 (d, *J* = 8.6 Hz, 2H); 7.34 (d, *J* = 8.6 Hz, 2H); 7.24 (d, *J* = 16.5 Hz, 1H); 7.11-7.02 (m, 4H); 6.92 (d, *J* = 16.3 Hz, 1H); 6.80-6.75 (m, 4H); 4.13 (t, *J* = 6.0 Hz, 2H); 2.50-2.35 (m, 2H); 2.16-2.06 (m, 2H). <sup>13</sup>C NMR (CD<sub>3</sub>OD, 100 MHz): δ 158.4; 158.2; 157.3; 139.4; 131.1; 130.4; 129.7; 129.5; 128.9; 128.6; 127.3; 127.1; 126.6; 121.1; 120.4; 116.5; 110.8; 67.8; 32.1; 31.8; 31.5; 31.2; 23.5; 23.4; 23.4. <sup>19</sup>F NMR (CD<sub>3</sub>OD, 375 MHz): δ 3.48 (t, *J* = 11.3 Hz, 3F). IR (neat): 3325.9; 1605.69; 1593.7; 1515.5; 1505.9; 1447.9; 1385.8; 1338.1; 1241.0; 1171.3; 1026.0; 961.8; 826.7; 621.1; 519.8.

### **(*E, E*)-1-(nonafluoro-*tert*-butoxy)-2,5-bis(4-hydroxy)styrylbenzene (22)**

Following general procedure **B**, diphosphonate **32** (0.55 g, 0.89 mmol) was reacted with aldehyde **33** (0.53 g, 2.2 mmol). After work-up, the crude product was purified by column chromatography (0 → 2% EtOAc/light petroleum) and the bis-TBDMS protected styrylbenzene was obtained as a bright yellow solid (0.22 g, 0.28 mmol, 32%). <sup>1</sup>H NMR (CDCl<sub>3</sub>, 400 MHz): δ 7.27-7.20 (m, 4H); 7.20-7.12 (m, 2H); 6.90-6.81 (m, 2H); 6.79-6.73 (m, 2H); 6.72-6.64 (m, 4H); 7.48 (d, *J* = 8.2 Hz, 1H); 0.84 (s, 1H); 0.06 (s, 6H); 0.06 (s, 6H). <sup>13</sup>C NMR (CDCl<sub>3</sub>, 100 MHz): δ 155.8; 155.8 150.5; 137.9; 130.5; 130.5; 130.2; 130.0; 129.3; 127.9; 127.8; 126.1; 125.3; 124.2; 120.5; 119.0; 31.9; 29.4; 25.7; -4.4. <sup>19</sup>F NMR (CDCl<sub>3</sub>, 375 MHz): δ 8.81 (s, 9F). IR (neat): 1600.0; 1508.4; 1472.0; 1249.8; 1169.5; 1155.1; 1124.8; 998.7; 965.7; 904.5; 833.8; 779.5; 726.0; 700.6; 537.4; 504.5. The bis-TBDMS protected styrylbenzene was treated with TBAF according to general procedure **C**. The crude product was subjected to column chromatography (10 → 25% EtOAc/light petroleum) and product **22** was obtained as a bright yellow solid (72 mg, 0.13 mmol, 47%).

<sup>1</sup>H NMR (CD<sub>3</sub>OD, 400 MHz): δ 7.72 (d, *J* = 8.3 Hz, 1H); 7.46-7.34 (m, 5H); 7.31 (s, 1H); 7.22 (d, *J* = 16.5 Hz, 1H); 7.05 (d, *J* = 16.4 Hz, 1H); 7.10 (d, *J* = 12.4 Hz, 1H); 6.96-6.90 (m, 1H); 6.82-6.77 (m, 4H). <sup>13</sup>C NMR (CD<sub>3</sub>OD, 100 MHz): δ 159.0; 158.9; 151.6; 139.6; 131.8; 131.7; 130.9; 130.1; 129.9; 129.3; 129.1; 127.4; 125.5; 125.1; 123.0; 120.1; 119.8; 118.7; 116.7; 116.6. <sup>19</sup>F NMR (CD<sub>3</sub>OD, 375 MHz): δ 10.93 (s, 9F). IR (neat): 3332.1; 1606.3; 1515.6; 1250.3; 1171.8; 1123.0; 1000.3; 965.1; 829.3; 727.4; 668.0; 529.1.

### **(*E, E*)-1-hydroxy-2,5-bis(3-trifluoromethyl-4-methoxy)styrylbenzene (23)**

Following general procedure **B**, diphosphonate **27** (0.52 g, 1 mmol) was reacted with aldehyde **38** (0.51 g, 2.5 mmol). After work-up, the crude product was purified by column chromatography (0 → 17% EtOAc/light petroleum), followed by preparative TLC (eluent: 50% EtOAc/light petroleum) and product **23** was obtained as a bright yellow solid (58 mg, 0.12 mmol, 12%).

<sup>1</sup>H NMR (acetone-*d*<sub>6</sub>, 400 MHz): δ 7.80-7.71 (m, 4H); 7.54 (d, *J* = 8.0 Hz, 1H); 7.39 (d, *J* = 16.6 Hz, 1H); 7.26-7.16 (m, 3H); 7.13 (d, *J* = 16.4 Hz, 1H); 7.10-6.98 (m, 3H); 3.90 (s, 6H). <sup>13</sup>C NMR (acetone-*d*<sub>6</sub>, 100 MHz): δ 156.2; 139.0; 132.5; 132.2; 131.9; 131.1; 129.0; 127.8; 127.6; 127.4; 125.8; 125.7; 125.6; 125.5; 125.0; 124.1; 119.3; 114.3; 113.9; 56.6; 56.6. <sup>19</sup>F NMR (acetone-*d*<sub>6</sub>, 375 MHz): δ 7.62 (s, 3F); 7.60 (s, 3F). IR (neat): 3523.0; 1615.5; 1512.0; 1501.5; 1428.0; 1327.6; 1274.3; 1261.6; 1119.8; 1058.0; 1017.1; 963.1; 823.7; 667.6; 645.9; 569.8; 544.1.

**(E, E)-1-methoxy-2,5-bis(3-trifluoromethyl-4-methoxy)styrylbenzene (24)**

Following general procedure **B**, diphosphonate **25** (0.41 g, 1 mmol) was reacted with aldehyde **38** (0.51 g, 2.5 mmol). After work-up, the crude product was purified by column chromatography (0 → 10% EtOAc/light petroleum) and product **24** was obtained as a bright yellow solid (0.14 g, 0.27 mmol, 27%).

$^1\text{H}$  NMR (DMSO- $d_6$ , 400 MHz):  $\delta$  7.97-7.83 (m, 3H); 7.81 (dd,  $J = 7.8$  Hz,  $J = 1.7$  Hz,  $^1\text{H}$ ); 7.76 (d,  $J = 1.7$  Hz,  $^1\text{H}$ ); 7.65 (d,  $J = 8.1$  Hz,  $^1\text{H}$ ); 7.46 (d,  $J = 16.8$  Hz,  $^1\text{H}$ ); 7.40-7.20 (m, 6H); 3.93 (s, 3H); 3.92 (s, 3H).  $^{13}\text{C}$  NMR (DMSO- $d_6$ , 100 MHz):  $\delta$  156.1; 137.9; 131.8; 131.5; 130.0; 129.7; 129.2; 128.8; 127.8; 127.3; 127.0; 126.6; 125.6; 125.1; 122.4; 122.2; 120.7; 119.3; 117.5; 117.2; 114.6; 113.4; 109.1; 56.3; 56.2.

$^{19}\text{F}$  NMR (DMSO- $d_6$ , 375 MHz):  $\delta$  17.26 (s, 3F); 17.2 (s, 3F). IR (neat): 1615.6; 1510.4; 1505.8; 1463.9; 1328.5; 1260.0; 1118.3; 1054.9; 1021.0; 959.3; 818.0; 667.8; 645.5; 541.1.

## References

1. Duyckaerts, C, Delatour, B, and Potier, MC. Classification and basic pathology of Alzheimer disease. *Acta Neuropathol.* 2009; 118:5-36.
2. Frisoni, GB, Fox, NC, Jack, CR, Jr., *et al.* The clinical use of structural MRI in Alzheimer disease. *Nat Rev Neurol.* 2010; 6:67-77.
3. Jack, CR, Jr., Knopman, DS, Jagust, WJ, *et al.* Hypothetical model of dynamic biomarkers of the Alzheimer's pathological cascade. *Lancet Neurol.* 2010; 9:119-128.
4. Vandenberghe, R, Van, LK, Ivanou, A, *et al.* 18F-flutemetamol amyloid imaging in Alzheimer disease and mild cognitive impairment: a phase 2 trial. *Ann Neurol.* 2010; 68:319-329.
5. Barthel, H, Gertz, HJ, Dresel, S, *et al.* Cerebral amyloid-beta PET with florbetaben (18F) in patients with Alzheimer's disease and healthy controls: a multicentre phase 2 diagnostic study. *Lancet Neurol.* 2011; 10:424-435.
6. GE beta-amyloid agent approved. *J Nucl Med.* 2013; 54:10N.
7. Yang, L, Rieves, D, and Ganley, C. Brain amyloid imaging--FDA approval of florbetapir F18 injection. *N Engl J Med.* 2012; 367:885-887.
8. Styren, SD, Hamilton, RL, Styren, GC, *et al.* X-34, a fluorescent derivative of Congo red: a novel histochemical stain for Alzheimer's disease pathology. *J Histochem Cytochem.* 2000; 48:1223-1232.
9. Zhuang, ZP, Kung, MP, Hou, C, *et al.* Radioiodinated styrylbenzenes and thioflavins as probes for amyloid aggregates. *J Med Chem.* 2001; 44:1905-1914.
10. Klunk, WE, Bacskai, BJ, Mathis, CA, *et al.* Imaging Abeta plaques in living transgenic mice with multiphoton microscopy and methoxy-X04, a systemically administered Congo red derivative. *J Neuropathol Exp Neurol.* 2002; 61:797-805.
11. Higuchi, M, Iwata, N, Matsuba, Y, *et al.* <sup>19</sup>F and <sup>1</sup>H MRI detection of amyloid beta plaques *in vivo*. *Nat Neurosci.* 2005; 8:527-533.
12. Flaherty, DP, Walsh, SM, Kiyota, T, *et al.* Polyfluorinated bis-styrylbenzene beta-amyloid plaque binding ligands. *J Med Chem.* 2007; 50:4986-4992.
13. Amatsubo, T, Morikawa, S, Inubushi, T, *et al.* Trifluoromethoxy-benzylated ligands improve amyloid detection in the brain using (19F) magnetic resonance imaging. *Neurosci Res.* 2009; 63:76-81.
14. Bacskai, BJ, Hickey, GA, Skoch, J, *et al.* Four-dimensional multiphoton imaging of brain entry, amyloid binding, and clearance of an amyloid-beta ligand in transgenic mice. *Proc Natl Acad Sci U S A.* 2003; 100:12462-12467.
15. Bolander, A, Kieser, D, Scholz, C, *et al.* Synthesis of Methoxy-X04 Derivatives and Their Evaluation in Alzheimer's Disease Pathology. *Neurodegener Dis.* 2013.
16. Saroja, G, Soujanya, T, Ramachandram, B, *et al.* 4-Aminophthalimide derivatives as environment-sensitive probes. *Journal of Fluorescence.* 1998; 8:405-410.
17. Raymond, SB, Skoch, J, Hills, ID, *et al.* Smart optical probes for near-infrared fluorescence imaging of Alzheimer's disease pathology. *Eur J Nucl Med Mol Imaging.* 2008; 35 Suppl 1:S93-S98.
18. Ran, C, Xu, X, Raymond, SB, *et al.* Design, synthesis, and testing of difluoroboron-derivatized curcumins as near-infrared probes for *in vivo* detection of amyloid-beta deposits. *J Am Chem Soc.* 2009; 131:15257-15261.
19. Lockhart, A, Ye, L, Judd, DB, *et al.* Evidence for the presence of three distinct binding sites for the thioflavin T class of Alzheimer's disease PET imaging agents on beta-amyloid peptide fibrils. *J Biol Chem.* 2005; 280:7677-7684.
20. Meadowcroft, MD, Connor, JR, Smith, MB, *et al.* MRI and histological analysis of beta-amyloid plaques in both human Alzheimer's disease and APP/PS1 transgenic mice. *J Magn Reson Imaging.* 2009; 29:997-1007.
21. Buell, AK, Esbjorner, EK, Riss, PJ, *et al.* Probing small molecule binding to amyloid fibrils. *Phys Chem Chem Phys.* 2011; 13:20044-20052.
22. Pike, VW. PET radiotracers: crossing the blood-brain barrier and surviving metabolism. *Trends Pharmacol Sci.* 2009; 30:431-440.
23. Benhaim, D and Grushka, E. Effect of n-octanol in the mobile phase on lipophilicity determination by reversed-phase high-performance liquid chromatography on a modified silica column. *J Chromatogr A.* 2008; 1209:111-119.
24. Lombardo, F, Shalaeva, MY, Tupper, KA, *et al.* ElogPoct: a tool for lipophilicity determination in drug discovery. *J Med Chem.* 2000; 43:2922-2928.
25. Lombardo, F, Shalaeva, MY, Tupper, KA, *et al.* ElogD(oct): a tool for lipophilicity determination in drug discovery. 2. Basic and neutral compounds. *J Med Chem.* 2001; 44:2490-2497.

26. Yanagisawa, D, Taguchi, H, Ibrahim, NF, *et al.* Preferred features of a fluorine-19 MRI probe for amyloid detection in the brain. *J Alzheimers Dis.* 2014; 39:617-631.
27. Brooks, AF, Rodnick, ME, Fawaz, MV, *et al.* Radiosynthesis of [18F]gem-difluoroalkenes and [18F]CF<sub>3</sub> Groups - Preparation of [18F]ansoprazole and related analogs for PET imaging of tau neurofibrillary tangles. *J Label Compd Radiopharm.* 2013; 56:S29.
28. van der Born, D, Herscheid, JDM, and Vught, DJ. Aromatic trifluoromethylation using [18F]fluoroform. *J Label Compd Radiopharm.* 2013; 56:S1.

## PART TWO | Development of Molecular Imaging strategies

1 Department of Radiology, Leiden University Medical Center, Leiden, Netherlands

2 Department of Bioorganic Synthesis, Leiden Institute of Chemistry, Leiden University, Leiden, Netherlands

3 Radionucleotide Laboratory, Free University, Amsterdam, Netherlands

4 Division of Drug Delivery Technology, Leiden Academic Center for Drug Research, Leiden University, Leiden, Netherlands

5 Department of Human Genetics, Leiden University Medical Center, Leiden, Netherlands

---



# Chapter 11

Bis-pyridylethenyl benzene as novel backbone  
for amyloid- $\beta$  binding compounds

*Submitted*

**Rob J.A. Nabuurs<sup>1</sup>**

Varsha V. Kapoerchan<sup>2</sup>

Athanasios Metaxas<sup>3</sup>

Sarah Hafith<sup>1</sup>

Maaïke de Backer<sup>1</sup>

Mick M. Welling<sup>1</sup>

Wim Jiskoot<sup>4</sup>

Adrianus M.C.H. van den Nieuwendijk<sup>2</sup>

Albert D. Windhorst<sup>3</sup>

Herman S. Overkleef<sup>2</sup>

Mark A. van Buchem<sup>1</sup>

Mark Overhand<sup>2</sup>

Louise van der Weerd<sup>1,5</sup>



## Abstract

Detection of cerebral  $\beta$ -amyloid ( $A\beta$ ) by targeted contrast agents is of great interest for *in vivo* diagnosis of Alzheimer's disease (AD). Partly because of their planar structure several bis-styrylbenzenes have been previously reported as potential  $A\beta$  imaging agents. However, these compounds are relatively hydrophobic, which likely limits their *in vivo* potential. Based on their structures, we hypothesized that less hydrophobic bis-pyridylethenylbenzenes may also label amyloid. We synthesized several bis-pyridylethenylbenzenes and tested whether these compounds indeed display improved solubility and lower LogP values, and studied their fluorescent properties and  $A\beta$  binding characteristics. Bis-pyridylethenylbenzenes showed a clear affinity for  $A\beta$  plaques on both human and murine AD brain sections. Competitive binding experiments suggested a different binding site than Chrysamine G, a well-known stain for amyloid. With a LogP value between 3 and 5, most bis-pyridylethenylbenzenes were able to enter the brain and label murine amyloid *in vivo* with overall the bis(4-pyridylethenyl)benzenes showing the most favorable characteristics. In conclusion, the presented results suggest that bis-pyridylethenylbenzene may serve as a novel backbone for amyloid imaging agents.

## Introduction

Cerebral accumulation of senile amyloid plaques plays an important role in the pathogenesis of Alzheimer's disease (AD), as it is thought to precede the onset of the first clinical symptoms by up to two decades.<sup>1,2</sup> These typical deposits of fibrillar amyloid- $\beta$  peptides (A $\beta$ ) thereby constitute an important target for the development of imaging agents capable of visualizing and quantifying them. Much progress has been made in the development of such A $\beta$ -targeting imaging ligands suitable for visualization by positron emission tomography (PET), single positron emission tomography (SPECT), fluorescence microscopy or magnetic resonance imaging (MRI).

Pittsburgh compound B (PiB, **1**, **Figure 11.1**), a [<sup>11</sup>C]-benzothiazole derivative, is the best characterized *in vivo* PET radiotracer thus far. The short half-life of <sup>11</sup>C however limits its use to medical centers with an on-site cyclotron. In addition longer-lived <sup>18</sup>F radiofluorinated derivatives have been synthesized, like flutemetamol (**2**)<sup>3</sup>, florbetapir (**3**) and florbetaben(**4**)<sup>4</sup>, of which the first two recently were approved by the U.S. Food and Drug Administration for commercial use.<sup>5,6</sup> However improved A $\beta$ -targeted imaging agents or backbones that could potentially outperform previous agents, bind to specific subtypes of cerebral amyloid or that are suitable for other clinical imaging modalities are still warranted.

The precise mechanisms that cause these small molecules to bind specifically to amyloid structures are still not completely understood.<sup>7</sup> An hydrophobic planarized  $\pi$  system is hypothesized as an important design feature for high binding specificity based on a well-known histological amyloid dye, Congo Red (**5**).<sup>8</sup> *In vivo* application of Congo Red however was not feasible due its limited brain entry. Its molecular structure served as backbone for the development of bis-styrylbenzene imaging probes for PET, SPECT and <sup>19</sup>F MRI, like **6** (Chrysamine G), **7** (X-34)<sup>9</sup>, **8** (ISB)<sup>10</sup>, **9** (FSB)<sup>12</sup> and **10** (Methoxy-X04)<sup>11</sup>. (**Figure 1**) The acidic functional groups appeared to be unnecessary for high affinity A $\beta$  binding, while bis-styrylbenzenes lacking these groups showed  $K_d$ 's ~300 fold lower compared to **9**.

Unfortunately, the use of amyloid targeting bis-styrylbenzenes is limited to preclinical imaging studies that exploit their fluorescent properties.<sup>15</sup> Despite the promising initial *in vivo* <sup>19</sup>F MRI performed with **9** the incorporation of multiple fluorine atoms thus far has not sufficiently increased their sensitivity for the use as an MRI contrast agent.<sup>13,14</sup> In general, many of these compounds are very hydrophobic, their poor aqueous solubility and blood-brain barrier (BBB) passage are likely to limit the *in vivo* imaging potential of these compounds or lead to an unfavorable cerebral washout that causes non-specific signal of unbound compound.

We envisioned that replacement of the phenyl outer rings of the (bis)styrylbenzene backbone with pyridine rings may overcome some of these hurdles, as the presence of the nitrogen atom is expected to improve solubility and lower LogP values. This study therefore aims to investigate whether bis-pyridylethenyl benzene may serve as a new backbone for the development of an amyloid- $\beta$  targeting imaging agent. Synthesized compounds were evaluated with respect to their *in vitro* A $\beta$  binding and specificity, and their fluorescent properties. Partition coefficients (LogP) were determined to assess hydrophobicity. *In vivo* affinity for amyloid plaques and cerebral entrance was evaluated following intravenous injection of the compound in a transgenic AD mouse model.

## Design

We designed a series of six different bis-pyridylethenylbenzenes (**11** – **16**) with the amyloid-targeting compound Methoxy-X04 (**10**)<sup>11</sup> set as starting point for the design and synthesis. (**Figure 11.2**) With an affinity for A $\beta$  plaques in the nanomolar range ( $K_i = 26.8$  nM), this fluorescent small molecule is frequently used for intravital microscopy studies *in vivo* following intravenous or intraperitoneal injection.<sup>11</sup> Compounds **11** – **13** have no substituents at all and can serve to evaluate whether the presence of the two nitrogen atoms can compensate for the hydroxy- and methoxy functionalities in Methoxy-X04. Compounds **14** – **16** contain a methoxy-substituent on the middle ring for a more direct comparison with Methoxy-X04.

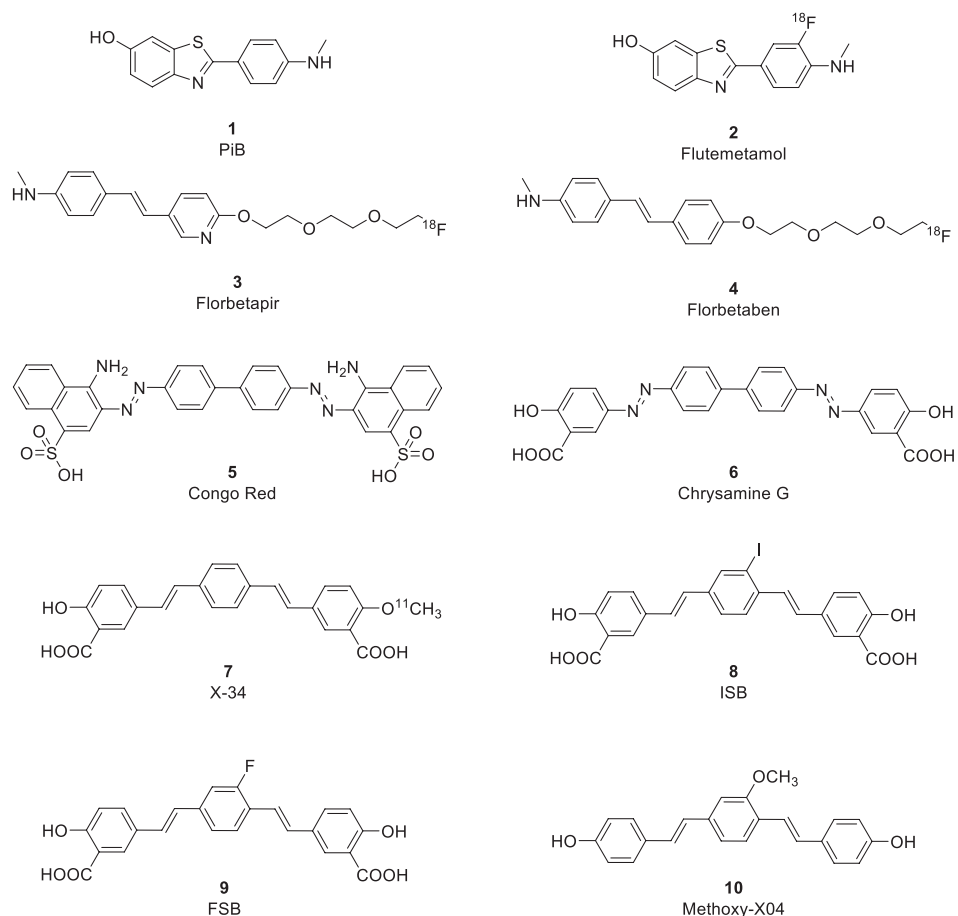


Figure 11.1 Previously reported amyloid- $\beta$  binding ligands

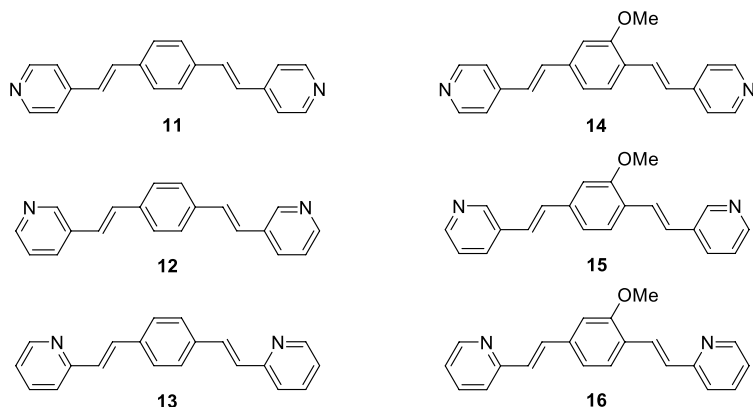
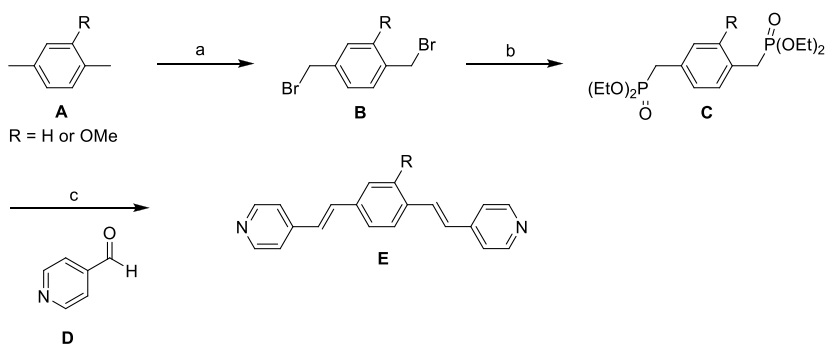


Figure 11.2 Envisioned bis-pyridylethylenylbenzenes

All these compounds are accessible using the general synthesis route recently separately published by ourselves<sup>14</sup> and the group of Boländer *et al.*<sup>16</sup>, which is depicted in **Scheme 11.1** with the key building blocks being diphosphonate **C** and an aldehyde **D**. p-xylene **A** is subjected to radical bromination to yield dibromide **B**. This dibromide is then treated with triethyl phosphite in an Arbuzov reaction to give diphosphonate **C**. A Horner-Wadsworth-Emmons reaction between diphosphonate **C** and an aldehyde **D** yields (E,E)-bis-pyridylethylenylbenzene **E**.

The building blocks needed for the synthesis of compounds **11** – **16** are either easily synthesized or commercially available. (**Figure 11.3**) With all building blocks in hand, compounds **11** – **16** were synthesized. The synthesis proceeded uneventful, and all compounds were obtained in reasonable yields (14 – 45%).



**Scheme 11.1** General synthesis route for the envisioned bis-pyridylethylenyl benzenes

Reagents and conditions: **a)** N-bromosuccinimide, benzoyl peroxide, CCl<sub>4</sub>, reflux, 16 h. **b)** Triethyl phosphite, 150 °C, 16 h. **c)** 1. KOtBu, THF, -10 °C, 20 min. then D, rt, 16 h.

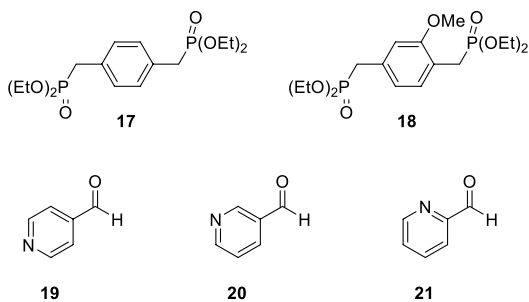


Figure 11.3 The required building blocks

## Results and Discussion

### Fluorescent properties

All synthesized compounds are expected to have fluorescent properties based on their conjugated ring structures. We therefore determined excitation and emission wavelength maxima of 300 nM solutions and the emission intensities were compared to that of Methoxy-X04. (Table 11.1) The intrinsic fluorescent intensity was typically higher for the bis(3-pyridylethenyl) benzenes compared to the bis(2-pyridylethenyl)benzenes.

It has been reported that binding to amyloid may have a significant effect on fluorescence properties<sup>17</sup>, and therefore the fluorescence was also measured in the presence of synthetic A $\beta$  fibrils. The parent compound **10** showed the highest fluorescence yield with a 10-fold increase in the presence of amyloid fibrils. All tested bis-pyridylethenylbenzenes showed an increase of fluorescence after binding, with compound **12** being the brightest. (Table 11.1) Several previously reported A $\beta$ -targeting fluorophores have shown a clear red-shifted emission spectrum following binding<sup>18,19</sup>, but such a spectral shift was not observed for any of the tested bis-pyridylethenylbenzenes.

### Qualitative assessment of human and murine amyloid plaques binding

Fluorescence microscopy was used for a qualitative *ex vivo* assessment of the amyloid-binding properties. A concentration series of each compound (1 – 10 – 100  $\mu$ M) was applied to brain sections of AD patients and of aged APP<sup>swe</sup>-PS1 $\Delta$ E9 (APP/PS1) mice, which have a high amyloid plaque load. At 100  $\mu$ M all compounds showed characteristic staining of amyloid plaques on murine APP-PS1 brain sections. Although all compounds bound to amyloid plaques at high concentration, differences in binding became visible at the lower concentrations. (Table 11.1 and Figure 11.4) No non-specific background labeling or labeling of neurofibrillary tangles (NFTs) was observed at these concentrations suggesting their specificity for amyloid.

As stated in the previous paragraph, the fluorescence intensity with and without amyloid fibrils differed significantly for the various compounds. Therefore, the fluorescence intensity in the presence of fibrils was calculated and expressed relative to the intensity of Methoxy-X04 (**10**). (Table 11.1) Assuming that the fluorescence yield in the presence of synthetic A $\beta$  is representative for that in the presence of amyloid plaques, the staining data was interpreted

Table 11.1 Fluorescent and binding characteristics

Compound	MW	$\lambda_{ex}^a$ (all $\pm$ 1nm)	$\lambda_{em}$ (all $\pm$ 1nm)	Fluorescence intensity <sup>b</sup> (%)	Fluorescence binding to fibrillar A $\beta^b$ (%)	Fold increase on binding to fibrillar A $\beta$	Ex vivo A $\beta$ binding <sup>c</sup>	
							Human	Murine
10	344.403	372	451	100	982	9.82	+	+
11	284.354	354	420	70	227	3.23	++	+++
12	284.354	352	412	225	505	2.24	+	++
13	284.354	356	415	57	312	5.48	++	+++
14	314.380	373	430	16	130	8.18	--	+
15	314.380	360	436	185	359	1.94	--	-
16	314.380	362	441	38	189	4.99	--	+

<sup>a</sup>Ex/Em wavelength maxima were determined of 300 nM solutions. <sup>b</sup>Fluorescence intensity was calculated relative to that of 10. <sup>c</sup>Staining of amyloid plaques in human and APP-PS1 murine at 1  $\mu$ M was scored whether the compound stained nothing (-), less (-), similar (+), slightly more (++) or much more (+++) for amyloid plaques in comparison to 10.

as follows. With no substitution on the inner ring bis-pyridylethenylbenzenes **11** – **13** displayed improved amyloid labeling compared to Methoxy-X04 (**10**). This was already shown for a similar bis-styrylbenzene lacking additional groups, suggesting that planarity indeed plays an important role.<sup>20</sup> Although compounds **12** and **15** expressed the highest fluorescent intensity after synthetic amyloid binding of all tested bis-pyridylethenylbenzenes, their ability to depict amyloid plaques on brain sections seemed less clear. This would suggest that incorporation of a nitrogen atom on the 3<sup>rd</sup> position results in less favorable binding characteristics. Incorporation of an additional methoxy-group (**14** and **16**) resulted in a slightly reduced binding on the murine sections. Compared to Methoxy-X04, however, their ability to depict murine amyloid seems better, as the fluorescence yield of compounds **14** and **16** is lower. This suggests that the nitrogen alone might be sufficient to replace the hydroxy groups present in Methoxy-X04 (**10**). Similar to Methoxy-X04, the affinity of the ligands for human plaques appears to be less than for the murine plaques. As amyloid plaques in humans and mice differ in composition and compactness<sup>21</sup>, this is likely the reason for the observed differences in staining between human and murine AD sections. Nevertheless, staining of human tissue could still be clearly observed for compounds **11** – **13**, and was improved compared to Methoxy-X04 for compound **11** and **13**.

#### Affinity for synthetic Amyloid- $\beta$ fibrils

A competition assay with tritiated amyloid dye Chrysamine G (**6**) was used to determine the binding inhibition coefficient (Ki) for the compounds.<sup>11</sup> Unlike compound **10**, none of the bis-pyridylethenylbenzenes showed any competitive binding to [<sup>3</sup>H]Chrysamine G using either synthetic amyloid fibrils (**Figure 11.5**) or

murine brain homogenate. (**Figure 11.6**) This implies that these compounds use a different binding site than Chrysamine G, and most likely Methoxy-X04 (**10**). Unfortunately, we were therefore unable to determine  $K_i$  values for the synthesized compounds.

### LogP values

The blood-brain barrier (BBB) is formed by a tight layer of endothelial cells in the wall of cerebral blood vessels that regulates the exit and entry of blood compounds into the brain. It is traditionally stated that for optimal passive BBB passage, compounds should preferably have moderately hydrophobicity (LogD or LogP 2.0 - 3.5), although several successful radiopharmaceuticals do not meet this requirement.<sup>22</sup> Therefore LogD or LogP should be

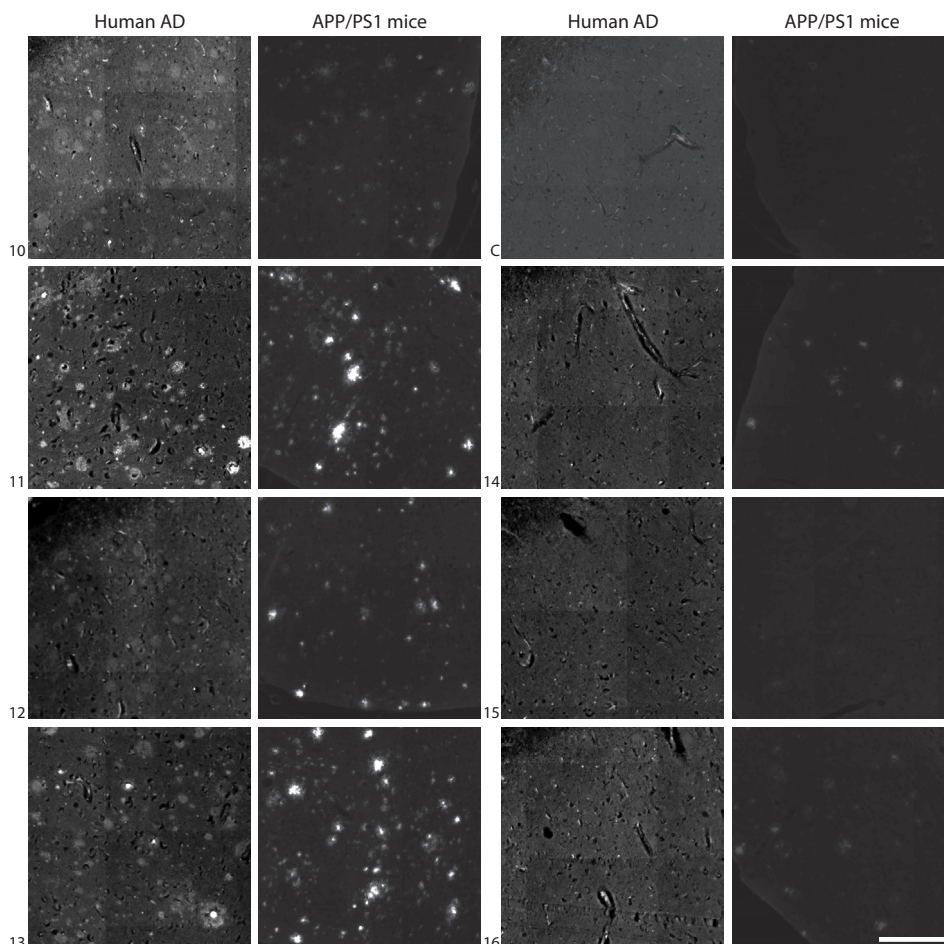


**Figure 11.4** Staining of human and APP/PS1 murine amyloid plaques

All bis-pyridylethenylbenzenes stained both human and murine amyloid plaques after applying 100  $\mu\text{M}$  (data not shown). At 1  $\mu\text{M}$  concentration, differences in binding between the compounds become apparent compared to each other or the negative controls (**C**). All images were taken with the same microscope settings. Scale bar = 200  $\mu\text{m}$ .



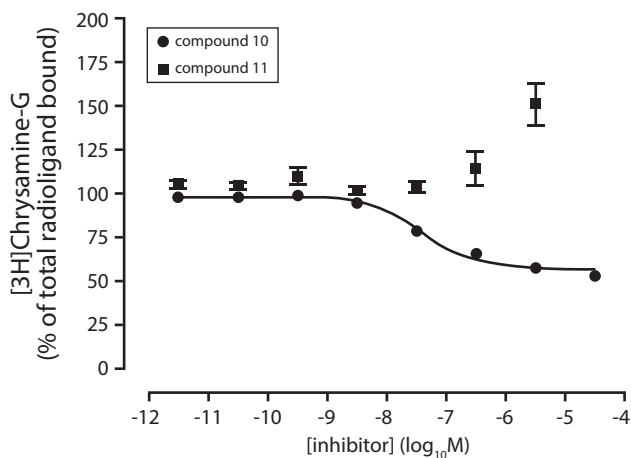


**Figure 11.5 Competition binding with synthetic A $\beta$  fibrils**

Displacement of [ $^3\text{H}$ ]Chrysamine-G binding by Methoxy-X04 (**10**) (closed circles) and compound **11** (open circles), on fibrilized synthetic A $\beta_{1-40}$ . Data are presented as the mean  $\pm$  SEM of one experiment, conducted in triplicate, and replicated three to seven independent times. **10** inhibited the binding of 5 nM [ $^3\text{H}$ ]Chrysamine G with a mean  $K_i$  value of  $24.1 \pm 8.0$  nM.

carefully considered as selection criterion, but when it is applied within one series of compounds it is nonetheless a valid parameter for selection. For each of the compounds **10** – **16**, LogP values were determined with an HPLC-based method according to Benhaim *et al.*<sup>23-25</sup> All compounds have a LogP below that of Methoxy-X04, although none of them meets the before mentioned criterion. (Table 11.2)

### ***In vivo* amyloid plaque labeling in transgenic AD mice**

To assess the ability of the compounds to pass the BBB *in vivo*, solutions of each compound were injected at 30  $\mu\text{mol/kg}$  in aged transgenic APP/PS1 mice, which have extensive cerebral amyloid plaques. One day after injection the mice were sacrificed, their brains were removed and sections were studied according to the fluorescence microscopy set-up used for the stained brain sections. All compounds were readily dissolved using a mixture of 0.05 M compound dissolved in 1:1 DMSO:Cremophor (volume ratio) diluted up to 200  $\mu\text{l}$  with PBS at pH 7.2. Dissolving bis(2-pyridylethenyl)benzenes **13** and **16** however resulted in a viscous substance that was not well tolerated by the animals. *In vivo* targeting of amyloid plaque however was observed for all compounds, showing their ability to pass the BBB. (Figure 11.7 and Table 11.2) No non-specific labeling was detected in the wild type brain. Direct comparison of the *in vivo* amyloid labeling between the different compounds remained difficult, as the amyloid load may differ between the transgenic animals and the fluorescence yield of the compounds varies considerably. Bis-pyridylethenylbenzene **11** showed a comparable signal intensity in individual labeled plaques after intravenous injection compared to Methoxy-X04, while having a 4-fold lower fluorescence yield. Also its methoxy variant, compound **14**, clearly crossed the BBB *in vivo* to label amyloid plaques despite of an almost 10-fold lower fluorescence yield after binding compared to Methoxy-X04.

Table 11.2 LogP values and *in vivo* amyloid labeling

compound	LogP (calc) <sup>a</sup>	LogP (determined)	In vivo amyloid labeling
10	5.55	4.84	+
11	3.94	3.93	+
12	3.94	3.73	+
13	4.12	3.75	+
14	3.86	3.73	+
15	4.03	4.32	+
16	4.16	4.25	+

<sup>a</sup>LogP values were calculated used web-based methods: [www.molinspiration.com](http://www.molinspiration.com) and <http://intro.bio.umb.edu/111-112/OLLM/111F98/jLogP/test.html>. The ability to label amyloid plaques in the brains of APP-PS1 mice following intravenous injection were scored absent (-) or present (+).

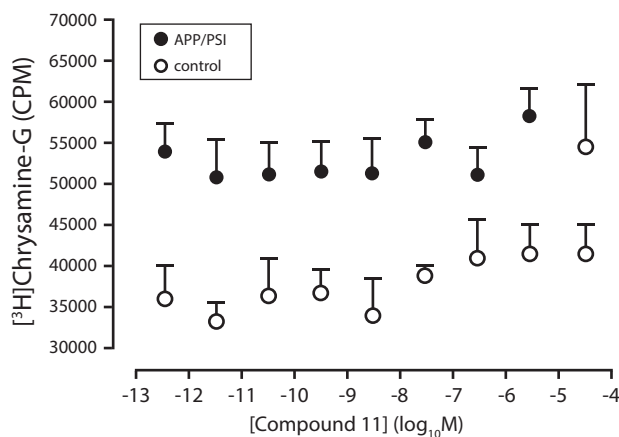
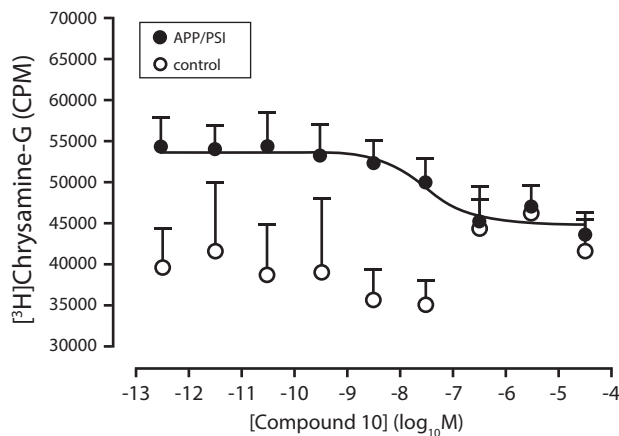


**Figure 11.6 Binding competition with APP/PS1 transgenic brain homogenates**

Displacement of [<sup>3</sup>H]Chrysamine G binding by Methoxy-X04 (**10**) (**A**) and compound **11** (**B**), on brain cortex homogenates of 11 months-old APP/PS1 transgenic and control mice. Data are presented as the mean ± SEM of one experiment, conducted in duplicate and replicated three independent times. **10** inhibited the binding of 5 nM [<sup>3</sup>H]Chrysamine G in APP/PS1 mice (closed circles) with a K<sub>i</sub> value of 27.5 ± 3.5 nM, which is in good agreement with literature.<sup>28</sup>

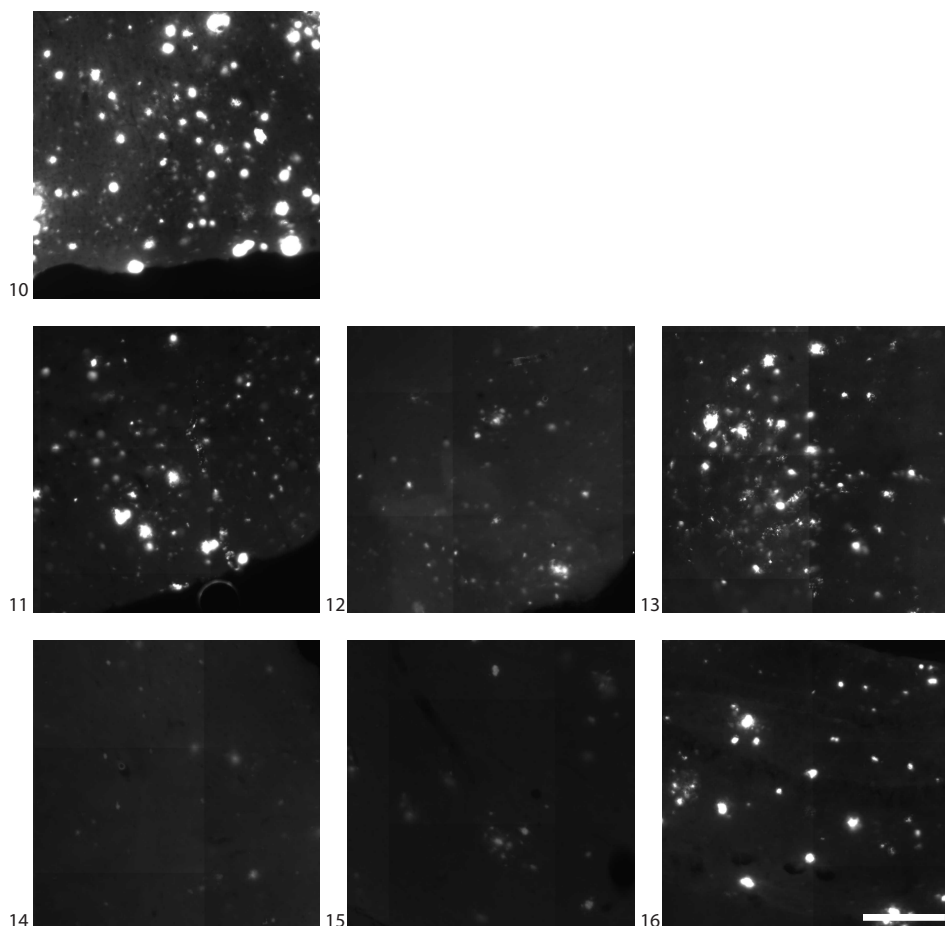


**Figure 11.7** *In vivo* amyloid labeling

Shown are thirty micrometer brain sections of APP/PS1 transgenic mice resected injected with compound **10** – **16**. None of the wild type mice showed amyloid plaques or aspecific labeling. Scale bar = 200  $\mu$ m

## Summary and Conclusion

Several bis-pyridylethenylbenzenes have been prepared and evaluated for their A $\beta$  binding properties and ability to pass the BBB. In general, all compounds showed affinity towards both human and murine fibrillar amyloid. Independent of the position of the nitrogen atom, the bis-pyridylethenylbenzenes without any additional groups seemed to show a higher affinity to amyloid in comparison with Methoxy-X04 (**10**). Besides the possible influence of the nitrogen atom, this might be due to their planar structure, which was previously suggested to be advantageous for a similar (bis)styrylbenzene with no further substituents.<sup>20</sup> The methoxy group on the inner ring structure seemed to result in a decrease in amyloid binding, particularly for human amyloid. However, in contrast to several known bis-styrylbenzenes, like **10**, the bis-pyridylethenylbenzenes did not share a common binding site with Chrysamine G.

In addition, all bis-pyridylethenylbenzenes seemed to cross the BBB and label amyloid *in vivo*. Based on the above results, compound **11**, (E,E)-1,4-bis(4-pyridylethenyl)benzene, showed the most favorable *ex* and *in vivo* characteristics and as such might serve as a starting point to further explore the potency of bis-pyridylethenylbenzenes.

A direct application of bis-pyridylethenylbenzenes for amyloid targeting would be their use in preclinical optical imaging. In addition we believe that the bis-pyridylethenylbenzene may serve as a novel backbone for the development of amyloid targeting PET or SPECT probes. As their binding sites may differ from existing amyloid targeting imaging probes, these compounds may provide additional information regarding accumulation of cerebral amyloid.

## Materials and Methods

### Preparation of A $\beta$ <sub>1-40</sub> fibrils

A $\beta$  fibrils were prepared by stirring a 0.5 mg/ml solution of A $\beta$ <sub>1-40</sub> peptide (RPeptide, Bogart, GA) at 37 °C for 3 days, which resulted in a cloudy solution. The presence of fibrils was confirmed by the presence of an emission peak at 482 nm (excitation 440 nm) upon addition of a 5  $\mu$ M solution in PBS of Thioflavin T (Sigma, Germany) to a small amount of fibrils. Aliquots of 10  $\mu$ l were transferred to Eppendorf vials and stored at -80 °C until the assay was to be performed.

### Fluorescence spectra

All compounds were dissolved in DMSO at 0.3 mM and diluted to 300 nM with 10 % ethanol in PBS (pH 7.2). Fluorescence spectra were measured on a Varian Cary Eclipse fluorescence spectrophotometer to obtain excitation and emission wavelength maxima, which were used to select the correct fluorescence filter settings for further microscopic evaluation. All measurements were carried out at 20 °C and in triplicate. 3D emission-excitation spectra were obtained by adding 500  $\mu$ l of the dissolved compounds to previously prepared A $\beta$  aliquots. After manual shaking for 30 sec, 300  $\mu$ l samples were measured (Infinity M1000, Tecan, Switzerland).

### Staining of human and transgenic AD brain sections

Stock solutions of 3 mM in DMSO were diluted to 1 – 10 – 100  $\mu$ M in 2:3 volume ratio PBS:ethanol and sonicated for 15 minutes. Paraffin sections (8  $\mu$ m) of human AD cortex, 14 months old transgenic murine APP/PS1 brain and age-matched control cortices were deparaffinized prior to staining for 10 minutes in absolute darkness. After gently rinsing with tap water, sections were placed in 0.1 % NaOH in 80% ethanol for 2 minutes, air dried and coverslipped using Aqua / Polymount. Fluorescence of the stained sections was analyzed using a whole microscopic slide scanner (Pannoramic MIDI, 3DHitech, Hungary) with a DAPI filter cube (Ex 365 nm; Em 445/50 nm) using the same intensity setting throughout all experiments.

### *In vivo* A $\beta$ plaque labeling in transgenic AD mice

Twelve-to-fourteen-month-old APP/PS1 mice or age-matched wildtype animals (n=2 per compound) were injected intravenously with 0.05 M dissolved in 1:1 volume ratio

DMSO:Cremophor diluted with PBS (pH 7.2) to a total volume of 200  $\mu$ l, resulting in a total dose of 30  $\mu$ mol/kg. One day after injection, animals were sacrificed using 200  $\mu$ l Euthanasol (AST Pharma) prior to transcardial perfusion with 4% paraformaldehyde in PBS (pH 7.2). Brains were removed and cryoprotected in 4% PFA with 10% sucrose for 4 hours, followed by immersion in 4% PFA with 30% sucrose overnight. Snap-frozen brains were cryosectioned (30  $\mu$ m) and fluorescence images were analyzed as described above.

### Brain homogenates

Male, control and transgenic APP/PS1 mice (11 months old) were killed by decapitation. The cortices were removed and homogenized using a DUALL tissue homogenizer (20 strokes, 2000 rpm), in a 20-fold excess (v/w) of ice-cold 0.25 M sucrose. Homogenates were isolated by centrifugation (40 min x 250,000 x g) in a refrigerated Beckman ultracentrifuge (rotor 60-Ti). The resulting pellet was suspended in 20 volumes of 150 mM Tris + 20 % ethanol buffer (pH 7.0) for competition binding experiments.

### Competition binding assay

Competition binding experiments were conducted at room temperature, in a final volume of 1 ml assay buffer (150 mM Tris-HCl, 20% ethanol, pH 7.0). Compounds were dissolved as 3 mM stock solutions in DMSO, sonicated for 15 min, and used in a final concentration range of 30  $\mu$ M to 30 pM. 10  $\mu$ l of unlabeled test compounds was combined with 890  $\mu$ l of assay buffer and 50  $\mu$ l of 100 nM [ $^3$ H]Chrysamine G stock (specific activity 33.8 Ci/mmol). The mixture was sonicated for 10 min, and the assay was subsequently started by the addition of 50  $\mu$ l synthetic A $\beta$ <sub>1-40</sub> fibrils or by addition of 400  $\mu$ l of the brain homogenate suspension. Nonspecific binding was determined in the presence of 1  $\mu$ M of **10**. Incubations were terminated after 1 h via filtration through Whatman GF/B filters (pre-soaked in binding buffer), using a 48-well Brandel harvester. The filters were washed two times with 3 ml of ice-cold binding buffer (pH 7.0), and radioactivity was determined by liquid scintillation spectrometry in 5 ml of Optiphase-HiSafe 3, at an efficiency of 40 %.

$K_i$  values were determined by nonlinear regression analysis using the equation:  $\log EC_{50} = \log[10 \wedge \log K_i * (1 + \text{Radioligand} / \text{Hot} K_d \text{NM})]$  where  $K_d = 200$  nM, and radioligand = 5nM. (GraphPad Software Inc., San Diego, CA)

### Procedure for LogP determinations

LogP determinations were performed using literature procedures.<sup>23</sup> The measurements were performed on a Jasco HPLC-system (detection simultaneously at 214 and 254 nm) coupled to a Perkin Elmer Sciex API 165 mass instrument with a custom-made Electrospray Interface (ESI). An analytical Gemini C<sub>18</sub> column (Phenomenex, 50 x 4.60 mm, 3 micron) was used in combination with buffers A) phosphate buffer of pH = 7.0 (0.02 M Na<sub>2</sub>HPO<sub>4</sub> adjusted to pH = 7.0 with phosphoric acid) and B) 0.25% octanol in methanol.

Of all compounds to be evaluated, stock solutions of 0.5 mg ml<sup>-1</sup> were prepared in methanol. These stock solutions were then diluted with water, making sure that the volume percentage of water was such that the compounds did not precipitate (max 40% water). A 0.25 mg ml<sup>-1</sup> solution of NaNO<sub>3</sub> in water was used as a non-retaining compound to determine the dead time

of the system. For calibration purposes known compounds were taken from the literature. (**Table 3**) Of these compounds, 0.25 mg ml<sup>-1</sup> solutions in either 75% H<sub>2</sub>O/MeOH or 50% H<sub>2</sub>O/MeOH were made.

For each sample, a series of four isocratic runs was performed, (for instance 55, 60, 65, 70% B), and the retention times (from UV-detection at 214 nm) thus obtained were converted to the retention factor  $k'$  according to the formula  $k' = (t_R - t_0)/t_0$ , with  $t_R$  being the retention time of the compound and  $t_0$  being the retention time of NaNO<sub>3</sub>. The retention factors were extrapolated to 0% B, yielding  $k'_w$ . As there is a linear relationship between LogP and log  $k'_w$  plotting LogP values of known compounds against obtained log  $k'_w$  values in this system yields a calibration curve. From this curve, LogP values of unknown compounds were calculated from their  $k'_w$  values.

## Synthesis Procedures

### General

Reagents and solvents were used as provided, unless stated otherwise. 2-pyridinecarboxaldehyde (**21**) and 4-pyridinecarboxaldehyde (**19**) were purchased from Acros, 3-pyridinecarboxaldehyde (**20**) was purchased from Sigma-Aldrich. THF was distilled over LiAlH<sub>4</sub> prior to use. Reactions were carried out under inert conditions and ambient temperature, unless stated otherwise. Prior to performing a reaction, traces of water were removed from the starting materials by repeated co-evaporation with anhydrous 1,4-dioxane or anhydrous toluene. These solvents were stored over 4 Å molsieves. Reactions were monitored by thin layer chromatography on aluminum coated silica sheets (Merck, silica 60 F254), using visualization either with iodine, or spraying with a solution of 25 g (NH<sub>4</sub>)<sub>2</sub>MoO<sub>4</sub>, 10 g (NH<sub>4</sub>)<sub>4</sub>Ce(SO<sub>4</sub>)<sub>4</sub> in 100 ml H<sub>2</sub>SO<sub>4</sub> and 900 ml H<sub>2</sub>O, or a solution of 20% H<sub>2</sub>SO<sub>4</sub> in ethanol, followed by charring at ~150°C. Column chromatography was carried out with silica gel (Screening Devices bv, 40-63 μm particle size, 60 Å), using technical grade solvents. NMR spectra were recorded at 298K on a Bruker AV400 using deuterated solvents. All carbon spectra are proton-decoupled. Chemical shifts (δ) are given in ppm, in <sup>13</sup>C spectra relative to the solvent peaks of CDCl<sub>3</sub> (77.0 ppm) or CD<sub>3</sub>OD (49.0 ppm), in <sup>1</sup>H spectra relative to the solvent peak of tetramethylsilane (0.0 ppm) or CD<sub>3</sub>OD (3.31 ppm). Coupling constants are given in Hz. LC-MS analysis was performed on a Finnigan Surveyor

**Table 11.3 Reference LogP values**

Compound	LogP
Resorcinol	0.8
p-nitroaniline	1.39
Phenol	1.46
m-nitrophenol	2
2-naphthol	2.7
Naphthalene	3.37

Based on known literature values, the LogP of several reference compounds yield a required calibration curve to determine the LogP values of our compounds.<sup>23-25</sup>

HPLC system with a Gemini C<sub>18</sub> 50 × 4.6 mm column (3 micron, Phenomenex, Torrance, CA, USA) (detection at 200-600 nm), coupled to a Thermo Finnigan LCQ Advantage Max mass spectrometer (Breda, The Netherlands) with electrospray ionization (ESI; system 1), with as eluents A: H<sub>2</sub>O; B: MeCN and C: 1% aq. TFA. For RP-HPLC purification of the peptides, a Gilson GX-281 automated HPLC system (Gilson), supplied with a preparative Gemini C<sub>18</sub> column (Phenomenex, 150 × 21.2 mm, 5 micron) was used. The applied buffers were A: 0.2% aq. TFA or 20 mM NH<sub>4</sub>OAc and B: MeOH.

IR spectra were recorded on a Perkin Elmer Paragon 1000 FT-IR Spectrometer. High resolution mass spectra were recorded by direct injection (2 μL of a 2 μM solution in H<sub>2</sub>O/MeCN; 50/50; v/v and 0.1% formic acid) on a mass spectrometer (Thermo Finnigan LTQ Orbitrap) equipped with an electrospray ion source in positive mode (source voltage 3.5 kV, sheath gas flow 10, capillary temperature 250 °C) with resolution R = 60000 at m/z 400 (mass range m/z = 150-2000) and dioctylphthalate (m/z = 391.28428) as a "lock mass". The high resolution mass spectrometer was calibrated prior to measurements with a calibration mixture (Thermo Finnigan). It should be noted that we did not obtain the suited HRMS data for every compound. This finding is in agreement with related compounds as reported earlier by us.. Based on the other characterization data obtained for each compounds we know for sure that our compounds are sound. For clarity, we here include the HMRS data that we did find: compound **14**: Exact mass: Calculated for [C<sub>21</sub>H<sub>19</sub>N<sub>2</sub>O]<sup>+</sup>: 315.14919. Found: 315.14901 [M + H]<sup>+</sup>. compound **15** Exact mass: Calculated for [C<sub>21</sub>H<sub>19</sub>N<sub>2</sub>O]<sup>+</sup>: 315.14919. Found: 315.14915 [M + H]<sup>+</sup>.

### General procedure for the Horner-Wadsworth-Emmons reaction

The diphosphonate (0.95 mmol) was dissolved in THF (20 mL) and cooled to -10° C. KOtBu (0.30 g, 2.45 mmol) was added and the black mixture stirred for 20 min. A solution of the aldehyde (2.37 mmol) in THF (6 mL) was added and the reaction stirred at rt for 16 h. The reaction was cooled to 0°C, quenched with water and extracted five times with EtOAc. The combined organic layers were dried (Na<sub>2</sub>SO<sub>4</sub>), filtered and concentrated. The crude product was subjected to column chromatography to yield the pure product.

#### (*E,E*)-1,4-bis(4-pyridylethenyl)benzene (**11**)

According to the general procedure, diphosphonate **17** (0.19 g, 0.5 mmol) was reacted with 4-pyridinecarboxaldehyde **19** (0.12 mL, 1.25 mmol). After work-up, the resulting yellow solids were purified by column chromatography (50 → 70% EtOAc/light petroleum) and the pure compound was obtained as a bright yellow solid (43 mg, 0.15 mmol, 30%).

<sup>1</sup>H NMR (CDCl<sub>3</sub>, 400 MHz): δ 8.59 (d, *J* = 5.6 Hz, 4H); 7.56 (s, 4H); 7.38 (d, *J* = 5.7 Hz, 4H); 7.30 (d, *J* = 16.3 Hz, 2H); 7.05 (d, *J* = 16.3 Hz, 2H). <sup>13</sup>C NMR (CDCl<sub>3</sub>, 100 MHz): δ 150.1; 144.4; 136.5; 132.4; 127.5; 126.4; 120.8. IR (neat): 3442.0; 1591.6; 1414.1; 1217.5; 1118.9; 973.4; 868.4; 830.6; 595.9; 556.2. LC-MS retention time: 3.86 min (10 → 90% MeCN, 15 min run). Mass (ESI): *m/z* 285.13 [M + H]<sup>+</sup>.

#### (*E,E*)-1,4-bis(3-pyridylethenyl)benzene (**12**)

According to the general procedure, diphosphonate **17** (0.19 g, 0.5 mmol) was reacted with 3-pyridinecarboxaldehyde **19** (0.12 mL, 1.25 mmol). After work-up, the resulting yellow solids

were purified by column chromatography (50 → 100% EtOAc/light petroleum) and the pure compound was obtained as a bright yellow solid (64 mg, 0.23 mmol, 45%).

$^1\text{H NMR}$  ( $\text{CDCl}_3$ , 400 MHz):  $\delta$  8.73 (s, 2H); 8.49 (d,  $J = 4.3$  Hz, 2H); 7.83 (d,  $J = 8.0$  Hz, 2H); 7.53 (s, 4H); 7.29 (dd,  $J = 8.2$  Hz,  $J = 5.1$  Hz, 2H); 7.16 (d,  $J = 16.4$  Hz, 2H); 7.09 (d,  $J = 16.4$  Hz, 2H).  $^{13}\text{C NMR}$  ( $\text{CDCl}_3$ , 100 MHz):  $\delta$  148.5; 148.5; 136.5; 132.9; 132.6; 130.1; 127.0; 125.0; 123.5. IR (neat): 3029.1; 1564.9; 1481.0; 1427.6; 1022.1; 965.9; 823.5; 704.8; 551.7. LC-MS retention time: 3.87 min (10 → 90% MeCN, 15 min run). Mass (ESI):  $m/z$  285.13 [ $\text{M} + \text{H}$ ] $^+$ .

#### **(*E,E*)-1,4-bis(2-pyridylethenyl)benzene (13)**

According to the general procedure, diphosphonate **17** (0.19 g, 0.5 mmol) was reacted with 2-pyridinecarboxaldehyde **21** (0.12 mL, 1.25 mmol). After work-up, the resulting yellow solids were purified by column chromatography (0 → 20% EtOAc/light petroleum) and the pure compound was obtained as a bright yellow solid (20 mg, 0.07 mmol, 14%).

$^1\text{H NMR}$  ( $\text{CDCl}_3$ , 400 MHz):  $\delta$  8.62 (d,  $J = 4.4$  Hz, 2H); 7.70-7.64 (m, 2H); 7.65 (d,  $J = 16.2$  Hz, 2H); 7.60 (s, 4H); 7.40 (d,  $J = 7.8$  Hz, 2H); 7.20 (d,  $J = 16.0$  Hz, 2H); 7.16 (dd,  $J = 7.0$  Hz,  $J = 5.4$  Hz, 2H).  $^{13}\text{C NMR}$  ( $\text{CDCl}_3$ , 100 MHz):  $\delta$  155.5; 149.6; 136.7; 136.6; 132.2; 128.0; 127.5; 122.2; 122.1. IR (neat): 1634.1; 1581.5; 1559.8; 1467.9; 1431.7; 1333.4; 1205.7; 1145.3; 981.8; 873.8; 829.9; 763.9; 736.2; 609.6; 547.6. LC-MS retention time: 3.84 min (10 → 90% MeCN, 15 min run). Mass (ESI):  $m/z$  285.13 [ $\text{M} + \text{H}$ ] $^+$ .

#### **(*E,E*)-1-methoxy-2,5-bis(4-pyridylethenyl)benzene (14)**

According to the general procedure, diphosphonate **18** (0.20 g, 0.5 mmol) was reacted with 4-pyridinecarboxaldehyde **19** (0.12 mL, 1.25 mmol). After work-up, the resulting yellow solids were purified by column chromatography (50% EtOAc/light petroleum → 2% MeOH/EtOAc) and the pure compound was obtained as a bright yellow solid (20 mg, 0.07 mmol, 14%).

$^1\text{H NMR}$  ( $\text{CDCl}_3$ , 400 MHz):  $\delta$  8.60-8.55 (m, 4H); 7.80 (s,  $^1\text{H}$ ); 7.64 (d,  $J = 16.3$  Hz,  $^1\text{H}$ ); 7.61 (d,  $J = 8.1$  Hz,  $^1\text{H}$ ); 7.42 (d,  $J = 6.1$  Hz, 2H); 7.40-7.36 (m, 4H); 7.17 (s,  $^1\text{H}$ ); 6.97 (d,  $J = 16.2$  Hz,  $^1\text{H}$ ); 3.98 (s,  $^3\text{H}$ ).  $^{13}\text{C NMR}$  ( $\text{CDCl}_3$ , 100 MHz):  $\delta$  156.5; 137.7; 131.7; 130.9; 128.7; 127.7; 127.3; 125.8; 120.9; 120.8; 119.9; 108.8; 55.9. IR (neat): 1633.9; 1590.5; 1463.7; 1417.6; 1389.6; 1323.3; 1297.7; 1116.6; 1029.2; 971.4; 819.7; 805.4; 616.0; 582.4; 548.1; 518.4. LC-MS retention time: 4.14 min (10 → 90% MeCN, 15 min run). Mass (ESI):  $m/z$  315.2 [ $\text{M} + \text{H}$ ] $^+$ .

#### **(*E,E*)-1-methoxy-2,5-bis(3-pyridylethenyl)benzene (15)**

According to the general procedure, diphosphonate **18** (0.20 g, 0.5 mmol) was reacted with 3-pyridinecarboxaldehyde **20** (0.12 mL, 1.25 mmol). After work-up, the resulting yellow solids were purified by column chromatography (50% → 100% EtOAc/light petroleum) and the pure compound was obtained as a bright yellow solid (54 mg, 0.17 mmol, 34%).

$^1\text{H NMR}$  ( $\text{CDCl}_3$ , 400 MHz):  $\delta$  8.79-8.65 (m, 2H); 8.48 (dd,  $J = 9.3$  Hz,  $J = 4.7$  Hz, 2H); 7.88-7.81 (m, 2H); 7.59 (d,  $J = 8.0$  Hz,  $^1\text{H}$ ); 7.52 (d,  $J = 16.6$  Hz,  $^1\text{H}$ ); 7.31-7.25 (m, 2H); 7.19-7.03 (m, 4H); 3.97 (s,  $^3\text{H}$ ).  $^{13}\text{C NMR}$  ( $\text{CDCl}_3$ , 100 MHz):  $\delta$  157.3; 148.6; 148.5; 148.3; 137.7; 133.6; 132.8; 132.6; 132.6; 130.5; 126.9; 125.9; 125.4; 125.2; 125.1; 123.5; 123.5; 119.5; 115.6; 108.9; 55.6. IR (neat): 1633.7; 1567.2; 1557.6; 1479.8; 1463.5; 1423.3; 1328.1; 1240.6; 1164.2; 1117.7; 1035.0; 1024.0; 964.2; 819.8; 799.3; 705.5; 643.8; 627.1; 549.8.



LC-MS retention time: 4.14 min (10 → 90% MeCN, 15 min run). Mass (ESI):  $m/z$  315.2 [M + H]<sup>+</sup>.

#### **(E,E)-1-methoxy-2,5-bis(3-pyridylethenyl)benzene (16)**

According to the general procedure, diphosphonate **18** (0.20 g, 0.5 mmol) was reacted with 2-pyridinecarboxaldehyde **21** (0.12 mL, 1.25 mmol). After work-up, the resulting yellow solids were purified by column chromatography (0% → 30% EtOAc/light petroleum) and the pure compound was obtained as a bright yellow solid (42 mg, 0.13 mmol, 27%).

<sup>1</sup>H NMR (CDCl<sub>3</sub>, 400 MHz): δ 8.61 (s, 2H); 7.93 (d,  $J$  = 16.3 Hz, 1H); 7.70-7.58 (m, 4H); 7.45 (d,  $J$  = 8.2 Hz, 1H); 7.41 (d,  $J$  = 7.9 Hz, 1H); 7.31-7.08 (m, 6H); 3.95 (s, 3H). <sup>13</sup>C NMR (CDCl<sub>3</sub>, 100 MHz): δ 157.6; 156.2; 155.5; 149.7; 149.5; 137.9; 136.6; 136.4; 132.4; 128.8; 128.2; 127.5; 127.4; 125.9; 122.1; 122.1; 121.8; 121.8; 119.9; 109.2; 55.5. IR (neat): 1584.0; 1562.5; 1467.9; 1430.5; 1248.3; 1036.0; 970.7; 769.3; 668.0. LC-MS retention time: 4.10 min (10 → 90% MeCN, 15 min run). Mass (ESI):  $m/z$  315.07 [M + H]<sup>+</sup>.

#### **Tetraethyl 1,4-xylylene diphosphonate (17)**

As described previously by Kikuchi *et al.*<sup>26</sup>, a solution of NaBrO<sub>3</sub> (12.1 g, 80 mmol) in H<sub>2</sub>O (40 mL) was added to a solution of p-xylene (2.47 mL, 20 mmol) in EtOAc (40 mL) and the mixture was vigorously stirred. A solution of NaHSO<sub>3</sub> (8.3 g, 80 mmol) in H<sub>2</sub>O (80 mL) was added dropwise within 15 min and the reaction was stirred for 5 h. After the reaction mixture was poured out in Et<sub>2</sub>O (300 mL), the layers were separated and the aqueous layer extracted twice with Et<sub>2</sub>O. The combined organic layers were washed with 2 M Na<sub>2</sub>S<sub>2</sub>O<sub>3</sub>, dried (Na<sub>2</sub>SO<sub>4</sub>), filtered and concentrated. The resulting white solids were subjected to column chromatography (0 → 5% EtOAc/light petroleum) and the product was obtained as a white solid (5.4 g), but not completely pure.

<sup>1</sup>H NMR (CDCl<sub>3</sub>, 400 MHz) δ 7.37 (s, 4H); 4.47 (s, 4H). <sup>13</sup>C NMR (CDCl<sub>3</sub>, 100 MHz) δ 129.5; 32.8. The impure 1,4-di(bromomethyl)benzene (5.4 g) was dissolved in triethyl phosphite (8.6 mL, 50 mmol) and the mixture was heated to reflux for 16 h. After cooling, the crude product was applied to a silica column and purified (50% EtOAc/light petroleum → 2% MeOH/EtOAc). The pure product was obtained as white fluffy powder (5.6 g, 14.8 mmol, 74% over two steps). <sup>1</sup>H NMR (CDCl<sub>3</sub>, 400 MHz) δ 7.25 (s, 4H); 4.07-3.95 (m, 8H); 3.13 (d,  $J$  = 20.2 Hz, 4H); 1.24 (t,  $J$  = 7.1 Hz, 12H). <sup>13</sup>C NMR (CDCl<sub>3</sub>, 100 MHz) δ 130.2; 130.1; 130.1; 129.9; 129.8; 129.7; 62.0; 62.0; 61.9; 34.0; 33.0; 16.3; 16.3; 16.2. <sup>31</sup>P NMR (CDCl<sub>3</sub>, 162 MHz): δ 26.7 (s).

#### **Tetraethyl 2-methoxy-1,4-xylylene diphosphonate (18)**

As described previously by Kumar *et al.*<sup>27</sup>, 2,5-dimethylanisole (1.36 g, 10 mmol) was dissolved in CCl<sub>4</sub> (22 mL). N-bromosuccinimide (3.92 g, 22 mmol) and benzoyl peroxide (20 mg) were added and the mixture heated to reflux for 2 h. After cooling to rt, the reaction mixture was filtered over Celite and concentrated. The resulting solids were purified by column chromatography (0 → 5% EtOAc/light petroleum). The dibromide was obtained as white solid (1.71 g, 5.8 mmol, 58%).

<sup>1</sup>H NMR (CDCl<sub>3</sub>, 400 MHz): δ 7.27 (d,  $J$  = 7.7 Hz, 1H); 6.92 (dd,  $J$  = 7.6 Hz,  $J$  = 1.2 Hz, 1H); 6.89 (s, 1H); 4.52 (s, 2H); 4.44 (s, 2H); 3.88 (s, 3H). <sup>13</sup>C NMR (CDCl<sub>3</sub>, 100 MHz): δ 157.4; 139.7; 131.0; 126.3; 121.1; 111.5; 55.6; 33.2; 28.3.

Next, the 2,5-di(bromomethyl)-methoxybenzene (1.71 g, 5.8 mmol) was dissolved in triethyl phosphite (2.5 mL, 14.5 mmol) and the mixture was heated to reflux for 16 h. The mixture was

cooled, and directly applied to a silica column (50% EtOAc/PE → 4% MeOH/EtOAc). The pure product was obtained as a yellowish solid (1.55 g, 3.8 mmol, 66%).

$^1\text{H}$  NMR ( $\text{CDCl}_3$ , 400 MHz):  $\delta$  7.25 (dd,  $J = 7.6$  Hz,  $J = 2.9$  Hz, 1H); 6.86 (s, 1H); 6.83 (d,  $J = 7.6$  Hz, 1H); 4.07-3.95 (m, 8H); 3.84 (s, 1H); 3.21 (d,  $J = 21.4$  Hz, 2H); 3.13 (d,  $J = 22.2$  Hz, 2H); 1.27-1.20 (m, 12H).  $^{13}\text{C}$  NMR ( $\text{CDCl}_3$ , 100 MHz):  $\delta$  157.2; 131.5; 131.1; 121.9; 121.900; 118.85; 112.1; 55.5; 34.4; 33.0; 27.0; 25.6; 16.3.  $^{31}\text{P}$  NMR ( $\text{CDCl}_3$ , 162 MHz):  $\delta$  27.39 (d,  $J = 9.0$  Hz), 26.77 (d,  $J = 9.1$  Hz).

## References

1. Frisoni, GB, Fox, NC, Jack, CR, Jr., *et al.* The clinical use of structural MRI in Alzheimer disease. *Nat Rev Neurol.* 2010; 6:67-77.
2. Jack, CR, Jr., Knopman, DS, Jagust, WJ, *et al.* Hypothetical model of dynamic biomarkers of the Alzheimer's pathological cascade. *Lancet Neurol.* 2010; 9:119-128.
3. Vandenberghe, R, Van, LK, Ivanoiu, A, *et al.* <sup>18</sup>F-flutemetamol amyloid imaging in Alzheimer disease and mild cognitive impairment: a phase 2 trial. *Ann Neurol.* 2010; 68:319-329.
4. Barthel, H, Gertz, HJ, Dresel, S, *et al.* Cerebral amyloid-beta PET with florbetaben (<sup>18</sup>F) in patients with Alzheimer's disease and healthy controls: a multicentre phase 2 diagnostic study. *Lancet Neurol.* 2011; 10:424-435.
5. GE beta-amyloid agent approved. *J Nucl Med.* 2013; 54:10N.
6. Yang, L, Rieves, D, and Ganley, C. Brain amyloid imaging--FDA approval of florbetapir F18 injection. *N Engl J Med.* 2012; 367:885-887.
7. Buell, AK, Esbjorner, EK, Riss, PJ, *et al.* Probing small molecule binding to amyloid fibrils. *Phys Chem Chem Phys.* 2011; 13:20044-20052.
8. Nesterov, EE, Koch, J, Hyman, BT, *et al.* *In vivo* optical imaging of amyloid aggregates in brain: design of fluorescent markers. *Angew Chem Int Ed Engl.* 2005; 44:5452-5456.
9. Styren, SD, Hamilton, RL, Styren, GC, *et al.* X-34, a fluorescent derivative of Congo red: a novel histochemical stain for Alzheimer's disease pathology. *J Histochem Cytochem.* 2000; 48:1223-1232.
10. Kung, MP, Hou, C, Zhuang, ZP, *et al.* IMPY: an improved thioflavin-T derivative for *in vivo* labeling of beta-amyloid plaques. *Brain Res.* 2002; 956:202-210.
11. Klunk, WE, Bacskai, BJ, Mathis, CA, *et al.* Imaging Abeta plaques in living transgenic mice with multiphoton microscopy and methoxy-X04, a systemically administered Congo red derivative. *J Neuropathol Exp Neurol.* 2002; 61:797-805.
12. Higuchi, M, Iwata, N, Matsuba, Y, *et al.* <sup>19</sup>F and <sup>1</sup>H MRI detection of amyloid beta plaques *in vivo*. *Nat Neurosci.* 2005; 8:527-533.
13. Flaherty, DP, Walsh, SM, Kiyota, T, *et al.* Polyfluorinated bis-styrylbenzene beta-amyloid plaque binding ligands. *J Med Chem.* 2007; 50:4986-4992.
14. Nabuurs, RJA, Kapourchan, VV, Metaxas, A, *et al.* Polyfluorinated bis-styrylbenzenes as amyloid-beta plaque binding ligands. *Bioorg Med Chem.* 2014.
15. Bacskai, BJ, Hickey, GA, Koch, J, *et al.* Four-dimensional multiphoton imaging of brain entry, amyloid binding, and clearance of an amyloid-beta ligand in transgenic mice. *Proc Natl Acad Sci U S A.* 2003; 100:12462-12467.
16. Bolander, A, Kieser, D, Scholz, C, *et al.* Synthesis of Methoxy-X04 Derivatives and Their Evaluation in Alzheimer's Disease Pathology. *Neurodegener Dis.* 2013.
17. Saroja, G, Soujanya, T, Ramachandram, B, *et al.* 4-Aminophthalimide derivatives as environment-sensitive probes. *Journal of Fluorescence.* 1998; 8:405-410.
18. Raymond, SB, Koch, J, Hills, ID, *et al.* Smart optical probes for near-infrared fluorescence imaging of Alzheimer's disease pathology. *Eur J Nucl Med Mol Imaging.* 2008; 35 Suppl 1:S93-S98.
19. Ran, C, Xu, X, Raymond, SB, *et al.* Design, synthesis, and testing of difluoroboron-derivatized curcumins as near-infrared probes for *in vivo* detection of amyloid-beta deposits. *J Am Chem Soc.* 2009; 131:15257-15261.
20. Flaherty, DP, Kiyota, T, Dong, Y, *et al.* Phenolic bis-styrylbenzenes as beta-amyloid binding ligands and free radical scavengers. *J Med Chem.* 2010; 53:7992-7999.
21. Meadowcroft, MD, Connor, JR, Smith, MB, *et al.* MRI and histological analysis of beta-amyloid plaques in both human Alzheimer's disease and APP/PS1 transgenic mice. *J Magn Reson Imaging.* 2009; 29:997-1007.
22. Pike, VV. PET radiotracers: crossing the blood-brain barrier and surviving metabolism. *Trends Pharmacol Sci.* 2009; 30:431-440.
23. Benhaim, D and Grushka, E. Effect of n-octanol in the mobile phase on lipophilicity determination by reversed-phase high-performance liquid chromatography on a modified silica column. *J Chromatogr A.* 2008; 1209:111-119.
24. Lombardo, F, Shalaeva, MY, Tupper, KA, *et al.* ELogPoct: a tool for lipophilicity determination in drug discovery. *J Med Chem.* 2000; 43:2922-2928.
25. Lombardo, F, Shalaeva, MY, Tupper, KA, *et al.* ElogD(oct): a tool for lipophilicity determination in drug discovery. 2. Basic and neutral compounds. *J Med Chem.* 2001; 44:2490-2497.
26. Kikuchi, D, Sakaguchi, S, and Ishii, Y. An Alternative Method for the Selective Bromination of Alkylbenzenes Using NaBrO(3)/NaHSO(3) Reagent. *J Org Chem.* 1998; 63:6023-6026.

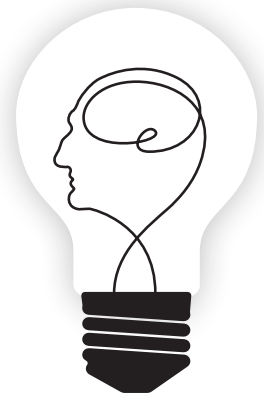
27. Kumar, P, Zheng, W, McQuarrie, SA, *et al.* <sup>18</sup>F-FESB: Synthesis and automated radiofluorination of a novel <sup>18</sup>F-labelled PET tracer for beta-amyloid plaques. *J Labelled Comp Radiopharm.* 2005;983-996.
28. Cohen, AD, Ikonomic, MD, Abrahamson, EE, *et al.* Anti-Amyloid Effects of Small Molecule Abeta-Binding Agents in PS1/APP Mice. *Lett Drug Des Discov.* 2009; 6:437.

---



# Chapter 12

Summary and General Discussion



## Summary

Alzheimer's disease (AD) is the predominant form of dementia in the aging population and its increasing incidence represents an important socio-economic and public health concern. The hallmarks of this disease, amyloid plaques and neurofibrillary tangles, are thought to develop early in the disease pathogenesis, up to decades before first clinical symptoms occur. However, these pathological hallmarks are still difficult to detect *in vivo*, and therefore a definitive diagnosis can only be made post-mortem. A clinical imaging technique or biomarker capable of visualizing and quantifying amyloid plaques and associated early changes thus may enable an earlier diagnosis, better understanding of the pathophysiology and eventually aid therapy development. The work presented in this thesis aimed to develop innovative diagnostic imaging techniques to detect the histological signatures of AD using emerging ultra-high field MRI technologies (**Part One**) and molecular imaging strategies (**Part Two**).

Detection of A $\beta$  plaques by MRI has previously been demonstrated both *in vivo* in several transgenic AD mouse models and in *ex vivo* human AD brain tissue. The high magnetic field strengths needed to obtain these results only recently became available for *in vivo* human use. These high field human MRI systems ( $\geq 7$  Tesla) offer new possibilities to specifically detect these neuropathological hallmarks, perhaps even at an earlier stadium than the traditional MRI biomarker of brain atrophy.

**Part One** of this thesis explores the correlation between intrinsic AD-induced MRI contrast changes and the underlying neuropathological changes, which is an essential step in the development of native contrast MRI techniques for diagnostic purposes.

After a brief general introduction into MRI (**Chapter 2**), we addressed the usability and limitations of post-mortem brain tissue for the development of novel MRI methods for AD (**Chapter 3**). Although post-mortem brain tissue is often exploited for this purpose, we strongly advise the use of formalin fixed brain tissue with fixation times less than two years, because prolonged fixation times induced destruction of normal brain tissue visible as hypointense imaging artifacts on MRI.

Correlating MRI contrast changes at high magnetic field strength to its underlying pathologic substrate is not straight-forward, due to the intrinsic differences in resolution between the techniques, and tissue deformation during processing. To solve these issues we designed a simple inductively-coupled microcoil setup that allowed us to obtain MRI images directly from a single 60  $\mu\text{m}$  thick histological section that could be stained histologically afterwards, thereby allowing a direct comparison between the MRI and histological data (**Chapter 4**). The design can easily be integrated into any MRI system using existing commercial hardware while improving the signal-to-noise ratio. Initial application on human AD brain tissue demonstrated that human A $\beta$  deposits indeed correspond to signal hypo-intensities on T $_2^*$ -weighted MRI.

Previous studies in the literature had suggested that A $\beta$  deposits, irrespective of associated iron, might induce detectable MRI contrast. The direct MR microscopy of histological sections offered a valuable tool to investigate the MR properties of the different forms of human cerebral A $\beta$  deposits (**Chapter 5**). We demonstrated that only when A $\beta$  is deposited in its fibrillar amyloid conformation, a decreased signal can be observed on T $_2^*$  and T $_2$ -weighted MRI. In addition, direct visualization of cerebral amyloid angiopathy (CAA) is possible, although signal attenuation



was not observed in all CAA-affected vessels. With regard to the cerebral presence of A $\beta$ , this would imply that MRI would depict the cerebral fibrillar amyloid load rather than the amount of cerebral A $\beta$  peptides.

In **Chapter 6** we examined changes in cortical appearance of AD patients using susceptibility weighted 7T MRI *in vivo*. Similar changes on MRI were found in post-mortem tissue of AD patients versus controls, which could be correlated to the histological changes found in the same tissue. On MRI, diffuse hypointense bands were frequently found in the cortex of the frontal lobes of AD patients (57%), but they were not observed in healthy age matched control subjects. Further histologic correlation revealed that the pattern of the susceptibility-weighted contrast in the cortex of AD patients does not primarily co-localize with amyloid plaques or neurofibrillary tangles, but with microglia- and myelin-associated iron accumulation and with an altered myelin cytoarchitecture. The current findings show great promise for the *in vivo* detection of the underlying pathological changes in AD. Nevertheless, future work should focus on the specificity of these findings for AD versus other neurodegenerative diseases.

**Part Two** is focused on the development of targeted contrast agents to allow the specific *in vivo* detection and visualization of different A $\beta$  deposits. In general *in vivo* application of these molecular imaging strategies to study or diagnose neurodegenerative diseases, especially with regard to MRI, depends on the ability to enter the brain as well as the characteristics of the available imaging ligand, as is explained in **Chapter 7**.

Previously, we have selected heavy chain antibody fragments (V<sub>H</sub>H) with high affinity specific for either cerebral amyloid angiopathy (CAA) or all types of human A $\beta$  deposits. Derived from the Camelid heavy chain antibody repertoire, which completely lack light chains, their single N-terminal domain (V<sub>H</sub>H) is fully capable of antigen binding with affinities comparable with those of conventional antibodies. The potential of V<sub>H</sub>H as *in vivo* imaging agent to assess CAA and cerebral amyloid load hinges on their ability to enter the brain, and in **Chapter 8** we tested their ability to cross the blood-brain barrier (BBB) using an *in vitro* BBB system. V<sub>H</sub>H ni3A showed the highest transmigration efficiency, which is to a large extent due to 3 different amino acid in its N-terminal domain, and occurred by means of active transport.

As a next step, in **Chapter 9** the *in vivo* properties of two V<sub>H</sub>H, ni3A and pa2H, were assessed in transgenic APP<sup>swe</sup>/PS1<sup>delta9</sup> mice. Following rapid renal clearance only <sup>99m</sup>Tc-pa2H showed a small yet significant higher cerebral uptake in the APP/PS1 animals one day post-injection. After circumventing the BBB, the *in vivo* specificity for A $\beta$  was confirmed for both fluorescently labeled V<sub>H</sub>H, where pa2H remained readily detectable for 24 hours or more after injection. Both V<sub>H</sub>H showed affinity for parenchymal and vascular deposits, this in contrast to human tissue, where ni3A specifically targeted only vascular A $\beta$ . Brain uptake as yet is too low for direct *in vivo* imaging, however this study provided evidence that V<sub>H</sub>H detect A $\beta$  deposits *in vivo* making them promising tools for further development.

A completely different approach is presented in **Chapter 10** in which we synthesized several novel fluorinated bis-styrylbenzenes to serve as potential <sup>19</sup>F MRI contrast agents and studied their fluorescent and A $\beta$  binding characteristics. Ideally these small organic molecules carrying normal fluorine might allow direct MR imaging of the amyloid binding compound, without any endogenous background signal. Most compounds showed a high affinity for both murine and human amyloid. Interestingly, they bind to a different binding site than chrysamine G, one of

the parent compounds from which our bis-styrylbenzenes were derived. Despite their high logP values, many bis-styrylbenzenes were able to enter the brain and label murine amyloid *in vivo*. Initial post-mortem  $^{19}\text{F}$  NMR studies using the most promising compound unfortunately showed that these compounds as yet do not warrant further MRI studies, mainly due to the severe reduction of the  $^{19}\text{F}$  signal in the environment of the brain.

**Chapter 11** presents a similar study in which we synthesized six bis-pyridylethenylbenzenes based on the assumption that the incorporation of nitrogen might lower the hydrophobicity of the previous compounds and perhaps thereby further improve their amyloid binding characteristics. These compounds did also not share a binding site with chrysamine G. With a logP value in between 3 and 5, most bis-pyridylethenylbenzenes were able to enter the brain and label murine amyloid *in vivo*. Based on its *in* and *ex vivo* binding characteristics and its solubility, bis(4-pyridylethenyl)benzene showed the most promise to serve as a novel amyloid-targeting backbone for amyloid imaging using fluorescence or for further development, e.g. as a PET tracer.

## General discussion

The current view on Alzheimer's disease (AD) is that the neuropathological changes start two decades before the clinical symptoms occur.<sup>1</sup> The cognitive decline associated with AD, represents a late stage of the disease when neurodegeneration is extensive and therapeutic interventions may be too late. The search for new imaging methods is driven by the promise that earlier diagnosis, preferably before overt dementia is present, may help to identify patients early enough to benefit from future treatments.

### Diagnostic biomarkers: Current status

Divided into two main categories, the most extensively characterized biomarkers for AD reflect either cerebral amyloid load or neuronal injury and degeneration. (Table 12.1) It is due to the increasing knowledge and understanding of the disease obtained by biomarker research that only recently, almost thirty years after its first publication, the clinical diagnostic criteria of AD as set by the NINDS-ADRDA have finally been revised. According to these new criteria a possible diagnosis of AD is no longer one of exclusion, solely based on clinical symptoms of dementia or mild cognitive impairment (MCI). The new criteria include the presence of one or more of the following five biomarkers: medial temporal lobe atrophy, abnormal cerebrospinal fluid levels of  $\text{A}\beta_{1-42}$  or tau, or specific patterns of glucose metabolism or  $\text{A}\beta$  ligands as detected by PET neuroimaging. Furthermore, a new set of criteria has been added to stage pre-clinical AD only based on positive biomarkers, but without clinical symptoms.<sup>2</sup>

The revised criteria are based on the hypothetical dynamic biomarker model for AD, as initially proposed by Jack *et al.*<sup>1</sup> With new biomarker data continuously being gathered this model requires constant revision. According to this model the different biomarkers change in a specific temporal order and it is assumed that the accumulation of cerebral amyloid is one of the earliest and leading events. Many independent cross-sectional observations are in line with this model. However, the exact order in which biomarkers change over time and the relationship of these

changes with the clinical outcome is currently the main topic of many ongoing longitudinal studies. Recently, the initial results of one of the largest prospective biomarker studies, the Australian Imaging, Biomarkers & Lifestyle Study of Ageing (AIBL), again affirmed the model.<sup>3</sup> In this study, researchers retrospectively compared cerebral atrophy and amyloid load at baseline with respect to the revised clinical criteria for (pre)clinical AD. Based on amyloid imaging as a predictor for AD its outcome again suggested a disease onset of twenty years or more before noticeable clinical symptoms.

Meanwhile a recent revision of the model by Jack and his colleagues confirmed the typical sigmoid shape of the changes of each marker over time but also adjusted their temporal order. CSF-A $\beta$  now is the first biomarker to change prior to amyloid detected by PET imaging. Subsequently, tau can be detected in CSF, and finally FDG PET changes and cerebral atrophy appear simultaneously.<sup>4</sup> (**Figure 12.1**) In addition, an initial attempt was taken to include cognitive or so-called brain reserve based on intelligence, education, occupation and leisure activities into the model to highlight the existing individual differences in clinical presentation with respect to the level of their biomarkers. Although A $\beta$  is still considered to be the major hallmark as well as an important initiating factor in the progression of the disease, there is increasing evidence that other primary or interacting causes exist, e.g. the accumulation of tau or changes in myelin and iron metabolism.<sup>5-7</sup> As these mechanisms may act alongside A $\beta$  accumulation or even further upstream in the disease process, it is important to continue improving A $\beta$  biomarkers but also to investigate new possible biomarkers that may project brain reserve or any of the aforementioned alternative mechanisms of disease, such as tau-targeting PET agents or novel MRI techniques.

In this thesis, we aimed at developing improved imaging biomarkers for AD following two approaches: development of novel techniques to detect AD pathology using MRI (**Part One: Chapter 3 - 6**), and development of new A $\beta$ - or amyloid-binding imaging probes (**Part Two**) based on either llama antibody fragments (**Chapter 8 and 9**) or small amyloid binding molecules (**Chapter 10 and 11**).

## MRI-based biomarker research

**Table 12.1 Classification of AD biomarkers** (adapted from Jack et al.<sup>16</sup>)

Biomarker	Type
<i>Amyloid accumulation</i>	
CSF A $\beta$ <sub>1-42</sub>	CSF Analysis
Amyloid PET	Imaging
<i>Neurodegeneration</i>	
CSF tau (total and phosphorylated)	CSF Analysis
Structural MRI	Imaging
FDG PET	Imaging

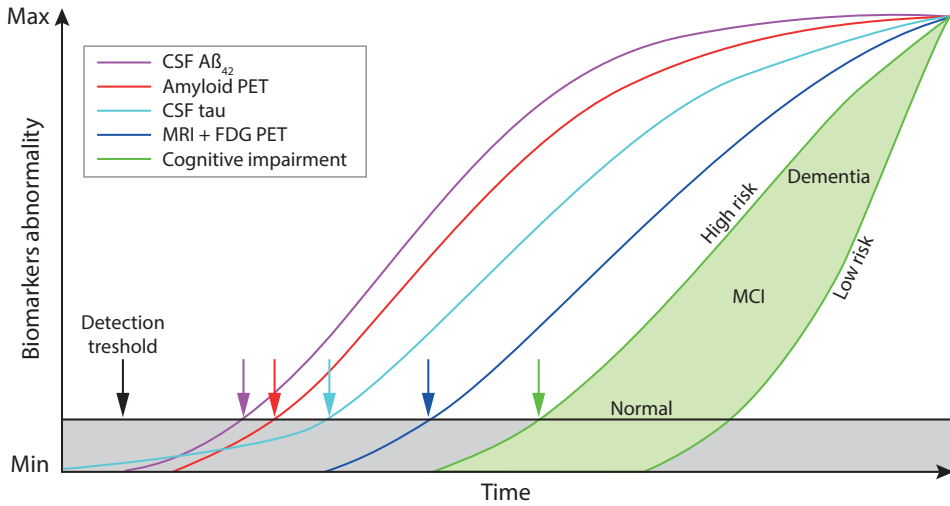


**Figure 12.1** The revised dynamic biomarker model (reproduced from Jack et al.<sup>4</sup>)

Pathophysiological changes that are below the detection threshold are visualized by the grey area. At a subthreshold level tau pathology is thought to precede A $\beta$  deposition. Based on the current diagnostic techniques the detection of A $\beta$  rises above the threshold first (purple and red arrows). As this accelerates tauopathy then comes CSF tau (light blue arrow). Later still, functional and metabolic biomarkers appear abnormal as seen by FDG PET and MRI (dark blue arrow). At last, a wide range of cognitive impairment becomes evident (green arrow) depending on the individual's risk profile (light green-filled area).

In AD patients structural MRI studies revealed specific patterns of regional cerebral atrophy.<sup>8</sup> Severity of atrophy was observed to correlate well with loss of cognitive function as well as with post-mortem Braak staging. Of all putative biomarkers, volumetric measures of hippocampal and medial temporal lobe atrophy showed the best correlation with the severity of clinical symptoms, and has therefore been incorporated as one of the five biomarkers in the revised diagnostic criteria. According to the dynamic marker model, however, brain atrophy is a late stage event, and therefore structural MRI may not be the method of choice for early or pre-symptomatic diagnosis.

As for other neuropathological hallmarks of AD, the development of MRI-based biomarkers has mainly focused on the detection of cerebral amyloid. Initial pre-clinical studies were able to detect individual amyloid plaques, as they induce a detectable decrease in T<sub>2</sub>\* or SWI signal due to the accumulation of iron or the protein aggregate itself.<sup>9-11</sup> The work in this thesis not only replicated these findings, but also showed that only the functionally relevant fibrillar amyloid induces detectable changes in MRI signal, and not just the presence of A $\beta$  peptide. A good understanding of the neuropathological substrate of changes on MRI is important for further development and interpretation of novel MRI biomarkers for AD. However, despite the arrival of novel high magnetic field ( $\geq 7$  Tesla) human MRI systems, it is not to be expected that direct detection of individual amyloid plaques by MRI is feasible in the near future. This is due to imaging artifacts based on physiological movements of patients, limited scan time, and the resulting limited resolution that can be obtained when scanning patients *in vivo*. As discussed in **Chapter 5**, although for the time being individual plaques may remain beyond *in vivo* detection the early and subtle changes in MRI signal due to cerebral amyloid accumulation might be

exploited by quantitative MRI methods. However, quantitative parameters reflecting bulk  $T_2$  and  $T_2^*$  signal in a region of interest will not only reflect cerebral amyloid, but also other tissue changes. In addition to amyloid, brain iron not directly associated with plaques and myelin also generate local variations in magnetic susceptibility, especially at high magnetic field strengths.<sup>12</sup> High-field ( $\geq 7$  Tesla) human MRI systems therefore show great promise in visualizing new iron- and myelin-driven contrasts in the human brain.

The findings in **Chapter 6** provide convincing evidence that myelin structure and iron distribution in the cortex are disturbed in AD patients. Furthermore, our findings suggest that these changes, detected on SWI images at 7 Tesla, may allow distinguishing “probable AD” subjects and healthy age-matched controls. Interestingly, changes in iron metabolism and myelin breakdown have both been mentioned as potential upstream mechanisms for AD.<sup>5,13</sup> The ability to visualize these changes *in vivo* by MRI thus creates a putative novel biomarker with the potential to reflect a yet underappreciated change that may accompany the progression of AD. As discussed previously, further studies are required, comprising larger patient series as well as patients with different types of dementia. And also several additional questions should be answered, such as whether the presence of cortical changes is associated with cognitive dysfunction, whether the changes appear early in the course of AD, and whether the frontal lobes are the best location to detect these changes.

An important but still poorly understood mechanism that also requires further investigation is the influence of the normal ageing process on SWI images at 7 Tesla. Previous histopathological studies already pointed out that the cortical distribution of myelin not only differed between cortical regions but it was also subject to changes during life.<sup>5</sup> Whether a similar relationship exists between cortical iron and age has not yet been shown, but given its effect on MRI signal it has become essential to gain a better understanding of the role of cortical iron accumulation in normal brain aging. Full characteristics of cortical myelin and iron distribution over the lifespan starting from as early as the mid-twenties serves as a solid basis for the comparison between normal brain ageing or alterations of cortical myelin and iron due to AD or other neurodegenerative diseases.

Besides its novel *in vivo* finding, our work described in **Chapter 6** also demonstrates a new approach to study neurodegenerative diseases using post-mortem material. Thus far most neuropathological MRI studies have attempted to investigate the histopathological substrate corresponding the observed MRI contrast using MR images with almost microscopic resolution to allow direct and detailed comparison of the histology, similar to the work described in **Chapters 3 - 5**. Although full understanding of this relationship is of crucial importance for further development of clinical techniques, the direct translation of these microscopic findings to clinical MR images that are acquired at a much lower resolution remains however difficult and understudied.

In **Chapter 6** we started with a comparison of the post-mortem MR images acquired at a low or almost clinical resolution alongside their histological sections on a mesoscopic scale rather than directly focusing on the microscopic MRI-histology correlation using the high resolution images. Based on visual inspection we aimed to examine whether any of the applied stainings expressed a pattern or distribution similar to that observed on the clinical and low resolution MRI. In contrary to normal pathological examination, this analysis of the histological data

required a helicopter view to allow a more mesoscopic pattern recognition before diving into the exact underlying microscopic details. This approach provided crucial information that otherwise might have been lost in the details. It for instance revealed the difference in cortical distribution of the myelin-related iron observed throughout the neuropil, which by normal microscopic evaluation would have been difficult to discriminate.

### Molecular imaging strategies

Since the mid-1990s, molecular imaging has gained interest as it attempts to detect non-invasively cellular and molecular signatures of disease processes by means of imaging. Crucial to molecular imaging is the availability of an imaging probe that targets a specific disease process, ideally allowing for an early and specific diagnosis.<sup>14,15</sup> For AD, thus far two molecular imaging strategies are used in the revised criteria: the detection of glucose hypometabolism using <sup>18</sup>F-DG-PET, and visualization of cerebral amyloid load by radioactive PET ligands. (**Table 1**) The cerebral pattern of glucose hypometabolism is considered to be an indicator of synaptic loss that accompanies neurodegeneration, and has demonstrated to be a sensitive and specific indicator for conversion of MCI to AD.<sup>16</sup> However, currently, the most sensitive methods for early detection of AD are based on detection of cerebral amyloid.<sup>3,4</sup> According to the dynamic biomarker model, amyloid plaque accumulation is the first change to be present, and thereby constitutes a well-defined specific target for the development of *in vivo* molecular imaging strategies as highlighted in Part Two. It is important, however, to realize that the presence of cerebral amyloid might allow an early diagnosis, but it does not allow to follow disease progression due to its early plateau level.<sup>3,4</sup>

Based on preclinical research on the modification of existing amyloid-binding dyes like Congo Red and Thioflavin into imaging agents, the initial *in vivo* breakthrough came with the development of Pittsburgh Compound B, a neutral <sup>11</sup>C derivative of Thioflavin.<sup>17</sup> Despite many *in vivo* human studies its broad applicability is hampered by its short radioactive half-life (<20min), requiring the availability of a cyclotron, and therefore it has been mainly used for research purposes. Recently Amyvid, a novel amyloid-binding PET probe, has been the first probe to receive approval for clinical use to image amyloid plaque burden by the American Food and Drug Administration (FDA).<sup>18</sup> This <sup>18</sup>F-containing stilbene derivative does not need the presence of a cyclotron in the vicinity due to its long half-life of 109 minutes. When this first FDA approved amyloid imaging probe will prove both its clinical and commercial value this may push the development of different or more specific AD imaging probes, like those presented in this thesis.

For molecular imaging tracers based on small molecular compounds, such as Amyvid and our bis-pyridylethenyl- and fluorinated bis-styrylbenzenes thus far PET, and not MRI, remains the imaging modality of choice due to its higher sensitivity.<sup>19</sup> If possible MR-based A $\beta$  targeting imaging agents are still desirable despite all the difficulties for the design of MR-based AD imaging probes as described in **Chapter 7**. Such agents could be used in one scan session comprising a comprehensive structural and functional scan protocol as well as a scan to detect the molecular imaging tracers, whereas one PET examination only provides one biomarker. Furthermore, the availability of MRI tracers would lower the threshold for performing amyloid scans given the wider availability of MRI systems as compared to PET systems, the lack of ionizing

irradiation and the lower costs involved in performing MRI as compared to PET. However, although existing PET-based amyloid tracers can be modified for MRI, e.g. by addition of  $^{19}\text{F}$ , current clinical MRI setups require an administration of such a high dose that it might create potential toxicity issues. Novel advances in brain delivery systems combined with AD targeting backbones, like  $\text{V}_\text{H}\text{H}$ , may perhaps overcome these hurdles in the future. Additionally, the recently introduced hybrid PET-MRI systems may be instrumental since they allow for acquiring PET and MRI data in one diagnostic imaging session.

### Theranostics

The integration of diagnostic and therapeutic components into a single compound or so-called theragnostic agent holds great promise for future drug development. The incorporation of an imaging moiety to a possible drug or drug delivery system enables the precise monitoring of *in vivo* temporal and spatial bioavailability and target engagement of the drug, and also treatment outcome.<sup>20</sup> During the development of the drug, crucial information can be obtained regarding the possible pharmacological challenges that have to be addressed to further enhance its efficacy, such as biodistribution, pharmacokinetics, fast metabolism, limited specificity and severe adverse effects.

With regard to AD, amyloid plaques have not only been an obvious target for diagnostics but the break-down or inhibition of these  $\text{A}\beta$  deposits has also attracted attention as a possible target for therapeutic intervention. Compounds that were initially probed for diagnostic purposes may also have a therapeutic effect. The development of anti- $\text{A}\beta$  antibodies for therapeutic purposes initially faced the same restrictions that are met in the development of diagnostic agents. Despite almost no cerebral uptake, however, both passive and active immunization studies using animal models showed a decrease in cerebral amyloid and improved cognitive performance.<sup>21</sup> Their effect was partly attributed to the so-called “peripheral sink” mechanism that assumes that the removal of  $\text{A}\beta$  from the bloodstream leads to a lower concentration of  $\text{A}\beta$  in the circulation which then leads to the efflux of the peptide from the brain. Unfortunately translation of these findings into the clinic was less successful as therapeutic human anti- $\text{A}\beta$  studies were stopped either due to unwanted side effects or because no significant clinical improvements were detected.<sup>21</sup> Besides their inability to gain sufficient entry into the brain, the general consensus on the reason for the therapeutic failure of these antibodies is that the trials started too late in the course of the disease. Several new trials, such as DIAN and A4, are starting this year with groups of pre-symptomatic, but amyloid-positive patients.<sup>22</sup> These drug development trials are only possible because of the progress that has been made over the last years in new diagnostic biomarkers, particularly PiB-PET.

Although initially designed for diagnostic purposes the llama antibody fragments or  $\text{V}_\text{H}\text{H}$  that we studied have many unique characteristics that make them especially interesting for theragnostics, as pointed out in **Chapter 9**. Several  $\text{V}_\text{H}\text{H}$  have already shown their potential therapeutic value *in vitro*, preventing aggregation of amyloid fibrils or oligomeric forms of  $\text{A}\beta$  and thus inhibiting formation of or disentangling amyloid plaques.<sup>23</sup> Compared to the conventional monoclonal antibodies or antibody fragments (Fab') used for clinical trials, like those described above,  $\text{V}_\text{H}\text{H}$  express a similar high level of specificity and affinity, but because of their single domain production and modification is relatively easy and cost-efficient.<sup>24</sup>

Possible immunologic reactions are easily avoided by humanization. Their selective binding to different A $\beta$  species, like CAA or oligomeric A $\beta$ , could shift A $\beta$  brain efflux in the favored direction, which could be used to tailor anti-A $\beta$  therapy, thereby further reducing therapy induced complications.

Although in this thesis a proof of principle is given regarding the specific brain uptake of V<sub>H</sub>H, their full therapeutic effect may be hampered by a limited ability to enter the brain. Similar to the adaptations needed to improve their value as a diagnostic marker, novel strategies will have to be addressed to improve their therapeutic value.

### **Concluding remarks**

In the next decade biomarker studies will play a crucial role in developing strategies for early detection and treatment of AD. It remains doubtful whether eventually one single biomarker will be able to give a final diagnosis, but the incorporation of biomarkers in the revised NINDS-ADRDA criteria mean an important step forward, and confirm the importance of AD biomarker research in general. Further evaluation and standardization of the included biomarkers may provide more insight on the yet unknown pathogenesis of AD and contribute to the development of effective treatment.

Finally, it should be noted that due to the current absence of an effective treatment the impetus to develop methods for early diagnosis for AD, particularly for the asymptomatic individual, is limited and creates a Catch 22 situation. However, as discussed earlier in this thesis, the ability to detect the early phases of the disease is expected to provide improve our understanding of the pathophysiology of the disease, which then sets the stage for developing more effective treatment. Once more effective treatment will be available, the same tools for early disease detection will become relevant to individual patients by opening the therapeutic window to the early phases of the disease they are suffering from.



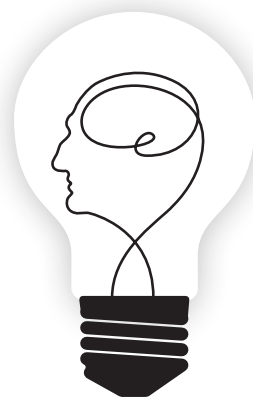
## References

1. Jack, CR, Jr., Knopman, DS, Jagust, WJ, *et al.* Hypothetical model of dynamic biomarkers of the Alzheimer's pathological cascade. *Lancet Neurol.* 2010; 9:119-128.
2. Sperling, RA, Aisen, PS, Beckett, LA, *et al.* Toward defining the preclinical stages of Alzheimer's disease: recommendations from the National Institute on Aging-Alzheimer's Association workgroups on diagnostic guidelines for Alzheimer's disease. *Alzheimers Dement.* 2011; 7:280-292.
3. Villemagne, VL, Burnham, S, Bourgeat, P, *et al.* Amyloid beta deposition, neurodegeneration, and cognitive decline in sporadic Alzheimer's disease: a prospective cohort study. *Lancet Neurol.* 2013; 12:357-367.
4. Jack, CR, Jr., Knopman, DS, Jagust, WJ, *et al.* Tracking pathophysiological processes in Alzheimer's disease: an updated hypothetical model of dynamic biomarkers. *Lancet Neurol.* 2013; 12:207-216.
5. Bartzokis, G. Alzheimer's disease as homeostatic responses to age-related myelin breakdown. *Neurobiol Aging.* 2011; 32:1341-1371.
6. Duce, JA, Tsatsanis, A, Cater, MA, *et al.* Iron-export ferroxidase activity of beta-amyloid precursor protein is inhibited by zinc in Alzheimer's disease. *Cell.* 2010; 142:857-867.
7. Lei, P, Ayton, S, Finkelstein, DI, *et al.* Tau deficiency induces parkinsonism with dementia by impairing APP-mediated iron export. *Nat Med.* 2012; 18:291-295.
8. Frisoni, GB, Fox, NC, Jack, CR, Jr., *et al.* The clinical use of structural MRI in Alzheimer disease. *Nat Rev Neurol.* 2010; 6:67-77.
9. Benveniste, H, Einstein, G, Kim, KR, *et al.* Detection of neuritic plaques in Alzheimer's disease by magnetic resonance microscopy. *Proc Natl Acad Sci U S A.* 1999; 96:14079-14084.
10. Chamberlain, R, Wengenack, TM, Poduslo, JF, *et al.* Magnetic resonance imaging of amyloid plaques in transgenic mouse models of Alzheimer's disease. *Curr Med Imaging Rev.* 2011; 7:3-7.
11. Meadowcroft, MD, Connor, JR, Smith, MB, *et al.* MRI and histological analysis of beta-amyloid plaques in both human Alzheimer's disease and APP/PS1 transgenic mice. *J Magn Reson Imaging.* 2009; 29:997-1007.
12. Fukunaga, M, Li, TQ, van, GP, *et al.* Layer-specific variation of iron content in cerebral cortex as a source of MRI contrast. *Proc Natl Acad Sci U S A.* 2010; 107:3834-3839.
13. Herrup, K. Reimagining Alzheimer's disease--an age-based hypothesis. *J Neurosci.* 2010; 30:16755-16762.
14. Massoud, TF and Gambhir, SS. Molecular imaging in living subjects: seeing fundamental biological processes in a new light. *Genes Dev.* 2003; 17:545-580.
15. Weissleder, R and Mahmood, U. Molecular imaging. *Radiology.* 2001; 219:316-333.
16. Jack, CR, Jr. Alzheimer disease: new concepts on its neurobiology and the clinical role imaging will play. *Radiology.* 2012; 263:344-361.
17. Klunk, WE, Engler, H, Nordberg, A, *et al.* Imaging brain amyloid in Alzheimer's disease with Pittsburgh Compound-B. *Ann Neurol.* 2004; 55:306-319.
18. Yang, L, Rieves, D, and Ganley, C. Brain amyloid imaging--FDA approval of florbetapir F18 injection. *N Engl J Med.* 2012; 367:885-887.
19. Buell, AK, Esbjorner, EK, Riss, PJ, *et al.* Probing small molecule binding to amyloid fibrils. *Phys Chem Chem Phys.* 2011; 13:20044-20052.
20. Wang, H and Chen, X. Applications for site-directed molecular imaging agents coupled with drug delivery potential. *Expert Opin Drug Deliv.* 2009; 6:745-768.
21. Weiner, HL and Frenkel, D. Immunology and immunotherapy of Alzheimer's disease. *Nat Rev Immunol.* 2006; 6:404-416.
22. Mullard, A. Sting of Alzheimer's failures offset by upcoming prevention trials. *Nat Rev Drug Discov.* 2012; 11:657-660.
23. Lafaye, P, Achour, I, England, P, *et al.* Single-domain antibodies recognize selectively small oligomeric forms of amyloid beta, prevent Abeta-induced neurotoxicity and inhibit fibril formation. *Mol Immunol.* 2009; 46:695-704.
24. Huang, L, Muyldermans, S, and Saerens, D. Nanobodies(R): proficient tools in diagnostics. *Expert Rev Mol Diagn.* 2010; 10:777-785.



# Appendices

- I Building blocks for polyfluorinated bis-styrylbenzenes
- II Samenvatting
- III Dankwoord
- IV Curriculum vitae
- V Publication list



## Synthesis of phosphonate building blocks

### General synthetic procedures

All phosphonate building blocks were prepared according to the general synthesis scheme below (**Scheme I.1**) starting from either commercially available dimethylbenzenes, or dimethylbenzenes prepared according to literature procedures.

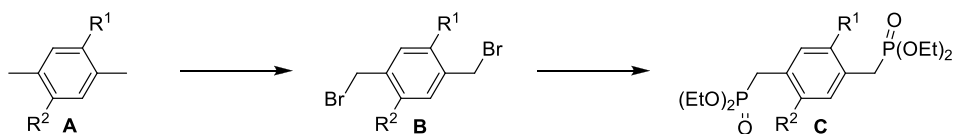
General procedure for bromination (A  $\rightarrow$  B): To a solution of the dimethyl compound (10 mmol) in  $\text{CCl}_4$  (22 ml) were added N-Bromosuccinimide (3.92 g, 22 mmol) and benzoyl peroxide (20 mg) and the mixture was heated to reflux for 16 h. After cooling to room temperature, the mixture was filtered over Celite, the filtrate concentrated and the residue applied to column chromatography (0  $\rightarrow$  5% EtOAc/light petroleum) to yield the pure product.

General procedure for Arbuzov (B  $\rightarrow$  C): To the dibromide (1 mmol) was added triethyl phosphite (0.42 ml, 2.5 mmol) and the mixture was heated to reflux (150  $^\circ\text{C}$ ) for 16 h. After cooling to room temperature, the mixture was directly applied to a silica column (50% EtOAc/light petroleum  $\rightarrow$  10% MeOH/EtOAc) to yield the pure product.

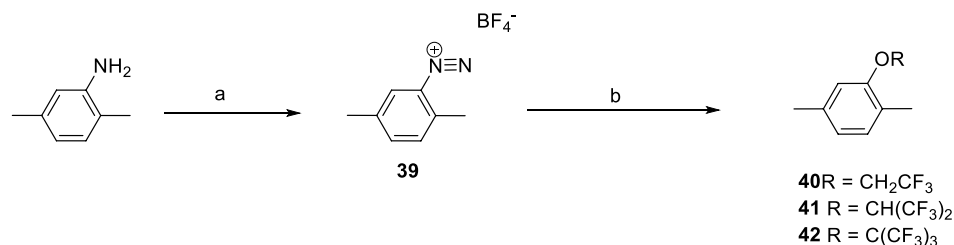
### Synthesis of dimethylbenzene precursors

The dimethylbenzene precursors **40** - **42** for phosphonates **29**, **31** - **32** were not commercially available and were prepared from 2,5-dimethylaniline as depicted in **Scheme I.2**.

Diazonium salt **39** was prepared according to literature procedures.<sup>1</sup> To a solution of  $\text{HBF}_4$  (50% in  $\text{H}_2\text{O}$ , 25.5 ml, 200 mmol) in water (25.5 ml), 2,5-dimethylaniline (12.5 ml, 100 mmol) was added and the reaction mixture was cooled to 0 $^\circ\text{C}$ . A solution of  $\text{NaNO}_2$  (6.9 g, 100 mmol) in water (6 ml) was added dropwise and the reaction mixture warmed to room temperature. The solids were filtered off and washed with 5% aq.  $\text{HBF}_4$ , EtOH and  $\text{Et}_2\text{O}$  and dried under vacuum. The resulting pinkish powder was dissolved in acetone and precipitated with  $\text{Et}_2\text{O}$ . After filtration, this procedure was repeated two times and after drying under vacuum, the product was



Scheme I.1 General procedure for preparation of phosphonates



Scheme I.2 Preparation of fluorinated dimethylbenzene precursors

Reagents and conditions: **a)**  $\text{HBF}_4$ ,  $\text{NaNO}_2$ ,  $\text{H}_2\text{O}$ , 0 $^\circ\text{C}$   $\rightarrow$  rt, 47%. **b)** fluorinated alcohol, reflux, 18 h.

obtained as an off-white powder (10.4 g, 47.4 mmol, 47%).  $^1\text{H}$  NMR (acetone- $d_6$ , 400 MHz):  $\delta$  8.54 (s,  $^1\text{H}$ ); 8.03 (d,  $J = 8.2$  Hz,  $^1\text{H}$ ); 7.78 (d,  $J = 8.0$  Hz,  $^1\text{H}$ ); 2.86 (s, 3H); 2.51 (s, 3H). IR (neat): 2275.8; 1506.6; 1303.6; 1210.7; 1029.3; 847.8; 521.4.

Fluorethers **40** – **42** were synthesized from diazonium salt **39** according to literature procedures.<sup>1</sup> Diazonium salt **39** (2.2 g, 10 mmol) was dissolved in the appropriate fluoruous alcohol (25 ml) and the mixture was heated to reflux for 18 h. After cooling to room temperature, 2 N NaOH and  $\text{Et}_2\text{O}$  were added and the layers separated. The organic layer was dried ( $\text{Na}_2\text{SO}_4$ ); filtered and concentrated (careful: product is volatile!). The crude product was purified by flash column chromatography (light petroleum) to yield the fluoruous ether as a colorless fluid. As the products are volatile, care needs to be taken during evaporation after work-up and column chromatography.

Following the general procedure above, **40** was obtained from reaction of **39** with 2,2,2-trifluoroethanol as a colorless liquid (1.14 g, 5.6 mmol, 56%).  $^1\text{H}$  NMR ( $\text{CDCl}_3$ , 400 MHz):  $\delta$  7.03 (d,  $J = 7.5$  Hz,  $^1\text{H}$ ); 6.75 (d,  $J = 7.5$  Hz,  $^1\text{H}$ ); 6.58 (s,  $^1\text{H}$ ); 4.30 (q,  $J = 8.2$  Hz,  $J = 8.2$  Hz, 2H); 2.31 (s, 3H); 2.20 (s, 3H).  $^{13}\text{C}$  NMR ( $\text{CDCl}_3$ , 100 MHz):  $\delta$  155.5; 136.8; 130.9; 124.9; 124.4; 122.8; 122.1; 112.8; 66.7; 66.3; 66.0; 65.6; 21.2; 15.4.  $^{19}\text{F}$  NMR ( $\text{CDCl}_3$ , 375 MHz):  $\delta$  3.36 (t,  $J = 8.1$  Hz, 3F).

Compound **41** was obtained from reaction of **39** with 1,1,1,3,3,3-hexafluoroisopropanol as a colorless liquid (1.79 g, 6.6 mmol, 66%).  $^1\text{H}$  NMR ( $\text{CDCl}_3$ , 400 MHz):  $\delta$  7.07 (d,  $J = 7.6$  Hz,  $^1\text{H}$ ); 6.85 (d,  $J = 7.6$  Hz,  $^1\text{H}$ ); 6.72 (s,  $^1\text{H}$ ); 4.91-4.80 (m,  $^1\text{H}$ ); 2.33 (s, 3H); 2.24 (s, 3H).  $^{13}\text{C}$  NMR ( $\text{CDCl}_3$ , 100 MHz):  $\delta$  155.6; 137.3; 131.4; 125.5; 124.7; 122.6; 122.6; 119.8; 114.6; 76.2; 75.9; 75.6; 21.2; 15.3.  $^{19}\text{F}$  NMR ( $\text{CDCl}_3$ , 375 MHz):  $\delta$  3.90 (d,  $J = 5.7$  Hz, 6F). IR (neat): 1511.8; 1368.9; 1250.5; 1218.2; 1192.2; 1155.7; 1134.3; 1104.1; 886.8; 809.9; 686.2.

Following the general procedure above, **42** was obtained from reaction of **39** with nonafluoro-tert-butanol as a colorless liquid (2.22 g, 6.5 mmol, 65%).

$^1\text{H}$  NMR ( $\text{CDCl}_3$ , 400 MHz):  $\delta$  7.00 (s,  $^1\text{H}$ ); 6.94 (d,  $J = 7.7$  Hz,  $^1\text{H}$ ); 6.81 (d,  $J = 9.0$  Hz,  $^1\text{H}$ ); 2.30 (s, 3H); 2.24 (s, 3H).  $^{19}\text{F}$  NMR ( $\text{CDCl}_3$ , 375 MHz):  $\delta$  8.23 (s, 9F).

### Synthesis of phosphonates **25** – **32**

Phosphonate **25** was prepared as described previously.<sup>2</sup> 2,5-dimethylanisole (1.36 g, 10 mmol) was brominated according to the general procedure for bromination. The dibromide was obtained as white solid (1.71 g, 5.8 mmol, 58%).

$^1\text{H}$  NMR ( $\text{CDCl}_3$ , 400 MHz):  $\delta$  7.27 (d,  $J = 7.7$  Hz,  $^1\text{H}$ ); 6.92 (dd,  $J = 7.6$  Hz,  $J = 1.2$  Hz,  $^1\text{H}$ ); 6.89 (s,  $^1\text{H}$ ); 4.52 (s, 2H); 4.44 (s, 2H); 3.88 (s, 3H).  $^{13}\text{C}$  NMR ( $\text{CDCl}_3$ , 100 MHz):  $\delta$  157.4; 139.7; 131.0; 126.3; 121.1; 111.5; 55.6; 33.2; 28.3.

The dibromide (1.71 g, 5.8 mmol) was subjected to the Arbuzov reaction according to the general procedure. The pure product was obtained as a yellowish solid (1.55 g, 3.8 mmol, 66%).

$^1\text{H}$  NMR ( $\text{CDCl}_3$ , 400 MHz):  $\delta$  7.25 (dd,  $J = 7.6$  Hz,  $J = 2.9$  Hz,  $^1\text{H}$ ); 6.86 (s,  $^1\text{H}$ ); 6.83 (d,  $J = 7.6$  Hz,  $^1\text{H}$ ); 4.07-3.95 (m, 8H); 3.84 (s,  $^1\text{H}$ ); 3.21 (d,  $J = 21.4$  Hz, 2H); 3.13 (d,  $J = 22.2$  Hz, 2H); 1.27-1.20 (m, 12H).  $^{13}\text{C}$  NMR ( $\text{CDCl}_3$ , 100 MHz):  $\delta$  157.2; 131.5; 131.1; 121.9; 121.900; 118.85; 112.1; 55.5; 34.4; 33.0; 27.0; 25.6; 16.3.  $^{31}\text{P}$  NMR ( $\text{CDCl}_3$ , 162 MHz):  $\delta$  27.39 (d,  $J = 9.0$  Hz), 26.77 (d,  $J = 9.1$  Hz).

To synthesize phosphonate **26** 1,4-bis(chloromethyl)-2,5-dimethoxybenzene (0.24 g, 1 mmol) was added to triethyl phosphite (0.42 ml, 2.5 mmol) and the mixture was heated to reflux for 16 h. After cooling to room temperature, the solids were filtered off, washed with light petroleum

and dried under vacuum, yielding the pure product as a white solid (0.37 g, 0.85 mmol, 85%).  $^1\text{H}$  NMR ( $\text{CD}_3\text{OD}$ , 400 MHz):  $\delta$  6.95 (d,  $J$  = 1.8 Hz, 2H); 4.03 (m, 8H); 3.82 (s, 6H); 3.24 (s, 2H); 3.22 (s, 2H); 1.25 (t,  $J$  = 7.1 Hz, 12H).  $^{13}\text{C}$  NMR ( $\text{CD}_3\text{OD}$ , 100 MHz):  $\delta$  152.5; 120.5; 115.3; 63.6; 56.6; 27.7; 26.3; 16.7. IR (neat): 1520.1; 1476.4; 1415.0; 1265.3; 1221.0; 1026.7; 963.8; 881.0; 837.8; 819.8; 768.0; 725.8; 700.2; 632.7; 518.4. LC-MS retention time: 6.70 min (10  $\rightarrow$  90% MeCN, 13.5 min run). Mass (ESI):  $m/z$  439.0  $[\text{M} + \text{H}]^+$ ; 876.9  $[2\text{M} + \text{H}]^+$ . Exact mass: Calculated for  $[\text{C}_{18}\text{H}_{33}\text{O}_8\text{P}_2]^+$ : 439.16452;  $[\text{C}_{18}\text{H}_{32}\text{O}_8\text{P}_2]^+$ : 461.14646. Found: 439.16446  $[\text{M} + \text{H}]^+$ ; 461.14583  $[\text{M} + \text{Na}]^+$ .

Phosphonate **27** was prepared as described previously.<sup>2</sup> 2,5-dimethylphenol (6.1 g, 50 mmol) was dissolved in DMF (30 ml), imidazole (3.4 g, 50 mmol) was added and the reaction mixture stirred for 10 min. Subsequently, TBDPS-Cl (15.6 ml, 60 mmol) was added. After stirring for 22 h, the mixture was poured out in water (250 mL) and the aqueous layer extracted three times with DCM. The combined organic layers were washed with water, dried ( $\text{Na}_2\text{SO}_4$ ), filtered and concentrated. The resulting yellow oil was purified by column chromatography (0  $\rightarrow$  2% EtOAc/light petroleum) to yield the pure product as a pale yellow oil (16.0 g, 44.3 mmol, 89%).

$^1\text{H}$  NMR ( $\text{CDCl}_3$ , 400 MHz):  $\delta$  7.76-7.64 (m, 4H); 7.45-7.33 (m, 1H); 7.01 (d,  $J$  = 7.6 Hz, 1H); 6.59 (d,  $J$  = 7.4 Hz, 1H); 6.22 (s, 1H); 2.33 (s, 3H); 1.94 (s, 3H); 1.10 (s, 9H).  $^{13}\text{C}$  NMR ( $\text{CDCl}_3$ , 100 MHz):  $\delta$  153.6; 150.2; 135.4; 133.1; 130.4; 129.8; 127.7; 121.4; 119.3; 26.6; 16.7.

The protected phenol (16.0 g, 44.3 mmol) was subjected to the general bromination procedure to yield the pure product as a white solid (9.2 g, 17.8 mmol, 40%).

$^1\text{H}$  NMR ( $\text{CDCl}_3$ , 400 MHz):  $\delta$  7.76-7.66 (m, 4H); 7.47-7.35 (m, 6H); 7.29 (d,  $J$  = 7.8 Hz, 1H); 6.85 (dd,  $J$  = 7.8 Hz,  $J$  = 1.7 Hz, 1H); 6.39 (d,  $J$  = 1.7 Hz, 1H); 4.69 (s, 2H); 4.04 (s, 2H); 1.15 (s, 9H).  $^{13}\text{C}$  NMR ( $\text{CDCl}_3$ , 100 MHz):  $\delta$  135.4; 131.1; 130.1; 130.0; 128.0; 121.7; 119.8; 32.7; 26.5; 26.5.

The dibromide (9.2 g, 17.8 mmol) was converted to the diphosphonate according to the general procedure and the pure product obtained as a viscous yellow oil (6.6 g, 10.4 mmol, 58%).

$^1\text{H}$  NMR ( $\text{CDCl}_3$ , 400 MHz):  $\delta$  7.76-7.69 (m, 4H); 7.45-7.30 (m, 7H); 6.82 (d,  $J$  = 7.8 Hz, 1H); 6.33 (s, 1H); 4.16-3.98 (m, 8H); 3.39 (d,  $J$  = 21.7 Hz, 2H); 2.74 (d,  $J$  = 21.5 Hz, 2H); 1.11 (s, 9H); 1.26 (t,  $J$  = 7.1 Hz, 6H); 1.04 (t,  $J$  = 7.1 Hz, 6H).  $^{13}\text{C}$  NMR ( $\text{CDCl}_3$ , 100 MHz):  $\delta$  153.1; 153.0; 135.3; 132.206; 131.2; 131.0; 129.9; 127.7; 122.4; 120.3; 120.3; 120.2; 120.2; 120.1; 120.0; 120.0; 120.0; 119.9; 61.7; 61.7; 61.7; 33.8; 32.5; 27.4; 26.4; 26.0; 16.4; 16.3; 16.2; 16.2.  $^{31}\text{P}$  NMR ( $\text{CDCl}_3$ , 162 MHz):  $\delta$  27.24 (d,  $J$  = 8.5 Hz); 25.77 (d,  $J$  = 8.5 Hz).

The dibromide precursor of **28** was prepared according to literature procedures.<sup>3</sup> To a solution of  $\text{NaBrO}_3$  (0.15 g, 1 mmol) in water (0.5 ml), a solution of 4-methyl-3-trifluoromethyl benzyl bromide (0.13 g, 0.5 mmol, in EtOAc (1 ml) was added and the mixture stirred vigorously. A solution of  $\text{NaHSO}_3$  (0.1 g, 1 mmol) in water (1 ml) was added dropwise and the deep-orange solution was stirred for 77 h. The mixture was poured out in  $\text{Et}_2\text{O}$  and the layers were separated. The aqueous layer was extracted two times with  $\text{Et}_2\text{O}$  and the combined organic layers were washed with 2 M  $\text{Na}_2\text{S}_2\text{O}_3$ , dried ( $\text{Na}_2\text{SO}_4$ ), filtered and concentrated. The resulting brown oil was subjected to column chromatography (0  $\rightarrow$  4% EtOAc/light petroleum) and the product was obtained as an off-white solid (0.11 g, 0.33 mmol, 66%).

$^1\text{H}$  NMR ( $\text{CDCl}_3$ , 400 MHz):  $\delta$  7.66 (s, 1H); 7.58 (s, 2H); 4.61 (s, 2H); 4.48 (s, 2H).  $^{13}\text{C}$  NMR ( $\text{CDCl}_3$ , 100 MHz):  $\delta$  138.5; 136.2; 133.3; 132.8; 126.7; 124.4; 122.3; 31.3; 27.8. IR (neat): 1319.7; 1297.0; 1224.7; 1197.7; 1169.2; 1144.5; 1122.0; 1055.7; 914.3; 908.2; 848.9; 776.2; 746.1; 667.7; 615.4;

583.4. The dibromide (0.96 g, 2.89 mmol) was treated with triethyl phosphite according to the general procedure, yielding diphosphonate **28** as a yellow oil (0.66 g, 1.47 mmol, 51%). <sup>1</sup>H NMR (CDCl<sub>3</sub>, 400 MHz): δ 7.64 (dd, *J* = 7.9 Hz, *J* = 1.4 Hz, 1H); 7.58 (s, 1H); 7.47 (d, *J* = 8.0 Hz, 1H); 4.09–3.98 (m, 8H); 3.35 (d, *J* = 22.6 Hz, 2H); 3.18 (d, *J* = 21.6 Hz, 2H); 1.25 (dd, *J* = 15.6 Hz, *J* = 7.1 Hz, 12H). <sup>13</sup>C NMR (CDCl<sub>3</sub>, 100 MHz): δ 132.8; 132.3; 130.9; 128.8; 127.3; 125.2; 122.4; 62.1; 62.0; 33.7; 32.3; 30.3; 28.9; 16.1.

<sup>19</sup>F NMR (CDCl<sub>3</sub>, 375 MHz) δ 18.38 (s, 3F). IR (neat): 1320.6; 1246.7; 1145.4; 1118.5; 1047.3; 1019.5; 958.9; 898.9; 856.8; 819.1; 730.0; 667.8; 641.7; 589.0; 556.2; 522.4. LC-MS retention time: 7.34 min (10 → 90% MeCN, 13.5 min run). Mass (ESI): *m/z* 447.1 [M + H]<sup>+</sup>; 892.8 [2M + H]<sup>+</sup>. Exact mass: Calculated for [C<sub>17</sub>H<sub>28</sub>F<sub>3</sub>O<sub>6</sub>P<sub>2</sub>]<sup>+</sup>: 447.13077. Found: 447.13058 [M + H]<sup>+</sup>.

Following the general procedure for bromination, the dibromide was obtained from 40 (0.85 g, 4.18 mmol) as a yellow solid (0.64 g, 1.76 mmol, 42%).

<sup>1</sup>H NMR (CDCl<sub>3</sub>, 400 MHz): 7.35 (d, *J* = 7.7 Hz, 1H); 7.06 (dd, *J* = 7.7 Hz, *J* = 1.5 Hz, 1H); 6.88 (s, *J* = 1.2 Hz, 1H); 4.53 (s, 2H); 4.45 (s, 2H); 4.46 (q, *J* = 8.0 Hz, *J* = 8.0 Hz, 2H). <sup>13</sup>C NMR (CDCl<sub>3</sub>, 100 MHz): δ 155.1; 140.0; 131.7; 127.4; 124.4; 123.2; 121.7; 113.0; 66.7; 66.3; 66.0; 65.6; 32.5; 27.1. <sup>19</sup>F NMR (CDCl<sub>3</sub>, 375 MHz): δ 3.79 (t, *J* = 8.0 Hz, 3F). IR (neat): 1611.8; 1582.2; 1508.7; 1423.7; 1289.7; 1259.7; 1224.4; 1204.4; 1158.2; 1099.9; 1068.0; 974.4; 855.9; 746.4; 663.3; 556.4; 539.8.

Following the general procedure for the Arbuzov reaction, 29 was obtained from the dibromide (0.64 g, 1.76 mmol) as a yellow oil (0.41 g, 0.86 mmol, 49%).

<sup>1</sup>H NMR (CDCl<sub>3</sub>, 400 MHz): δ 7.32 (dd, *J* = 7.8 Hz, *J* = 2.4 Hz, 1H); 6.94 (d, *J* = 7.8 Hz, 1H); 6.88 (s, 1H); 4.41 (q, *J* = 8.2 Hz, *J* = 8.2 Hz, 2H); 4.08–3.96 (m, 8H); 3.23 (d, *J* = 21.0 Hz, 2H); 3.12 (d, *J* = 21.0 Hz, 2H); 1.25 (dt, *J* = 7.1 Hz, *J* = 2.2 Hz, 12H). <sup>13</sup>C NMR (CDCl<sub>3</sub>, 100 MHz): δ 154.9; 132.0; 132.0; 131.9; 131.9; 131.6; 131.6; 131.6; 131.6; 124.6; 124.0; 124.0; 123.9; 123.9; 121.8; 120.1; 120.1; 120.0; 120.0; 113.9; 113.9; 113.9; 66.9; 66.6; 66.2; 65.9; 62.1; 62.0; 61.8; 61.8; 34.1; 32.7; 26.8; 25.4; 16.3; 16.2; 16.2; 16.1. <sup>31</sup>P NMR (CDCl<sub>3</sub>, 162 MHz): δ 26.58 (d, *J* = 8.7 Hz); 26.27 (d, *J* = 8.3 Hz).

<sup>19</sup>F NMR (CDCl<sub>3</sub>, 375 MHz): δ 3.61 (t, *J* = 11.3 Hz, 3F). IR (neat): 1615.8; 1581.8; 1429.8; 1393.3; 1243.0; 1158.0; 1019.8; 957.2; 845.9; 670.0; 624.4; 512.2. LC-MS retention time: 7.38 min (10 → 90% MeCN, 15 min run). Mass (ESI): *m/z* 477.0 [M + H]<sup>+</sup>; 952.8 [2M + H]<sup>+</sup>. Exact mass: Calculated for [C<sub>18</sub>H<sub>30</sub>F<sub>3</sub>O<sub>7</sub>P<sub>2</sub>]<sup>+</sup>: 477.14134; [C<sub>18</sub>H<sub>30</sub>F<sub>3</sub>O<sub>7</sub>P<sub>2</sub>Na]<sup>+</sup>: 499.12328. Found: 477.14118 [M + H]<sup>+</sup>; 499.12261 [M + Na]<sup>+</sup>.

To obtain compound **30** a chilled (0°C) solution of 2,5-dimethylphenol (1.22 g, 10 mmol) in DMF (50 ml) NaH (60% wt. dispersion in mineral oil, 0.8 g, 20 mmol) was prepared and the mixture was stirred for 10 min. A solution of 1-bromo-4,4,4-trifluorobutane (2.28 g, 12 mmol) in DMF (25 ml) was added and the mixture was stirred at room temperature for 16 h. After cooling to 0°C and quenching with water, the reaction mixture was extracted thrice with EtOAc and the combined organic layers were dried (Na<sub>2</sub>SO<sub>4</sub>); filtered and concentrated. The resulting yellow oil was subjected to column chromatography (0 → 10% EtOAc/light petroleum) and the pure product was obtained as a yellow fluid (2.13 g, 9.2 mmol, 92%).

<sup>1</sup>H NMR (CDCl<sub>3</sub>, 400 MHz): δ 7.01 (d, *J* = 7.5 Hz, 1H); 6.68 (d, *J* = 7.5 Hz, 1H); 6.61 (s, 1H); 3.99 (t, *J* = 5.9 Hz, 2H); 2.31 (s, 3H); 2.39–2.25 (m, 2H); 2.17 (s, 3H); 2.10–2.00 (m, 2H). <sup>13</sup>C NMR (CDCl<sub>3</sub>, 100 MHz): δ 156.5; 136.6; 130.4; 128.6; 125.8; 123.5; 121.1; 111.8; 65.8; 31.2; 31.0; 30.7; 30.4; 22.4; 21.3; 15.7. <sup>19</sup>F NMR (CDCl<sub>3</sub>, 375 MHz): δ 11.26 (t, *J* = 10.9 Hz, 3F). IR (neat): 1615.9; 1586.1; 1508.8; 1385.3; 1337.0; 1285.9; 1248.6; 1231.1; 1149.9; 1128.0; 1026.7; 804.7; 661.7; 598.8; 586.4; 553.3.

Following the general procedure for bromination, this dimethyl compound (0.2 g, 0.86 mmol) was converted into the dibromide, which was obtained as a yellow solid (0.26 g, 0.66 mmol, 77%).  $^1\text{H}$  NMR ( $\text{CDCl}_3$ , 400 MHz):  $\delta$  7.27 (d,  $J = 7.7$  Hz,  $^1\text{H}$ ); 6.95 (dd,  $J = 7.7$  Hz,  $J = 1.3$  Hz,  $^1\text{H}$ ); 6.87 (s,  $^1\text{H}$ ); 4.50 (s, 2H); 4.44 (s, 2H); 4.10 (t,  $J = 5.9$  Hz, 2H); 2.48-2.31 (m, 2H); 2.19-2.06 (m, 2H).  $^{13}\text{C}$  NMR ( $\text{CDCl}_3$ , 100 MHz):  $\delta$  156.5; 139.9; 131.1; 128.5; 126.4; 121.4; 112.1; 66.3; 33.1; 30.9; 30.6; 28.2; 22.2.  $^{19}\text{F}$  NMR ( $\text{CDCl}_3$ , 375 MHz):  $\delta$  11.4 (t,  $J = 10.6$  Hz, 3F). IR (neat): 1685.6; 1607.6; 1496.0; 1450.6; 1383.7; 1337.9; 1249.6; 1230.4; 1149.1; 1025.9; 835.7; 663.2; 626.2; 553.0.

Following the general procedure for the Arbuzov reaction, **30** was obtained from the dibromide (0.26 g, 0.66 mmol) as a yellow oil (0.23 g, 0.45 mmol, 68%).

$^1\text{H}$  NMR ( $\text{CDCl}_3$ , 400 MHz):  $\delta$  7.26 (dd,  $J = 7.5$  Hz,  $J = 2.7$  Hz,  $^1\text{H}$ ); 6.86 (s,  $^1\text{H}$ ); 6.84 (d,  $J = 9.8$  Hz,  $^1\text{H}$ ); 4.08-3.95 (m, 10H); 3.20 (d,  $J = 21.6$  Hz, 2H); 3.11 (d,  $J = 21.5$  Hz, 2H); 2.44-2.30 (m, 2H); 2.14-2.04 (m, 2H); 1.24 (dd,  $J = 12.8$  Hz,  $J = 6.9$  Hz,  $^1\text{H}$ ).  $^{13}\text{C}$  NMR ( $\text{CDCl}_3$ , 100 MHz):  $\delta$  156.0; 156.0; 155.9; 155.9; 131.6; 131.6; 131.5; 131.5; 131.1; 131.0; 131.0; 131.0; 128.3; 125.6; 122.1; 122.1; 122.1; 122.0; 118.8; 118.8; 118.7; 118.7; 112.8; 112.8; 112.7; 112.7; 66.1; 61.9; 61.9; 61.7; 61.6; 34.1; 32.8; 30.6; 30.3; 30.0; 29.5; 27.1; 25.7; 22.0; 22.0; 16.2; 16.1; 16.1.  $^{19}\text{F}$  NMR ( $\text{CDCl}_3$ , 375 MHz):  $\delta$  11.28 (t,  $J = 10.9$  Hz, 3F). IR (neat): 1612.1; 1581.7; 1511.6; 1431.2; 1391.5; 1248.9; 1149.2; 1050.8; 1019.6; 954.9; 819.9; 627.5; 518.1. LC-MS retention time: 8.01 min (10  $\rightarrow$  90% MeCN, 15 min run). Mass (ESI):  $m/z$  505.07 [ $\text{M} + \text{H}$ ] $^+$ ; 1008.87 [ $2\text{M} + \text{H}$ ] $^+$ . Exact mass: Calculated for  $[\text{C}_{20}\text{H}_{34}\text{F}_3\text{O}_7\text{P}_2]^+$ : 505.17264;  $[\text{C}_{20}\text{H}_{33}\text{F}_3\text{O}_7\text{P}_2\text{Na}]^+$ : 527.15458. Found: 505.17254 [ $\text{M} + \text{H}$ ] $^+$ ; 527.15411 [ $\text{M} + \text{Na}$ ] $^+$ .

Compound **31** was prepared as follows. Following the general procedure for bromination, the dibromide was obtained from **41** (1.36 g, 5 mmol) as a yellow solid (0.97 g, 2.25 mmol, 45%).

$^1\text{H}$  NMR ( $\text{CDCl}_3$ , 400 MHz):  $\delta$  7.40 (d,  $J = 7.8$  Hz,  $^1\text{H}$ ); 7.14 (d,  $J = 7.8$  Hz,  $^1\text{H}$ ); 6.99 (s,  $^1\text{H}$ ); 5.11-4.95 (m,  $^1\text{H}$ ); 4.52 (s, 2H); 4.44 (s, 2H).  $^{13}\text{C}$  NMR ( $\text{CDCl}_3$ , 100 MHz):  $\delta$  154.5; 140.3; 132.2; 128.2; 124.9; 122.3; 119.4; 114.0; 75.9; 75.6; 75.2; 75.0; 74.6; 74.2; 73.9; 32.0; 26.0.  $^{19}\text{F}$  NMR ( $\text{CDCl}_3$ , 375 MHz):  $\delta$  4.47 (d,  $J = 5.6$  Hz, 6F). IR (neat): 1616.7; 1578.9; 1507.6; 1425.5; 1368.6; 1256.1; 1193.7; 1147.8; 1103.3; 890.7; 758.3; 686.3; 662.9; 532.8.

Following the general procedure for the Arbuzov reaction, **31** was obtained from the dibromide (0.97 g, 2.25 mmol) as a yellow oil (0.76 g, 1.48 mmol, 66%).

$^1\text{H}$  NMR ( $\text{CDCl}_3$ , 400 MHz):  $\delta$  7.40 (dd,  $J = 7.8$  Hz,  $J = 1.6$  Hz,  $^1\text{H}$ ); 7.04 (d,  $J = 7.8$  Hz,  $^1\text{H}$ ); 7.00 (s,  $^1\text{H}$ ); 5.13-5.02 (m,  $^1\text{H}$ ); 4.09-3.97 (m, 8H); 3.23 (d,  $J = 20.6$  Hz, 2H); 3.14 (d,  $J = 20.5$  Hz, 2H); 1.24 (t,  $J = 7.1$  Hz, 12H).  $^{13}\text{C}$  NMR ( $\text{CDCl}_3$ , 100 MHz):  $\delta$  155.8; 155.8; 155.8; 155.7; 133.8; 133.8; 133.7; 133.7; 133.0; 132.9; 126.5; 126.4; 126.4; 126.4; 124.1; 121.4; 121.3; 121.3; 116.7; 116.6; 75.4; 75.0; 74.7; 63.8; 63.7; 63.6; 63.5; 34.2; 32.8; 27.4; 26.0; 16.7; 16.6; 16.5.  $^{31}\text{P}$  NMR ( $\text{CDCl}_3$ , 162 MHz):  $\delta$  25.77 (d,  $J = 1.45$  Hz).  $^{19}\text{F}$  NMR ( $\text{CDCl}_3$ , 375 MHz):  $\delta$  4.25 (d,  $J = 7.5$  Hz, 6F).

Phosphonate **32** was obtained similarly. Following the general procedure for bromination, the dibromide was obtained from **42** (0.34 g, 1 mmol) as a yellow solid (0.31 g, 0.62 mmol, 62%).

$^1\text{H}$  NMR ( $\text{CDCl}_3$ , 400 MHz):  $\delta$  7.47 (d,  $J = 2.4$  Hz,  $^1\text{H}$ ); 7.28 (d,  $J = 1.4$  Hz,  $^1\text{H}$ ); 6.58 (s,  $^1\text{H}$ ); 4.49 (s, 2H); 4.42 (s, 2H).  $^{13}\text{C}$  NMR ( $\text{CDCl}_3$ , 100 MHz):  $\delta$  150.7; 143.6; 132.2; 130.7; 127.1; 124.1; 121.45; 116.5; 31.7; 25.8.

Following the general procedure for the Arbuzov reaction, **32** was obtained from the dibromide (0.34 g, 0.68 mmol) as a yellow oil (0.10 g, 0.16 mmol, 24%).

$^1\text{H}$  NMR ( $\text{CDCl}_3$ , 400 MHz):  $\delta$  7.47 (dd,  $J = 7.9$  Hz,  $J = 1.8$  Hz,  $^1\text{H}$ ); 7.22 (s,  $^1\text{H}$ ); 7.15 (d,  $J = 8.0$  Hz,



<sup>1</sup>H); 4.06-3.97 (m, 8H); 3.20 (d, *J* = 20.9 Hz, 2H); 3.12 (d, *J* = 20.6 Hz, 2H); 1.24 (t, *J* = 7.0 Hz, 12H). <sup>13</sup>C NMR (CDCl<sub>3</sub>, 100 MHz): δ 150.7; 150.7; 150.7; 132.2; 132.1; 132.1; 132.1; 131.7; 127.5; 127.5; 123.6; 123.6; 123.5; 123.5; 121.3; 121.1; 118.2; 61.8; 61.8; 61.7; 61.7; 33.7; 32.3; 27.0; 25.6; 16.0; 15.9; 15.9; 15.8; 15.8. <sup>31</sup>P NMR (CDCl<sub>3</sub>, 162 MHz): δ 25.57 (q, *J* = 7.8 Hz, *J* = 7.8 Hz). <sup>19</sup>F NMR (CDCl<sub>3</sub>, 375 MHz): δ 8.71 (s, 9F). IR (neat): 1506.3; 1425.1; 1393.4; 1250.4; 1135.7; 1022.1; 999.7; 965.7; 849.4; 816.5; 727.5; 629.2; 524.4. LC-MS retention time: 8.85 min (10 → 90% MeCN, 15 min run). Mass (ESI): *m/z* 613.07 [M + H]<sup>+</sup>; 1224.73 [2M + H]<sup>+</sup>. Exact mass: Calculated for [C<sub>20</sub>H<sub>28</sub>F<sub>9</sub>O<sub>7</sub>P<sub>2</sub>]<sup>+</sup>: 613.11611; [C<sub>20</sub>H<sub>28</sub>F<sub>9</sub>O<sub>7</sub>P<sub>2</sub>Na]<sup>+</sup>: 635.09805. Found: 613.11622 [M + H]<sup>+</sup>; 635.09790 [M + Na]<sup>+</sup>.

## Synthesis of aldehyde building blocks 33 and 34

### Aldehyde 33

The silyl-protected aldehyde was prepared according to literature procedures.<sup>4</sup> 4-hydroxybenzaldehyde (1.22 g, 10 mmol) was dissolved in DMF (25 ml), imidazole (0.95 g, 14 mmol) was added and the reaction mixture cooled to 0 °C. A solution of TBDMS-Cl (1.8 g, 12 mmol) in DMF (5 ml) was added dropwise and the reaction stirred at room temperature for 4 h. After removal of the solvent, the residue was taken up in EtOAc and washed with sat. aq. NaHCO<sub>3</sub> and sat. aq. NaCl, dried (Na<sub>2</sub>SO<sub>4</sub>), filtered and concentrated. The crude product was subjected to column chromatography (0 → 5% EtOAc/light petroleum) and obtained as a pale yellow oil (2.12 g, 9.0 mmol, 90%).

<sup>1</sup>H NMR (CDCl<sub>3</sub>, 400 MHz): δ 9.89 (s, 1H); 7.79 (d, *J* = 8.6 Hz, 2H); 6.95 (d, *J* = 8.5 Hz, 2H); 1.00 (s, 9H); 0.25 (s, 6H). <sup>13</sup>C NMR (CDCl<sub>3</sub>, 100 MHz): δ 190.8; 161.4; 131.9; 130.3; 120.4; 25.5; 18.2; -4.4.

### Aldehyde 34

*p*-hydroxymethylbenzaldehyde was prepared following literature procedures.<sup>5</sup> Terephthalaldehyde (6.71 g, 50 mmol) was dissolved in THF (50 ml). The mixture was cooled to 0 °C, NaBH<sub>4</sub> (0.66 g, 17.5 mmol) was added and the reaction stirred for 4 h. After concentration of the reaction mixture, the residue was taken up in EtOAc, water was added and the layers separated. The organic layer was washed with water, sat. aq. NaCl, dried (Na<sub>2</sub>SO<sub>4</sub>), filtered and concentrated. The residue was purified by column chromatography (10 → 40% EtOAc/light petroleum) and the pure compound was obtained as an off-white solid (1.88 g, 13.8 mmol, 28%).

<sup>1</sup>H NMR (CDCl<sub>3</sub>, 400 MHz): δ 9.99 (s, 1H); 7.87 (d, *J* = 8.1 Hz, 2H); 7.53 (d, *J* = 8.0 Hz, 2H); 4.80 (s, 2H). <sup>13</sup>C NMR (CDCl<sub>3</sub>, 100 MHz): δ 192.1; 147.8; 135.6; 129.9; 126.9; 64.5.

*p*-hydroxymethylbenzaldehyde (1.88 g, 13.8 mmol) was protected with the TBDMS functionality as described for **33**, yielding **34** as a yellow fluid (3.0 g, 12.0 mmol, 87%).

<sup>1</sup>H NMR (CDCl<sub>3</sub>, 400 MHz): δ 10.00 (s, 1H); 7.85 (d, *J* = 8.3 Hz, 2H); 7.49 (d, *J* = 8.0 Hz, 2H); 4.82 (s, 2H); 0.96 (s, 9H); 0.12 (s, 6H). <sup>13</sup>C NMR (CDCl<sub>3</sub>, 100 MHz): δ 192.0; 148.6; 135.3; 129.8; 126.2; 64.4; 25.9; 18.4; -5.3.

## References

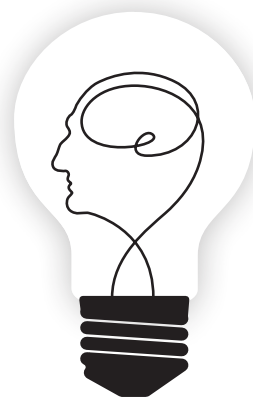
1. Canning, PSJ, Maskill, H, McCruddem, K, et al. A product analytical study of the thermal and photolytic decomposition of some arenediazonium salts in solution. *Bull Chem Soc Jpn.* 2002; 75:789-800.
2. Kumar, P, Zheng, W, McQuarrie, SA, et al. <sup>18</sup>F-FESB: Synthesis and automated radiofluorination of a novel <sup>18</sup>F-labelled PET tracer for beta-amyloid plaques. *J Labelled Comp Radiopharm.* 2005;983-996.
3. Kikuchi, D, Sakaguchi, S, and Ishii, Y. An Alternative Method for the Selective Bromination of Alkylbenzenes Using NaBrO(3)/NaHSO(3) Reagent. *J Org Chem.* 1998; 63:6023-6026.
4. Azuma, H, Miyasaka, K, Yokotani, T, et al. Lipase-catalyzed preparation of optically active 1'-acetoxychavicol acetates and their structure-activity relationships in apoptotic activity against human leukemia HL-60 cells. *Bioorg Med Chem.* 2006; 14:1811-1818.
5. Mak, CC, Bampos, N, Darling, SL, et al. A strategy for the assembly of multiple porphyrin arrays based on the coordination chemistry of Ru-centered porphyrin pentamers. *J Org Chem.* 2001; 66:4476-4486.





# Appendices

- I Building blocks for polyfluorinated bis-styrylbenzenes
- II Samenvatting
- III Dankwoord
- IV Curriculum vitae
- V Publication list



## Samenvatting

De ziekte van Alzheimer (AD) is de meest prevalentie vorm van dementie met veroudering als belangrijkste risicofactor. De toenemende vergrijzing gaat dan ook gepaard met een stijgende incidentie van AD en drukt hierbij een zware stempel op zowel sociaaleconomisch vlak als op de volksgezondheid. De precieze etiologie van deze aandoening is echter onbekend en helaas ontbreekt een adequate therapie. Histologisch kenmerkt deze ziekte zich door de ophoping van een tweetal eiwitten in de cortex van het brein, namelijk gehyperfosforyleerd  $\tau$  in neurofibrillary tangles en amyloid- $\beta$  (A $\beta$ ) peptiden in amyloid plaques. Deze eiwitophoping lijkt zich al te voltrekken tientallen jaren voordat de eerste klinische symptomen merkbaar zijn. Detectie van deze accumulatie *in vivo* in een preklinisch stadium is echter nog niet mogelijk. Het stellen van de definitieve diagnose is daarom tot op heden afhankelijk van obductie.

Een diagnostische methode die in staat is de specifieke accumulatie van amyloid plaques en de bijbehorende vroege corticale veranderingen te visualiseren of kwantificeren heeft niet alleen de potentie voor vroegdiagnostiek, maar leidt daarnaast ook tot een beter begrip van de pathofysiologie. Daarnaast kan zo'n methode uiteindelijk zelfs bijdragen tot de ontwikkeling en follow-up van een therapie. In dit proefschrift heb ik me dan ook gericht op het ontwikkelen van nieuwe diagnostische beeldvormende technieken om de specifieke histologische kenmerken van de ziekte van Alzheimer te kunnen detecteren. Daarvoor zijn enerzijds de nieuwe mogelijkheden van ultra-hoogveld MRI verkend (**Deel Eén**) en zijn anderzijds nieuwe molecular imaging strategieën ontwikkeld (**Deel Twee**).

Dat MRI in staat is om individuele amyloid plaques te detecteren is reeds aangetoond in zowel transgene AD muismodellen *in vivo* als in post-mortem humaan hersenweefsel. Recentelijk zijn de hiervoor benodigde hoge magnetische veldsterktes ( $\geq 7$  Tesla) beschikbaar gekomen voor klinisch gebruik. Door de verhoogde gevoeligheid voor veranderingen in magnetische susceptibiliteit en toegenomen resolutie bieden deze ultra hoogveld MRI-systemen nieuwe mogelijkheden om AD neuropathologie op te sporen, en wellicht zelfs eerder dan de huidige MRI biomarker van atrofie van de hersenen.

In **Deel Eén** wordt de relatie tussen optredende veranderingen in MRI-contrast of wel natief contrast met bijbehorende neuropathologische veranderingen tot op microscopisch niveau bestudeerd. Dit begrip is van essentieel belang voor de verdere ontwikkeling van klinisch toepasbare MRI-technieken.

Na een korte uitleg over de werking van MRI (**hoofdstuk 2**), onderzochten we allereerst de toepasbaarheid en beperkingen van post-mortem formale gefixeerd hersenmateriaal voor de ontwikkeling van nieuwe MRI-technieken voor het diagnosticeren van AD. (**hoofdstuk 3**) Langdurige fixatietijden veroorzaakte destructie van het normale hersenweefsel zichtbaar als hypo-intense gebieden op verscheidene MRI-sequenties. Aangezien vaak formale gefixeerd post-mortem hersenmateriaal voor dit doel wordt gebruikt, raden wij aan alleen met hersenweefsel te werken dat minder dan twee jaar gefixeerd is met regelmatige verversing van de formale ter voorkoming van deze artefacten.

De verschillen in resolutie tussen microscopie en MRI evenals de vervormingen die optreden tijdens de histologische bewerking bemoeilijken het precies correleren van het MRI contrast met het bijbehorende verantwoordelijke pathologische substraat. Om deze

registratieproblemen te minimaliseren hebben we een inductie-gekoppelde microcoil ontworpen die het mogelijk maakt om rechtstreeks MRI-beelden te vervaardigen van een histologische coupe van 60  $\mu\text{m}$ . (**hoofdstuk 4**) Achtereenvolgens kan deze coupe zonder verdere bewerking direct aan de gewenste histologische kleuring worden onderworpen. Aangezien zowel de MRI als de histologie op precies dezelfde coupe plaatsvinden is directe vergelijking mogelijk. Het ontwerp kan eenvoudig worden geïntegreerd in elke MRI-systeem met behulp van bestaande commerciële hardware waarbij een evidente verbetering van de signaal-ruisverhouding kan worden bereikt. Initiële toepassing op humaan AD hersenweefsel bevestigde voornoemde studies waarbij de accumulatie van A $\beta$  in het brein gepaard gaat met een focale hypointensiteit op T $_2^*$ -gewogen MRI.

Eerder onderzoek suggereerde dat louter de neerslag van A $\beta$ -peptiden in het hersenparenchym in plaques al zou kunnen leiden tot een signaalreductie op MRI onafhankelijk van de mogelijk gepaard gaande ijzeraccumulatie. Middels de bovenstaande MR-microscopie setup hebben wij getracht de MRI-karakteristieken van de verschillende vormen A $\beta$ -deposities in het brein in kaart te brengen. (**hoofdstuk 5**) Alleen de fibrillaire aggregatie in amyloid en niet de diffuse plaques leidde tot een signaalverandering in T $_2^*$  en T $_2$ -gewogen MRI. Tevens bleek ook cerebrale amyloid angiopathie (CAA) een negatief effect op het MRI signaal te hebben, alhoewel niet voor alle soorten CAA een zelfde signaalreductie werd waargenomen. De consequentie van deze resultaten is dat MRI in principe in staat is om niet zo zeer de totale cerebrale A $\beta$ -load te bepalen, maar het A $\beta$ -gerelateerde signaalverandering alleen samen hangt met aanwezigheid van amyloid plaques, één van de belangrijkste markers van AD.

In **hoofdstuk 6** hebben we veranderingen in corticale patronen van gezonde ouderen en AD-patiënten *in vivo* onderzocht middels susceptibiliteit gewogen 7T MRI. Tegelijkertijd werden soortgelijke corticale patronen eveneens waargenomen bij MRI verricht op post-mortem AD hersenmateriaal. Dit materiaal bood tevens de mogelijkheid tot correlatie met de onderliggende corticale pathologie verantwoordelijk voor deze signaal veranderingen. De frontale cortex van AD-patiënten presenteerde zich *in vivo* met een diffuse hypointense corticale band (57%), terwijl deze niet werden geobserveerd bij gezonde controles van dezelfde leeftijd. Uit de histologische studie bleek dat het corticale patroon op MRI niet primair overeenkwam met de distributie van amyloid plaques of neurofibrillaire tangles, maar het liet een duidelijk correlatie zien met microglia- en myeline-geassocieerde ijzer ophoping alsmede een veranderde corticale myeline cytoarchitectuur. Deze resultaten zijn veelbelovend voor de *in vivo* detectie van de onderliggende pathologische veranderingen in AD middels MRI. Toekomstig onderzoek dient uit te wijzen of dit corticaal patroon specifiek is voor AD.

**Deel Twee** beschrijft de ontwikkeling van doelgerichte contrastmiddelen voor de specifieke *in vivo* detectie en visualisatie van verschillende A $\beta$ -aggregaten, zoals CAA en amyloid plaques. *In vivo* implementatie van zulke moleculaire imaging strategieën voor het bestuderen of diagnosticeren van neurodegeneratieve ziekten is in sterkte mate afhankelijk van de karakteristieken van de gekozen imaging ligand, zoals de detectielimiet en het vermogen om de bloed-hersen barrière (BBB) te passeren. In dit kader bespreekt **Hoofdstuk 7** de mogelijkheden met betrekking tot moleculaire neuro-imaging middels MRI.

Voorafgaand aan deze thesis hebben we heavy chain antilichaamfragmenten (V<sub>H</sub>H) geselecteerd die zich uitsluitend binden aan CAA versus verscheidene V<sub>H</sub>Hs die zowel CAA als alle parenchymateuze humane A $\beta$ -deposities herkennen. Afkomstig uit het antilichaamrepertoire van de *Camelidae* ontbreekt bij deze klasse antilichamen de licht ketens, maar desondanks heeft het N-terminale domein ofwel het V<sub>H</sub>H-fragment een vergelijkbare hoge en specifieke affiniteit als die van conventionele antilichamen. De potentie van V<sub>H</sub>H om als *in vivo* contrastmiddel CAA en/of cerebraal A $\beta$  te detecteren hangt af van hun vermogen om in het brein te geraken. In **Hoofdstuk 8** is de mogelijke BBB passage getest met een middels een *in vitro* BBB systeem. De CAA-specifieke V<sub>H</sub>H ni3A transmigreerde het meest efficiënt over deze barrière via een actief transport mechanisme. Het verschil in transmigratie ten opzichte van andere V<sub>H</sub>H lijkt grotendeels te berusten op aanwezigheid van een drietal specifieke aminozuren in het N-terminale domein.

Als volgende stap, zijn in **hoofdstuk 9** de *in vivo* eigenschappen onderzocht van een tweetal radioactief of fluorescent gelabelde V<sub>H</sub>H, ni3A en pa2H, na toediening in transgeen AD muismodel. Na een initiële snelle renale klaring liet <sup>99m</sup>Tc-pa2H een dag na de injectie een significant hogere opname zien in het brein van de transgene AD muizen. Na het omzeilen van de BBB werd voor beide fluorescent gelabelde V<sub>H</sub>H de *in vivo* specificiteit voor A $\beta$  bevestigd, waarbij pa2H zelfs 24 uur na toediening goed zichtbaar bleef. Opvallend echter was dat beide V<sub>H</sub>H affiniteit vertoonden voor zowel het parenchymale als het vasculaire A $\beta$  in het muizenbrein, dit in tegenstelling tot eerdere toepassing op humaan hersenweefsel, waarbij ni3A uitsluitend CAA detecteerde. Ondanks dat de cerebrale accumulatie zich nog ver beneden de detectielimiet bevindt nodig voor *in vivo* beeldvorming, laat deze studie zien dat V<sub>H</sub>Hs in staat zijn om cerebraal A $\beta$  te detecteren en vormt hiermee een basis voor verdere ontwikkeling en verbetering.

Hiernaast is een geheel andere strategie gekozen voor de detectie van amyloid plaques, namelijk door het ontwikkelen van kleine organische amyloid bindende moleculen. **Hoofdstuk 10** beschrijft de synthese van gefluorineerde bis-styrylbenzenes als mogelijke <sup>19</sup>F-MRI contrastmiddelen alsmede hun fluorescente en A $\beta$  bindingskarakteristieken. Idealiter passeren deze kleine organische moleculen de BBB en binden daar aan amyloid waarbij het geïncorporeerde fluor direct detecteerbaar is middels MRI zonder enig endogeen achtergrondsignaal. De meeste verbindingen vertoonden een hoge affiniteit voor A $\beta$  plaques van zowel muizen als mensen. Ze bleken echter een andere bindingsplaats te hebben dan chrysamine G, één van de oorspronkelijke verbindingen waarvan onze bis-styrylbenzenes zijn afgeleid. Ondanks een hoge logP waarde waren bijna alle gefluorineerde bis-styrylbenzenes in staat om *in vivo* de BBB te passeren en aan amyloid te binden in de transgene AD muizen. Initiële post-mortem <sup>19</sup>F nuclear spin resonantie (NMR) verricht voor de meest veelbelovende verbinding toonde echter aan dat verder MRI studies nog niet te rechtvaardigen zijn gezien de significante reductie van de <sup>19</sup>F-sigitaal, welke voornamelijk een direct gevolg lijkt te zijn van samenstelling van het hersenweefsel.

Om de farmacokinetiek mogelijk te verbeteren wordt in **Hoofdstuk 11** de synthese en karakteristieken van zes bis-pyridylethylbenzenes beschreven met het idee dat het incorporeren van een stikstofatoom dergelijke structuren meer hydrofiel zou kunnen. Ook deze verbindingen delen geen bindingsplaats met chrysamine G. Met een logP waarde tussen 3 en 5 waren alle verbindingen in staat om *in vivo* de BBB te passeren en het amyloid in het brein

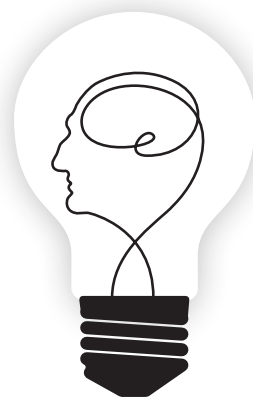


te labelen. Op basis van de in en *ex vivo* eigenschappen en de oplosbaarheid toonde bis-(4-pyridylethenyl)benzene de meeste potentie om als backbone te dienen voor verdere ontwikkeling tot een amyloid imaging biomarker, bijvoorbeeld als mogelijke PET-tracer.



# Appendices

- I Building blocks for polyfluorinated bis-styrylbenzenes
- II Samenvatting
- III Dankwoord
- IV Curriculum vitae
- V Publication list



## Dankwoord

Terwijl je jezelf steeds dieper ingraaft in je eigen onderzoek, leer je het meest van de mensen die af en toe vanaf een berg zand met je mee kijken. Dank aan allen die op welke wijze dan ook hebben bijgedragen aan deze promotie en de tijd eromheen.

*Prof.dr. M.A. van Buchem*; Beste Mark, met jouw onbegrensde nieuwsgierigheid om bruggen te bouwen tussen onderwerpen danwel mensen vormde Boston een onmisbare avontuurlijke start van mijn promotie, zowel op persoonlijk als op onderzoeksgebied. Jouw manier om grootst te durven denken mét oog voor detail inspireert om wilde plannen om te zetten tot daden. Dat je hierbij tevens ruimte laat voor de ander om te groeien erop vertrouwend dat dit juist eenieders gedrevenheid ten goede komt, is een bijzondere zeldzame eigenschap die het nastreven waard is.

*Ir.dr. L. van der Weerd*; Beste Louise, als co-promotor wist jij je feilloos mijn ongebreidelde enthousiasme te kanaliseren en vormde je één van de belangrijkste pijlers van dit proefschrift. Jouw persoonlijkheid, kennis en kunde waren een belangrijke steun tijdens de uiteenlopende uitdagingen van dit project. Dank voor de wetenschappelijke ruimte die je me hebt gegeven, alsmede het tijdig inperken hiervan.

*Prof.dr. E.C. Klasen, prof.dr. P.C.W. Hogendoorn*; "The job of an educator is to teach students to see vitality in themselves" by Joseph Campbell says it all, waarvoor dank.

*Prof.dr. A.G. Webb*; Dear Andrew, je inburgering is voltooid, alhoewel je je verhuld onder 't Nederlands motto "doe maar normaal dan doe je gek genoeg" ben je een onmisbare spil in resonantieland en verbaas je me telkens weer met simpele oplossingen voor complexe problemen.

*Prof.dr. S.M. van der Maarel, professor H.J. Tanke*; Dank voor de ruimte die ik kreeg om binnen en met jullie afdeling te werken.

*Many thanks to Brian Bacskaj, Matthew Frosch, Steve Greenberg, Anna Moore and Mike McMahon* for a great and meaningful time in Boston and Baltimore.

Dear Brian, the way your research group and lab is run made me feel right at home every time, and sets an inspiring example that gained my deepest respect.

*Collega's van de radiologie, humane genetica en het Gorter Centrum*; Niet alleen voor de nodige wetenschappelijke kritische noten, maar vooral, dank voor alle behulpzaamheid en gezelligheid.

*Sanneke, Jasper, Daan, Sara, Kim, Mick, Brigit, Maaïke, Ernst, Maarten, Dana en Egbert*; Intra- en extracurriculaire beslommingen, alles passeerde de revue om voorzien van jullie reflectie en projectie menig euvel te verhelpen zonder een lach te schuwen.

*Elmi, Pauline, Marjo*; De onmisbare schakel voor velen, zo ook voor mij; behulpzaam, betrokken en relativerend, en dat alles altijd met een lach!

*Ingrid, Frans, Peter, Corry, Annelies*; Dank voor jullie kennis en kunde om gezamenlijk de oplossingen te maken en vast te leggen, het liefst onder het genot van een grap, een rol en een dropje.

*Fons, Kees, Karthick, Liesbeth en het LIC*; Geen resonantie op het Gorlaeus zonder jullie, dank voor jullie eindeloze geduld!

*Remco en Sjoerd*; Dank voor jullie pathologische blik leidend tot onweerlegbare correlaties.

*Bert en Geert*; Geen barrière moeilijker dan het venijn van het brein hetgeen een boeiende en vruchtbare samenwerking op heeft geleverd.

*Varsha, Mark, Thanos en Bert*; Dank voor de (ver)b(l)indende chemie.

*Vrienden van St. Hubert e.o., Heeren van Elschendael, Bostonians, RT54, clubgenoten, Van Leeuwen's, Roefjes, (oud)huisgenoten, Vincent, Bart F, Emile et al.*; Dank voor jullie vriendschap en bijdrage in de vorm van de broodnodige afleiding in welke vorm dan ook.

*Paranimf Maarten*; Mister CCLB, geen sugar rush, maar pure aSpartaan van het begin tot aan het einde. Resonerend op jouw resting state met een haarscherpe humoreuze relativering wist je vaak alle veldlijnen weer de juiste richting in te duwen. Fijn om je aan mijn zijde te hebben!

*Paranimf David*; Davidemus, not your regular kind of guy, vanaf de eerste Beantown bitterbal was any limit far beyond the sky. Met jouw credo 'Niet mokken maar boven de A4 wokken' kwamen we immer uit en in dezelfde schuit. Wetenschap wellicht de rode draad en vriendschap opzoekers de kabel, maar in de ether immer de gedeelde spanning voor een nieuw onmogelijk avontuur.

*Bram en Katarina, Christine en Jaap*; See one, do one, teach one, als jullie kleine broertje ontdekte ik de wereld deels door jullie ogen en nog steeds laat ik mij leiden door af te kijken van jullie beiden. Dank voor jullie steun en vertrouwen. First there were three, and soon there will be three again!

*Ons mam en ons pap*; Rustig kijkend van de zijkant slaan jullie mij al jaren gade en weten vaak beter dan ik mijn richting. Klaarstaand voor in het geval dat, laten jullie mijzelf alles ontdekken in de wetenschap dat er altijd een veilig thuis is, vroeger al en nu nog steeds.

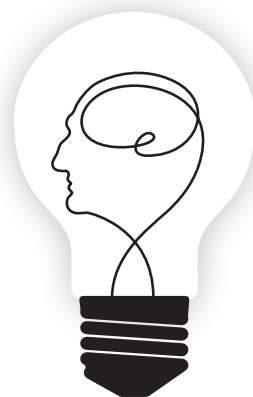
*Anne*; Samen gek en niets te gek... Dank voor je blinde steun en de ruimte die je me geeft.

Jouw onderzoek is nog maar net begonnen, *Pim*!



# Appendices

- I Building blocks for polyfluorinated bis-styrylbenzenes
- II Samenvatting
- III Dankwoord
- IV Curriculum vitae
- V Publication list







## Curriculum vitae

Rob Nabuurs was born on the August 19, 1981 in Nijmegen, the Netherlands, and spend his childhood in Sint Hubert. In 1999 he graduated from the Elzendaal College in Boxmeer with honours. After two years of studying Aerospace Engineering at the Technical University of Delft, he switched to the medical school of the Leiden University. He passed his propedeuse exam with honours, and participated in two Honours Classes of the Leiden University Medical Center (LUMC).

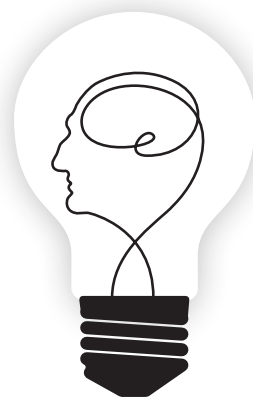
During his medical study he was awarded a research scholarship in the Excellent Student Program of the LUMC and as part of the program he started as a junior research student at the Neuroimaging Research Group led by prof.dr. M.A. van Buchem. Together they joined the Molecular Imaging group of the A. Martinos Institute for Neuroimaging, Massachusetts General Hospital (supervisor prof.dr. Anna Moore) to work on contrast agents that may enter the brain. During this year he expanded this research by starting a collaboration with the Alzheimer's Research Group, MassInstitute of Neurological Diseases (supervisor dr. Brian Bacskai). These combined experiences formed the foundation of the current thesis and after obtaining his doctorate degree in 2007 he started as a full time Ph.D. student working on this thesis at the LUMC.

In order to finish his medical degree he enrolled in his clinical rotations in 2011 ended in May 2013 with a final internship at the dept. of Neurosurgery of the Medical Center Haaglanden. In July 2013 he started as a radiologist in training at the LUMC. However drawn by his previous experiences in the field of neurosurgery he decided to change his career and as of April 1, 2014 he will start working as a resident (ANIOS) in the department of Neurosurgery at the Vrije Universiteit medical center (VUmc) in Amsterdam.



# Appendices

- I Building blocks for polyfluorinated bis-styrylbenzenes
- II Samenvatting
- III Dankwoord
- IV Curriculum vitae
- V Publication list



## Publication list

**Nabuurs RJA**, Thomas DL, Thornton JS, Lythgoe ML, van der Weerd L; *MRI of Animal models of brain disease* Essential Bioimaging Methods (2009) 1<sup>st</sup> edition, ch. 13.

van Rooden S, Maat-Schieman ML, **Nabuurs RJA**, van der Weerd L, van Duijn S, van Duinen SG, Natté R, van Buchem MA, van der Grond J; *Cerebral amyloidosis: post-mortem detection with human 7.0-T MR imaging system* Radiology (2009) 253(3):788-96

**Nabuurs RJA**, de Backer M, van der Weerd L, van Buchem MA; *MR-based molecular imaging of the brain: the next frontier* AJNR (2010) 31(9):1577-83

Fry BG, Winter K, Norman JA, Roelants K, **Nabuurs RJA**, van Osch MJ, Teeuwisse WM, van der Weerd L, McNaughtan JE, Kwok HF, Scheib H, Greisman L, Kochva E, Miller LJ, Gao F, Karas J, Scanlon D, Lin F, Kuruppu S, Shaw C, Wong L, Hodgson WC; *Functional and structural diversification of the Anguimorpha lizard venom system* Mol Cel Proteomics (2010) 9(11):2369-90

**Nabuurs RJA**, Hegeman I, Natté R, van Duinen S, van Buchem MA, van der Weerd L, Webb AG; *High field MRI of single histological slices using a inductively-coupled self-resonant microcoil: application to ex-vivo samples of patients with Alzheimer's disease* NMR Biomed (2011) 24(4):351-7

**Nabuurs RJA**, van Duijn S, van Rooden S, Maat-Schieman MLC, van Duinen SG, van Buchem MA, van der Weerd L, Natté R; *MRI artefacts in human brain tissue after prolonged formalin storage* Magn Reson Med (2011) 65(6):1750-58

Rutgers KS, **Nabuurs RJA**, Schenk GJ, Verrips T, van Duinen SG, Maat-Schieman MLC, van Buchem MA, de Boer AG, van der Maarel SM; *Transmigration of beta amyloid specific heavy chain antibody fragments across the in vitro blood-brain barrier* Neuroscience (2011) 190:37-42

**Nabuurs RJA**, Rutgers KS, Welling MM, Metaxas A, de Backer ME, Bacskai BJ, van Buchem MA, van der Maarel SM, van der Weerd L; *In vivo detection of amyloid- $\beta$  deposits using heavy chain antibody fragments* PLoS One (2012) 7(6):e38284

van Duijn S, **Nabuurs RJA**, van Duinen SG, Natté R, van Buchem MA, Alia A; *Longitudinal monitoring of sex-related in vivo metabolic changes in the brain of Alzheimer's disease transgenic mouse using magnetic resonance spectroscopy* J Alzheimers Dis (2013) 34(4):1051-9

**Nabuurs RJA**, Natté R, de Ronde F, Hegeman-Kleinn I, Dijkstra J, van Duinen SG, Webb AG, Rozemuller AJ, van Buchem MA, van der Weerd L; *MR Microscopy of human amyloid- $\beta$  deposits: Characterization of parenchymal amyloid, diffuse plaques, and vascular amyloid.* J Alzheimers Dis (2013) 34(4):1037-49

Fry BG, Undheim AEB, Ali SA, Debono J, Scheib H, Ruder T, Jackson TNW, Morgenstern D, Cadwallader L, Whitehead D, **Nabuurs RJA**, van der Weerd L, Vidal N, Roelants K, Hendrikx I, Gonzalez SP, Jones A, King GF, Antunes A, Sunagar K; *Squeezers and leaf-cutters: differential diversification and degeneration of the venom system in toxiciferan reptiles* Mol Cell Proteomics 2013

van Duijn S, **Nabuurs RJA**, van Duinen SG, Natté R; *Comparison of histological techniques to visualize iron in paraffin embedded brain tissue of patients with Alzheimer's disease* J Histochem Cytochem 2013

Welling MM, **Nabuurs RJA**, van der Weerd L; *Pathogens in chronic brain infections and amyloid deposits as a potential target for detecting early events in Alzheimer's disease* Alzheimers Dement 2014 (accepted)

**Nabuurs RJA**, Kapoerchan V, Metaxas A, de Jongh S, de Backer M, Welling MM, Jiskoot W, Windhorst A, Overkleef H, van Buchem MA, Overhandt M, van der Weerd L; *Polyfluorinated bis-styrylbenzene as amyloid- $\beta$  plaque binding ligands* Bioorg Med Chem (accepted)

## Publications in progress

Pratt JS, Kung M, **Nabuurs RJA**, Moore AV, Sorensen AG *Direct incubation of donor lymphocytes with ferumoxides labels monocytes and B cells* (Submitted)

Muskulus M, Scheenstra AEH, **Nabuurs RJA**, Dijkstra J, van der Weerd L, Verduyn-Lunel S; *The generalized Moore-Rayleigh test* (Submitted)

Cohen D, **Nabuurs RJA**, Steup-Beekman GM, Versluis MJ, Emmer BJ, Zandbergen M, Luyendijk J, van Buchem MA, Allaart CF, Wolterbeek R, Bruijn JA, van Duinen SG, Huizinga TWJ, Bajema IM; *Complement in neuropsychiatric SLE links antibodies to thrombo-ischemia* (Submitted)

**Nabuurs RJA**, van Rooden S, van Duijn S, Versluis MJ, Emmer BJ, Liem MK, Milles JR, Webb AG, Frosch MP, van Duinen SG, van der Weerd L, Natté R, van der Grond J, van Buchem *Detection of cortical changes in Alzheimer's disease at ultra-high field MRI* (Submitted)

**Nabuurs RJA**, Kapoerchan V, Metaxas A, Hafjit S, de Backer M, Welling MM, Jiskoot W, Windhorst A, Overkleef H, van Buchem MA, Overhandt M, van der Weerd L; *Bis-pyridylethenylbenzenes as novel backbone for amyloid- $\beta$  binding compounds* (Submitted)

**Nabuurs RJA**, Welling MM, van Buchem MA, van der Weerd L, de Boer AG, Schenk GJ; *In vivo targeted tumor-uptake using CRM197* (in preparation)

Van Duijn S, **Nabuurs RJA**, van Duinen SG, Natté R; *Distribution of cortical iron and myelin in Alzheimer's disease patients* (in preparation)

Rotman M, Welling MW, Bunschoten A, de Backer ME, Rip J, **Nabuurs RJA**, Gaillard PJ, van Buchem MA, van der Maarel SM, van der Weerd L; *Optimized delivery of an anti-amyloid VHH-2H heavy chain antibody fragment to the mouse brain* (in preparation)

## Patents

Van der Weerd L, **Nabuurs RJA**, Kapoerchan V, Overhand M, van Buchem MA. *<sup>18</sup>F and <sup>19</sup>F based amyloid tracers and their applications* (patent filed)

## Abstracts

Pham W, **Nabuurs RJA**, van Buchem MA, Moore A; *Design and synthesis of novel myristoylated polyarginine peptides for in vivo molecular neuroimaging*. Proceedings of the 14<sup>th</sup> Annual Meeting of the International Society for Magnetic Resonance Imaging, Seattle 2006, p.369

**Nabuurs RJA**, van Duijn S, Milles JR, van Rooden S, van der Grond J, Reiber JH, van Buchem MA, van der Weerd L; *High resolution T2\* and Phase contrast of human AD brain tissue at 9.4 T: a structural comparison* Proceedings of the 16<sup>th</sup> Annual Meeting of the International Society for Magnetic Resonance Imaging, Toronto 2008

**Nabuurs RJA**, Webb AG, van der Weerd L; *MRI of a Single Histological Slice Using Inductively Coupled Self-resonant Microcoils* World Molecular Imaging Meeting, Montreal 2009 (oral presentation)

**Nabuurs RJA**, Versluis MJ, van Duijn S, van Duinen SG, Webb AG, van Buchem MA, van der Weerd L; *Effects of A $\beta$  deposits in ex vivo human brains on MRI as a function of spatial resolution* International Conference on Alzheimer's Disease, Hawaii 2010

**Nabuurs RJA**, Rutgers KS, Welling MM, de Backer ME, van Buchem MA, van der Maarel SM, van der Weerd L; *In vivo use of fluorescently and radiolabeled single chain antibody fragments for the detection of A $\beta$  in an Alzheimer's disease mouse model* World Molecular Imaging Meeting, Kyoto 2010

**Nabuurs RJA**, Que I, Chan A, Ma G, Löwik CWGM, van der Weerd L; *In vivo NIR imaging of amyloid- $\beta$  deposits in APP-PS1 mice: a spatial-temporal and lifetime profile of AOI987* World Molecular Imaging Meeting, Kyoto 2010

**Nabuurs RJA**, Rutgers KS, Metaxas A, Welling MM, Metaxas A, Bacskai BJ, de Backer ME, van Buchem MA, van der Maarel SM, van der Weerd L; *In vivo detection of amyloid- $\beta$  deposits using heavy chain antibody fragments* European Molecular Imaging Meeting, Leiden 2011





